Proceedings of

the 29th Grain Formation Workshop /

Dust in Galaxies 2011

held at Center of Planetary Science (CPS), Kobe, Japan

9—11 November 2011

Eds.: S. Okuzumi, I. Sakon, Y. Kimura, A. Inoue, H. Kimura, H. Miura, T. Muto, T. Yamamoto

Online materials; https://www.cps-jp.org/~gfw/pub/2011-11-09/

Proceedings of the 29th Grain Formation Workshop / Dust in Galaxies 2011

held at Center of Planetary Science (CPS), Kobe, Japan

9—11 November 2011

Eds.: S. Okuzumi, I. Sakon, Y. Kimura, A. Inoue, H. Kimura, H. Miura, T. Muto, T. Yamamoto

Online materials; https://www.cps-jp.org/~gfw/pub/2011-11-09/

Program

9th November, 2011

13:30-13:40 Tetsuo Yamamoto (Hokkaido University) / Akio Inoue (Osaka Sangyo University)
"Opening Remarks"
13:40-14:00 Akemi Tamanai (Heidelberg University)
"A study of dust grain formation: A role of minor elements"
14:00-14:20 Chiyoe Koike (Osaka University)
"IR spectra of silica (SiO2) polymorphs"
14:20-14:40 Steffen Wetzel (Heidelberg University)
"Condensation and solid phase reactions of Mg silicate system"

(coffee break)

15:00-15:40 Aki Takigawa (University of Tokyo)
"Morphological analyses of presolar alumina grains towards understanding the circumstellar dust formation and evolution processes"
15:40-16:00 Yuki Kimura (Tohoku University)
"Homogeneous nucleation experiment of cosmic dust"

(coffee break)

16:20-16:40 Akane Sakurai (Nagoya university)
"Star formation and dust extinction properties of local galaxies seen from AKARI"
16:40-17:00 Tsutomu Takeuchi (Nagoya University)
"A Study on the Star Formation History of Galaxies Revealed by the UV-IR Bivariate Luminosity Function"

(coffee break)

17:20-17:40 Shogo Masaki (Nagoya University)
"An analytic model for the distribution of matter and dust around galaxies"
17:40-18:00 Daisuke Yamasawa (Hokkaido University)
"From dust to galaxy in the early universe"
18:00-18:20 Ryosuke Asano (Nagoya University)
"Evolution of grain size distribution of galaxies"

10th November, 2011

9:20-9:40 Hitoshi Miura (Tohoku University)
"A new diagnostic method for growth condition of rock-forming minerals"
9:40-10:00 Nagisa Machii (kobe University Graduate school of science)
"Conditions for chondrules to be intruded and embedded into matrix"

(coffee break)

10:20-10:40 Masafumi Matsumura (Kagawa University)
"Verification on the Alignment Mechanism of Dust Grains by Radiative Torques: Correlation between the Interstellar Polarization and Dust Temperature"
10:40-11:00 Mitsuyoshi Yamagishi (Nagoya University)
"An analytic model for the distribution of matter and dust around galaxies"
11:00-11:20 Mina Ishikura (Hokkaido University)
"Lyman alpha transfer in multiphase system - effect of internal motion of cloud"

-- poster presentation (5min talk) --

11:20-11:25 Chihiro Kaito (Ritsumeikan University)
"Laboratory analogy of amorphous enstatite fine grain formation and crystallization"
11:25-11:30 Takuya Ikeda (Kyoto University)
"Development of Mercury Dust Monitor (MDM) for BepiColombo MMO"
11:30-11:35 Itsuki Sakon (University of Tokyo)
"Mid-Infrared Multi-Epoch Observations of Dust Forming Nova V1280Sco"
11:35-11:40 Okuzumi Satoshi (Nagoya University)
"Coagulation and Radial Drift of Porous Dust Aggregates in Protoplanetary Disks"

(lunch break)

13:20-14:00 Akira Tsuchiyama (Osaka University)
"Three-dimensional structure of Itokawa regolith particles."
14:00-14:40 Eizo Nakamura (Okayama University)
"Comprehensive analyses of micro-grains from the surface of asteroid returned by Hayabusa: Implications for collisional space environments"

(coffee break)

15:10-15:30 Hiroki Senshu (Chiba Institute of Technology Planetary Exploration Research Center)
"Levitation dust: a source of IDPs"
15:30-15:50 Junya Matsuno (Osaka University)
"An synthesis experiment of GEMS analogue material produced by thermal plasma"

(coffee break)

16:10-16:50 Shota Nunomura (National Institute of Advanced Industrial Science and Technology)
"Coagulation and growth of Dust in Plasma by Charge Fluctuations ~from Molecules to clusters and dust"

16:50-17:10 Yasuaki Hayashi (Kyoto Institute of Technology Faculty of Engineering and Design)
"Coulomb-Crystallization and Behavior of Fine Particles in Experimental Plasmas"

11th November, 2011

9:20-9:40 Koji Wada (Chiba Institute of Technology Planetary Exploration Research Center)
"Numerical simulation of collisions between dust aggregates consisting of particles with a size distribution"

9:40-10:00 Hiroshi Kobayashi (Friedrich Schiller University Jena)
"Necessary condition for gas giant formation"

10:00-10:20 Yuri Fujii (Nagoya University)
"Ionization Degrees with Dust Grains in Circumplanetary Disks"

(coffee break)

10:40-11:20 Masashi Arakawa (Kyushu University)
"Hydrogen ordering in ice observed from neutron diffraction: Application to planetary science"

11:20-11:40 Kyoko Tanaka (Hokkaido University, Institute of Low Temperature Science)
"Evaporation of icy planetesimals due to planetesimal bow shocks"

(lunch break)

13:40-14:20 Atsuo Okazaki (Hokkai-Gakuen University)
"Structure of the Wind-Wind Collision Shocks in Massive Binaries"

14:20-14:40 Toshiya Ueta (University of Denver Division of Natural Science and Mathematics)
"Interactions between stellar winds and the interstellar medium and their effects on dust grains"

(coffee break)

15:00-15:20 Toru Kondo (Nagoya University)
"Properties of dust and PAHs in clouds with high-energetic phenomena based on the AKARI all-sky-survey maps"

15:20-15:40 Kohji Tsumura (ISAS/JAXA)
"Distribution of the 3.3μm PAH band in our Galaxy detected by the AKARI IRC"

Abstract

"A study of dust grain formation: A role of minor elements"
TAMANAI, Akemi (Heidelberg University)
Large amount of silicate dust grains has been detected in many astronomical environments. However, silicate dust grain formation itself is not well understood yet. Although theoretical simulations for possible condensates illustrate how abundant the different silicate dust materials are in astronomical surroundings and they give us a key to clarify the formation of silicates, these simulations do not cover all dust species, which possibly exist. In order to deepen the understanding from the first species condensing out of the gas to the entire condensation sequence of dust materials present in the environments, first we take into account the species, which contain minor elements (Al, Na, and Li) and perform the mid-IR spectroscopic measurements for obtaining benchmark spectra.

"IR spectra of silica (SiO_2) polymorphs"
KOIKE, Chiyoe (Osaka University)
As for circumstellar dust, Mg-rich silicates such as forsterite and enstatite were mainly detected. Recently, silica SiO_2 is detected in debris disks. This referred silica is various crystal types such as quartz, fused quartz, annealed silica. We report on the infrared spectra of various types' silica and discuss on possibility of silica and observation.

"Condensation and solid phase reactions of Mg silicate system"
WETZEL, Steffen (Heidelberg University)
We have been performing in-situ IR spectroscopy during formation process of layers by co-evaporation of Fe, Mg, MgO, and SiO under well-defined pressure and temperature in ultra high vacuum (UHV) system in order to deepen the understanding of IR spectral changes upon condensation conditions, especially effects related to elemental Fe particles enclosed in silicates.

“Morphological analyses of presolar alumina grains towards understanding the circumstellar dust formation and evolution processes”

TAKIGAWA, Aki (University of Tokyo)

Presolar grains are the condensates around evolved stars, which have survived the isotopic exchange processes in the early solar system. Alumina (Al2O3), one of the first condensates around O-rich evolved stars, is observed by infrared spectroscopy for many AGB stars and present in chondrites as presolar grains. In order to understand the mineralogical nature of presolar alumina and the formation and evolution processes of circumstellar alumina grains, we performed systematic analyses of morphology, crystal structure, and oxygen isotopic compositions of alumina grains in unequilibrium ordinary chondrites, and dissolution experiments of alumina polymorphs

“Homogeneous nucleation experiment of cosmic dust”

KIMURA, Yuki (Tohoku University)

Homogeneous condensation is a first occurring process to obtain solid materials around evolved stars. Since there is no or very few heterogeneous nucleation site, solid materials must condense by themselves homogeneously. However, there is no data that how large super-saturation is required for the condensation. To investigate the homogeneous nucleation and growth process of cosmic dust, interferometric observation was attempted for the fist time to the gas evaporation method in laboratory. In preliminary experiment, we found the degree of super-saturation for nucleation was extremely high, 10^6-10^7, which was determined from the interferogram. Surface free energy, sticking probability and growth velocity can also be deduced from the calculated values by the semi-phenomenological nucleation theory.

“Star formation and dust extinction properties of local galaxies seen from AKARI”

SAKURAI, Akane (Nagoya university)

Accurate estimation of the star formation -related properties of galaxies is crucial for understanding the evolution of galaxies. In galaxies, ultraviolet (UV) light emitted by formed massive stars is attenuated by the dust which is also produced by the SF activity, and is reemitted at mid- and far-infrared wavelengths (IR). In this study, we investigated the star formation rate (SFR) and dust extinction using data at UV and IR. We selected local galaxies, which are detected at AKARI FIS 90um band. We measured flux densities at FUV and NUV from the GALEX images. We examined the SF and extinction by using 4 wave bands given by AKARI. Then, we calculated FUV and total IR luminosities, and obtained the so called SF luminosity (the total luminosity related to star formation activity) and the SFR. We found that in most of galaxies, SF luminosity is dominated by luminosity of dust. We also found that galaxies with higher SF activity have a higher fraction of SF hidden by dust. Especially, SF of galaxies which have SFRs>20Myr is almost completely hidden by dust. Although

these results were claimed by previous studies, confirming them precisely using much larger samples from AKARI and GALEX all sky surveys has a great impact on our understanding of the SF in Local galaxies.

“A Study on the Star Formation History of Galaxies Revealed by the UV-IR Bivariate Luminosity Function”

TAKEUCHI, Tsutomu (Nagoya University)

Star formation in galaxies is tightly connected to the dust grain formation through the production of heavy elements. Observationally, it is the most direct to measure the star formation rate by the amount of ionizing UV photons, but dust formed by the star formation scatter and absorb these photons, and finally re-emit the energy at the IR. Hence, it is necessary to observe galaxies at both UV and IR to explore their star formation in the cosmic history. In this presentation, first we introduce a statistical method to handle the two datasets, which have been treated independently at each wavelength in a unified manner, and reveal the star formation in galaxies hidden by dust.

“An analytic model for the distribution of matter and dust around galaxies”

MASAKI, Shogo (Nagoya University)

We develop a simple analytic model to make a quick interpretation of the observed mass and dust surface density profiles around galaxies reported by Menard et al. (2010). Our model is based on the so-called halo model. We show our model reproduces the observed profiles very well, and discuss how far dust spreads from galaxies.

“From dust to galaxy in the early universe”

YAMASAWA, Daisuke (Hokkaido University)

We present a semi-analytic model for the formation and evolution of high-redshift galaxies. We investigate cosmic star formation rates and the reionization history, using our galaxy model in which we include a novel implementation of dust size evolution and resulting molecular hydrogen (H_2) formation on dust grains in the early universe. We show cosmic star formation efficiency of our model is low, because the H_2 formation rate on dust grains is suppressed by the dust destruction by reverse shocks in supernova remnants. Our results show need of additional reioniation sources or top-heavy IMF in $z>6$ for the cosmological reionization. We conclude that not only the amount but also the size distribution of dust strongly affects the cosmic star formation efficiency and the IMF transition from Pop III to Pop II.

“Evolution of grain size distribution of galaxies”

ASANO, Ryosuke (Nagoya University)

To understand the galaxy evolution, it is essential to understand the evolution of dust in galaxies. Up to now, dust evolution has been studied with various dust evolution models, but most of them are based on the assumption of a typical size of grains. However, since grain size distribution of galaxies varies by various processes (dust destruction by SN shocks, metal accretion onto surface of grains and etc.) [Yamasawa et al. (2011), Hirashita et al. (2011)], grain size distribution is a very important ingredient to understand the dust evolution. In this talk, we would introduce the dust evolution model with grain size distribution and report our first results.

“A new diagnostic method for growth condition of rock-forming minerals”

MIURA, Hitoshi (Tohoku University)

Chondritic meteorites contain rock-forming minerals in which the chemical compositions are not uniform. The in-homogeneity is termed as zoning profile, which is considered to reflect the growth condition (cooling rate, closed- or open-system, super-cooling, and so forth) when they were formed in early solar system. We investigated the zoning profile, growth rate, and mineral morphology formed under a constant cooling rate based on a numerical scheme. We derived a new analytic expression to predict the growth rate and zoning profile with respect to the cooling rate. The analytic formula can be used as a diagnostic tool to evaluate the growth condition of solid-solution minerals, (e.g., olivine) from its zoning profile.

“Conditions for chondrules to be intruded and embedded into matrix”

MACHII, Nagisa (Kobe University)

Collision experiments were performed using glass bead of 3 mm in diameter as a chondrule analog and polydisperse silica particles of about 0.8 μm in diameter as a matrix analog. We investigated impact velocity and matrix size needed to capture the colliding chondrules. We showed that to embed a chondrule into matrix, impact pressure should be larger than the static strength of matrix. The minimum size for capturing a chondrule is at least 3 cm in diameter.

“Verification on the Alignment Mechanism of Dust Grains by Radiative Torques: Correlation between the Interstellar Polarization and Dust Temperature”

MATSUURA, Masafumi (Kagawa University)

N/A

“An analytic model for the distribution of matter and dust around galaxies”

YAMAGISHI, Mitsuyoshi (Nagoya University)

We develop a simple analytic model to make a quick interpretation of the observed mass and dust surface density profiles around galaxies reported by Menard et al.(2010). Our model is based on the so-called halo model. We show our model reproduces the observed profiles very well, and discuss how far dust spreads from galaxies.

“Lyman alpha transfer in multiphase system - effect of internal motion of cloud”

ISHIKURA, Mina (Hokkaido University)

For study of high-redshift galaxies, Lyα observation is crucial. Strong Lyα emission observed from high-redshift galaxies is problem, because of large optical depth for Lyα. Neufeld(1991) shows that assumption of multiphase structure (cloud and inter-cloud medium) permits higher escape fraction. However he neglects effect of internal motion of cloud. I will talk about Neufeld model, and results of my simulation with assumption of internal motion of dusty cloud.

“Laboratory analogy of amorphous enstatite fine grain formation and crystallization”

KAITO, Chihiro (Ritsumeikan University)

Amorphous enstatite ($MgSiO_3$) grains were produced by the simultaneous evaporation of SiO and Mg vapor by up and down double heaters method in Ar gas pressure of 10 Torr. Produced particles were mixture of MgO crystallites and amorphous $MgSiO_3$ structure. High-resolution electron microscopy showed the crystallites of MgO and $MgSiO_3$ crystallites less than 10nm. Crystallization of $MgSiO_3$ amorphous structure have been determined by heating in vacuum.

“Development of Mercury Dust Measurement (MDM) for BepiColombo MMO”

IKEDA, Takuya (Kyoto University)

N/A

“Mid-Infrared Multi-Epoch Observations of Dust Forming Nova V1280Sco”

SAKON, Itsuki (University of Tokyo)

V1280Sco is a slow dust-forming nova that appeared only at a distance of 1.6kpc. The evidence of dust formation was reported on 23 days after the discovery. We have carried out mid-infrared photometric and spectroscopic observations of this nova on day 150 with Subaru/COMICS and on days 1272 and 1616 with Gemini-S/TReCS. Then the near- to mid-infrared spectral energy distributions (SEDs) of V1280Sco on days 150, 1272 and 1616 are fitted by multi-components dust emission model. We have found that the astronomical silicate emission features only appear in the spectra obtained on 1272 and 1616, suggesting the later formation of silicate grains in the case of V1280Sco. In this presentation I will discuss the chemical evolution of dust grains formed in the ejecta of nova V1280Sco.

“Coagulation and Radial Drift of Porous Dust Aggregates in Protoplanetary Disks”

OKUZUMI, Satoshi (Nagoya University)

Rapid orbital drift of macroscopic dust particles is one of the major obstacles against planetesimal formation in proto-planetary disks. We reexamine this problem by considering porosity evolution of dust aggregates. We show that dust particles can evolve into highly porous aggregates (with internal densities of much less than 0.1 g/cc) even if collisional compression is taken into account. Furthermore, we find that the high porosity triggers significant acceleration in collisional growth. Thanks to this rapid growth, the highly porous aggregates are found to overcome the radial drift barrier at distances less than 10 AU from the central star. This suggests that, if collisional fragmentation is truly insignificant, formation of icy planetesimals is possible via direct collisional growth of submicron-sized icy particles.

“Three-dimensional structure of Itokawa regolith particles.”

TSUCHIYAMA, Akira (Osaka University)

Particles recovered by the Hayabusa spacecraft are considered to be regolith particles on asteroid Itokawa. Their 3D structures and external shapes were obtained using x-ray micro-tomography at SPring-8. The modal abundances of minerals and density of the bulk sample are similar to those of LL chondrites. Any large-scale melting textures, such as agglutinates in lunar regolith, were not observed. The size distribution and shape distribution are also different from those of lunar regolith. Based on these data, formation and evolution of regolith particles on Itokawa will be discussed.

“Comprehensive analyses of micro-grains from the surface of asteroid returned by Hayabusa: Implications for collisional space environments”

NAKAMURA, Eizo (Okayama University)

Meteorites are regarded as fragments of asteroids that fall to Earth's surface. However, information regarding the outer surface of asteroids is presumably destroyed during atmospheric entry, resulting in our inability to study the solar space-exposed exteriors of planetary bodies other than the moon sampled by the Apollo missions. JAXA conducted the Hayabusa mission. The original plan of the mission was to collect rocks from an S-type asteroid, Itokawa's surface by an impact sampling method; however, at the time of the touchdown, no projectile was fired, resulting in only minimal sample recovery from very near the surface. The sample capsule was successfully returned to Earth. Five lithic grains with diameters near 50 μm, collected during the Hayabusa sample-return mission, were comprehensively examined for surface texture and geochemistry. Oxygen isotope compositions indicate that the grains are extraterrestrial. Also considering the major-element compositions of the grains, it appears that Itokawa's surface is dominantly of ordinary-chondrite composition. Because the grains were sampled from very near the surface of the asteroid, grain surfaces retain textures reflecting the space environment influencing the physical nature of the asteroid exterior. The surfaces are dominated by fractures, and the fracture planes contain sub-um-sized craters and a large number of sub-μm- to several-μm-sized adhered particles, some of them glasses. The size distribution and chemical compositions of randomly sampled adhered objects, and the occurrences of sub-um sized craters, suggest formation by hypervelocity collisions of micrometeorites down to nm-scale, a process expected in the physically hostile environment at an asteroid's surface.

“Levitation dust: a source of IDPs”

SENSHU, Hiroki (Chiba Institute of Technology Planetary Exploration Research Center)

In this talk we will explain the mechanism of photoelectric dust levitation. A dust smaller than 1 μm can escape the gravitational field of asteroid due to electric repulsion making one of sources of IDPs.

“An synthesis experiment of GEMS analogue material produced by thermal plasma”

MATSUNO, Junya (Osaka University)

GEMS (Glass with Embedded Metal and Sulfide), which is included in cometary IDPs, is a sub-micron sized grain composed of an amorphous silicate with embedded Fe, Ni metals and sulfides. Keller and Messenger (2011) proposed that GEMS is condensed products from gases in the early solar system. However, no condensate experiments reported producing similar materials to GEMS. ITP (induction thermal plasma) provides so high temperature (~ 10,000 K) environment with rapid cooling rate (10^5-10^6 K/sec) that it makes vapor phase easily and produces nano-sized and non-equilibrium materials. We injected MgO, Fe, SiO_2 on the mean composition of GEMS into ITP. Run products were characterized by XRD and TEM. Sub-micron sized (about 50 nm) spherical grains were observed and their morphology were that each grains have amorphous silicate with embedded an iron (about 10 nm).

“Coagulation and Growth of Dust in Plasma by Charge Fluctuation ~ from Molecules to Clusters and Dust”

NUNOMURA, Shota (National Institute of Advanced Industrial Science and Technology)

N/A

“Coulomb-Crystallization and Behavior of Fine Particles in Experimental Plasmas”

HAYASHI, Yasuaki (Kyoto Institute of Technology Faculty of Engineering and Design)

Because the behavior of fine particles in a experimental plasma on the ground can be directly observed, the results obtained by observation more or less may contribute to the study on dusts in space, although conditions of plasmas are different to each other. Mono-disperse spherical fine particles can form a Coulomb crystal when they exist in a glow-discharge plasma with a large amount. We present Coulomb crystals formed by growing fine particles in plasma and the revolutional and rotational behaviors of fine particles in relation to magnetic field.

“Numerical simulation of collisions between dust aggregates consisting of particles with a size distribution”

WADA, Koji (Chiba Institute of Technology Planetary Exploration Research Center)

We have been performing numerical simulations of collisions between dust aggregates consisting of equal-sized particles. Particles in proto-planetary disks are, however, expected to have a size distribution. In this study we carry out numerical simulations of collisions between dust aggregates consisting of particles with a size distribution to evaluate the influence of the size distribution on the dust growth process. A preliminary result will be shown and discussed.

“Necessary condition for gas giant formation”

KOBAYASHI, Hiroshi (Friedrich Schiller University Jena)

In final stage of planet formation, planetary embryos grow through collisions with planetesimals. The gravitational scattering by the large embryo induces destructive collisions between planetesimals. Fragments produced by such collisions are ground down by successive collisions until the collisional velocities of very small bodies are sufficiently dumped by gas drag. They are consequently removed by the gas drag. As a result, the surface density of bodies around planetary embryos decreases. Since embryos grow through collisions with such bodies, their growth halts by collisional fragmentation. The final planetary mass, which is determined by the equilibrium between the growth of the embryos and the depletion of planetesimals by collisional fragmentation, is smaller than the critical core mass for gas giant formation through core accretion. However, since planetary atmosphere enhance their collisional cross section with small bodies, planetary embryo can exceed the critical core mass from large initial planetesimals in massive proto-planetary disks.

“Ionization Degrees with Dust Grains in Circum-planetary Disks”

FUJII, Yuri (Nagoya University)

During the formation of gas giants, disks appear around them. They are called circum-planetary disks. The most promising mechanism of accretion is the turbulence driven by magneto-rotational instability (MRI). MRI occurs when the ionization degree is high enough for magnetic fields to couple to gas. We calculate the ionization degrees to investigate if MRI really causes accretion of circum-planetary disks. Our result suggests that ionization degrees in circum-planetary disks are too low for MRI to be active.

“Hydrogen ordering in ice observed from neutron diffraction: Application to planetary science”

ARAKAWA, Masashi (Kyushu University)

Laboratory experiments and infrared observations suggest that a lot of water ice exists in a crystalline phase in our solar system. At ambient pressure, crystalline ice has two kinds of structure, ice Ih and ice XI. Ice Ih is normal ice with disordered hydrogen atoms. In contrast, ice XI is a hydrogen-ordered phase of ice Ih, and the ordered arrangement of hydrogen atoms makes ice XI ferroelectric. Existence of hydrogen-ordered ice in space is the subject of continuing astronomical debate. Electrostatic forces, caused by the ferro-electricity, increase the sticking probability of icy grains, and might play an important role in grain evolution and planetary formation in space. To discuss the existence of hydrogen-ordered ice in space, we need to investigate the kinetics and formation process of ice XI. For precise understanding of nucleation and growth process of ice XI, we performed neutron diffraction measurements of ice doped with various kinds of dopant as a catalyst

for the transformation to ice XI. In this presentation, I will talk about how temperature history, kind of dopant and concentration of dopant affect the formation of ice XI. In particular, I will discuss "memory effect" of hydrogen ordering in ice.

“Evaporation of icy planetesimals due to planetesimal bow shocks”
TANAKA, Kyoko (Hokkaido University)
We investigated heating and evaporation of a planetesimal due to planetesimal bow shocks associated with a planetesimal orbiting with supersonic velocity relative to the gas in a protoplanetary disk. We evaluated surface temperatures and evaporation rates of planetesimals based on the results of the previous studies of planetesimal bow shocks and formation of protoplanets. We found that icy planetesimals evaporate efficiently by bow shock heating in the stage of formation of protoplanets, where strong bow shocks are produced by gravitational perturbations by the protoplanets.

“Structure of the Wind-Wind Collision Shocks in Massive Binaries”
OKAZAKI, Atsuo (Hokkai-Gakuen University)
In binaries consisting of two massive stars, strong stellar winds from these stars collide each other. Shocked region produced by the wind-wind collision is thought to be a place where not only the particle acceleration and resulting high-energy emission but also the dust formation takes place. Studying the wind-wind collision shocks is thus of multi-facet importance. Numerical simulations suit it very well, given that massive binaries, in general, have large orbital eccentricities. In this talk, I will report on the structure of the wind-wind collision shocks in two massive binaries, eta Carinae and WR 140, obtained from 3-D numerical simulations.

“Interactions between stellar winds and the interstellar medium and their effects on dust grains”
UETA, Toshiya (University of Denver)
Latest results of far-IR imaging by AKARI, Spitzer, and Herschel have suggested that interactions between stellar winds and the interstellar medium (ISM) are not uncommon. These findings imply that circumstellar dust grains can be processed at the interface between stellar winds and the ISM before they are injected into the ISM and become ISM dust grains, and that there may be significant implications to our understanding of "Galactic dust grains". I will review the latest far-IR observations on the interface regions between stellar winds and the ISM and discuss what follow-up studies with ALMA and SPICA will help enhance our understanding of dust "production" by stars.

“Properties of dust and PAHs in clouds with high-energetic phenomena based on the AKARI all-sky-survey maps”

KONDO, Toru (Nagoya University)

Very recent radio, X-ray, and gamma-ray observations have revealed various kinds of high energetic phenomena from interstellar clouds in our Galaxy, such as the shock heating of clouds by supernovae and the production of TeV gamma-rays through interaction of high-energy cosmic-ray particles with clouds. Under such harsh interstellar environments, PAHs are processed and destroyed quite easily, while submicron dust grains survive for a relatively long time, which are collisionally heated to high temperatures. Therefore, spatial variations of the properties of dust and PAHs can provide observational evidence that energetic phenomena really take place in the corresponding regions from entirely different aspects from the radio, X-ray, and gamma-ray observations. We are currently conducting intensive reduction of AKARI all-sky-survey diffuse data, aiming at the public release of the all-sky maps within a year. By using part of the diffuse maps so far created at 9, 18, 90, and 140 micron, we have made a correlation study of the AKARI all-sky survey with the NANTEN, Suzaku, and HESS data. Among the AKARI data, the 9 μm map is sensitive only to PAHs without contribution from the mid-IR continuum, while the 18 micron map is important to trace shock-heated hot dust. As a result, we find that the ratios of the PAH to dust emission brightness significantly change in the clouds likely associated with high energetic phenomena. In the presentation, we summarize the overall results so far obtained, and also briefly introduce our activities on the all-sky-survey data reduction.

“Distribution of the 3.3μm PAH band in our Galaxy detected by the AKARI IRC”

TSUMURA, Kohji (ISAS/JAXA)

Polycyclic aromatic hydrocarbon (PAH) is a good tracer of distribution and physical properties of the interstellar dust because PAH has distinct emission bands in the near-infrared region. We analyzed the spectral data of the interstellar diffuse emission obtained with the low-resolution prism spectroscopy mode on the AKARI Infra-Red Camera (IRC) NIR channel in (2.0-5.0μm) wavelength region. As a result, a good correlation of the 3.3μm PAH band emission to the thermal emission from the interstellar dust was confirmed. We also construct the reference diffuse Galactic light (DGL) spectrum at 2-5μm by using this 3.3μm PAH band correlation as a tracer.

Proceedings

A study of dust grain formation: A role of minor elements

Akemi Tamanai[1,2], Harald Mutschke[2], Jürgen Blum[3]

1. Kirchhoff Institute for Physics, Heidelberg University, Im Neuenheimer Feld 227, D-69120 Heidelgerg, Germany
2. Astrophysical Institute and University Observatory, Friedrich-Schiller-University Jena, Schillergaesschen 3, D-07745, Germany
3. Institute for Geophysics and Extraterrestrial Physics, Technical University Braunschweig, Mendelssohnstr. 3, D-38106, Braunschweig, Germany

Abstract

A large amount of silicate dust grains has been detected in many astronomical environments. However, silicate dust grain formation itself is not well understood yet. Although theoretical simulations for possible condensates illustrate how abundant the different silicate dust materials are in astronomical surroundings and providing us with a key to clarify the formation of silicates, these simulations do not cover all dust species which possibly exist. In order to deepen the understanding from the first species condensing out of the gas to the entire condensation sequence of dust materials present in the environments, we take into account the species which contain minor elements (Al, Na, and Li) and perform the mid-IR spectroscopic measurements for obtaining benchmark spectra.

1. Introduction

Olivine as well as pyroxene dust grains have been observationally confirmed in various astronomical environments. Still it is not straightforward to obtain the precise chemical compositions (e.g. the ratio of Mg and Fe) and morphological aspects (e.g. size, shape, aggregate state) through the observed spectra. Meteorites, on the other hand, have provided us with exactly these detailed information. For instance, more than 10 different types of silicates have been discovered in the Allende meteorite including phyllosilicates (e.g. $Mg_3Si_4O_{10}(OH)_2$ (talc), $(Mg, Fe)_7Si_8O_{22}(OH)_2$ (anthophyllite)), but also different types of oxides and fullerene-like carbon (Jarosewich et al. 1987; Brearley 1996; Rubin 1997; Harris et al. 2000; Nozawa et al. 2009; Ma et al. 2010). Although it is possible to extract and analyze a small amount of a particular dust grain embedded in a meteorite, it is difficult to identify that via observations if the dust species is small in quantity. In other words, only very abundant dust grains can be detected and show their absorption peaks in the mid-infrared (MIR) regions of the electromagnetic spectrum. Though the less abundant grains definitely take part in the dust evolution process, the chemical pathways with regard to dust grain formation have not clearly understood yet. Especially, the formation process of one of the most abundant dust grains, i.e. the silicates, has not been elucidated evidently so far so that questions like the following remain: What is the highest-temperature condensation material? How does silicate dust formation take place? How much silicates are formed? Does silicate formation start by surface growth on high-temperature condensates such as, corundum and spinel, or directly from the gas phase? Understanding the evolution and formation of silicate dust grains can lead us not only to the properties and processing history of the entire grain population, but also to the transition and role of them in various surroundings in connection with star and planet formation. For that, we have taken into account the less abundant elements (Na, Li, Al), compared to Si and Mg, and have performed MIR spectroscopic extinction measurements of Al_2SiO_5 (kyanite), $NaAlSi_2O_6$ (jadeite), and $LiAlSi_2O_6$ (spodumene) by means of aerosol spectroscopy. The outcoming spectra will set criteria for MIR spectra obtained by condensation experiments in our group in the future (see more details in Wetzel et al. in this proceedings).

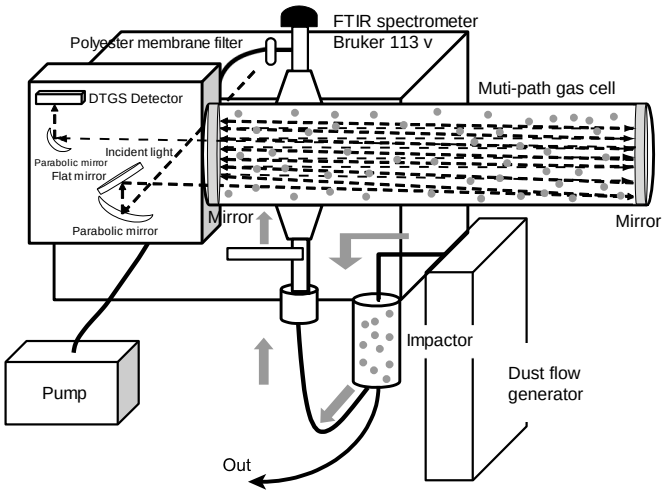

Fig. 1 A schematic diagram of the experimental apparatus for aerosol spectroscopy.

2. Experimental Setup

Fig. 1 shows the setup of the apparatus for the aerosol spectroscopic measurement. We have utilized a dust flow generator (Palas RBG1000) for dispersing a powdered sample into a nitrogen (N_2) gas stream. The dense aerosol is carried to a two-stage impactor which separated the large particles from the small ones (< 1 μm). The small-sized grains are concentrated by the impactor until a concentration of 10^6 particles per cubic centimeter is reached. In the end, only the small particles arrive in a White-type long-path infrared cell (MARS-8L/20V, Gemini Scientific Instr.) which retained 18 m path length by taking advantage of multiple reflection between two gold mirrors mounted on both sides in order to intensify the sensitivity. Since a Fourier Transformation Infrared Spectrometer (FTIR, Bruker 113v) with DTGS detector with CsI windows is fixed to the cell, it is possible to measure the extinction spectrum of the suspended dust particles in N_2 gas. As a consequence, we can avoid the environmental effect during the aerosol measurements, and the measurement condition is closer to a vacuum with regard to the dielectric function of medium (N_2: $\varepsilon \approx 1.0$) compared with the KBr (potassium bromide; $\varepsilon = 2.3$). Moreover, the risk of causing the powdered sample structurally deforms by the high pressurization required for the pellet technique, this problem is avoidable with aerosol spectroscopy. For clarifying the environmental effect, we have performed extinction measurements obtained by CsI (cesium iodine) pellets as well. CsI is particularly transparent between 2 and 50 μm in wavelengths, and has a higher value of optical constants than that of KBr (CsI n=1.74 & KBr n=1.52). The aerosol particles are extracted on a polyester-membrane filter that is mounted a little above the cell. The morphological aspect of the extracted particles was investigated by making use of a scanning electron microscope (SEM) (see more details in Tamanai & Mutschke 2010).

3. Samples

Silicate minerals, which contain the less abundant refractory elements, such as Al, Na, and Li, are discussed in this investigation.

A chemical composition of Al_2SiO_5 is a polymorph with three minerals, which are kyanite, andalusite, and sillimanite. Kyanite is formed under conditions of low temperatures (< 800°C) and high pressures, whereas sillimanite formation takes place at high temperatures (> 800°C) and a relatively wide range of pressures. On the other hand, andalusite is formed at a limited range of temperatures (~200°C and < 800°C) and pressures (< 4 kbar) (e.g. Althaus 1967; Whitney 2002). Here we only consider kyanite, which belongs to triclinic crystal system (e.g. Deer et al. 1997).

The presence of corundum (Al_2O_3) and quartz (SiO_2) induce formation of kyanite. This reversible chemical reaction will be described as

$$\mathbf{Al_2O_3 + SiO_2 \rightleftharpoons Al_2SiO_5}$$

(Mueller et al. 1977).

According to the equilibrium condensation calculations for the solar nebular (Davis & Richter 2003), albite ($NaAlSi_3O_8$) formation is expected at temperatures of approximately < 1000K and pressure of 10^{-3} bar. In fact, albite has been found in a unique unequilibrated chondrite, Kakangari (Brearley 1989) and a carbonaceous chondrite (type CR2), the Kaidun meteorite (Ivanov et al. 2001). Albite is not a target material for this investigation. It is closely related to jadeite ($NaAlSi_2O_6$) which has a monoclinic crystal structure and is possibly formed by a chemical reaction of jadeite and quartz. Since this is a reversible chemical reaction as well, albite decomposes to yield jadeite and quartz as below

$$\mathbf{NaAlSi_2O_6 + SiO_2 \rightleftharpoons NaAlSi_3O_8}$$

(Bucher & Grapes 2011).

Formation of spodumene ($LiAlSi_2O_6$: lithium aluminum silicate) occurs at low temperatures (<700°) and high pressure (> 2 kbar) (Stewart 1978) and has a monoclinic crystal structure (e.g. Deer et al. 2004). These rare elements have been engaged in discussions of isotopes in meteorites. Hydrogen, Helium, and Lithium were produced in the big bang nucleosynthesis so that Lithium is one of the primordial elements. According to Israelian et al. 2009, Lithium has been depleted effectively in our Sun like planet-hosting stars as compared with planet-free ones. In this manner, the existence of Lithium plays an important role in extrasolar planet search as well as mineral formation with different lithium isotopes.

Unfortunately, kyanite, jadeite, and spodumene have not been detected observationally, nor in meteorites. However, it is still worth investigating the optical properties of these materials for future potential. Table 1 represents a list of the measured samples, including their chemical and physical properties. All three samples are naturally formed minerals. Thus, the relative abundance of the elements (subscripts) is not exactly like the chemical formulae in Table 1. Note that fact-based chemical formulae (by EDX analysis) will be described elsewhere.

Table 1: Properties of the three samples

Mineralogical Name	Chemical Formula	Product	Particle size (μm)	Particle shape (μm)
Kyanite	Al_2SiO_5	Natural	< 1	Irregular
Jadeite	$NaAlSi_2O_6$	Natural (China)	< 1	Irregular
Spodumene	$LiAlSi_2O_6$	Natural (South Africa)	< 1	Irregular

4. Extinction Measurements

As described in Sec. 2, we have performed extinction measurements of kyanite, jadeite, and spodumene by making use of aerosol spectroscopy in the wavelength range between 2 and 50 μm. In order to clarify the environmental effect by the surrounding medium, spectra obtained by the aerosol spectroscopy are plotted together with spectra taken by the CsI pellet technique in Fig. 2. All plotted spectra are normalized since aerosol spectroscopic measurements are not quantitative. Redshift of bands can be observed along the entire extinction spectra of the three materials investigated by the pellet technique, due to the effect of electromagnetic polarization induced by the medium, CsI (e.g. Tamanai et al. 2006). Also, the disparity in band profiles

between the aerosol and CsI pellet measurements may result from: (1) sample structure deformation due to the high pressurization for making the CsI pellets, (2) the homogeneity and uniformity of particle dispersion in the measurement environment (localized or delocalized), (3) particle orientation, (4) distortion of crystal lattice during the grinding procedure (by hand or by a ball mill) (Imai et al. 2009), (5) the particle morphology, especially size and shape of aggregates (see also Tamanai et al. 2009).

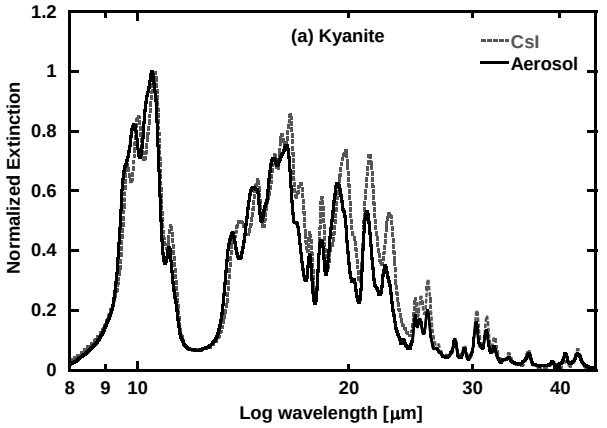

Aero.					
9.88	**10.49**	11.10	13.66	14.64	15.64
16.31	17.60	18.27	**19.27**	20.34	**21.23**
22.55	23.90	24.88	25.25	25.91	26.63
28.32	29.22	30.39	31.40	32.22	33.79
36.14	39.03	40.71	42.36		
CsI					
9.69	10.03	**10.59**	11.16	12.17	14.01
14.85	15.70	16.06	**16.52**	17.08	17.60
18.32	**19.81**	**21.42**	22.88	24.91	25.36
25.96	26.80	28.36	29.25	30.44	31.46
32.28	33.82	36.08	37.72	39.09	40.77
42.40					

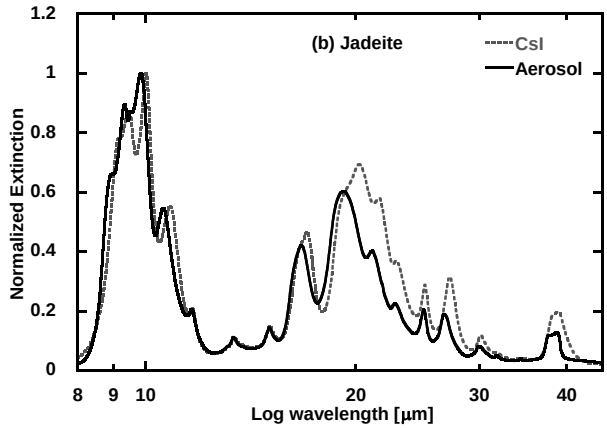

Aero.					
8.94	9.34	9.52	**9.86**	10.61	11.65
13.37	15.04	16.71	**19.25**	21.13	22.77
25.01	26.74	30.00	31.75	34.42	38.75
CsI					
9.19	9.42	9.52	**10.02**	10.86	11.67
13.39	15.07	17.04	**20.22**	21.60	22.84
25.11	27.24	30.17	31.85	34.47	38.96

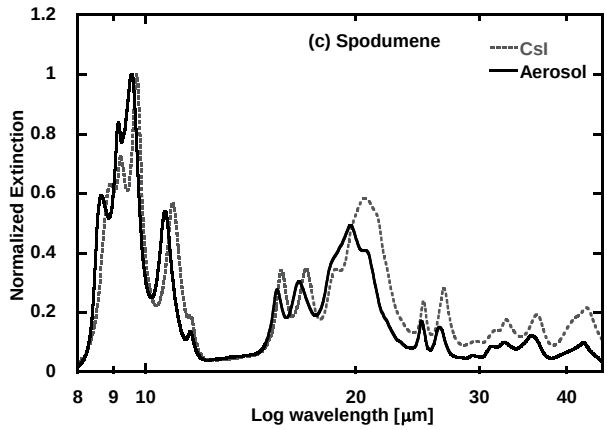

Aero.					
8.65	9.16	**9.56**	10.69	11.60	15.44
16.59	**19.69**	20.65	24.85	26.33	29.38
31.25	32.66	35.65	42.32		
CsI					
8.93	9.22	**9.72**	10.95	11.61	15.66
16.99	18.76	**20.53**	26.70	29.68	31.68
32.79	36.34	42.69			

Fig. 2 Normalized extinction vs. log wavelength of (a) Kyanite; (b) Jadeite; (c) Spodumene spectra obtained by the aerosol and CsI pellet measurements. The black solid line indicates the aerosol measurements, and the grey dotted line denotes the CsI pellet measurements. All peak positions are listed in the tables on the right hand side. The boldface numbers are the strong peaks in each material.

Both Jadeite and spodumene belong to inosilicates, which can be expressed by a general structural formula of XYZ_2O_6. In the case of jadeite and spodumene, the octahedral site (X) is filled with a different element (Li or Na), whereas Y and Z are occupied by the same elements (Y=Al and Y=Si). However, the strongest Si-O stretching vibration band of jadeite is situated to the long wavelength side (9.56 μm) compared to that of spodumene (9.34 μm).

5. Summary and Outlook

MIR spectroscopic measurements of silicate materials (kyanite, jadeite, spodumene), which contain less abundant elements such as Al, Na, and Li as compared with Si and Mg, are performed in medium-effect-free environments. These experimentally obtained spectra will be benchmarks for spectr, which will be measured by condensation experiments in the future.

Acknowledgements

We greatly appreciate Prof. A. Pucci for giving us an opportunity to present this project at GFW. We are thankful to Prof. H.-P. Gail for insightful opinions and comments. We are grateful to G. Born for her assistance with sample preparation and analysis and W. Teuschel for his technical support of our experimental apparatus. A. Tamanai expresses to Prof. T. Yamamoto her gratitude for the financial support of the workshop participation and CPS visit. Astronomical research has been supported by Deutsche Forschungsgemeinschaft (DFG) under the grant FOR 759.

Reference:

Althaus, E. 1967, Contr.Mineral.and Petrol., 16, 29-44

Brearley, A.J. 1989, Geochim. Cosmochim. Ac., 53, 2395-2411

Davis, A.M., and Richter, F.M. 2003, in Meteorites, Comets, and Planets, ed. A.J. Davis, Vol.1, Treatise on Geochemistry, eds. H.D. Holland, and K.K. Turekian (Oxford: Elsevier-Pergamon)

Brearley, A.J., and Prinz, M. 1996, LPS, 1081, 161-162

Bucher, K., and Grapes, R. 2011, Petrogenesis of Metamorphic Rocks (Berlin: Springer-Verlag)

Deer, W.A., Howie, R.A., and Zussman, J. 1997, Rock-Forming Minerals: Orthosilicates (UK: The Geological Society)

Deer, W.A., Howie, R.A., and Wise, V.S. 2004, Rock-Forming Minerals: Framework Silicates, Silica Minerals, Feldspathoids, and Zeolites (UK: The Geological Society)

Harris, P.J.F., Vis, R.D., and Heymann, D. 2000, Earth and Planetary Science Letters, 183, 355-359

Imai, Y., Koike, C., Chihara, H., Murata, K., Aoki, T., Tsuchiyama, A. 2009, A&A, 507, 277-281

Israelian, G., Mena, E.D., Santos, N.C., Sousa, S.G., Mayor, M. et al. 2009, Nature, 462, 189-191

Ivanov, A.V., Kononkova, N.N., Zolensky, M.E., Migdisova, L.F., and Stronganov, I.A. 2001, Lunar and Planetary Science, XXXII, 1386

Jarosewich, E., Clarke, R.S.Jr., and Barrows, J.N. 1987, The Allende Meteorite Reference Sample (Washington D.C.: Smithsonian Institution Press)

Ma, C. 2010, American Mineralogist L., 95, 188-191

Mueller, R.F., and Saxena, S.K. 1977, Chemical Petrology with applications to the Terrestrial Planets and Meteorites (N.Y.: Springer-Verlag)

Nozawa, J., Tsukamoto, K., Kobatake, H., Yamada, J., Satoh, H. et al. 2009, Icarus, 204, 681-686

Rubin, A.E. 1997, Meteoritics & Planetary Science, 32, 231-247

Stewart, D.B. 1978, Am. Mineral., 63, 970-980

Tamanai, A., Mutschke, H., Blum, J., and Meeus, G. 2006, ApJ, 648, L147-L150

Tamanai, A., Mutschke, H., Blum, J., Posch, Th., Koike, C., and Ferguson, J.W. 2009, A&A, 501, 251-267

Tamanai, A., and Mutschke, H. 2010, Infrared spectroscopy of dust particles in aerosols for astronomical application, in Fundamentals and Applications in Aerosol Spectroscopy, eds. J. Reid and R. Signorell, pp.101-123 (Florida: Taylor & Francis Group)

Whitney, D.L. 2002, Am. Mineral., 87, 405-416

IR spectra of silica (SiO_2) polymorphs

Koike C., Imai Y., Noguchi R., Chihara H.,
Ohtaka O., Tsuchiyama A.,
Department of Earth and Space Science,
Graduate School of Science, Osaka University,

Abstract

Recently, silica SiO_2 was detected in the protoplanetary disk around the T Tauri stars and in the debris disks. In some objects, annealed silica (cristobalite and/or tridymite) was main mineral among observation. Contrary to the silica, Mg-rich silicates such as forsterite (Mg_2SiO_4) and enstatite ($MgSiO_3$) were detected as for main mineral of circumstellar dust. This referred silica is quartz or annealed silica among the various crystal type such as quartz, fused quartz, cristobalite, coesite, stishovite. We prepared these various type of silica in natural, synthetic, and commercial. We report on the infrared spectra of these silica and discuss on the possibility of detection silica for observation.

1 Introduction

Silica (silicon dioxide SiO_2) of terminology is used in solid state and astronomy as for fused quartz, vitreous silica, quartz, cristobalite, etc. in case by case, and many workers were confused to use this terminology in many field. Especially, astronomers used *Silica* of terminology as for quartz in some case, and for annealed silica in some case. Astronomers used *Silica* not giving a clear definition of this term.

Mineral of *Silica* was taken into as major component to explain the spectra of T Tauri star HEN 3-600A, and in this case *Silica* is introduced into as quartz (Honda et al. 2003). A few T Tauri stars (TTS) show prominent narrow emission features indicating annealed silica, where two polymorphs of silica, tridymite and cristobalite, are the dominant forms in the TTS (Sargent et al., 2009). The annealed silica was firstly introduced into the component of circumstellar dust, and this 'annealed silica' was synthesized after annealed of fused quartz at 1220 K (947 °C) for 4.5-5 h (Fabian et al. 2000). Recently, some strange features were detected in debris disks (HD 172555, HD 15407A, HD 23514A, HD 23514), where prominent peaks showed at about 9.3, 12, 21 μm (Lisse et al. 2009), and at about 9, 16, and 20-22 μm (Melis et al. 2010, Rhee et al., 2008, Fujiwara et al., 2009). HD 172555 has infrared spectra at about 9.3 and 19 μm with subtle peaks at 7.5 - 8.2, 11.2 , and 33 μm, where the spectra of silica such as obsidian and tektite were well fitted to the observation (Lisse et al., 2009). The strange spectra of HD 15407 by Fujiwara et al.(2009 (GFWS)) were noticed especially and these spectra were fitted with amorphous silicate (amorphous pyroxene) and fused silica. But, the 16 μm band was not fitted by their model (Fujiwara et al. 2009).

Further, coesite and stishovite were discovered in lunar meteorite Asuka-881757 (Ohtani et al. 2010), and these high-pressure polymorphs of SiO_2 indicate that the meteorite experienced an equilibrium shock-pressure of at least 8-30 GPa. High-pressure impact metamorphism and formation of high-pressure minerals may be common phenomena in debris disks.

These minerals of silica polymorphs, if exist in circumstellar or debris disks, may be ascertained by those of infrared spectra. Neverthless, the infrared spectra of silica polymorphs in wide wavelength region were not measured in laboratory, where even measured data of silica polymorphs were only limited wavelength region.

Here we measured the infrared spectra of the various type of silica in wide wavelength region. Following to our result for annealing fused quartz, we discuss on the possibility of detection silica for observation.

Proceedings of 29th Grain Formation Workshop 2011, Nov.9

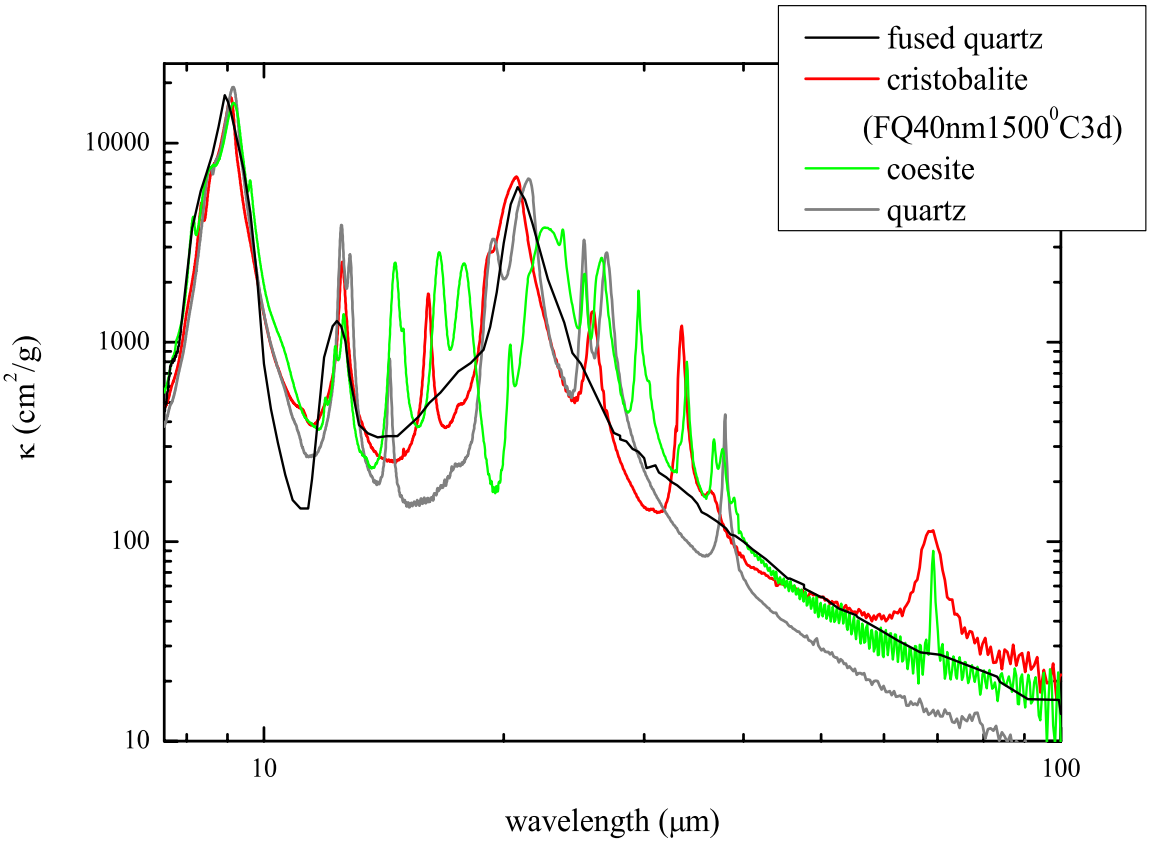

Figure 1: Infrared spectra of silica for present samples.

2 Preparing samples and measurements

We prepared many kinds of silica such as fused quartz, quartz, cristobalite, coesite and stishovite.

- Fused quartz
  Commercial fused quartz were obtained by Nippon Aerosil Co. Ltd. (details in Koike et al. 1994).
- Quartz
  Natural quartz (production area is not known) was ground by hand and further ground by ball mill gently.
- Cristobalite
  Fine powder of cristobalite were prepared by synthesized, by commercial, and by natural samples. Fine powder of fused quartz were annealed at 800 - 1200 °C for various duration times, and 1500 °C for 3 and 6 days. Further, fine powder of commercial cristobalite was obtained from Omura Ceratec Inc.(Japan). Natural cristobalite was obtained from Cougar, Siskiyou Co., California, USA.
- Coesite
  The fine powder of fused quartz was pressed at 6 GPa and 1300 °C for 30 min at Osaka University. The compressed powder became coesite, which was confirmed with XRD.
- Stishovite
  The natural quarzt was compressed at 13 GPa and 1200 °C. The samples was synthesized by Tani (2000), and kindly given to us for measuring infrared spectra.

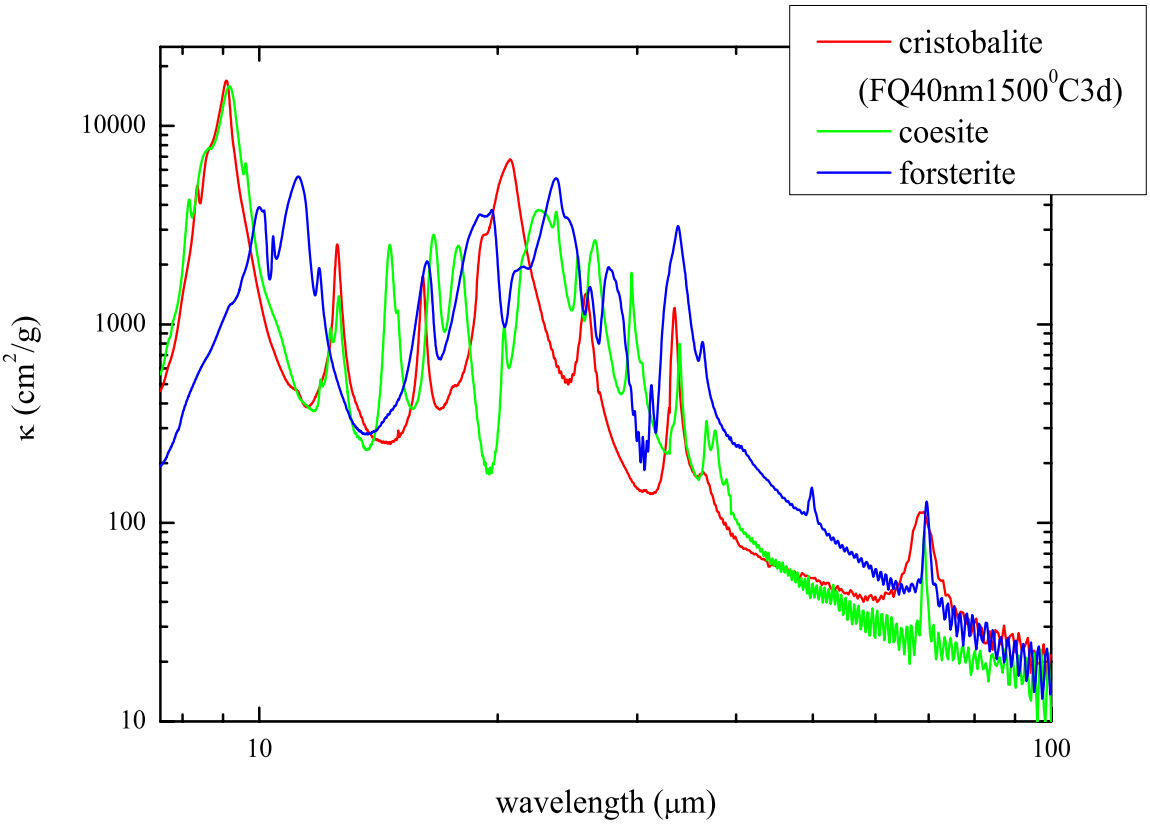

Figure 2: infrared spectra of cristobalite and coesite compared with that of forsterite.

The fine particles of silica polymorphs were well dispersed in KBr and polyethylen powder, and pressed into KBr pellts and polyethylene sheet. Then the transmittance of pellets and sheets were measured with Nicolet 670 and/or 6700 in mid- and far-infrared region. The mass coefficiency κ was derived from transmittance T as follows.

$$\kappa = \frac{S}{M} ln \frac{1}{T} \tag{1}$$

Here, S is surface area of pellets or sheets and M is weight mass of sample particles in pellets or sheets.

3 Results and discussion

3.1 Cristobalite

The powder of fused quartz was annealed at 1000 °C for 1 h following to the results by Fabian et al., where cristobalite appeared at 1220 K (947 °C) for 4.5 - 5h. But, these samples had no change of infrared spectra from starting spectra. Further changing the temperature and duration time for annealing fused quartz at 800-1000 °C for 1 - 7h, the infrared spectra were also not changed from the starting spectra. Even after annealing at 1100, 1150 , 1200 °C and for long duration time (2 days - 8 days), the fused quartz was not changed into cristobalite with IR spectra, although small quantity of cristobalite was ascertained by XRD. This is inconsistent to the results by Fabian et al. (2000), where fused silica was annealed at 1220 K (947 °C) for 4.5-5 h and changed into cristobalite both by IR and XRD. Usually in solid state field, cristobalite appeared at above 1400 °C by phase diagram of silica (Šimon et al. 1953, Plendl et al. 1967, Swaison et al.2003, Lakshtanov et al. 2007). Following to phase diagram of silica, the

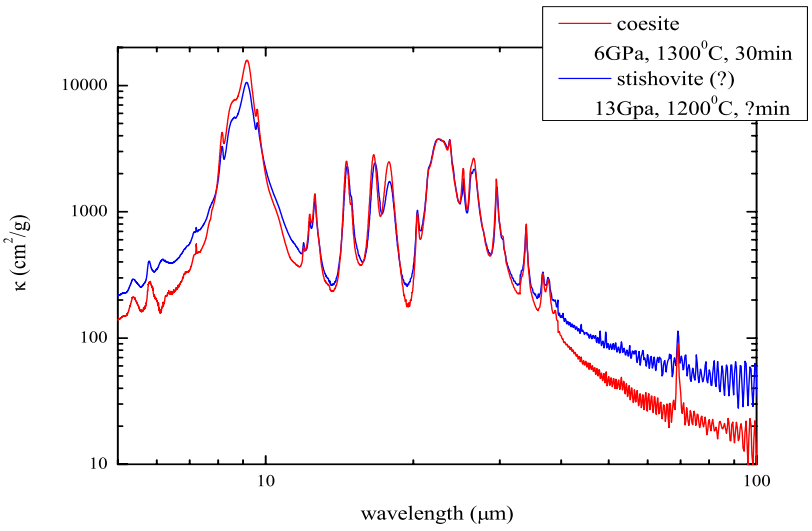

Figure 3: The infrared spectra of coesite and stishovite (?) . The sample of stishovite is not confirmed and marked as ?.

cristobalite changed after annealing at low temperature of about 950 °C is very curious result, and this may be due to some impurity effects or some unique condition.

After annealed fused quartz at 1500 °C for 3 and 6 days, cristobalite was confirmed with XRD, and the infrared spectra were measured to be same with each other, and similar with the spectra by Fabian et al.(2000). Where some peaks were shifted, and the peak of 68 μm band was shifted about 1 μm. The infrared spectra of annealed silica at 1500 °C were almost same with those of commercial cristobalite. Natural cristobalite showed strange spectra due to contamination of some minerals.

Here after, the infrared spectra of cristobalite were shown as annealed at 1500 °C for 3d. The characteristic peak appeared as the strong and broad band at 68 μm. The 68 μm band show very broad band compared with the 69 μm band of forsterite (Mg_2SiO_4). But, the 33 μm band of cristobalite showed very sharp compared with the 33 μm band of forsterite. Forsterite is main component of circumstellar dust and observed as prominent peaks at 11.2, 16, 33, and 69 μm.

3.2 Coesite

The infrared spectra of coesite were shown as many sharp fine peaks in Fig. 1 and 2, and as the sharp peak detected at 69 μm, which is very similar to those of forsterite. The 69 μm band of coesite is very sharp compared with that of forsterite. This peak was firstly detected definitely.

3.3 Stishovite

The spectra of stishovite showed similar to those of coesite. Usually, stishovite showed strong peaks at about 12-18 μm compared with the data by Lyon (1962), and the present spectra is very curious. So, we marked this sample as ? until it is confirmed to ascertain as stishovite. The similar spectra as coesite might be due to some aging effects, but it is not clear. We must make clear why this strange spectra were appeared.

3.4 Fused quartz and Quartz

The spectra of fused quartz (400 Åsample; average size is about 40 nm) were shown in Fig. 1 (Koike et al. 1994). The three broad peaks appeared at 8.9, 12.3, and 20.8 μm.

The spectra of quartz showed sharp peaks at about 9, 12, 14, 19-21, 25, 27, and 38 μm. The weak peak at 78 μm was very subtle, and was ascertained with bulk quartz sample (Russel et al. 1967). This peak was not appeared with reflectance measurements due to weak band by FT/IR Nocolet 670 , and

the measured reflectance spectra between 270 - 2000 cm^{-1} were almost similar as those by Spitzer and Kleinman (1961).

3.5 All samples

The spectra of all samples are compared with each other. The strength and peak position of 9 μm band are almost all similar for all samples. But, for another bands, many sharp peaks appear for coesite and quartz. In far infrared region at about 69 μm, the strong and broad band appears for cristobalite, and the strong and sharp peak appears for coesite.

3.6 Spectra at low temperature compared with those of forsterite

The spectra of cristobalite and coesite show similar bands at 16, 33 and 69 μm as those of forsterite. The mineral of forsterite is main component in circumstellar dust, and ascertained by peak positions from infrared spectra of observation. In order to discriminate between the samples (cristobalite and coesite) and forsterite, the spectra of coesite and cristobalite were measured at low temperature from 8 K to RT. Those spectra at low temperature were shown in Figs. 4, and the peak positions of cristobalite and coesite were compared with those of forsterite as shown in Fig. 5 and 6. Most peak positions of each band shifted to shorter wavelength as cooling from RT to 8 K, but some peak positions shifted to longer wavelength as cooling to 8 K. In the case of cristobalite, the peak positions of 33 and 36 μm bands shift to longer wavelength as cooling to low temperature. In the case of coesite, those of 34, 38, 39, and 69 μm bands shift to longer wavelength as cooling to low temperature. The differences between cristobalite, coesite and forsterite are clear for 16 μm band as peak positions are different and distinguished between each other. As for 33 μm band, the peaks of cristobalite and coesite are sharper than that of forsterite. As for 69 μm band, the band of cristobalite is very broad and peak position is clearly different from that of forsterite. The band of coesite is very sharper than that of forsterite, and shift to longer wavelength than that of forsterite, although the peak position became same as that of forsterite at 200 K .

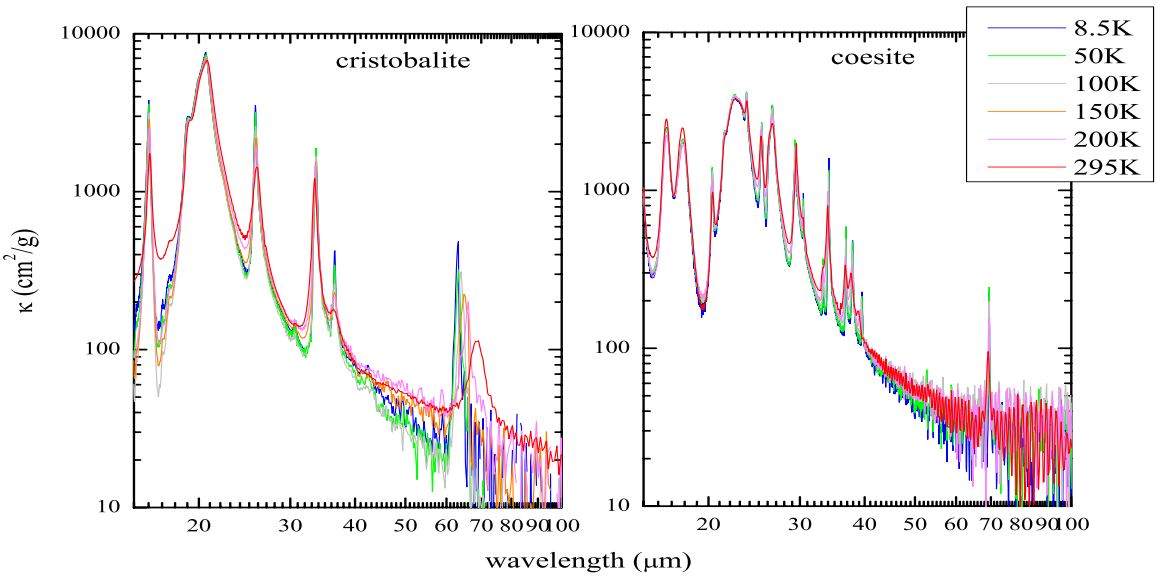

Figure 4: The spectra of cristobalite and coesite at low temperature.

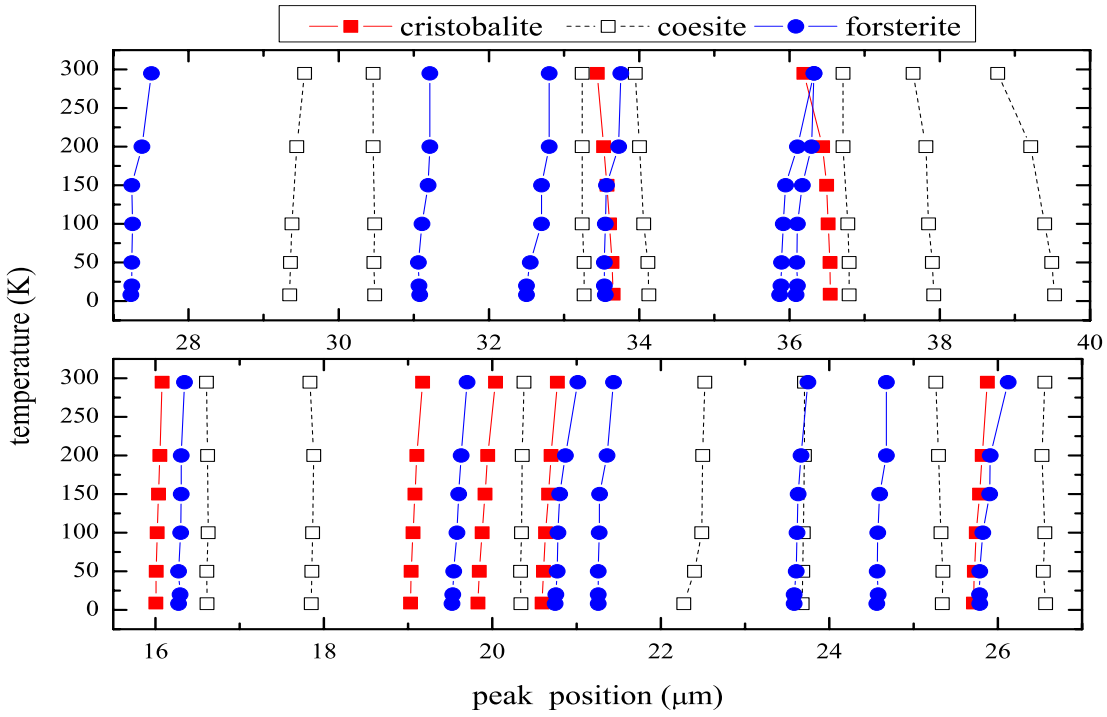

Figure 5: The peak positions of cristobalite and coesite at low temperature compared with those of forsterite.

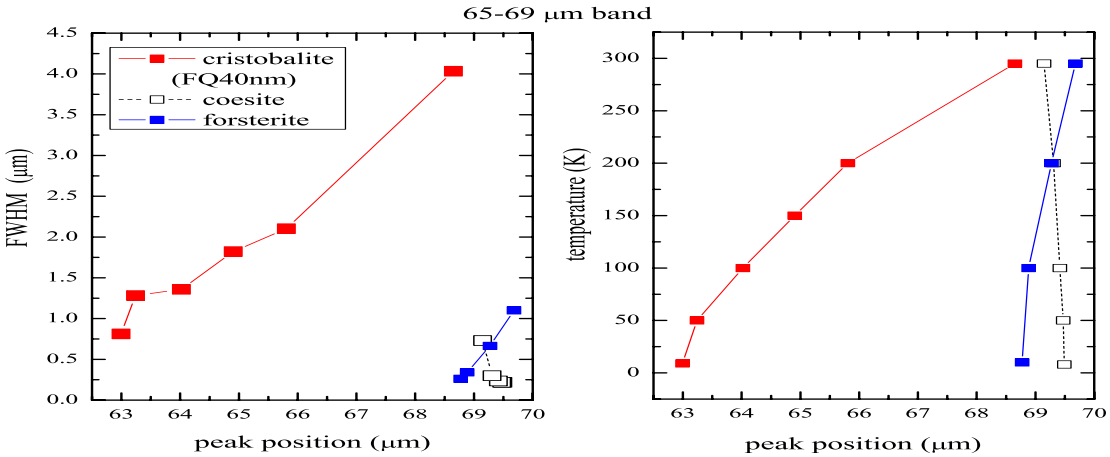

Figure 6: The peak position of 69 μm band of cristobalite and coesite at low temperature compared with those of forsterite.

4 Implication to the observation

Cristobalite was ascertained with XRD and infrared spectra after annealing of fused quartz at 1500 °C for 3 days and 6 days. This annealing temperature is consistent with the results by many workers (Šimon et al. 1953, Plendl et al. 1967, Swaison et al. 2003). The temperature of 1220 K (947 °C) by Fabian et al. is too low compare with our value and may be due to some unique condition. Around T Tauri stars, annealed silica (cristobalite and/or tridymite) would exist from observation of mid infared , where annealing amorphous silica around T Tauri stars was proposed (Sargent et al. 2009). In this case, it is very important whether temperature of the circumstellar disk can be raised to above 1400 - 1500 °C or not instead 947 °C. If annealed temperature could not be raised to above 1400 - 1500 °C, another process such as collision must be introduced.

As for the evidence of existing cristobalite, the broad and strong band at about 68-62 μm could be detected if more detailed observation would be worked in far infrared region. If dust mineral of coesite and cristobalite might exist around debris disks production by high speed collisions among planetesimals, the charcteristic bands could be detected by the high resolution observations in 60-70 μm region.

As for the observed spectra of the debris disks of HD 15407 (Fujiwara et al. 2009), the present cristobalite may be fitted well the observed peaks at 9, 16, and 20-22 μm band instead of fused quartz. The broadness of peaks may be explained after heating up to RT to 250 °C, where 16 μm band exist clearly (Zhang et al. 2007), instead of increase of size of dust particles.

Acknowledgements

We wish to thank Dr. A. Tani for providing the stishovite samples.

References

Fabian D., Jäger C., Henning T., et al., 2000, A&A, 364, 282
Fujiwara et al., Grain Formation Workshop, 2009, pdf file
Honda M., Kataza H., Okamoto Y., et al. , 2003, APJ, 585, L59
Koike C. and Shibai H., 1994, Mon. Not. R. Astron. Soc., 269, 1011
Lakshtanov D. L. and Sinogeikin S. V., 2007, Phys. Chem. Minerals 34, 11
Lisse C. M., Chen C. H., Wyat M. C., et al., 2009, APJ, 701, 2019
Lyon R. J. P., 1962, Nature 196, 267
Melis C., Zuckerman B., Rhee J., and Song I., 2010, APJ 717, L57
Ohtani E., Ozawa S., Miyahara M. et al. 2010, PNAS 108, 463@
Plendl J. N., Mansur L. C., Hadni A., et al., 1967, J. Phys. Chem. Minerals, 14, 527
Rhee J., Song I., and Zuckerman, 2008, APJ 675, 7777
Russell E. E., and Bell E. E., 1967, J. Optical Society America 57, 341
Sargent B., Forrest W., Tayrien C., et al., 2009, APJ 690, 1193
Šimon I. and McMahon H. O., 1953, J. Chem. Phys. 21, 23
Spitzer W. G. and Kleinman D. A., 1961, Phys. Rev. 121, 1324
Swaison I. P., Dove M. T., and Palmer D. C., 2003, Phys. Chem., Minerals. 30, 353
Tani A., Yamanaka C., Ikeya M., et al., 2000, Appl. Magn. Reson. 18, 559
Zhang M., and Scott J. F., 2007, J. Phys.: Condens. Matter 19, 275201

Vibrational spectroscopy of SiO and Mg silicate systems

S. Wetzel, A. Tamanai, and A. Pucci

Kirchhoff-Institut für Physik der Universität Heidelberg;

Im Neuenheimer Feld 227; 69120 Heidelberg

Abstract

Silicates are the most abundant minerals in space and their IR spectral features depend on physical properties such as the chemical composition and on the formation conditions e.g. temperature and pressure. Therefore they can provide information not only on the relative abundance of the elements, but also on formation processes and the environment in which the dust is formed. To perform sophisticated analysis of IR spectra obatined by space observations a comprehensive database is required, including materials with various compositions and interfacial interaction effects have to be considered. In order to deepen the understanding of IR spectra of silicates, we performed *in situ* IR spectroscopy of layers produced by condensation of evaporated SiO, Mg and Fe, respectively. Details on the experimental setup and first results from the measurements are presented in this work.

I. INTRODCUTION

The strong absorption feature at around 10 μm is attributed to the Si-O stretching vibration which is sensitive to changes of surrounding bonding parameters as it has been for example demonstrated for the SiO/Si(111) interface[1]. To better understand the IR spectra of silicates, we investigate materials involved in silicate formation by *in situ* IR spectroscopy under ultra high vacuum (UHV) conditions.

II. EXPERIMENTAL

A schematic drawing of the experimental setup is shown in Fig. 1. It consists of a FTIR-spectrometer that is coupled to an UHV chamber, with a base pressure of 1×10^{-10} mbar, in which the condensation experiments were performed. Equipped with a triple evaporator that allows individual, subsequent or simultaneous evaporation of up to three different materials one can measure single layers, multilayer structures and layers produced by co-evaporation. The evaporation rate is determined with a quartz crystal microbalance (QCM), that can be inserted into the particle beam, before and after each spectroscopic experiment. With a known density of the material, this allows to calculate the film thickness corresponding to each measured spectrum. The sample holder is attached to a cryostat and can be heated by electron bombardment, that allows to vary the substrate temperature from 40 to 1300 K; therefore, it also makes annealing experiments possible. The chamber is additionally equipped with a low-energy-electron-diffraction (LEED) system to investigate crystalline surfaces, a gas system and quadrupole mass spectrometer (QMS) for experiments under well-defined partial pressures of gases. The beam path outside the UHV chamber is evacuated to 4 mbar. IR spectra were measured with a mercury-cadmium-telluride (MCT) detector in the wavelength range between 2 μm (5000 cm^{-1}) and 22 μm (450 cm^{-1}) with a spectral resolution of 4 cm^{-1} under normal incidence of light and normalized to the spectrum of the bare substrate. Si(111) wafers with dimensions of $10 \times 10\,\mathrm{mm}^2$ and a thickness of 0.525 mm were used as substrate. Before deposition of the metal films the natural oxide was removed by heating the wafer to 1300 K. In the case of SiO deposition the natural oxide was left on the surface as it only effects the first stages of film growth below 1 nm film thickness.[1]

III. BASICS

Approximate transmittance formulas of a thin film with the thickness d ($d \ll \lambda$ (wavelength)) can be derived by using the Fresnel equations.[2] On the other hand, the normal transmittance of a thin film on a thick substrate ($d \gg \lambda$)[3,4] is given by

$$T_{\mathrm{rel}} \approx 1 - \frac{2d\frac{\omega}{c}}{1+\sqrt{\epsilon_{\mathrm{s}}}}\,\mathrm{Im}(\epsilon_{\mathrm{f}}) \tag{1}$$

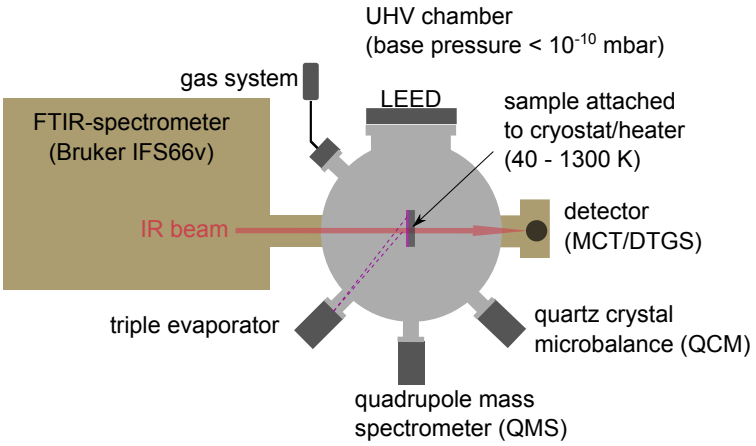

FIG. 1: A schematic drawing of the experimental setup. A FTIR spectrometer (Bruker IFS66/v) is coupled to an UHV chamber with a base pressure of 1×10^{-10} mbar. The setup is equipped with a triple evaporator that allows individual, subsequent or simultaneous evaporation of up to three different materials. The temperature of the substrate can be controlled between 40 and 1300 K

($\omega = 2\pi\frac{c}{\lambda}$; ϵ_s: the dielectric function of the substrate; ϵ_f: the dielectric function of the film). Only the transverse optical (TO) modes with their frequency at the maximum of the imaginary part of the dielectric function ϵ can be detected under normal incidence of light .

An appropriate model has to be used to determine the dielectric function from such a measurement.[5] The oscillator model introduced by Brendel[6]

$$\epsilon(\omega) = \epsilon_\infty + \sum_{j=1}^{N} \frac{1}{2\pi\sigma_j} \int_{-\infty}^{\infty} e^{-\frac{(x-\omega_{0,j})^2}{2\sigma_j^2}} \frac{\Omega_j}{x^2 - \omega^2 - i\omega\gamma_j} \mathrm{d}x \ , \tag{2}$$

has been used to describe our measured spectra, as it is especially suited to describe disordered amorphous systems. It consists of a dielectric background ϵ_∞ and N Gaussian distributions of Lorentz oscillators with resonance frequencies $\omega_{0,j}$, damping constants γ_j, standard deviations σ_j of the Gaussian distributions and oscillator strengths Ω_j. For are more detailed description we refer to the work by Klevenz *et. al.*[5] and the references therein.

IV. RESULTS & DISCUSSION

Relative transmittance spectra taken during the condensation of SiO on a Si(111) substrate at room temperature are shown in Fig. 3 . Two broad peaks with resonance frequencies at 10.163 μm as well as 14.085 μm and a shoulder at longer wavelength develop as film thick-

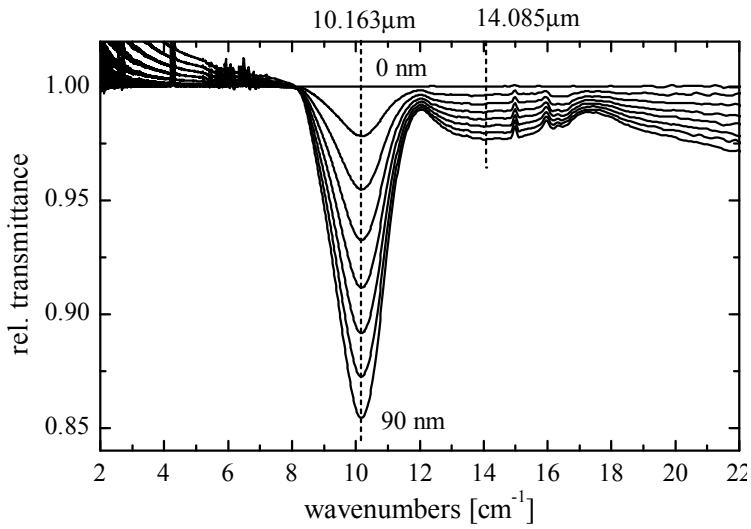

FIG. 2: IR spectra measured during the condensation of evaporated SiO on Si(111). Between two spectra 12.9 nm of SiO were deposited and the last spectrum corresponds to a final film thickness of 90 nm. The data was first published in Klevenz *et. al.* 2010[5].

ness increases. The strongest peak can be assigned to a vibration of the oxygen against the Si atoms, the so-called Si-O strecthing mode (AS1). The second mode at 14.085 μm is connected with the Si-Si strecthing (SS) mode. Those spectra were successfully described using a dielectric function model according to equation (2) and the derived dielectric function shows a good accordance to existing literature data based on ellipsometry measurements.[5]

The development of the relative transmittance with thickness of Mg and Fe is shown in Fig. 2, respectively. In both cases the expected Drude-like behaviour at higher thickness can be observed as soon as the percolation is reached after an island-like growth in the beginning. We also deposited a Fe film at 110 K and were able to reproduce the results by Federov *et. al.*[7] that demonstrated a strong quantum size effect in ultrathin Fe layers that leads to an increased IR absorbance.

First studies on multilayer structures show a Fano-type interaction of the metal films with the main vibrational band of SiO that leads to an additional feature in the 10 μm region. Detailed analysis of this effect and further measurements on more complex structures are work in progress.

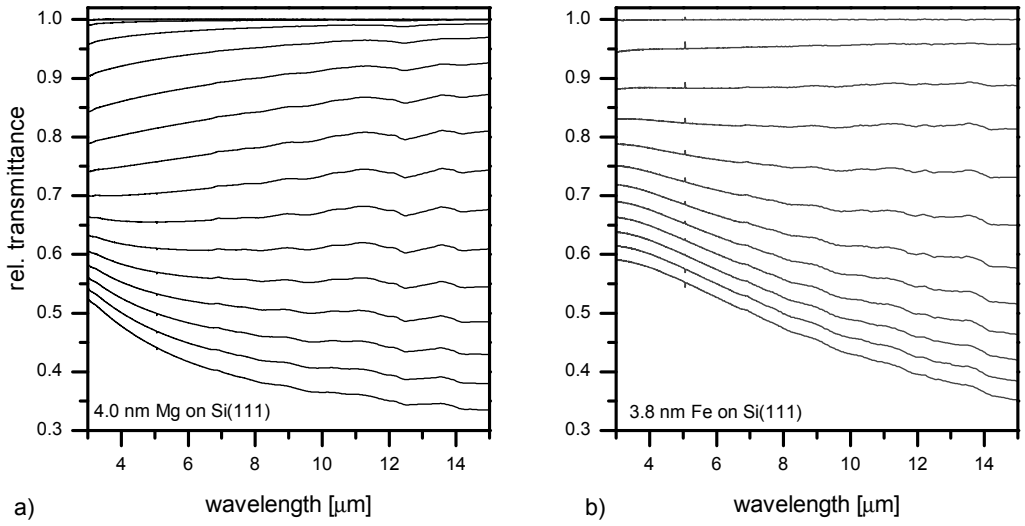

FIG. 3: In a) and b) IR spectra measured during the condensation of evaporated Mg and Fe on Si(111) at room temperature are shown, respectively. The final film thickness of each measurement is given in the graph. For the evaporation of Mg between two adjacent spectra 0.29 nm were deposited and in the case of Fe evaporation 0.39nm, respectively.

Acknowledgment

This research has been supported in part by the Deutsche Forschungsgemeinschaft DFG through grant Schwerpunktprogramm 1385 "The First 10 Million Years of the Solar System - a Planetary Materials Approach". The authors acknowledge fruitful discussions with H.-P. Gail. S. Wetzel and A. Tamanai gratefully acknowledge financial support by T. Yamamoto and by the DFG through grant FOR759 to attend the grain formation workshop.

---

[1] M. Klevenz, S. Wetzel, M. Trieloff, H.-P. Gail, and A. Pucci, phys. stat. sol. (b) **247**, 2179 (2010).

[2] D. W. Berreman, Phys. Rev. **130**, 2193 (1963).

[3] A. Lehmann, phys. stat. sol. (b) **148**, 401 (1988).

[4] U. Teschner and K. Hübner, phys. stat. sol. (b) **159**, 917 (1990).

[5] M. Klevenz, S. Wetzel, M. Möller, and A. Pucci, Appl. Spectrosc. **64**, 298 (2010).

[6] R. Brendel and D. Bormann, J. Appl. Phys. **71**, 1 (1992).

[7] D. V. Fedorov, G. Fahsold, A. Pucci, P. Zahn, and I. Mertig, Phys. Rev. B **75**, 245427 (2007).

Surface structures of presolar alumina grains from unequilibrated ordinary chondrites

A. Takigawa[1], S. Tachibana[1], K. Nagashima[2], K. Makide[2,3], G. R. Huss[2], A. N. Krot[2], H. Nagahara[1], and K. Ozawa[1]

[1]Department of Earth & Planetary Science, The University of Tokyo, 7-3-1 Hongo, Tokyo 113-0033, Japan. takigawa@eps.s.u-tokyo.ac.jp, [2] Hawai'i Institute of Geophysics and Planetology, Univerity of Hawai'i at Mānoa, [3]Department of Chemistry, Gakushuin University

1. Introduction

Corundum (α-Al_2O_3) is one of the first refractory minerals that condense directly from gas of the solar composition (Wood & Hashimoto 1993) [1]. Presolar alumina grains, which have highly unusual oxygen isotopic compositions compared to solar-system materials, are condensates in outflows from oxygen-rich AGB stars and/or supernovae (e.g., Nittler et al. (1997) [2]). It is therefore important to understand the formation conditions of corundum grains in order to understand the first stage of dust formation around evolved stars. The morphological and crystallographic features of presolar alumina grains should reflect the formation conditions and subsequent thermal history of the grains (Takigawa et al. (2009a, b) [3,4]). Moreover, morphology of presolar alumina grains may provide clues to understand the 13-μm features of oxygen-rich evolved stars, which seem to be consistent with disk-like corundum grains flattened to the crystallographic c-axis (Takigawa et al. (2009a) [3]). However, morphological and crystallographical information of presolar alumina is very limited (Choi et al. 1998; Stroud et al. 2004 [5,6]) because the abundance of presolar alumina in chondrites is low (1−100 ppm) and because most of grains were found by ion mapping [e.g., Nittler et al. (1997) [2]], which destroys grain morphology due to ion beam sputtering. In this study, in order to understand the morphology and crystallographic orientation of presolar alumina grains, we made detailed observations of morphology and crystallography of alumina grains from residues unequlibrated ordinary chondrites using field-emission scanning electron microscopy (FE-SEM) and electron back-scattered diffraction (EBSD) prior to the oxygen isotopic analyses to identify the circumstellar condensates.

2. Samples and analytical techniques

The acid-residues of ordinary chondrites, Semarkona (LL3.0), Bishunpur (LL3.1), and Roosevelt County (RC) 075 (LL3.2), prepared by Huss et al. (1995, 2003) [7,8] were used for this study. The residues, consisting of acid-resistant grains such as corundum, spinel, hibonite, and SiC, were dispersed

onto gold substrates cleaned by ion milling. Alumina candidate grains were found with cathodoluminescence imaging by a field emission electron microprobe, and 198 corundum grains (0.5–2 μm in size) were confirmed by EDS (energy dispersive spectroscopy) equipped to a field emission scanning microscope, among which 31, 74, and 93 grains were from Semarkona, Bishunpur, and RC 075, respectively. For individual grains, secondary electron images were taken from four different directions and crystallographical information was obtained by EBSD.

Oxygen isotopic compositions of 111 grains were measured with UH Cameca ims-1280 ion microprobe. The details of analytical technique are described in Makide et al. (2009) [9]. A 0.5–2.5 nA Cs^+ primary ion beam was defocused to ~30 μm for uniform sputtering of grains having different morphologies and sizes (0.5−3 μm). A field aperture of 1500 × 1500 μm^2 corresponding to ~10 μm on the sample was used to minimize contribution of oxygen signals from the substrate and other grains surrounding the grain of interest. Secondary $^{16}O^-$, $^{17}O^-$, and $^{18}O^-$ ions were measured in multicollection mode with the magnetic field controlled by a nuclear magnetic resonance probe. $^{16}O^-$ and $^{18}O^-$ were measured by a multicollector Faraday cup and EM (electron multiplier), respectively, with mass resolving power (MRP) of ~ 2000, and $^{17}O^-$ was measured using the axial monocollector EM with MRP of ~ 5600 to separate the interfering $^{16}OH^-$ signal. The primary beam current was adjusted to obtain $^{16}O^-$ signal of $>\sim 10^6$ cps. Acquisition time was typically 200 s (10 s × 20 cycles), but it was reduced to 50 – 130 s (10 s × 5–13 cycles) during analyses for grains showing presolar signatures of oxygen isotopes to keep grains from being completely sputtered. After the isotopic measurements, the presolar alumina grains were reexamined by FE-SEM and EBSD.

3. Results

The 198 alumina grains discovered were classified into three types (A, B, and C) according to their morphology. Type A grains have smooth surfaces or crystal faces (98 grains; Fig. 1a). Type B grains are irregularly shaped and have rough surfaces with 10 to 100 nm-sized fine structures without crystal faces (67 grains; Fig. 1b). Type C grains have both type A and type B surface structures (33 grains), which include two grains with clear bilateral surface structures having crystal faces on half of the grain surface and irregularly fine structures on another half of the surface (Fig. 1c). EBSD measurements for 170 grains showed that 87 % of grains are crystalline α-Al_2O_3 (corundum).

Oxygen isotopic compositions of most grains plot along the Carbonaceous Chondrite Anhydrous Mineral (CCAM) line. Nine presolar alumina grains were found (~8% of measured grains): seven grains have oxygen isotopic compositions with positive ^{17}O excesses and small ^{18}O depletions (Group I);

two grains show ^{17}O depletions (Group III). The presolar grains consist of 7 type B (Fig. 2) and 2 type A grains. We note that both type A grains were attached to tens-nm-sized type B grains that could be carriers of presolar isotopic signatures. The observed presolar/solar corundum ratio of 8% is similar to that of 7% by Choi et al. (1998) [5], but higher than those of 3% and <0.8 % reported by Nittler et al. (1997) [2] and Makide et al. (2009) [9], respectively, in spite of essentially the same chemical treatment of samples and procedure of measurements as ours. This difference could be attributed to the difference in size of grains analyzed. The size of grains measured in our study and in Choi et al. (1998) [5] is about 1 μm on average, but only larger grains (1-5 μm) were measured by Makide et al. (2009) [9]. Most of presolar alumina in Tieschitz (H3.6), which were measured by ion-mapping technique, were reported to be <1.5 μm (Nittler et al. 1997 [2]) being consistent with higher abundances of presolar alumina in our study and in Choi et al. (1998) [5] than that in Makide et al. (2009) [9].

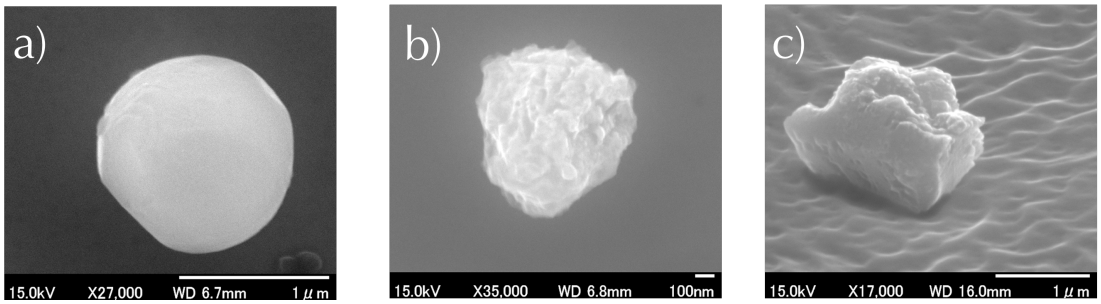

Fig. 1 Alumina grains extracted from unequilibrated ordinary chondrites. a) type A, b) type B, and c) type C grains.

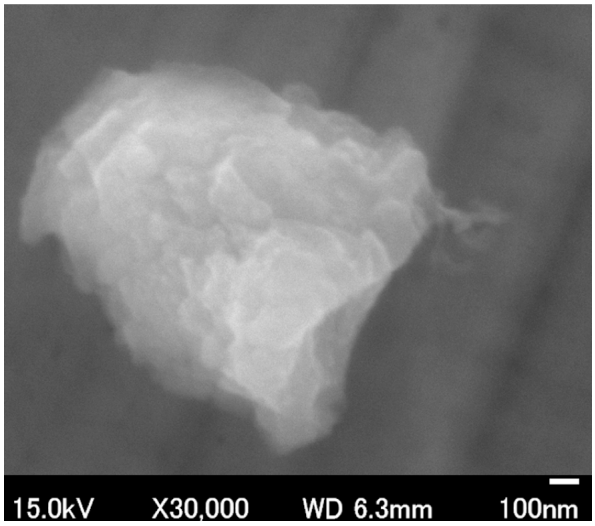

Fig. 2 Presolar alumina grain (type B) (RC 075 59-08).

4. Origin of the type B surface structures

The surfaces of type B alumina grains consist of very fine structures (10-100 nm in size). Such surface features are observed not only for presolar alumina but also for one third of solar alumina grains. The type B surface could be the original structure formed in space, but one may suspect that the acid treatments to extract alumina and other acid-resistant grains from bulk chondrites alter the surface structures of alumina grains by dissolution. In order to evaluate the type B surface structures are original formed in space or artifacts during acid treatments of the meteorites and to assess the resistance of alumina polymorphs to acid treatments, dissolution experiments of several kinds of crystalline and amorphous alumina particles were conducted.

The dissolution experiments of alumina particles were conducted following the procedure of acid treatments by Huss & Lewis (1995) [7], based on which the acid residues of chondrites used in this study were prepared. In this study, three acid treatments were performed for α-alumina (corundum); (1) 12M HF - 6M HCl at 25°C for 10 days, (2) 2M H_2SO_4 + 0.5N $K_2Cr_7O_4$ at 75°C for 12 hours, and (3) $HClO_4$ at 190-200°C for 2 hours. No recognizable change of surface structures was seen for the α-alumina powders that experienced the acid treatment (1)-(3) in the order. This leads to the conclusion that the surface structures of meteoritic corundum grains in this study are not the artifact formed during acid treatments but the original features reflecting processes in space. A possible process that formed the presolar

alumina with type B (fluffy and fine-structured) surfaces could be surface sputtering of grains in supernova-induced shockwaves in interstellar medium or the protosolar disk (Jones et al. 1994 [10]).

References

[1] Wood, J. A. & Hashimoto, A. (1993), "Mineral equilibrium in fractionated nebular systems", *Geochimica et Cosmochimica Acta*, **57**, 2377

[2] Nittler, L. R., Alexander, C. M. O'd., Gao, X., Walker, R. M., & Zinner, E. (1997), "Stellar Sapphires: The Properties and Origins of Presolar Al_2O_3 in Meteorites", *Astrophysical Journal*, **483**, 475

[3] Takigawa A., Tachibana S., Nagahara H. and Ozawa K. (2009) "Condensation anisotropy of corundum around AGB stars and its effect on infrared spectra", *Lunar & Planetary Science,* **XXXX**, abstract #1731

[4] Takigawa, A., Tachibana, S., Nagahara, H. Ozawa, K., and Yokoyama, M. (2009), "Anisotropic Evaporation of Forsterite and Its Implication for Dust Formation Conditions in Circumstellar Environments", *Astrophysical Journal*, **707**, L97

[5] Choi, B.-G.-, Huss, G. R., Wasserburg, G. J., and Gallino, R. (1998), "Presolar alumina and Spinel in Ordinary Chondrites: Origins from AGB Stars and a Supernova", *Science*, **282**, 1284

[6] Stroud, R. M., Nittler, L. R., & Alexander, C. M. O'D. (2004), "Polymorphism in Presolar Al_2O_3 Grains from Asymptotic Giant Branch Stars", *Science*, **305**, 1455

[7] Huss, G. R. & Lewis, R. S. (1995), "Presolar diamond, Sic, and graphite in primitive chondrites: Abundances as a function of meteorite class and petrologic type", *Geochimica et Cosmochimica Acta*, **59**, 115

[8] Huss, G. R., Meshik, A. P., Smimth, J. B., & Hohenberg, C. M. (2003), "Presolar diamond, silicon carbide, and graphite in carbonaceous chondrites: Implications for thermal processing in the solar nebula", *Geochimica et Cosmochimica Acta*, **67**, 4823

[9] Makide, K., Nagashima, K., Krot, A. N., & Huss, G. R. (2009), "Oxygen Isotopic Compositions of Solar Corundum Grains", *Astrophysical Journal*, **706**, 142

[11] Jones, A. P., Tielens, A. G. G. M., Hollenbach, D. J., & McKee, C. F. (1994), "Grain destruction in shocks in the interstellar medium", *Astrophysical Journal*, **433**, 797

Grain Formation Workshop 2011

Star formation and dust extinction properties of local galaxies seen from AKARI

A. Sakurai[1], T.T.Takeuchi[1], F-T.Yuan[1], V. Buat[2], D. Burgarella[2]

[1] *Division of Particle and Astrophysical Science, Nagoya University, Furo-cho, Chikusa-ku, Nagoya 464-8602, Japan*
[2] *Laboratoire d'Astrophysique de Marseille, OAMP, Université Aix-Marseille, CNRS, 38 rue Frédéric Joliot-Curie, 13388 Marseille cedex 13, France*

Abstract

Accurate estimation of the star formation-related properties of galaxies is crucial for understanding the evolution of galaxies. In galaxies, ultraviolet (UV) light emitted by formed massive stars is attenuated by the dust which is also produced by the SF activity, and is reemitted at mid- and far- infrared wavelengths (IR). In this study, we investigated the star formation rate (SFR) and dust extinction using data at UV and IR. We selected local galaxies which are detected at AKARI FIS 90 μm band. We measured flux densities at FUV and NUV from the GALEX images. We examined the SF and extinction of Local galaxies by using four wavebands of AKARI. Then, we calculated FUV and total IR luminosities, and obtained the SF luminosity ($L_{\rm SF}$:the total luminosity related to star formation activity) and the SFR. We found that in most of galaxies, $L_{\rm SF}$ is dominated by $L_{\rm dust}$. We also found that galaxies with higher SF activity have a higher fraction of SF hidden by dust. Especially, the SF of galaxies whose SFRs are > 20 M$_\odot$ yr^{-1} is almost completely hidden by dust. Though these results were qualitatively suggested by previous studies, in this work we could determine the SF and extinction properties with great precision thanks to much larger samples from AKARI and GALEX all sky surveys.

1 Introduction

Accurate estimation of the star formation -related properties of galaxies is crucial for understanding the evolution of galaxies. In galaxies, ultraviolet (UV) light emitted by formed massive stars is attenuated by the dust which is also produced by the SF activity, and is reemitted at mid- and far- infrared wavelengths (IR). In this study, we investigated the star formation rate (SFR) and dust extinction using data at UV and IR.

The total mass of newly formed stars in a galaxy per year is referred to as the star formation rate (SFR). In order to know the star romation (SF) activity, massive stars are good indicators because they have much shorter lifetime ($\sim 10^6$ yr) than the age of galaxies and the Universe (order of $\sim 10^{10}$ yr). Massive stars (OB stars) are hot and emit ultraviolet light. Then, we can *in principle* obtain the SFR of galaxies directly by measuring their UV luminosity. However, as mentioned above, stars produce heavy elements (or metals) and release them out through the phenomena during the latest phase of stellar evolutoin, as planetary nebulae, supernova explosions, and some other mass ejection processes (e.g., Asano et al., 2012) .

These metals are not in the state of gas in the interstellar medium (ISM), but form tiny solid grains, whose typical size is less than 1 μm. This means that the SF activity in galaxies is always accompanied by the dust formation, except the very first formation of stars in the Universe. Then, the dust grains are gradually mixed with the interstellar medium. The UV photons from massive stars are easily absorbed and/or scattered by dust grains and re-emitted as mid- and far-infrared photons. This is referred to as the dust extinction. Then, we should stress that if we only measure the UV photons from massive stars in galaxies, the SF activity would be seriously underestimated because significant amount of the energy is obscured by dust (e.g., Kennicutt, 1998) .

So, we investigated star formation -related properties from UV and IR data.

2 Observational data

AKARI is an IR satellite and we used the data of AKARI FIS All-Sky Survey which has four wavebands at FIR, centered at 65 μm (*N60*), 90 μm (*WIDE-S*), 140 μm (*WIDE-L*), 160 μm (*N160*). IRAS is also an IR satellite and its all sky survey was brought with four wavebands before AKARI.

GALEX is a UV satellite which has two wavebands, FUV (Far UV, 1350-1750 $\mathring{A}$, $\lambda_{\rm mean} = 1530$ $\mathring{A}$) and NUV (Near UV, 1750-2750 $\mathring{A}$, $\lambda_{\rm mean} = 2310$ $\mathring{A}$) with detection limits of 19.9 mag and 20.8 mag (Morrissey et al., 2007) . We used the data of GALEX releases GR4/GR5 all sky survey imaging survey (AIS) in this study.

We started from the AKARI FIS bright source catalog (BSC) v.1 from AKARI all sky survey (Yamamura et al., 2010) to construct our galaxy sample. In order to have a secure sample of galaxies with redshift data, we made a cross match of AKARI sources with the Imperial IRAS-FSC Redshift Catalogue (IIFSCz), a redshift catalog recently publishedj (Wang and Rowan-Robinson, 2009) .

After some selection processes, we obtained 6674 galaxies as IR selected sampleand used the GALEX photometry.

We measured FUV and NUV flux densities using GALEX GR4/GR5 images for the 6674 galaxies. Then we deleted the wrong images and finaly we obtained available 3891 galaxies.

3 Results

We first obtained the total IR (TIR) luminosity $L_{\rm TIR}$ from AKARI FIS four bands.

$$L_{\rm TIR} = L^{\rm 2band}_{\rm AKARI} = \Delta\nu(\textit{WIDE-S})L_\nu(90\ \mu{\rm m}) + \Delta\nu(\textit{WIDE-L})L_\nu(140\ \mu{\rm m})\ ,$$
$$\Delta\nu(\textit{WIDE-S}) = 1.47\times10^{12}\ [{\rm Hz}]$$
$$\Delta\nu(\textit{WIDE-L}) = 0.831\times10^{12}\ [{\rm Hz}]\ .$$

Figure. 1 shows the relation between the FUV luminosity, $L_{\rm FUV}$ from GALEX photometry and $L_{\rm TIR}$. Then we caliculate the star formation luminosity $L_{\rm SF}$ using the FUV luminosity $L_{\rm FUV}$ from GALEX photometry and $L_{\rm TIR}$. The $L_{\rm SF}$ luminosity is expressed as

$$L_{\rm SF} \equiv L_{\rm FUV} + (1-\eta)L_{\rm TIR}$$

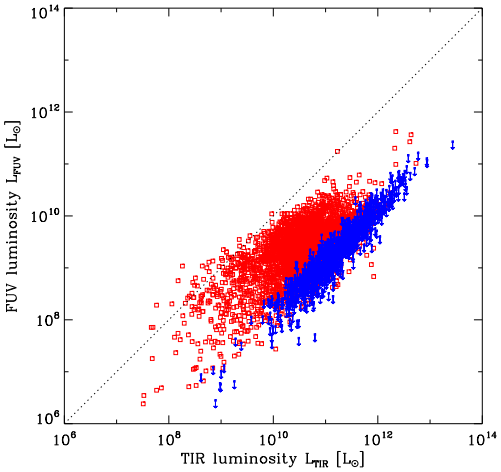

Fig.1 The relation between $L_{\rm FUV}$ and $L_{\rm TIR}$.The diagonal dotted line represents the case if $L_{\rm FUV}$ equals $L_{\rm TIR}$.The blue symbols shows the galaxies which have UV flux densities below the detection limit of GALEX.

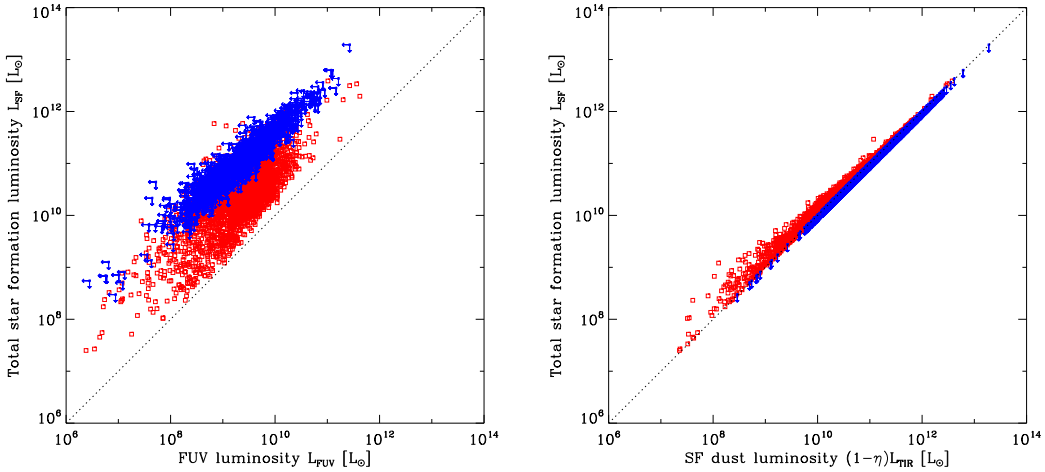

Fig.2 The left panel shows the relation between $L_{\rm FUV}$ and $L_{\rm SF}$. The right panel shows the relation between $L_{\rm dust}$ and $L_{\rm SF}$.

where η is the fraction of the IR emission produced by dust heated by old stars, which is not related the current star formation. We adopted 30 % for this fraction (Hirashita et al., 2003). Figure. 2 shows the contribution of $L_{\rm FUV}$ and $L_{\rm dust}$ ($\equiv (1-\eta)L_{\rm TIR}$) to the $L_{\rm SF}$. With an spectral evolutionary synthesis model Starburst99 (Leitherer et al., 1999), and assuming a constant SFR over 10^8 yr, the Salpeter IMF ((Salpeter, 1955) mass range $0.1M_\odot$–$100M_\odot$), and the solar metallicity, we obtain the relation between the SFR and $L_{\rm FUV}$ as (Iglesias-Páramo et al., 2006)

$$\log \mathrm{SFR_{FUV}} = \log \mathrm{L_{FUV}} - 9.51$$

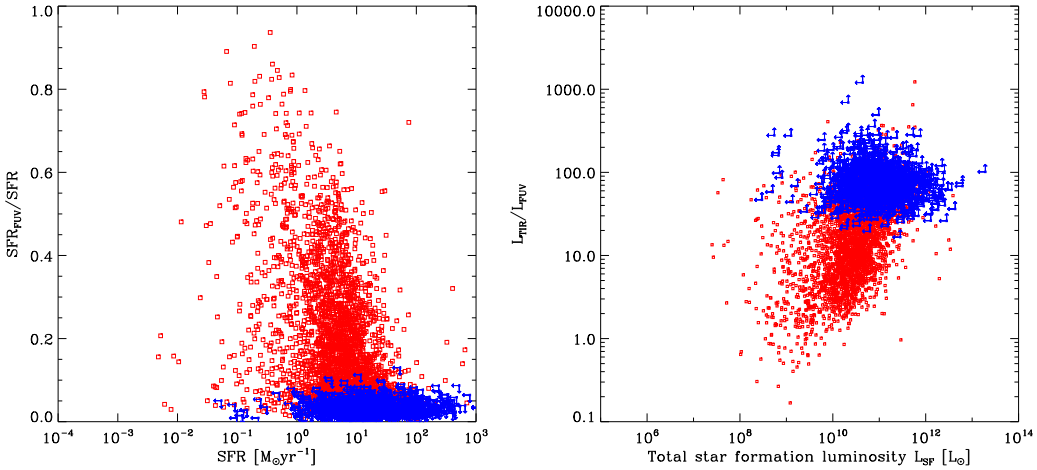

Fig.3 The left panel shows the contribution of the fraction of $\mathrm{SFR_{FUV}}$ to the total SFR. The right panel shows the relation between L_{SF} and $L_{\mathrm{TIR}}/L_{\mathrm{FUV}}$.

The relation between SFR and TIR luminosity is

$$\log \mathrm{SFR_{dust}} = \log L_{\mathrm{TIR}} - 9.75 + \log(1-\eta)$$

We assume that all stellar light is absorbed by dust. Then we can the total SFR contained FUV and IR lumionsity.

$$\mathrm{SFR} = \mathrm{SFR_{FUV}} + \mathrm{SFR_{dust}}$$

The fraction of $\mathrm{SFR_{FUV}}$ to the total SFR for the sample galaxies is shown in the left panel of Fig. 3. There is a sudden drop at SFR > 20 $\mathrm{M_\odot yr^{-1}}$. In the relation between L_{SF} and the extinction rate, $L_{\mathrm{TIR}}/L_{\mathrm{FUV}}$ is shown in the right panel in Fig. 3. We expected high dust extinction rate because of IR selected galaxies.

4 Conclusion

We analyzed star formation-related properties of local galaxies by using AKARI and GALEX data. Summary and conclusions of this study are as follows:

1. The star formation luminosity, L_{SF}, is dominated by the total infrared luminosity from dust, L_{TIR}.
2. The contribution of the ultraviolet luminosity, L_{FUV}, has a larger scatter tha that of the contribution of L_{TIR}.
3. It is difficult to estimate the star formation activity only from the relation between L_{SF} and L_{FUV}.
4. Galaxies with higher SF activity (SFR > 20 $M_\odot$ $\mathrm{yr^{-1}}$) have a higher fraction of SF hidden by dust.
5. This analysis clearly proved that there is a class of glaxies that have small $L_{\mathrm{FUV}}/L_{\mathrm{TIR}}$. These galaxies were dropped on the previous study that used only bright galaxies in AKARI catalog.

From this study, we obtain the similar conclusions with Takeuchi et al. (2010), but with much smaller errors. The newly constructed data in this study will provide us with a large potential of new interesting studies.

References

Asano, R. S., Takeuchi, T. T., Hirashita, H., Inoue, A. K., Dust formation history of galaxies: a critical role of metallicity for the dust mass growth by accreting materials in the interstellar medium, *Earth, Planets, & Space*, submitted, 2011.

Hirashita, H., Buat, V., & Inoue, A. K., Star formation rate in galaxies from UV, IR, and Hα estimators, *Astronomy and Astrophysics*, **410**, 83–100, 2003.

Iglesias-Páramo, J., et al., Star Formation in the Nearby Universe: The Ultraviolet and Infrared Points of View, *The Astrophysical Journal Supplement Series*, **164**, 38–51, 2006.

Kennicutt, R. C., Jr., Star Formation in Galaxies Along the Hubble Sequence. *Annual Review of Astronomy and Astrophysics*, **36**, 189–232, 1998.

Leitherer, C., Schaerer, D., Goldader, J. D., et al., Starburst99: Synthesis Models for Galaxies with Active Star Formation, *The Astrophysical Journal Supplement Series*, **123**, 3–40, 1999.

Morrissey, P., et al., The Calibration and Data Products of GALEX, *Astronomy and Astrophysics*, **173**, 682–697, 2007.

Pollo, A., Rybka, P., & Takeuchi, T. T., Star-galaxy separation by far-infrared color-color diagrams for the AKARI FIS all-sky survey (bright source catalog version β-1, *Astronomy and Astrophysics*, **514**, A3, 2010.

Salpeter, E. E., The Luminosity Function and Stellar Evolution., *The Astrophysical Journal*, **121**, 161, 1955.

Takeuchi, T. T., Buat, V., Heinis, S., Giovannoli, E., Yuan, F.-T., Iglesias-Páramo, J., Murata, K. L., & Burgarella, D., Star formation and dust extinction properties of local galaxies from the AKARI-GALEX all-sky surveys . First results from the most secure multiband sample from the far-ultraviolet to the far-infrared, *Astronomy and Astrophysics*, **514**, A4, 2010.

Wang, L., Rowan-Robinson, M., The Imperial IRAS-FSC Redshift Catalogue, *Monthly Notices of the Royal Astronomical Society*, **398**, 109-118, 2009.

Yamamura I., Makiuti S., Ikeda N., Fukuda Y., Oyabu S., Koga T., White G. J., AKARI/FIS All-Sky Survey Bright Source Catalogue Version 1.0 Release Note, ISAS/JAXA, 2010.

A Study on the Star Formation History of Galaxies Revealed by the UV-IR Bivariate Luminosity Function

Tsutomu T. Takeuchi[1], Akane Sakurai[1], Fang-Ting, Yuan[1]
Véronique Buat[2], and Denis Burgarella[2]

[1]Division of Particle and Astrophysical Science, Nagoya University, Furo-cho, Chikusa-ku, Nagoya 464-8602, Japan
[2]Laboratoire d'Astrophysique de Marseille, OAMP, Université Aix-Marseille, CNRS, 38 rue Frédéric Joliot-Curie, 13388 Marseille cedex 13, France

Abstract

Star formation in galaxies is tightly connected to the dust grain formation through the production of heavy elements. Observationally, it is the most direct to measure the star formation rate by the amount of ionizing UV photons, but dust formed by the star formation scatter and absorb these photons, and finally re-emit the energy at the IR. Hence, it is necessary to observe galaxies at both UV and IR to explore their star formation in the cosmic history. In this work, first we introduce a statistical method to handle the two datasets which have been treated independently at each wavelength in a unified manner, and reveal the star formation in galaxies hidden by dust.

1 Introduction

Exploring the star formation history of galaxies is one of the most important topics in modern observational cosmology. Especially, the "true" absolute value of the cosmic star formation rate (hereafter SFR) has been of a central importance to understand the formation and evolution of galaxies.

However, it has been a difficult task for a long time because of dust extinction. Active star formation (SF) is always accompanied by dust production through various dust grain formation processes related to the final stage of stellar evolution (e.g., Dwek & Scalo, 1980; Dwek, 1998; Nozawa et al., 2003; Takeuchi et al., 2005c; Asano et al., 2011). Observationally, SFR of galaxies are, in principle, measured by the ultraviolet (UV) luminosity from massive stars because of their short lifetime ($\sim 10^6$ yr) compared with the age of galaxies or the Universe. However, since the UV photons are easily scattered and absorbed by dust grains, SFR of galaxies is always inevitably affected by dust produced by their own SF activity. Since the absorbed energy is re-emitted at wavelengths of far-infrared (FIR), we need observations both at UV and FIR to have an unbiased view of their SF (e.g., Buat et al., 2005; Seibert et al., 2005; Cortese et al., 2006; Takeuchi et al., 2005a, 2010; Haines et al., 2011; Bothwell et al., 2011; Hao et al., 2011).

After great effort of many researchers, the cosmic history of the SFR density is gradually converging at $0 < z < 1$. This "latter half" of the cosmic SFR is characterized by the rapid decline of the total SFR, especially the decrease of the contribution of dusty IR galaxies toward $z = 0$: While at $z = 0$, the contribution of the SFR hidden by dust is 50–60 %, it becomes > 90 % at $z = 1$ (Takeuchi et al., 2005a). This difference of decrease in SFR obtained from FUV and FIR has been already recognized mainly in IR studies (e.g., Takeuchi et al., 2000, 2001a,b). Later works confirmed this " dusty era of the Universe ", and revealed that the dominance of the hidden SF continues even toward higher redshifts ($z \sim 3$) (e.g., Murphy et al., 2011; Cucciati et al., 2011).

Then, a natural question arises: what does the different evolution at different wavelengths represent? To address this problem, it is very important to understand how we select sample galaxies and what we see in them. Each time we find some relation between different properties, we must understand clearly which is real (physical) and which is simply due to a selection effect. Structure of the sample is schematically described by the Venn diagram in Fig. 1. Some are detected at both bands, but some are detected only at one of the observed wavelength and appear as upper limits at the other wavelength. In previous studies it was often found that various claims were inconsistent with each other, mainly because they did not construct a well-controled sample of FUV and FIR selected galaxies.

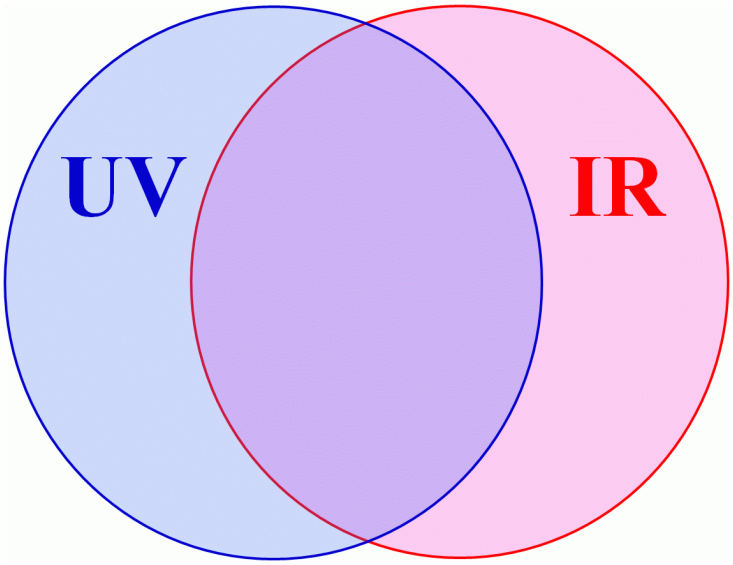

Figure 1: A Venn diagram describing the structure of UV- and FIR-wavelength observational dataset. Some are detected at both bands, but some are detected only at one of the observed wavelength and appear as upper limits at the other wavelength.

Recently, thanks to new large surveys, some attempts to explore the SFR distribution of galaxies in bivariate way have been made, through the "SFR function" (e.g., Buat et al., 2007, 2009; Haines et al., 2011; Bothwell et al., 2011). These works are based on the FUV and FIR LFs and their sum, but have not yet address their dependence on each other. To explore the bivariate properties of the SF in galaxies further, the proper tool is the UV-IR bivariate luminosity function (BLF).

However, constructing a BLF from two-wavelength data is not a trivial task. When we have a complete flux-limited[1] multiwavelength dataset, we can estimate a univariate luminosity function (LF) at each band, but what we want to know is *the dependence structure* between luminosities at different bands. Mathematically, this problem is rephrased as follows: can we (re)construct a multivariate probability density function (PDF) satisfying prescribed marginals? Although there is an infinite number of degrees of freedom to choose the original PDF, if we can model the dependence between variables, we can construct such a bivariate PDF. A statistical tool for this problem is the so-called "copula" (see Sec. 2 for the definition).

A copula has been extensively used in financial engineering, for instance, but until recently there were very few applications to astrophysical problems (e.g., Koen, 2009; Benabed et al., 2009; Scherrer et al., 2010; Sato et al., 2010, 2011). Takeuchi (2010) introduced the copula to the estimation problem of a BLF. In this work, we apply the copula-based BLF estimation to the FUV-FIR two-wavelength dataset from $z = 0$ to $z = 1$, using data from IRAS, AKARI[2], Spitzer[3], and GALEX[4].

The layout of this paper is as follows. We define a copula, especially the Gaussian copula, and formulate the copula-based BLF in Sec. 2. We then describe our FUV-FIR data in Sec. 3. In Sec. 4, we first formulate the likelihood function for the BLF estimation. Then we show the results, and discuss the possible interpretation of the evolution of the FUV-FIR BLF. Section 5 is devoted to summary.

Throughout the paper we will assume $\Omega_{\rm M0} = 0.3$, $\Omega_{\Lambda 0} = 0.7$ and $H_0 = 70\ {\rm km\ s^{-1}\ Mpc^{-1}}$. The luminosities are defined as νL_ν and expressed in solar units assuming $L_\odot = 3.83 \times 10^{33}\ {\rm erg\ s^{-1}}$.

[1] Or any other observational condition.
[2] URL: http://www.ir.isas.ac.jp/ASTRO-F/index-e.html.
[3] URL: http://www.spitzer.caltech.edu/.
[4] URL: http://www.galex.caltech.edu/.

2 The Bivariate Luminosity Function Based on the Copula

2.1 Copula: general definition

First, we briefly introduce a copula. A copula $C(u_1, u_2)$ is defined as follows:

$$G(x_1, x_2) \quad = \quad C\left[F_1(x_1), F_2(x_2)\right] \tag{1}$$

where $F_1(x_1)$ and $F_2(x_2)$ are two univariate marginal cumulative distribution functions (DFs) and $G(x_1, x_2)$ is a bivariate DF. We note that all bivariate DFs have this form and we can safely apply this method to any kind of bivariate DF estimation problem (Takeuchi, 2010). In various applications, we usually know the marginal DFs (or equivalently, PDFs) from the data. Then, the problem reduces to a statistical estimation of a set of parameters to determine the shape of a copula $C(u_1, u_2)$. In the form of the PDF,

$$g(x_1, x_2) = \frac{\partial^2 C\left[F_1(x_1), F_2(x_2)\right]}{\partial x_1 \partial x_2} f_1(x_1) f_2(x_2) \equiv \quad c\left[F_1(x_1), F_2(x_2)\right] f_1(x_1) f_2(x_2), \tag{2}$$

where $f_1(x_1)$ and $f_2(x_2)$ are the PDFs of $F_1(x_1)$ and $F_2(x_2)$, respectively. On the second line, $c(u_1, u_2)$ is referred to as a differential copula.

2.2 Gaussian copula

Since the choice of copula is literally unlimited, we have to introduce a guidance principle. In many data analyses in physics, the most familiar measure of dependence might be the linear correlation coefficient ρ. Mathematically speaking, ρ depends not only on the dependence of two variables but also the marginal distributions, which is not an ideal property as a dependence measure. Even so, a copula having an explicit dependence on ρ would be convenient. In this work, we use a copula with this property, the Gaussian copula.

One of the natural candidate with ρ may be a copula related to a bivariate Gaussian DF (for other possibilities, see Takeuchi, 2010). The Gaussian copula has an explicit dependence on a linear correlation coefficient by its construction. Let

$$\psi_1(x) = \frac{1}{\sqrt{2\pi}} \exp\left(-\frac{x^2}{2}\right), \tag{3}$$

$$\Psi_1 = \int_{-\infty}^{x} \Psi(x')\mathrm{d}x', \tag{4}$$

$$\psi_2(x_1, x_2; \rho) = \frac{1}{\sqrt{(2\pi)^2 \det \mathbf{\Sigma}}} \exp\left(-\frac{1}{2}\mathbf{x}^T \mathbf{\Sigma}^{-1} \mathbf{x}\right), \tag{5}$$

and

$$\Psi_2(x_1, x_2; \rho) = \int_{-\infty}^{x_1} \int_{-\infty}^{x_2} \psi_i(x_1', x_2')\mathrm{d}x_1'\mathrm{d}x_2', \tag{6}$$

where $\mathbf{x} \equiv (x_1, x_2)^T$, $\mathbf{\Sigma}$ is a covariance matrix

$$\mathbf{\Sigma} \equiv \begin{pmatrix} 1 & \rho \\ \rho & 1 \end{pmatrix}, \tag{7}$$

and superscript T stands for the transpose of a matrix or vector.

Then, we define a Gaussian copula $C^{\mathrm{G}}(u_1, u_2; \rho)$ as

$$C^{\mathrm{G}}(u_1, u_2; \rho) = \Psi_2\left[\Psi_1^{-1}(u_1), \Psi_1^{-1}(u_2); \rho\right]. \tag{8}$$

The density of $C^{\rm G}$, c^G, is obtained as

$$\begin{aligned} c^{\rm G}(u_1,u_2;\rho) &= \frac{\partial^2 C^{\rm G}(u_1,u_2;\rho)}{\partial u_1 \partial u_2} = \frac{\partial^2 \Psi_2\left[\Psi_1^{-1}(u_1),\Psi_1^{-1}(u_2);\rho\right]}{\partial u_1 \partial u_2} \\ &= \frac{\psi_2(x_1,x_2;\rho)}{\psi_1(x_1)\psi_1(x_2)} \\ &= \frac{1}{\sqrt{\det \boldsymbol{\Sigma}}} \exp\left\{-\frac{1}{2}\left[\boldsymbol{\Psi^{-1}}^T\left(\boldsymbol{\Sigma}^{-1}-\mathbf{I}\right)\boldsymbol{\Psi^{-1}}\right]\right\}, \end{aligned} \tag{9}$$

where $\boldsymbol{\Psi^{-1}} \equiv \left[\Psi^{-1}(u_1),\Psi^{-1}(u_2)\right]^T$ and $\mathbf{I}$ stands for the identity matrix.

2.3 Construction of the FUV-TIR BLF

In this work, we define the luminosity at a certain wavelength band by $L \equiv \nu L_\nu$ (ν is the corresponding frequency). Then the LF is defined as a number density of galaxies whose luminosity lies between a logarithmic interval $[\log L, \log L + {\rm d}\log L]$:

$$\phi^{(1)}(L) \equiv \frac{{\rm d}n}{{\rm d}\log L}\ , \tag{10}$$

where we denote $\log x \equiv \log_{10} x$ and $\ln x \equiv \log_e x$. For mathematical simplicity, we define the LF as being normalized, i.e.,

$$\int \phi^{(1)}(L){\rm d}\log L = 1\ . \tag{11}$$

Hence, this corresponds to a PDF. We also define a cumulative LF as

$$\Phi^{(1)}(L) \equiv \int_{\log L_{\rm min}}^{\log L} \phi^{(1)}(L'){\rm d}\log L'\ , \tag{12}$$

where $L_{\rm min}$ is the minimum luminosity of galaxies considered. This corresponds to the DF. If we denote univariate LFs as $\phi_1^{(1)}(L_1)$ and $\phi_2^{(1)}(L_2)$, then the BLF $\phi^{(2)}(L_1,L_2)$ is described by a differential copula $c(u_1,u_2)$ as

$$\phi^{(2)}(L_1,L_2) = c\left[\phi_1^{(1)}(L_1),\phi_2^{(1)}(L_2)\right]\ . \tag{13}$$

For the Gaussian copula, the BLF is obtained as

$$\phi^{(2)}(L_1,L_2;\rho) = \frac{1}{\sqrt{\det \boldsymbol{\Sigma}}} \exp\left\{-\frac{1}{2}\left[\boldsymbol{\Psi^{-1}}^T\left(\boldsymbol{\Sigma}^{-1}-\mathbf{I}\right)\boldsymbol{\Psi^{-1}}\right]\right\}\phi_1^{(1)}(L_1)\phi_2^{(1)}(L_2)\ , \tag{14}$$

where

$$\boldsymbol{\Psi^{-1}} = \left[\Psi^{-1}\left(\Phi_1^{(1)}(L_1)\right),\ \Psi^{-1}\left(\Phi_2^{(1)}(L_2)\right)\right]^T. \tag{15}$$

For the UV, we adopt the Schechter function (Schechter, 1976).

$$\phi_1^{(1)}(L) = (\ln 10)\ \phi_{*1}\left(\frac{L}{L_{*1}}\right)^{1-\alpha_1}\exp\left[-\left(\frac{L}{L_{*1}}\right)\right]. \tag{16}$$

For the IR, we use the analytic form for the LF proposed by Saunders et al. (1990),

$$\phi_2^{(1)}(L) = \phi_{*2}\left(\frac{L}{L_{*2}}\right)^{1-\alpha_2}\exp\left\{-\frac{1}{2\sigma^2}\left[\log\left(1+\frac{L}{L_{*2}}\right)\right]^2\right\}. \tag{17}$$

We use the re-normalized version of eqs. (17) and (16) so that they can be regarded as PDFs, as mentioned above.

2.4 Selection effects: another benefit of a copula BLF

Another benefit of copula is that it is easy to incorporate observational selection effects which always exist in any kind of astronomical data. In a bi(multi)variate analysis, there are two categories of observational selection effects.

1. Truncation

   We do not know if a source would exist below a detection limit.

2. Censoring

   We know there is a source, but we have only an upper (sometimes lower) limit for a certain observable.

As we mentioned above, we have to deal with both of these selection effects carefully to construct a BLF from data at the same time. It is terribly difficult to incorporate these effects by heuristic methods, particularly for a nonparametric methods (Takeuchi 2012, in preparation). In contrast, since we have an analytic form for the BLF, the treatment of upper limits is much more straightforward (Takeuchi, 2010). We see how it is treated in the likelihood function in Sec. 4.

3 Data

3.1 FUV-FIR data construction

We have constructed a dataset of galaxies selected at FUV and FIR by *GALEX* and *IRAS* for $z = 0$. At higher redshifts, *GALEX* and *Spitzer* data are used for $z = 0.7$ and EIS and *Spitzer* for $z = 1.0$ in the Chandra Deep Field South (CDFS). We explain the details of each sample in the following.

In the Local Universe, we used the sample compiled by Buat et al. (2007). This sample was constructed based on IRAS all-sky survey and GALEX All-Sky Imaging Survey (AIS). This dataset consists of UV- and IR-selected samples. The UV-selection was made by GALEX FUV (1530 Å) band with FUV < 17 mag (hereafter, all magnitudes are presented in AB mag). This corresponds to the luminosity lower limit of $L_{\rm FUV} > 10^8\ L_\odot$. Redshift information was taken from HyperLEDA (Paturel et al., 2003) and NED. The IR-selection is based on the IRAS PSCz (Saunders et al., 2000). The detection limit of the PSCz is $S_{60} > 0.6$ Jy. Redshifts of all PSCz galaxies were measured. All UV fluxes were remeasured with the package we have developed (Iglesias-Páramo et al., 2006) to avoid the shredding of galaxies. Details of the sample construction are explained in Buat et al. (2007). The number of sample galaxies is 644.

We also constructed a new, much larger sample of IR-selected galaxies by AKARI FIS All-Sky Survey. We started from the AKARI FIS bright source catalog (BSC) v.1 from AKARI all sky survey (Yamamura et al., 2010) to construct this sample. This sample is selected at *WIDE-S* band ($\lambda = 90$ m) of the AKARI FIS (Kawada et al., 2007). The detection limit is $S_{90} > 0.2$ Jy. We first selected AKARI sources in the SDSS footprints. Then, to have a secure sample of galaxies with redshift data, we made a cross match of AKARI sources with the Imperial IRAS-FSC Redshift Catalogue (IIFSCz), a redshift catalog recently published (Wang & Rowan-Robinson, 2009), with a search radius of 36 arcsec.. Since about 90 % of galaxies in the IIFSCz have spectroscopic or photometric redshifts at $S_{60} > 0.36$ Jy, the depth of the sample is defined by this matching. We measured the FUV and NUV flux densities with the same procedure as the IRAS-GALEX sample. The detection limits at FUV and NUV of this sample are 19.9 mag and 20.8 mag (Morrissey et al., 2007). A corresponding UV-selected sample is under construction, hence we have only IR-selected sample. The number of galaxies is 3,891. For more information on this sample and properties of galaxies, see Sakurai et al. (2011).

At higher-z, our samples are selected in the CDFS. GALEX observed this field at FUV and NUV (2300 Å) as a part of its deep imaging survey. We restricted the field to the subfield observed by Spitzer/MIPS as a part of the GOODS key program (Elbaz et al., 2007) to have the corresponding IR data. The area of the region is 0.068 deg^2. Precise description of our high-z samples are presented in Buat et al. (2009) and Burgarella et al. (2006).

At $z = 0.7$, the NUV-band corresponds to the FUV rest frame of the sample galaxies. We thus constructed the sample based on NUV-selection. Redshifts were taken from the COMBO-17 survey (Wolf et al., 2004). Data reduction and redshift association are explained in Burgarella et al. (2006). We truncated the sample at NUV = 25.3 mag so that more than 90 % of the GALEX sources are identified in COMBO-17 with $R < 24$ mag. We set the MIPS 24 m upper limit as 0.025 mJy. For the IR-selected sample, we based on the GOODS sample and

matched the GALEX and COMBO-17 sources. The sizes of both the UV- and IR-selected samples are 340 and 470, respectively.

In contrast to $z = 0.7$, since NUV-band of GALEX corresponds to 1155 Å in the restframe of galaxies at $z = 1.0$, we cannot use NUV as the primary selection band as restframe FUV. Instead, we start from U-band selection. The CDFS/GOODS field is covered by the EIS survey (Arnouts et al., 2001). We then cross-matched the U-band sources with the COMBO-1 sample to have redshifts. We set the limit at $U = 24.3$ mag to avoid source confusion. The IR flux densities were taken from Spitzer MIPS 24 m data, and the same upper limit is put for non-detections. Again the IR-selected sample was constructed from the GOODS, as the $z = 0.7$ sample. The sizes of the $z = 1.0$ UV and IR-selected samples are 319 and 1033, respectively.

3.2 Far-UV and total IR luminosities

We are interested in the SF activity of galaxies and its evolution. Hence, luminosities of galaxies representative of SF activity would be ideal. As for the directly visible SF, obviously the UV emission is appropriate for this purpose. We define the FUV luminosity of galaxies $L_{\rm FUV}$ as $L_{\rm FUV} \equiv \nu L_\nu$@FUV. For $z = 0$ galaxies, FUV corresponds to 1530 Å. At higher redshifts, as we explained, $L_{\rm FUV}$ is calculated from NUV flux density at $z = 0.7$ and U-band flux density at $z = 1.0$, respectively.

In contrast, at IR, the luminosity related to the SF activity is the one integrated over a whole range of IR wavelengths ($\lambda = 8$–1000 m), $L_{\rm TIR}$. For the Local IRAS-GALEX sample, it is quite straightforward to define $L_{\rm TIR}$ since the *IRAS* galaxies are selected at 60 m. We adopted a formula $L_{\rm TIR} = 2.5\nu L_\nu$@$60$ m. This rough approximation is, in fact, justified by SEDs of galaxies with ISO 160 m observations (Takeuchi et al., 2006).

Also, for AKARI-GALEX sample, we have excellent flux density data at FIR. We used the following TIR estimation formula from AKARI two wide bands (Takeuchi et al., 2005b, 2010),

$$L_{\rm AKARI}^{\rm 2band} = \Delta\nu(\textit{WIDE-S}) L_\nu(90 \quad {\rm m}) + \Delta\nu(\textit{WIDE-L}) L_\nu(140 \quad {\rm m}), \tag{18}$$

where

$$\begin{aligned} \Delta\nu(\textit{WIDE-S}) &= 1.47 \times 10^{12}\ [{\rm Hz}]\,, \\ \Delta\nu(\textit{WIDE-L}) &= 0.831 \times 10^{12}\ [{\rm Hz}]. \end{aligned} \tag{19}$$

However, since deep FIR data of higher-z galaxies are not easily available to date, we should rely on the data taken by *Spitzer* MIPS 24 m. we should use conversion formulae from MIR luminosity to $L_{\rm TIR}$:

$$\log L_{\rm TIR}[{\rm L}_\odot] = 1.23 + 0.972 \log L_{15}[{\rm L}_\odot]\,, \tag{20}$$

$$\log L_{\rm TIR}[{\rm L}_\odot] = 2.27 + 0.707 \log L_{12}[{\rm L}_\odot] + 0.0140 \left(\log L_{12}[{\rm L}_\odot]\right)^2\,, \tag{21}$$

which are an updated version of the formulae proposed by Takeuchi et al. (2005b) and also used by Buat et al. (2009). Here L_{15} and L_{12} are luminosities νL_ν@15 m and 12 m, i.e., $24/(1+z)$ at $z = 0.7$ and 1.0, respectively. The estimated $L_{\rm TIR}$ slightly depends on which kind of conversion formula is used, but for our current purpose, it does not affect our conclusion and we do not discuss extensively here. We can find intercomparison of the MIR-TIR conversion formula in Buat et al. (2009).

This situation will be greatly improved with Herschel[5] data. We will leave this as our future work with Herschel H-ATLAS (Eales et al., 2010) and GAMA (Driver et al., 2011) data (Takeuchi et al. 2012, in preparation).

4 Results and Discussion

4.1 FUV and TIR univariate LFs

In order to estimate the FUV-TIR BLF, first we have to examine our setting for the FUV and TIR univariate LFs. The IRAS-GALEX sample, the validity of the Local univariate LFs are already proved (see Fig. 3 of Buat et al., 2007). Hence, we can safely use the analytic formulae of FUV and TIR LFs at $z = 0$ [eqs. (16) and (17)].

We use the Schechter parameters presented by Wyder et al. (2005) for *GALEX* FUV: $(\alpha_1, L_{*1}, \phi_{*1}) = (1.21, 1.81 \times 10^9 h^{-2}\ [{\rm L}_\odot], 1.35 \times 10^{-2} h^3\ [{\rm Mpc}^{-3}])$. For the TIR, we used the parameters $(\alpha_2, L_{*2}, \phi_{*2}, \sigma) = (1.23, 4.34 \times$

[5]URL: http://herschel.esac.esa.int/.

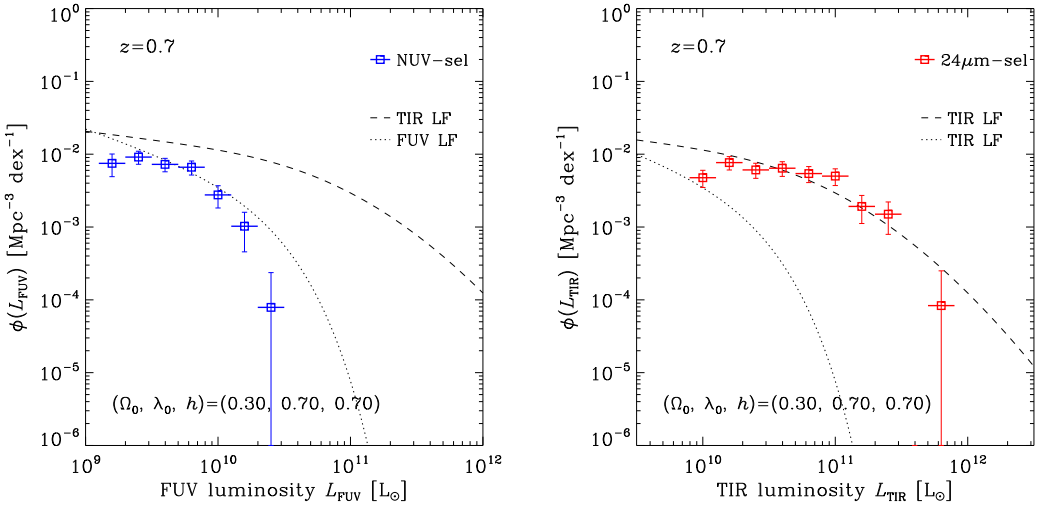

Figure 2: The FUV and TIR LFs at $z = 0.7$ (left and right panel, respectively). Open squares are a nonparametric LFs estimated from our CDFS multiwavelength data with GALEX NUV- and Spitzer MIPS 24 m-selections. Dotted lines represent the FUV LFs at this redshift bin taken from Arnouts et al. (2005). Dashed lines depict the TIR LFs derived from the evolutionary parameters at $z = 0.7$ given by Le Floc'h et al. (2005). Because of a well-known large density enhancement at this redshift, we renormalized to remove the overdensity.

$10^8 h^{-2}$ $[\mathrm{L}_\odot], 2.34 \times 10^{-2} h^3$ $[\mathrm{Mpc}^{-3}], 0.724)$ (Takeuchi et al., 2003) obtained from the *IRAS* PSCz galaxies (Saunders et al., 2000), and multiplied L_{*1} with 2.5 to convert the 60- m LF to the TIR LF.

For higher redshifts, ideally we should estimate from the BLF estimation simultaneously. It is, however, quite difficult for our current samples because of the limited number of galaxies. We instead used the LF parameters at $z = 0.7$ and 1.0 obtained by previous studies on univariate LFs and modeled the FUV and TIR univariate LFs at these redshifts and examined their validity with nonparametric LFs estimated from the data. We use the parameters compiled by Takeuchi et al. (2005a). Parameters of the evolution of the TIR LF are obtained by approximating the evolution in the form

$$\phi_2^{(1)}(L_2, z) = \mathfrak{g}(z)\phi_{2,0}^{(1)}\left[\frac{L_2}{\mathfrak{f}(z)}\right] \tag{22}$$

where $\phi_{2,0}^{(1)}(z)$ is the local functional form of the TIR LF. Le Floc'h et al. (2005) assumed a power-law form for the evolution functions as

$$\mathfrak{f}(z) = (1+z)^{\mathfrak{Q}},\ \mathfrak{g}(z) = (1+z)^{\mathfrak{P}} \tag{23}$$

and obtained $\mathfrak{P} = 0.7$ and $\mathfrak{Q} = 3.2$, with α remaining constant. The Schechter parameters at $z = 0.7$ and 1.0 are directly estimated by Arnouts et al. (2005) and we adopt their values (see Table 1 of Takeuchi et al., 2005a).

Then we estimated the FUV and TIR LFs with the stepwise maximum likelihood method and the variant of C^- method from our CDFS multiwavelength data (for the estimation method, see, e.g., Takeuchi et al., 2000; Johnston, 2011, and references therein). The obtained univariate LFs at $z = 0.7$ and 1.0 are presented in Figs. 2 and 3. We also show the analytic model LFs in these figures. We note that a well-known large density enhancement locates in the CDFS at $z = 0.7$ (e.g., Salimbeni et al., 2009), we have renormalized the LFs to remove the effect of overdensity. In the following analysis, we normalize the univariate LFs according to eq. (11) so that we can treat the univariate LFs as PDFs, hence this does not affect the following analysis at all.

Because of the small sample size, the LF shape is not perfectly agree with the supposed functional forms, but the nonparametric LFs acceptably similar to the analytic functions both for the FUV and TIR at each redshift. We stress that the analytic functions are *not* the fit to the data, but estimated from other studies. This implies that the estimated evolutionary parameters of the LFs work generally well. Thus, we can use the higher-z univariate LFs as the marginal PDFs for the estimation of the FUV-TIR BLFs.

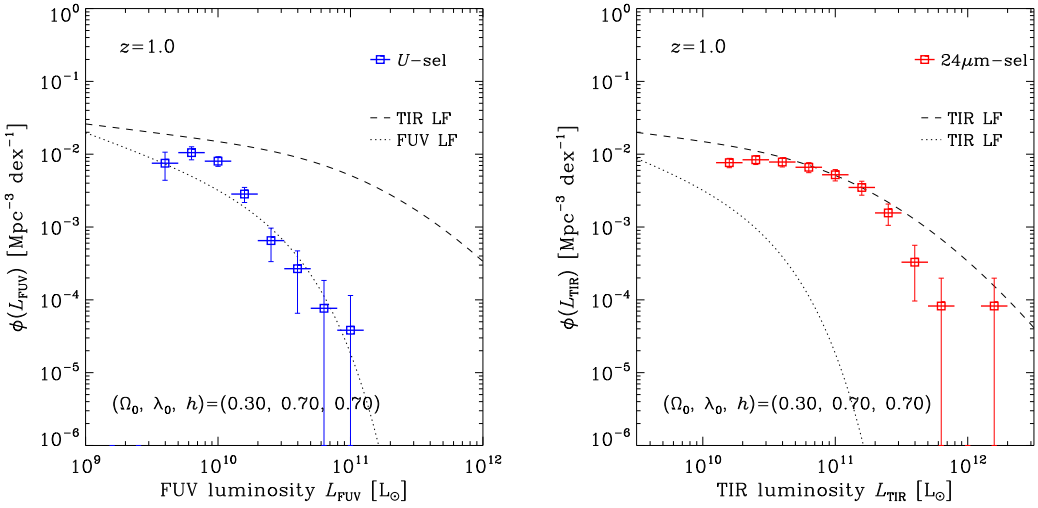

Figure 3: The FUV and TIR LFs at $z = 1.0$. Symbols are the same as in Fig. 2, but FUV samples are selected at U-band.

4.2 Copula likelihood for the BLF estimation

By using the estimated univariate FUV and TIR LFs as given marginals, we can estimate only one parameter, the linear correlation ρ by maximizing the likelihood function. The structure of a two-band selected data is $(L^{i_k}_{\rm FUV}, j^{i_k}_{\rm UV}, L^{i_k}_{\rm TIR}, j^{i_k}_{\rm IR}), i_k = 1 \ldots n_k$. Here, $j_{\rm band}$ (band: FUV or TIR) stands for the upper limit flag: $j_{\rm band} = 0$: detection and $j_{\rm band} = -1$: upper limit. Another index k is the indicator of the selected band, i.e., $k = 1$ means a sample galaxy is selected at UV and $k = -1$ means it is selected at IR. The likelihood function is as follows.

$$
\begin{aligned}
&\ln \mathcal{L}\left(L^{i_k}_{\rm FUV}, L^{i_k}_{\rm TIR} \middle| \, i_k = 1, \cdots n_k, k = 1, -1\right) \\
&= \sum_{k=\left\{\begin{smallmatrix} 1 & : \text{UV sel} \\ -1 & : \text{IR sel} \end{smallmatrix}\right.} \sum_{i_k=1}^{n_k} \Bigg\{ \ln\left[p^{\rm det}\left(L^{i_k}_{\rm FUV}, L^{i_k}_{\rm TIR}\right)\right]^{(1+j^{i_k}_{\rm UV})(1+j^{i_k}_{\rm IR})} \\
&\quad + \ln\left[p^{\text{UL: UV}}\left(L^{i_k}_{\rm FUV}, L^{i_k}_{\rm TIR}\right)\right]^{\frac{(1+k)(-j^{i_k}_{\rm UV})}{2}} + \ln\left[p^{\text{UL: IR}}\left(L^{i_k}_{\rm FUV}, L^{i_k}_{\rm TIR}\right)\right]^{\frac{(1-k)(-j^{i_k}_{\rm IR})}{2}} \Bigg\},
\end{aligned}
\tag{24}
$$

where $p^{\rm det}\left(L^{i_k}_{\rm FUV}, L^{i_k}_{\rm TIR}\right)$ is the probability for i_kth galaxy to be detected at both bands and to have luminosities $L^{i_k}_{\rm FUV}$ and $L^{i_k}_{\rm TIR}$,

$$
p^{\rm det}\left(L^{i_k}_{\rm FUV}, L^{i_k}_{\rm TIR}\right) \equiv \frac{\phi^{(2)}\left(L^{i_k}_{\rm FUV}, L^{i_k}_{\rm TIR}; \rho\right)}{\displaystyle\int_{L^{\rm lim}_{\rm FUV}(z_{i_k})}^{\infty} \int_{L^{\rm lim}_{\rm TIR}(z_{i_k})}^{\infty} \phi^{(2)}\left(L'_{\rm FUV}, L'_{\rm TIR}; \rho\right) {\rm d}L'_{\rm TIR} {\rm d}L'_{\rm FUV}}, \tag{25}
$$

$p^{\text{UL: UV}}\left(L^{i_k}_{\rm FUV}, L^{i_k}_{\rm TIR}\right)$ is the probability for i_kth galaxy to be detected at IR band and have a luminosity $L^{i_k}_{\rm TIR}$, but not detected at UV band and only an upper limit $L^{i_k}_{{\rm FUV},j_k}$ is available,

$$
p^{\text{UL: UV}}\left(L^{i_k}_{\rm FUV}, L^{i_k}_{\rm TIR}\right) \equiv \frac{\displaystyle\int_0^{L^{i_k}_{{\rm FUV},j_k}} \phi^{(2)}\left(L'_{\rm FUV}, L^{i_k}_{\rm TIR}\right) {\rm d}L'_{\rm FUV}}{\displaystyle\int_0^{\infty} \int_{L^{\rm lim}_{\rm TIR}(z_{i_k})}^{\infty} \phi^{(2)}\left(L'_{\rm FUV}, L'_{\rm TIR}; \rho\right) {\rm d}L'_{\rm TIR} {\rm d}L'_{\rm FUV}}, \tag{26}
$$

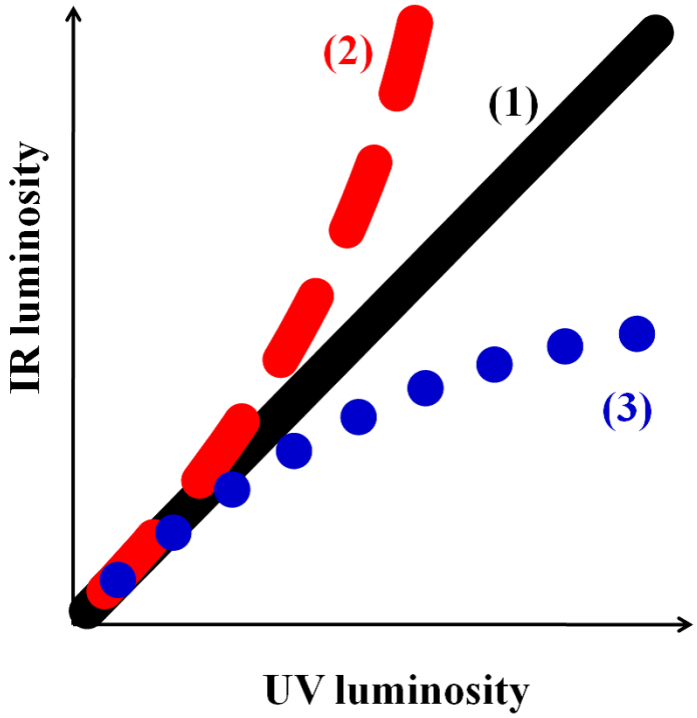

Figure 4: Schematic BLF. (1) Diagonal: The energy from SF is emitted equally at UV and IR with any SF activity. (2) Upward: The more active the SF in a galaxy is, the more luminous at the IR (dusty SF). (3) Downward: The more active the SF is, the more luminous at the UV (“ transparent ” SF).

and $p^{\text{UL: IR}}\left(L_{\text{FUV}}^{i_k}, L_{\text{TIR}}^{i_k}\right)$ is the probability for i_kth galaxy to be detected at UV band and have a luminosity $L_{\text{FUV}}^{i_k}$, but not detected at IR band and only an upper limit $L_{\text{TIR},j_k}^{i_k}$ is available,

$$p^{\text{UL: IR}}\left(L_{\text{FUV}}^{i_k}, L_{\text{TIR}}^{i_k}\right) \equiv \frac{\displaystyle\int_0^{L_{\text{TIR},j_k}^{i_k}} \phi^{(2)}\left(L_{\text{FUV}}^{i_k}, L'_{\text{TIR}}\right) \mathrm{d}L'_{\text{TIR}}}{\displaystyle\int_{L_{\text{FUV}}^{\lim}(z_{i_k})}^{\infty}\int_0^{\infty} \phi^{(2)}\left(L'_{\text{FUV}}, L'_{\text{TIR}}; \rho\right) \mathrm{d}L'_{\text{TIR}}\mathrm{d}L'_{\text{FUV}}}. \tag{27}$$

The denominator in eq. (25) is introduced to take into account the truncation in the data by observational flux selection limits at both bands (e.g., Sandage et al., 1979; Johnston, 2011). We should also note that it often happens that the same galaxies are included both in UV- and IR-selected sample. In such a case, we should count the same galaxies only once to avoid double counting of them. Practically, such galaxies are included in any of the samples, because they are detected at both bands and are symmetric between UV- and IR-selections.

4.3 The BLF and its evolution

Using the Gaussian copula, now we can estimate the BLF. The visible and hidden SFRs should be directly reflected to this function. Dust is produced by SF activity, but also destroyed by SN blast waves as a result of the SF. Many physical processes are related to the evolution of the dust amount. Thus, first of all, we should describe statistically how it evolved, as stated in Introduction.

First, we summarize how to interpret the UV-IR BLF schematically in Fig. 4. First, we see the case that the ridge of the BLF is straight and diagonal [see (1) in Fig. 4]. This means that the energy from SF is emitted equally at UV and IR with any SF activity. If the relation is diagonal but has an offset horizontally or vertically, this suggests that a constant fraction of energy is absorbed by dust and reemitted. Second, if the ridge is curved upward, it means that the more active the SF in a galaxy is, the more luminous at the IR [dusty SF: (2) in Fig. 4].

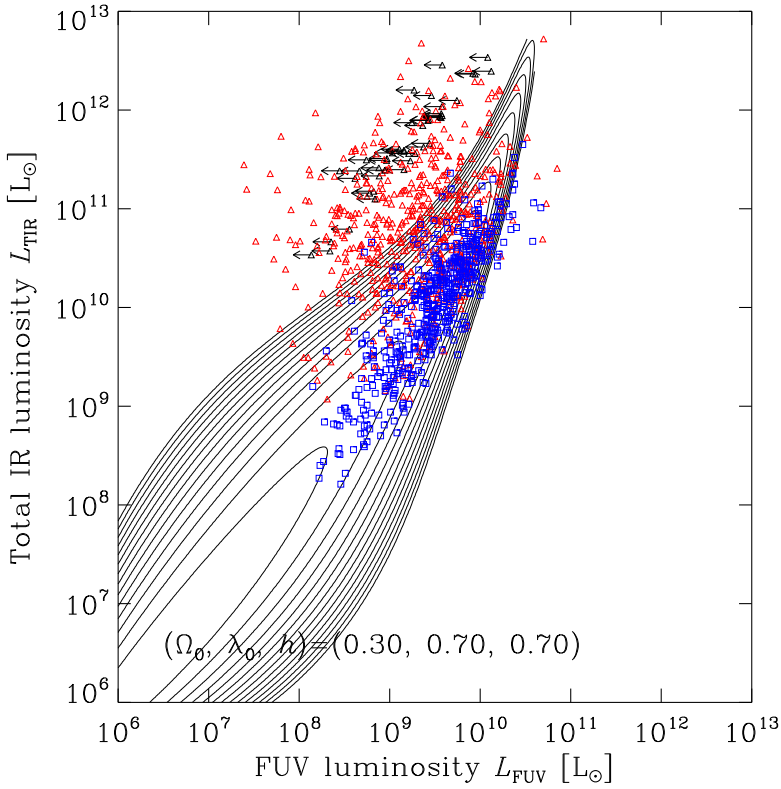

Figure 5: The BLF of galaxies from IRAS and GALEX at $z = 0$. Contours are the analytic model constructed by a Gaussian copula and univariate FUV and TIR LFs.

Third, if the ridge is bent downward, the more active the SF is, the more luminous at UV ['transparent' SF: (3) in Fig. 4].

Now we show the estimated BLFs in Figs. 5–8. In the Local Universe, the BLF is quite well constrained. The estimated correlation coefficient ρ is very high ~ 0.95, both from IRAS-GALEX and AKARI-GALEX datasets. The apparent scatter of the $L_{\rm FUV}$–$L_{\rm TIR}$ is found to be due to the nonlinear shape of the ridge of the BLF. This bent shape of the BLF was implied by preceding studies (Martin et al., 2005), and we could quantify this feature. The copula BLF naturally reproduced it.

At higher redshifts ($z = 0.7$–1.0), the linear correlation remains tight ($\rho \sim 0.85$–0.9), even though it is difficult to constrain the low-luminosity end from the data in this analysis (Spitzer-GALEX in the CDFS). It will be interesting to apply this method to better forthcoming data.

Though the whole shape cannot be perfectly determined by the current data, we find that ρ in the copula LF is high and remarkably stable with redshifts (from 0.95 at $z = 0$ to 0.85 at $z = 1.0$). This implies the evolution of the UV-IR bivariate LF is mainly due to the different evolution of the univariate LFs, and may not be controled by the evolution of the dependence structure.

In this study, we did not try to examine if the Gaussian copula would be a proper choice as a model of the FUV-TIR BLF. At $z = 0$, for example, when UV-selected data comparably large as the AKARI sample are ready, we will be able to specify (a family of) copulas appropriate for this analysis. At higher redshifts, our current data are not deep enough to do it. Herschel, ALMA, and SPICA[6] data, together with optical deep surveys, will enable us to explore and constrain the BLF evolution in the whole history of galaxy evolution.

[6]URL: http://www.ir.isas.jaxa.jp/SPICA/SPICA_HP/index_English.html.

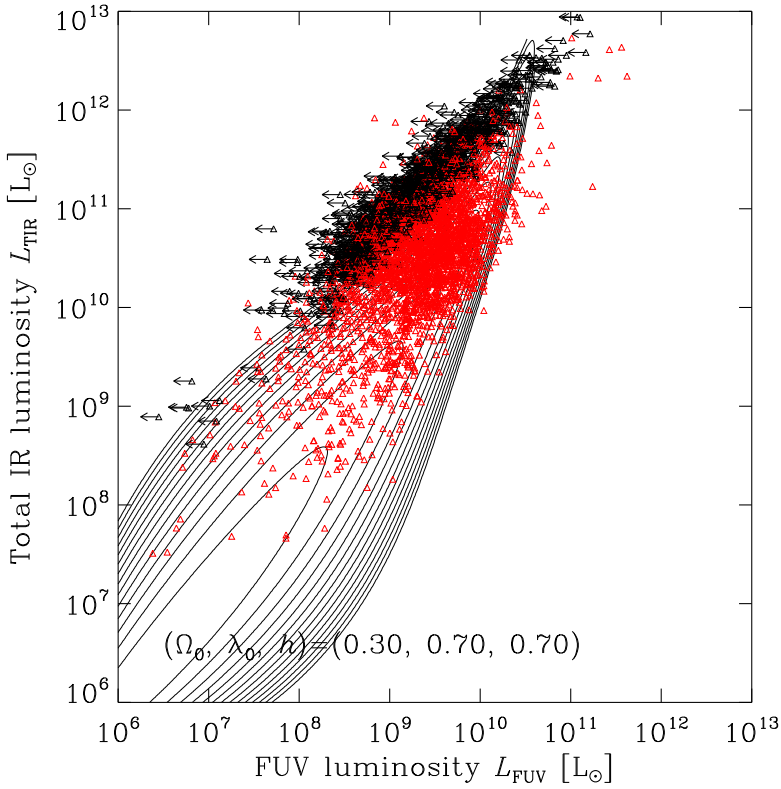

Figure 6: The same as Fig. 5 but from AKARI and GALEX.

5 Conclusion

To understand the visible and hidden SF history in the Universe, it is crucial to analyze multiwavelength data in a unified manner. The copula is an ideal tool to combine two marginal univariate LFs to construct a bivariate LFs. It is straightforward to extend this method to multivariate DFs.

1. The Gaussian copula LF is sensitive to the linear correlation parameter ρ.
2. Even so, ρ in the copula LF is remarkably stable with redshifts (from 0.95 at $z = 0$ to 0.85 at $z = 1.0$).
3. The nonlinear structure of the BLF is naturally reproduced by the Gaussian copula.
4. This implies the evolution of the UV-IR BLF is mainly due to the different evolution of the univariate LFs, and may not be controled by the dependence structure.

The data from Herschel, ALMA, and SPICA data will improve the estimates drastically, and we expect to specify the full evolution of the UV-IR BLF in the Universe. We stress that the copula will be a useful tool for any other kind of bi- (multi-) variate statistical analysis.

Acknowledgments

This work is based on observations with AKARI, a JAXA project with the participation of ESA. This research has made use of the NASA/IPAC Extragalactic Database (NED) which is operated by the Jet Propulsion Laboratory, California Institute of Technology, under contract with the National Aeronautics and Space Administration. TTT has been supported by Program for Improvement of Research Environment for Young Researchers from Special

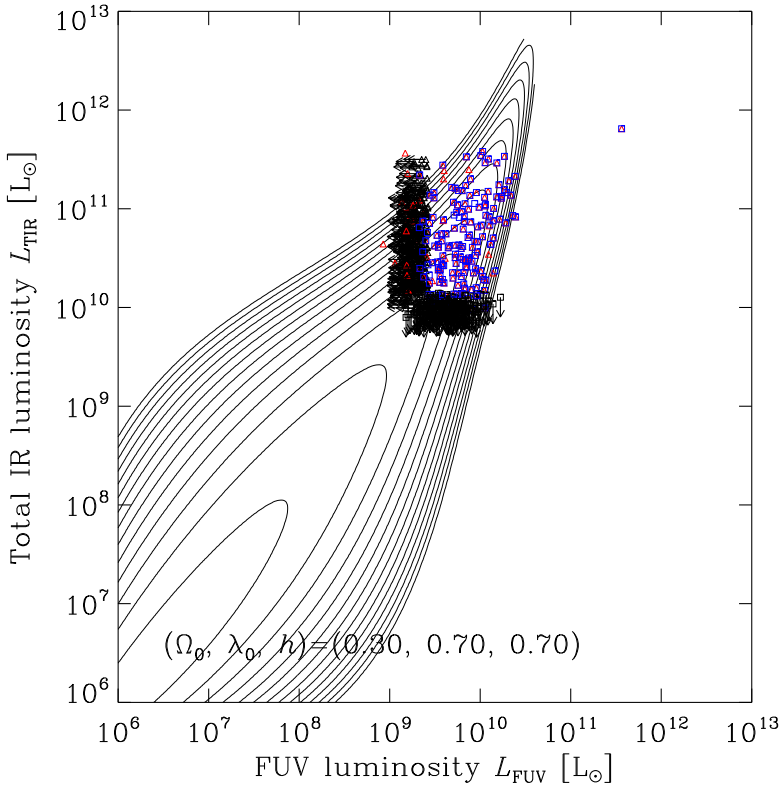

Figure 7: The same as Fig. 5 but from Spitzer and GALEX at $z = 0.7$.

Coordination Funds for Promoting Science and Technology, and the Grant-in-Aid for the Scientific Research Fund (20740105, 23340046) commissioned by the MEXT. TTT, AS, and FTY have been partially supported from the Grand-in-Aid for the Global COE Program “Quest for Fundamental Principles in the Universe: from Particles to the Solar System and the Cosmos” from the Ministry of Education, Culture, Sports, Science and Technology (MEXT) of Japan. &

References

Arnouts, S., Schiminovich, D., Ilbert, O., et al. 2001, A&A, 379, 740

Arnouts, S., Vandame, B., Benoist, C., et al. 2005, ApJ, 619, L43

Asano, R. S., Takeuchi, T. T., Hirashita, H., Inoue, A. K., 2011, Earth, Planets, & Space, submitted

Benabed, K., Cardoso, J.-F., Prunet, S., Hivon, E., 2009, MNRAS, 400, 219

Bothwell, M. S., Kennicutt, R. C., Johnson, B. D., Wu, Y., Lee, J. C., Dale, D., Engelbracht, C., Calzetti, & D., Skillman, E., 2011, MNRAS, 415, 1815

Buat, V., & Burgarella, D. 1998, A&A, 334, 772

Buat, V., Iglesias-Páramo, J., Seibert, M., et al. 2005, ApJ, 619, L51

Buat, V., Takeuchi, T. T., Iglesias-Páramo, J., et al. 2007, ApJS, 173, 404

Buat, V., Takeuchi, T. T., Burgarella, D., Giovannoli, E., & Murata, K. L. 2009, A&A, 507, 693

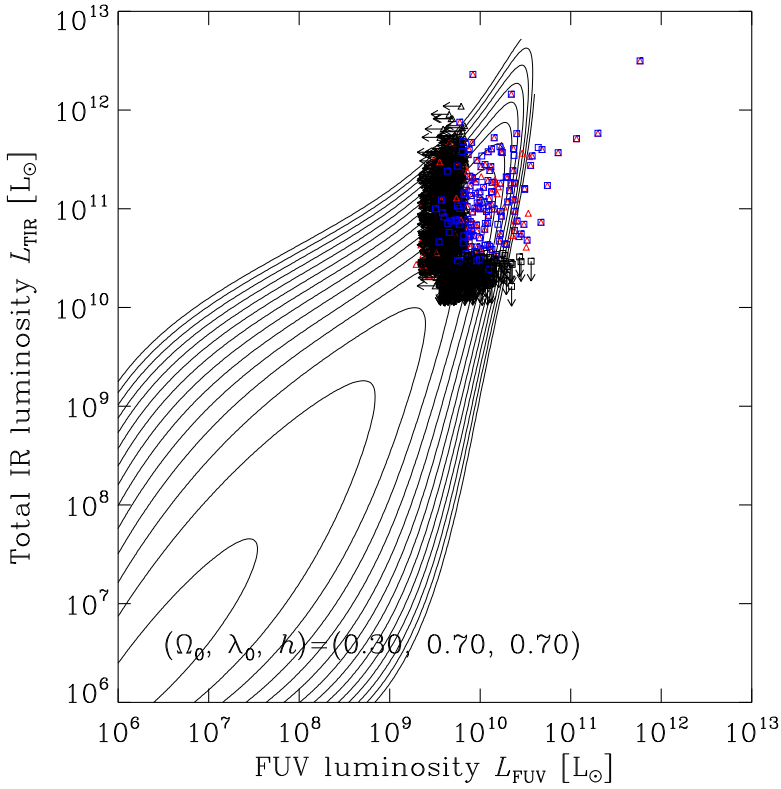

Figure 8: The same as Fig. 5 but from Spitzer and GALEX at $z = 1.0$.

Burgarella, D., et al., 2006, A&A, 450, 69

Cortese, L., Boselli, A., Buat, V., Gavazzi, G., Boissier, S., Gil de Paz, A., Seibert, M., Madore, B. F., & Martin, D. C. 2006, ApJ, 637, 242

Cucciati, O., et al., 2011, A&A, submitted (arXive: astro-ph/1109.1005)

Dale, D. A., Helou, G., Contursi, A., Silbermann, N. A., & Kolhatkar, S., 2001, ApJ, 549, 215

Driver, S. P., et al., 2011, MNRAS, 413, 971

Dwek, E., & Scalo, J. M., 1980,ApJ, 239, 193

Dwek, E., 1998, ApJ, 501, 643

Eales, S., et al., 2010, PASP, 122, 499

Elbaz, D., et al., 2007, A&A, 468, 33

Haines, C. P., Busarello, G., Merluzzi, P., Smith, R. J., Raychaudhury, S., Mercurio, A., & Smith, G. 2011, MNRAS, 412, 127

Hao, C.-N., Kennicutt, R. C., Johnson, B. D., Calzetti, D., Dale, D. A., & Moustakas, J., D. 2011, ApJ, 741, 124

Iglesias-Páramo, J., et al., 2006, ApJS, 164, 38

Johnston, R., 2011, A&A Review, 19, 41

Kawada, M., et al., 2007, PASJ, 59, 389

Koen, C., 2009, MNRAS, 393, 1370

Le Floc'h, E., et al., 2005, ApJ, 632, 169

Martin, D. C., et al. 2005, ApJ, 619, L59

Morrissey, P., et al., 2007, ApJS, 173, 682

Murphy, E. J., Chary, R.-R., Dickinson, M., Pope, A., & Frayer, D. T., 2011, ApJ, 732, 126

Nozawa, T., Kozasa, T., Umeda, H., Maeda, K., & Nomoto, K., 2003,ApJ, 598, 785

Paturel, G., Petit, C., Prugniel, P., Theureau, G., Rousseau, J., Brouty, M., Dubois, P., & Cambrésy, L., 2003, A&A, 412, 45

Sakurai, A., Takeuchi, T. T., Yuan, F.-T., Buat, V., & Burgarella, D., 2011, Earth, Planets & Space, submitted

Salimbeni, S., et al., 2009, A&A, 501, 865

Sandage, A., Tammann, G. A., & Yahil, A., 1979,ApJ, 232, 352

Sato, M., Ichiki, K., & Takeuchi, T. T., 2010, PRL, 105, 251301

Sato, M., Ichiki, K., & Takeuchi, T. T., 2011, PRD, 83, 023501

Saunders, W., Rowan-Robinson, M., Lawrence, A., Efstathiou, G., Kaiser, N., Ellis, R. S., & Frenk, C. S., 1990, MNRAS, 242, 318

Saunders, W., et al., 2000, MNRAS, 317, 55

Schechter, P., 1976, ApJ, 203, 297

Scherrer, R. J., Berlind, A. A., Mao, Q., & McBride, C. K., 2010, ApJ, 708, L9

Seibert, M., et al., 2005, ApJ, 619, L55

Takeuchi, T. T., Yoshikawa, K., & Ishii, T. T. 2000, ApJS, 129, 1

Takeuchi, T. T., Ishii, T. T., Hirashita, H., et al. 2001, PASJ, 53, 37

Takeuchi, T. T., Kawabe, R., Kohno, K., et al. 2001, PASP, 113, 586

Takeuchi, T. T., Yoshikawa, K., & Ishii, T. T. 2003, ApJ, 587, L89

Takeuchi, T. T., Buat, V., & Burgarella, D. 2005, A&A, 440, L17

Takeuchi, T. T., Buat, V., Iglesias-Páramo, J., Boselli, A., & Burgarella, D. 2005, A&A, 432, 423

Takeuchi, T. T., Ishii, T. T., Nozawa, T., Kozasa, T., & Hirashita, H. 2005, MNRAS, 362, 592

Takeuchi, T. T., Ishii, T. T., Dole, H., et al. 2006, A&A, 448, 525

Takeuchi, T. T. 2010, MNRAS, 406, 1830

Takeuchi, T. T., Buat, V., Heinis, S., et al. 2010, A&A, 514, A4

Wang, L., & Rowan-Robinson, M., 2009, MNRAS, 398, 109

Wolf, C., et al., 2004, A&A, 421, 913

Wyder, T. K., et al., 2005, ApJ, 619, L15

Yamamura I., Makiuti S., Ikeda N., Fukuda Y., Oyabu S., Koga T., & White G. J., 2010, AKARI/FIS All-Sky Survey Bright Source Catalogue Version 1.0 Release Note, ISAS/JAXA

An analytic model for the distribution of matter and dust around galaxies

Shogo Masaki
Department of physics, Nagoya University, shogo.masaki@nagoya-u.jp

ABSTRACT

We develop an analytic halo model for the distribution of matter and dust around galaxies. The model results are compared with the observed surface matter and dust density profiles measured through gravitational lensing magnification and reddening of background quasars in Sloan Digital Sky Survey reported by Menard et al.(2010). We show that our model reproduces, for the first time, both the observed matter and dust distribution profile very well over a wide range of radial distance of 10- 10^4 h^{-1}kpc. Through the model fitting of the mass profile, we determine the typical host halo mass of the sample galaxies used in the measurement to be 2×10^{12} $h^{-1}M_{sun}$. We assume that the dust distribution around a galaxy is described similarly to the mass distribution, but with a sharp cut-off at αR_{vir} where R_{vir} is the galaxy's virial radius and α is a model parameter. Our model reproduces the observed dust profile well if α is greater than unity, and thus suggests that dust is distributed to over 100kpc - 1Mpc from the galaxies.

1. METHOD

We describe our formulation to calculate the mean surface density profile of matter and dust around galaxies. Our model is based on the so-called halo model approach (Seljak 2000; Cooray & Sheth 2002). The approach is known as a powerful method to describe statistical quantities, e.g., the correlation function of galaxy and the cross-correlation function of galaxy-matter. In this model, the mean surface density profile is divided into two terms:

$$\Sigma_X(R) = \Sigma_X^{1h}(R) + \Sigma_X^{2h}(R)$$

where "X" denotes matter or dust and R is the distance in the projected two-dimensional plane. The one-halo term $\Sigma_X^{1h}(R)$ arises from the central halo, and the two-halo term $\Sigma_X^{2h}(R)$ from the neighbouring halos.

The contribution from an individual galaxy halo with mass M_h to the one-halo term $\Sigma_X^{1h}(R)$ is given by the projection of the radial halo density profile $\rho_X(r|M_h)$ along the line-of-sight χ

$$\Sigma_X(R|M_h) = \int \mathrm{d}\chi\, \rho_X(r = \sqrt{\chi^2 + R^2}\ |M_h).$$

The one-halo term is a number-weighted average of $\Sigma_X(R|M_h)$

$$\Sigma_X^{1\mathrm{h}}(R) = \frac{1}{n_{\mathrm{halo}}} \int_{M_{\mathrm{min}}}^{\infty} \mathrm{d}M_h \frac{\mathrm{d}n}{\mathrm{d}M_h} \Sigma_X(R|M_h), \quad n_{\mathrm{halo}} = \int_{M_{\mathrm{min}}}^{\infty} \mathrm{d}M_h \frac{\mathrm{d}n}{\mathrm{d}M_h},$$

where $\mathrm{d}n/\mathrm{d}M_h$ is the halo mass function and M_{min} is the threshold halo mass for the sample galaxies. The threshold mass corresponds to the typical host halo mass of the observed galaxies.

On the other hand, for the two-halo term, we calculate the halo-matter/dust cross-power spectrum. We obtain the mean surface density profile from the cross-correlation function converted from the cross-power spectrum. For the formulation, see e.g., Seljak (2000) and Cooray & Sheth (2002).

We adopt the NFW profile derived from cosmological N-body simulations (Navarro et al. 1997) for the radial mass profile

$$\rho_m(r|M_h) = \frac{\rho_s}{(r/r_s)(1 + r/r_s)^2}.$$

We assume that the dust distribution around a galaxy is described similarly to the mass distribution, but with a sharp cut-off at αR_{vir}

$$\rho_d(r|M_h) \propto \frac{1}{(r/r_s)(1+r/r_s)^2} \exp(-r/\alpha R_{\rm vir})[1-\exp(-r/R_{\rm disk})]$$

where $R_{\rm vir}$ is the galaxy's virial radius, $R_{\rm disk}$ is size of galactic disk and α is a model parameter. The amplitude is determined via

$$\int_0^\infty {\rm d}r\, 4\pi r^2 \rho_d(r|M_h) = M_d = \Gamma \times M_h$$

where M_d is the total halo dust mass associated with a halo with mass M_h and Γ is the dust-halo mass ratio.

For the dust-halo mass ratio Γ, we propose two models. The first one is *constant model*, i.e., Γ is independent of halo mass. The dust-halo mass ratio is simply the global density ratio (Komatsu et al. 2011; Fukugtia 2011)

$$\Gamma = 1.73 \times 10^{-5} = \Omega_{\rm galaxy\ dust}/\Omega_{\rm m}.$$

Because the heavy elements that constitute dust are produced by stars, it may be reasonable to expect that the dust mass is proportional to the steller mass. In our second model, we model the halo mass dependence of Γ. We call the model as *mass dependent model*. We combine three observed relations; the stellar-halo mass (Leauthaud et al. 2011), the stellar mass-metallicity (Tremonti et al. 2004) and the stellar-hydrogen mass (Evoli et al. 2011). The derived Γ is shown and compared with that of the constant model in Fig. 1.

2. RESULTS

We fit our matter distribution model to the observed surface matter density through least chi-squared minimization. We choose $M_{\rm min}$ as a free parameter for this fit. The obtained best-fit threshold mass is

$$M_{\rm min} = (2.1 \pm 0.4) \times 10^{12} h^{-1} M_\odot\ (1\sigma),$$

which is consistent with the value derived by Masaki, Fukugita & Yoshida (2012) using cosmological *N*-body simulations. Fig. 2 compares the best-fit model profile with the observed one. The data points with error bars are taken from Menard et al. (2010, hereafter MSFR). The dotted and dashed lines represent the one-halo and the two-halo terms respectively. The solid line is the resulting matter profile. Our model reproduces the observed matter profile remarkably well from ~10kpc to ~10Mpc. The obtained value of $M_{\rm min}$ roughly corresponds to the halo mass of L^*-galaxies. For more detailed discussion on $M_{\rm min}$, see Masaki, Fukugita & Yoshida (2012).

It is encouraging that our simple physical model for the matter distribution yields an excellent fit to the observation. We follow the same halo model approach to predict the mean surface dust density profile.

For dust distribution, we have two physical parameters, $M_{\rm min}$ and α. We have found that poor constraints are obtained on the parameters when both of them are treated as free parameters. Because $M_{\rm min}$ is already estimated using the observed matter distribution, it is sensible to fit our dust distribution model by treating only α as a free param- eter. After the same least chi-squared minimization procedure, the obtained best-fit α for the constant and the mass dependent models are, respectively,

$$\begin{aligned} \alpha &= 1.88^{+0.693}_{-0.443}\ (1\sigma)\ \ \text{for constant model,} \\ \alpha &= 5.67^{+2.23}_{-1.44}\ (1\sigma)\ \ \text{for mass dependent model.} \end{aligned}$$

Figs.3 and 4 shows the best-fit dust profile of the constant model with α = 1.88 and that of the mass dependent model with α = 5.67. The data points are from MSFR. Both models for Γ reproduce the observed result fairly well.

Overall, our simple models reproduce the observed dust profile very well. Intriguingly, both our models suggest α ~ O(1), i.e., halo dust is distributed over ~ 100kpc from the galaxy. It is also important that the observed power law surface density $\Sigma_{\rm d} \propto R^{-0.8}$ at R = 10kpc − 10Mpc can be explained with α ~ O(1). The apparent large-scale dust distribution is explained by the two-halo contributions.

REFERENCES
Cooray, A., & Sheth, R. 2002, PhR, 372, 1
Evoli, C., et al. 2011, ApJ, 743, 45
Fukugita, M. 2011, arXiv:1103.4191
Komatsu, E., Smith, K. M., Dunkley, J., et al. 2011, ApJs,192, 18
Leauthaud, A., Tinker, J., Bundy, K., et al. 2011, arXiv:1104.0928
Masaki, S., Fukugita, M. & Yoshida, N. 2012, ApJ, 746, 38
Menard, B., Scranton, R., Fukugita, M., & Richards, G. 2010, MNRAS, 405, 1025 (MSFR)
Navarro, J. F., Frenk, C. S., & White, S. D. M. 1997, ApJ, 490, 493
Seljak, U. 2000, MNRAS, 318, 203
Tremonti, C., et al. 2004, ApJ, 613, 898

Figure 1

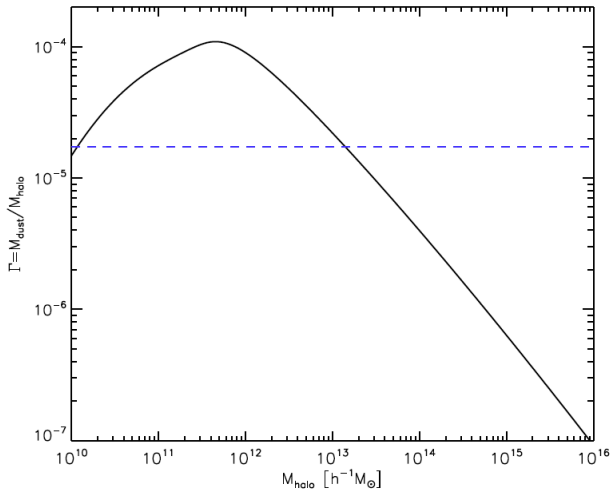

Figure 2

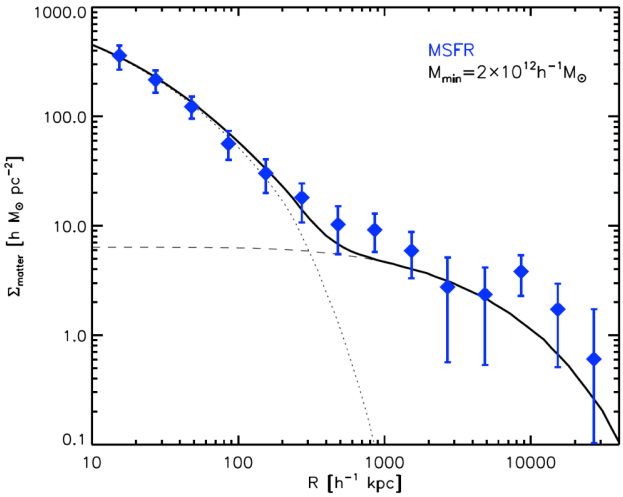

Figure 3

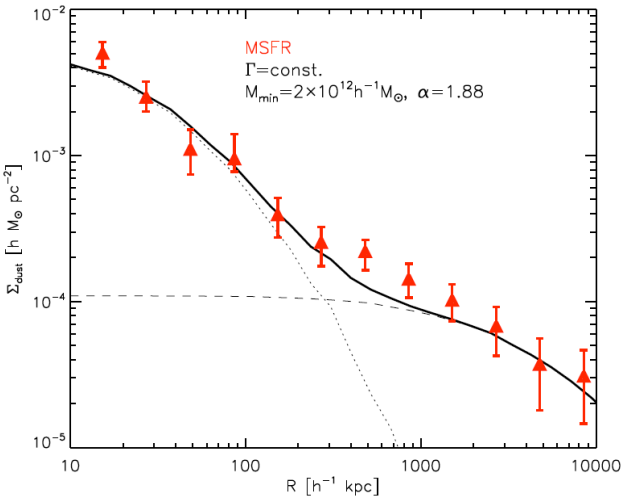

Figure 4

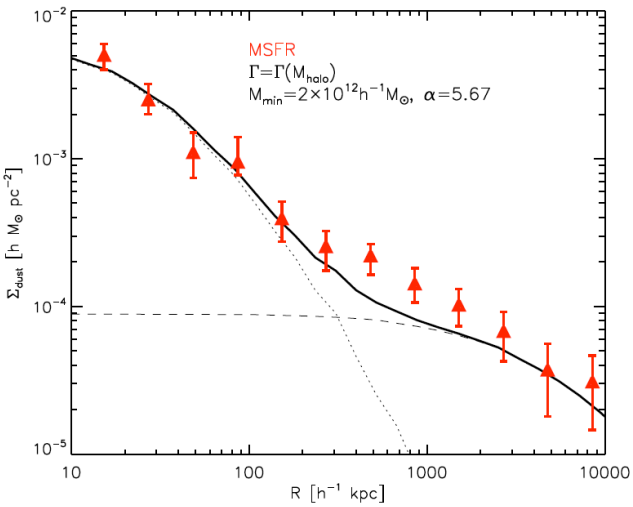

Evolution of grain size distribution in galaxies

Ryosuke S. Asano[1], Tsutomu T. Takeuchi[1], Hiroyuki Hirashita[2], Akio K. Inoue[3] and Takaya Nozawa[4]

[1] *Depertment of Particle and Astrophysical Science, Nagoya University, Japan*

[2] *Institute of Astronomy and Astrophysics, Academia Sinica, Taiwan*

[3] *College of General Education, Osaka Sangyo University, Japan*

[4] *Institute for the Physics and Mathematics of the Universe, University of Tokyo, Japan*

Abstract

We investigate the evolution of the grain size distribution in galaxies by constructing a dust evolution model taking into account grain size distribution. In order to examine the evolution of the grain size distribution, we consider the following two processes: (i) dust destruction by SN shocks, and (ii) metal accretion onto the surface of grains (referred to as grain growth). We found that the grains with radii $0.4 - 0.6$ μm become dominant on the dust mass in galaxies after grain growth occurs. Also, the increase of the number of smaller grains are suppressed by the SN shocks and metal accretion. The grain size distribution in galaxies depends strongly on the processes in the ISM.

1 Introduction

Dust grains influence various processes which are important to understand the galaxy evolution. For example, star formation. Star formation is thought to occur in the cold and dense clouds (molecular clouds). Since hydrogen molecules are mainly formed on the surface of dust grains, the molecular formation rate is really higher for the case with dust (e.g., Hirashita & Ferrara, 2002). Furthermore, dust grains and molecules work as a coolant of the interstellar medium (ISM) where stars can be formed. Thus, dust grains drive star formation in galaxies. Also, dust grains absorb and scatter the stellar light at shorter wavelengths, and they re-emit the far-infrared and submillimeter wavelengths. Therefore dust affects the spectral energy distributions of galaxies. Consequently, dust is one of the fundamental factor to understand the evolution of galaxies (e.g., Yamasawa et al., 2011).

Dust grains are formed by the condensation of heavy elements. Most of these heavy elements (heavier than helium) released by stellar mass loss during stellar evolution or supernovae (SNe) condense into dust grains. However, dust grains are not only formed from stars but also destroyed by SNe blast waves (e.g., Nozawa et al., 2003; Zhukovska, Gail, & Trieloff, 2008). In addition, we should consider the grain growth in the ISM by accretion of heavy elements (e.g., Draine, 2009). Thus, dust evolution passes through various processes closely related to each other in the ISM.

Up to now, dust evolution has been studied with various dust evolution model (e.g., Inoue, 2003; Zhukovska, Gail, & Trieloff, 2008; Valiante et al., 2009), but most of them are based on the assumption of a typical size of grains. However, since the effects of dust grains to the galaxy evolution, which are already mentioned above, depend on the grain size distribution in galaxies, the grain size distribution is important information to understand the evolution of galaxies.

Grain size distribution produced by asymptotic giant branch stars (AGB stars) are thought to be the log-normal distribution at the peak of ~ 0.1 μm (e.g., Winters et al., 1997). As for SNe II, Nozawa et al. (2007) showed that the grain size distributions produced by SNe are biased to large sizes (≥ 0.01 μm). Small grains are selectively destroyed by the shocks (Nozawa et al., 2006). Also, Hirashita & Kuo (2011) showed that the contribition of the grain growth to the dust evolution depends on the grain size distribution. Thus, since grain size distributions in galaxies are affected by various processes simultaneously, we investigate the evolution of dust mass and the grain size distribution in galaxies by constructing a dust evolution model taking into account these processes.

2 Dust evolution model

In this study, we consider AGB stars, SNe II, dust destruction by SN shocks, and the grain growth in the ISM as a process which changes the grain size distribution in galaxies. Here we do not consider the contribution of the SNe Ia. However, for example, Nozawa et al. (2011) proved that it is inefficient to the total dust budget in galaxies, and there are no observtional support for SNe Ia. Hence we do not take into account SNe Ia in this study. In this section, we briefly introduce four processes mentioned above. Throughout this paper, we assume that the shape of dust grains is spherical for simplicity. So, we have

$$m(a) = \frac{4\pi a^3}{3}\rho_j, \tag{1}$$

where a is the grain size, and ρ_j is the bulk density of each species j.

2.1 AGB stars

The grain size produced by AGB stars is uncertain to date. Here, we assume log-normal distribution at the peak of ~ 0.1 μm (Winters et al., 1997) (left panel of Fig. 1). Recently, Yasuda & Kozasa (2012) have examined the size distribution of SiC grains produced by Carbon-rich AGB stars, and their results also have suggested that the size distribution is roughly log-normal. As for the AGB dust mass, we adopt the data of Zhukovska, Gail, & Trieloff (2008).

2.2 SNe II

The data of dust mass and grain size distribution produced by SNe II are taken from Nozawa et al. (2007) (right panel of Fig. 1). Nozawa et al. (2007) examined the dust mass and grain size distribution processed by sputtering due to the passage of the forward and reverse shocks. They calculated two cases for the mixing in the helium core, unmixed and mixed model. In our study, we adopt the results for unmixed model, since the grain size distributions obtained by unmixed model are consisitent with observation (e.g., Hirashita et al., 2005). The grain size distribution is like a broken power-law.

2.3 Dust destruction by SN shocks

Dust grains in the ISM become smaller size or are destroyed by sputtering due to the passage of SN shocks. Thus, in order to trace the evolution of grain size distribution, it is neccesary to consider dust destruction taking into account the grain size. As for the efficiency of dust destruction for each size, we adopt the results of Nozawa et al. (2006).

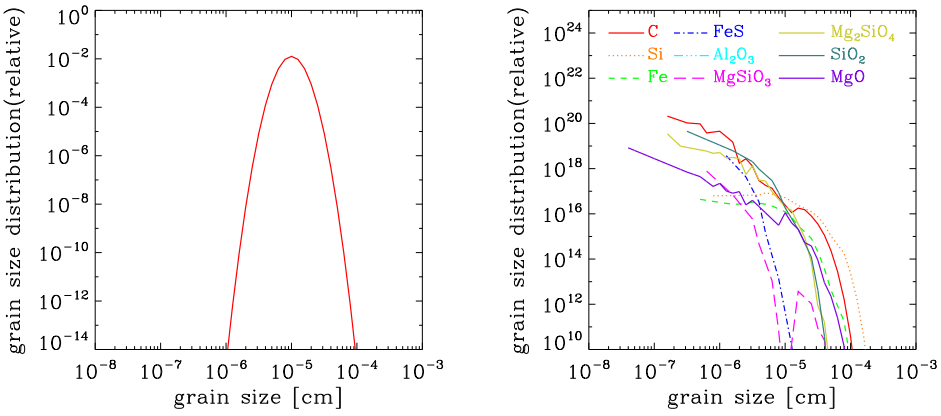

Figure 1: Grain size distribution produced by AGB stars (left panel) or SNe II with 20 $M_\odot$ (right panel).

We formulate the dust destruction as follows. The number of grains with radii between a and a+da, $f(a)$da, is expressed as

$$f(a)\mathrm{d}a = \xi(a, a^{'})f(a^{'})\mathrm{d}a, \tag{2}$$

where $\xi(a, a^{'})$ is the conversion efficiency, which is defined as the number fraction of grains with radius between $a^{'}$ and $a^{'}$+d$a^{'}$ eroded to grains with radius between a and a+da by sputtering. We note that if $a^{'} \leq a$, $\xi(a, a^{'}) = 0$. Thus, the change in the number of dust grains with radii between a and a+da after the passage of a SN shock, d$N(a)$, is given by

$$\mathrm{d}N(a) = \int_0^\infty \xi(a, a^{'})f(a^{'})\mathrm{d}a^{'} - f(a)\mathrm{d}a. \tag{3}$$

The conversion efficiency ξ depends on the ISM density surrounding the SN $n_{\rm SN}$, and large $n_{\rm SN}$ increases the destruction efficiency of dust grains (Nozawa et al., 2006; Yamasawa et al., 2011). In this study, we assume $n_{\rm SN} = 1.0$ cm^{-3}.

The swept mass by a SN shock $M_{\rm swept}$ depends on $n_{\rm SN}$ and metallicity in the ISM. Here, we adopt the fitting formula derived by Yamasawa et al. (2011),

$$M_{\rm swept}/M_\odot = 1535 n_{\rm SN}^{-0.202}[(Z/Z_\odot) + 0.039]^{-0.289}, \tag{4}$$

where Z is the metallicity in the ISM. We set $Z_\odot = 0.02$ (Anders & Grevesse, 1989) throughout this paper.

2.4 Grain growth in the ISM

In this subsection, we formulate the evolution of the grain size distribution by the accretion of heavy elements onto the surface of grains (grain growth). Here we only treat the grain growth as the growth of refractory materials. In fact, volatile also grow, but they evapolate if the clouds disapper. As for volatile, we will treat it in our future work.

We define $f(a, t)$da as the number of grains with radii between a and a+da at time t. If we consider only the accretion of heavy elements, the following equation holds,

$$\frac{\partial f(a,t)}{\partial t} + \frac{\partial}{\partial a}[f(a,t)\dot{a}] = 0, \tag{5}$$

where $\dot{a} \equiv \mathrm{d}a/\mathrm{d}t$ is the growth rate of the grain radius. Also, the growth rate of the grain mass is expressed as

$$\frac{\mathrm{d}m(a)}{\mathrm{d}t} = \pi a^2 \alpha \rho_Z^{\mathrm{cl}} \langle v \rangle, \tag{6}$$

where α is the sticking coefficient, ρ_Z^{cl} is the mass density of gaseous metals, and $\langle v \rangle$ is the meal velocity of metals in gas phase. And,

$$\rho_Z^{\mathrm{cl}} = \rho_{\mathrm{ISM}}^{\mathrm{cl}} Z (1 - \delta), \tag{7}$$

where $\rho_{\mathrm{ISM}}^{\mathrm{cl}}$ is the ISM density, and δ is the dust abundance in the metal mass. From Eq. (1), (6), (7), we obtain

$$\dot{a} \equiv \frac{\mathrm{d}a}{\mathrm{d}t} = \frac{\alpha \rho_{\mathrm{ISM}}^{\mathrm{cl}} Z (1 - \delta) \langle v \rangle}{4 \rho_j}. \tag{8}$$

From this equation, we note that the growth rate does not depend on the grain size.

2.5 Formulation of dust mass evolution for a grain size

From previous subsections, we can formulate the time evolution of the mass of dust species j with radii between a and a+da, $M_{\mathrm{d},j}(a,t) = \frac{4\pi}{3} a^3 \rho_j f_j(a,t) \mathrm{d}a$, which is expressed as

$$\begin{aligned}
\frac{\mathrm{d}M_{\mathrm{d},j}(a,t)}{\mathrm{d}t} = & - \frac{M_{\mathrm{d},j}(a,t)}{M_{\mathrm{ISM}}(t)} \mathrm{SFR}(t) + Y_{\mathrm{d},j}(a,t) & (9) \\
& - \frac{M_{\mathrm{swept}}}{M_{\mathrm{ISM}}(t)} \gamma_{\mathrm{SN}}(t) \left[M_{\mathrm{d},j}(a,t) - \frac{4\pi}{3} a^3 \rho_j \int_0^\infty \xi_j(a,a') f_j(a',t) \mathrm{d}a' \right] & (10) \\
& - \eta \frac{\partial}{\partial a} [M_{\mathrm{d},j}(a,t) \dot{a}], & (11)
\end{aligned}$$

where $f_j(a,t)\mathrm{d}a$ is the number of the dust grains of species j with radii between a and a+da at time t, M_{ISM} is the total mass in the ISM (total mass of gas, metals and dust), η is the mass fraction of the clouds where the grain growth occurs. Here, SFR(t), $Y_{\mathrm{d},j}(t)$, and $\gamma_{\mathrm{SN}}(t)$ are the star formation rate, the total dust mass ejected by stars per unit time, and the SN rate, respectively. For SFR, we assume the schmidt law; SFR(t) $\propto M_{\mathrm{ISM}}^n$. Thus, they are expressed as

$$\begin{aligned}
\mathrm{SFR}(t) &= \frac{M_{\mathrm{ISM}}(t)}{\tau_{\mathrm{SF}}}, & (12) \\
Y_{\mathrm{d},j}(t) &= \int_{m_{\mathrm{cut}}(t)}^{100\ \mathrm{M}_\odot} m_{\mathrm{d},j}(m, Z(t - \tau_m), a) \phi(m) \mathrm{SFR}(t) \mathrm{d}m, & (13) \\
\gamma_{\mathrm{SN}}(t) &= \int_{m_{\mathrm{cut}}(t) > 8\ \mathrm{M}_\odot}^{40\ \mathrm{M}_\odot} \phi(m) \mathrm{SFR}(t) \mathrm{d}m, & (14)
\end{aligned}$$

where τ_{SF} is the star formation timescale, τ_m is the lifetime of a star of mass m, $m_{\mathrm{d},j}(m,Z,a)$ is the mass of grains with radii a of a star of mass m and metallicity Z, and $m_{\mathrm{cut}}(t)$ is the mass of a star with lifetime $\tau_m = t$. In this study, we assume the case with index $n = 1$ for simplicity. Since we assume a closed-box model, which assumes the total baryon mass (M_{tot}) is constant, if $t = 0$, $M_{\mathrm{ISM}}(0) = M_{\mathrm{tot}}$. Also, $\phi(m)$ is the initial mass function (IMF), and we adopt the Larson IMF (Larson, 1998) in the mass range (0.1 – 100) $\mathrm{M}_\odot$.

3 Results and Discussions

In Fig. 2, we show the contributions of various propcesses (stars, dust destruction, and the grain growth) to the grain size distribution in galaxies. We set $\tau_{\rm SF} = 5$ Gyr, $M_{\rm tot} = 10^{10}$ M$_\odot$, and $\eta = 1.00$. It is seen that the dominant sources of dust are stars (AGB stars and SNe II) at the stage of galaxy evolution. However, since the contribution of SN shocks becomes effective at $t > 1$ Gyr (the dust destruction timescale is defined as about $0.1\tau_{\rm SF}$), small grains are effectively destroyed by SN shocks after 1 Gyr. Also, heavy elements accrete onto smaller grains because small grains govern the grain surface. Thus, the increase of the number of smaller grains are suppressed by the SN shocks and the grain growth. We find that if the contribution of the grain growth becomes effective, the grains with radius 0.4–0.6 μm become dominant on the dust mass in galaxies. In the dense regions where grain growth occurs, Weingartner & Draine (2001) suggested that the grain size distribution are biased to large grains. Therefore, the larger grains are expected to be dominant on the total dust mass in galaxies after the grain growth occurs. The grain size distribution in galaxies depends strongly on the processes in the ISM. Other mechanisms which have potential of changing the grain size distribution (especially, shattering and coagulation) are left in future work.

Acknowledgments.

RSA has been supported from the Grant-in-Aid for JSPS Research under Grant No. 23-5514. RSA and TTT have been also partially supported from the Grand-in-Aid for the Global COE Program "Quest for Fundamental Principles in the Universe: from Particles to the Solar System and the Cosmos" from the Ministry of Education, Culture, Sports, Science and Technology (MEXT) of Japan. TTT and AKI have been supported by Program for Improvement of Research Environment for Young Researchers from Special Coordination Funds for Promoting Science and Technology, and the Grant-in-Aid for the Scientific Research Fund (TTT: 23340046, AKI: 19740108) commissioned by the MEXT. HH is supported by NSC grant 99-2112-M-001-006-MY3.

References

Anders, E., & Grevesse, N. 1989, GCA, 53, 197

Draine, B. T. 2009, in Cosmic Dust - Near and Far, ASP Conference Series, in press

Hirashita, H., & Ferrara, A. 2002, MNRAS, 337, 921

Hirashita, H., Nozawa, T., Kozasa, T., Ishii, T. T., & Takeuchi, T. T. 2005, MNRAS, 357, 1077

Hirashita, H. & Kuo, T-M. 2011, MNRAS, 416, 1340

Inoue, A. K. 2003, PASJ, 55, 901

Larson, R. B. 1998, MNRAS, 301, 569

Mathis, J. S., Rumpl, W., & Nordsieck, K. H. 1977, ApJ, 217, 425,

Nozawa, T., Kozasa, T., Umeda, H., Maeda, K., & Nomoto, K. 2003, ApJ, 598, 785

Nozawa, T. Kozasa, T., & Habe, A. 2006, ApJ, 648, 435

Nozawa, T., Kozasa, T., Habe, A., Dwek, E., Umeda, H., Tominaga, N., Maeda, K., & Nomoto, K. 2007, ApJ, 666, 955

Nozawa, T., Maeda, K., Kozasa, T., Tanaka, M., Nomoto, K., & Umeda, H. 2011, ApJ, 736, 45

Valiante, R., Schneider, R., Bianchi, S., Andersen, A. C. 2009, MNRAS, 397, 1661

Weingartner, J. C., & Draine, B. T. 2001, ApJ, 548, 296

Winters, J. M., Fleischer, A. J., Le, Bertre, T., & Sedlmayr, E. 1997, A&A, 326, 305

Yamasawa, D., Habe, A., Kozasa, T., Nozawa, T., Hirashita, H., Umeda, H.,& Nomoto, K. 2011, ApJ, 735, 44

Yasuda, Y., & Kozasa, T. 2012, ApJ, 745, 159

Zhukovska, S., Gail, H. P., Trieloff, M. 2008, A&A, 479, 453

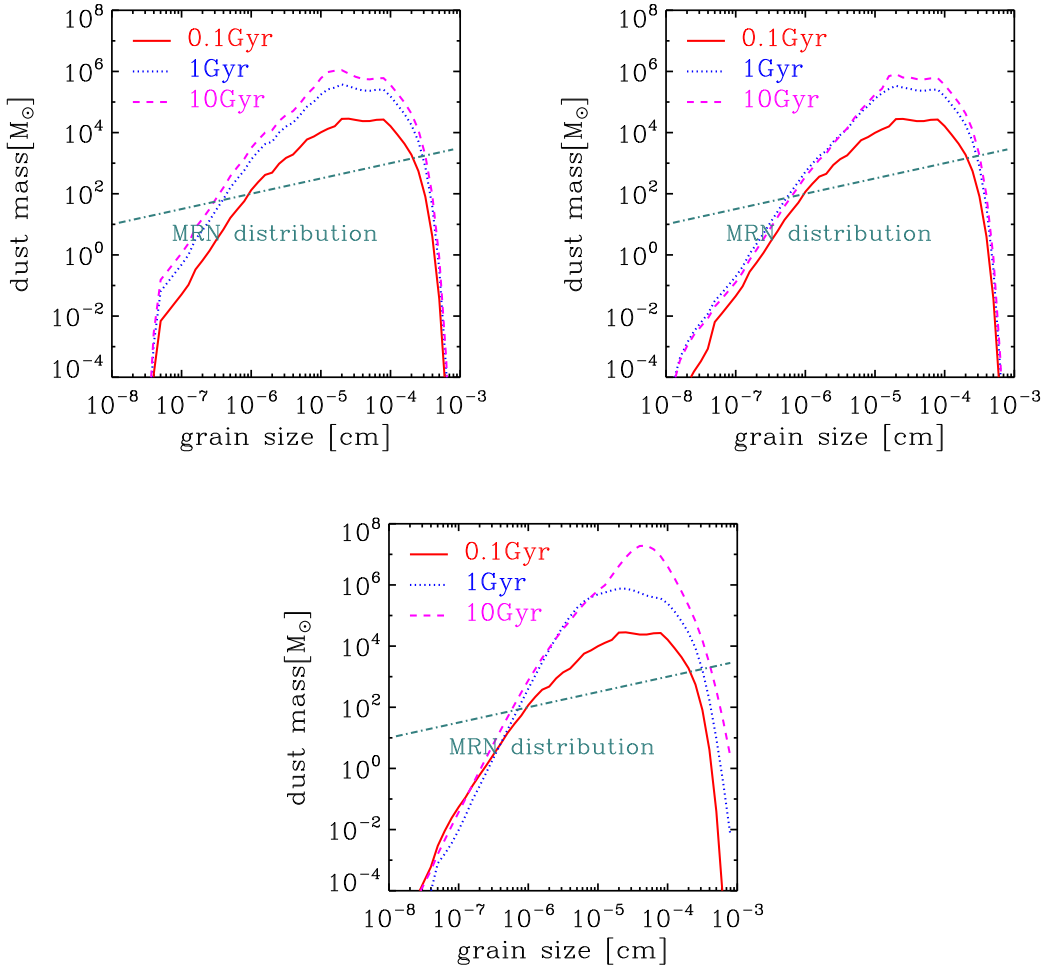

Figure 2: Contributions of various processes to the grain size distribution with $M_{\rm tot} = 10^{10}$ M$_\odot$, $\tau_{\rm SF} = 5$ Gyr and $\eta = 1.00$ (bottom panel only). Upper left: stars (AGB stars and SNe II) only, upper right: stars and SN shocks (dust destruction), bottom: stars, SN shocks, and the grain growth. Solid, dotted, and dashed lines represent the galactic age $t = 0.1, 1.0, 10$ Gyr, respectively. Dot-dashed line represent the MRN distribution (Mathis, Rumpl, & Nordsieck, 1977) for reference.

A new diagnostic method to evaluate growth condition of rock-forming minerals

Hitoshi Miura[1,2], and Katsuo Tsukamoto[1]

[1] *Department of Earth Sciences, Tohoku University, 6-3 Aoba, Aramaki, Aoba-ku, Sendai 980-8578, Japan*

[2] *Corresponding Author E-mail address: miurah@m.tohoku.ac.jp*

Abstract

Chondritic meteorites contain rock-forming minerals in which the chemical compositions are not uniform. The inhomogeneity is termed as zoning profile, which is considered to reflect the growth condition (cooling rate, closed- or open-system, supercooling, and so forth) when they were formed in early solar system. We investigated the zoning profile, growth velocity, and mineral morphology formed under a constant cooling rate based on a numerical scheme. From the numerical simulations for a wide range of the cooling rate, we found some simple power-law relationships in the zoning profile at very beginning of solidification. This results may give us a very useful diagnostic guideline to speculate the cooling rate from zoning profiles recorded in minerals.

1 Introduction

Rock-forming minerals such as olivine, pyroxene, and anorthite show inhomogeneities in the chemical compositions in certain phenocrysts. This is termed as zoning profiles, which are considered to have been formed during solidification of the phenocrysts and/or in alteration processes in their parent bodies. Therefore, we may obtain significant information about the origins of these minerals by analyzing how their zoning profiles were formed. In this paper, we investigate the formation process of zoning profile, especially at the very beginning of solidification.

Let us consider that the solid phase comes in contact with the liquid phase at a planar interface in equilibrium (see Fig. 1). Each phase has its own uniform concentration determined by the phase diagram. The growth of solid is triggered when the equilibrium is perturbed by changes of temperature, pressure, and chemical composition. Onset of growth causes rejection of incompatible elements from solid to liquid. If the growth velocity is too large to homogenize the incompatible element distribution in liquid phase, these elements are concentrated in front of the advancing solid-liquid interface (boundary layer). The complex time-dependent behavior of solute redistribution causes significant zoning in solid (initial transient). The solute distribution in the initial transient was formulated by Tiller et al. [1], then extended by Smith et al. [2]. The Smith' solution suggested that the uptake of incompatible elements into crystal is enhanced as the growth velocity increases. The enhanced uptake of incompatible elements plays important roles in trace element partitioning between phenocrysts and host lava [3], incompatible element concentration in melt inclusion [4], and isotopic fractionation during solidification [5].

Although the Smith model assumed that the growth velocity is constant for the entire solidification process, it is not necessarily correct in general [6, 7, 8]. The constant growth velocity is certainly an approximation of the complex growth history of crystals in experiments and in nature [4]. The effect of non-constant growth velocity on the formation of zoning profile should be investigated because it will give us greater insight to understand the formation of zoned minerals. In addition, it is also important to consider how to speculate the formation condition of mineral from its zoning profile. Previous researches did not provide any relationship between the growth velocity and the growth conditions, e.g., cooling rate, bulk composition, supercooling, and so forth [3, 4, 5]. The relationship between the growth

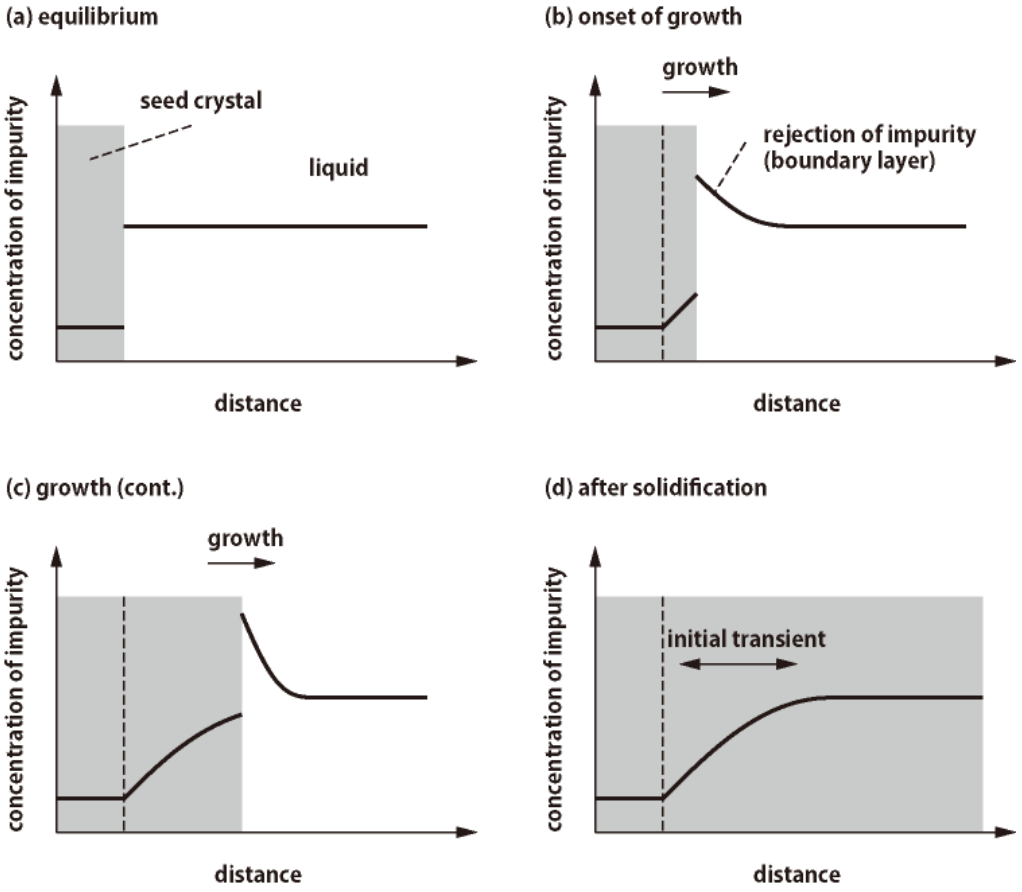

Figure 1: Solute redistribution process at the very beginning of solidification. (a) A crystal comes in contact with liquid at the equilibrium condition. Each concentration of impurity in crystal and liquid is determined by the phase diagram at the given temperature. (b) Onset of growth. Rejection of impurity from crystal to liquid makes boundary layer at the advancing crystal-liquid interface. (c) Further growth. (d) After complete solidification. The crystal shows a significant zoning termed as initial transient.

velocity and these growth conditions is essential to consider the formation environment of minerals.

The aim of this paper is to investigate the formation of zoning profile during initial transient without an assumption of constant growth velocity. We consider a case that the temperature decreases at a constant rate from equilibrium temperature at which crystal coexists with liquid. We numerically solve the crystal growth, elemental partitioning at the solid-liquid interface, and elemental diffusion in liquid phase consistently to obtain the growth history and the zoning profile in solid. We carry out the numerical simulations for wide ranges of growth conditions; cooling rate and bulk composition to show some simple power-law trends with respect to the cooling rate, which may be useful for diagnostics of zoning profile in minerals.

2 Methods

2.1 Phase-field method

The classical approach to the modeling of first order phase transformations involves tracking the free boundary that separates the growing phase (e.g., crystal) from the parent phase (e.g., supercooled liquid). A phase-field method provides an alternative approach, according to which a new variable, the phase field , is introduced to keep track of the phase, taking on constant values indicative of each of the bulk phases and making a transition between these values over a thin transition layer that plays the role of the classically sharp interface. One of the advantages of the phase-fiield method is not to require explicit tracking of the free boundary. This makes the numerical model simpler than the classical approach. The detailed review of the phase-field method would be found in [9], for example.

2.2 Basic equations

The thermodynamically consistent phase-field model for a binary alloy based on the entropy functional is adopted here [10, 11]. This model has been applied for unidirectional solidification of binary alloys [12, 13, 8]. We give a uniform temperature field T in the present simulations, so two equations for phase field and concentration field C must be solved. The governing equations are as follows [11]:

$$\frac{\partial}{\partial t} = M_\phi \ (1 \quad 16a\chi g(\ )) \{H_{\rm A}(1 \quad C) + H_{\rm B}C\} + \epsilon_\phi^2 \nabla^2 \quad , \tag{1}$$

$$\frac{\partial C}{\partial t} = \nabla \ \left\{ D \left[\nabla C \quad \frac{v_{\rm m}}{\mathcal{R}} C(1 \quad C)(H_{\rm B} \quad H_{\rm A}) \nabla \ \right] \right\}, \tag{2}$$

where D, $v_{\rm m}$, and $\mathcal{R}$ are the solute diffusivity, the molar volume, and the gas constant. a is the amplitude of stochastic noise that is introduced only at the crystal-liquid interface, and χ is a random number distributed uniformly from -1 to 1 [10, 8]. We use $a = 0.3$ in this paper. The solute diffusivity D depends on , so we postulate a form

$$D = D_{\rm S} + p(\ )(D_{\rm L} \quad D_{\rm S}), \tag{3}$$

where $D_{\rm S}$ and $D_{\rm L}$ are diffusivities in solid and liquid phases, respectively. Here, $H_{\rm A}$ and $H_{\rm B}$ are defined by

$$H_{\rm A,B} = p'(\ ) L_{\rm A,B} \quad \frac{1}{T_{\rm A,B}} \quad \frac{1}{T} \qquad W_{\rm A,B} g'(\ ), \tag{4}$$

where $L_{\rm A,B}$ and $T_{\rm A,B}$ are the latent heat of crystallization per unit volume and the melting point of pure materials A and B, respectively. We may allow M_ϕ to depend on composition, and so postulate a form

$$M_\phi = (1 \quad C) M_{\rm A} + C M_{\rm B}. \tag{5}$$

The variables of $W_{\rm B}$, $M_{\rm A}$, $M_{\rm B}$, and ϵ_ϕ are related to the measurable quantities as follows:

$$W_{\rm A,B} = \frac{3\sqrt{2}}{2}\frac{\quad_{\rm A,B}}{h_{\rm A,B}T_{\rm A,B}},\ M_{\rm A,B} = \frac{\sqrt{2}}{12}\frac{\mu_{\rm A,B}T_{\rm A,B}^2}{h_{\rm A,B}L_{\rm A,B}},\ \epsilon_\phi^2 = 6\sqrt{2}\ \frac{\quad_{\rm A,B}h_{\rm A,B}}{T_{\rm A,B}}, \tag{6}$$

where $\quad_{\rm A,B}$, $\mu_{\rm A,B}$, and $h_{\rm A,B}$ are the interfacial energy between solid and liquid, the kinetic coefficient, and the interface thickness of pure materials A and B. It should be noted that there is a relationship between $h_{\rm A}$ and $h_{\rm B}$ as

$$\frac{h_{\rm B}}{h_{\rm A}} = \frac{\quad_{\rm A}}{\quad_{\rm B}}\frac{T_{\rm B}}{T_{\rm A}} \tag{7}$$

because ϵ_ϕ does not depend on concentration (see Eq. 6). Finally, $g(\ \ )$ is the double-well potential and $p(\ \ )$ is a monotonically increasing function which satisfies $p(0) = 0$ and $p(1) = 1$. They are respectively defined by

$$p(\ \ ) = \ \ ^3(10\quad 15\ \ +6\ \ ^2),\ g(\ \ ) = \ \ ^2(1\quad\ \ )^2. \tag{8}$$

2.3 Input parameters

In this study, we adopt olivine as a model mineral. The olivine is one of the major rock-forming minerals with the chemical formula $(\rm Mg,Fe)_2SiO_4$. The ratio of magnesium and iron varies between the two endmembers of the solid solution series: forsterite (Mg-endmember) and fayalite (Fe-endmember). The concentration C in Eq. (2) means molar fraction of Fe with respect to the total of Mg and Fe. We can find the equilibrium composition at a given temperature from the phase diagram [14]. Input parameters that we adopt in this paper are listed in Table 1. The diffusion coefficient in solid is set zero to investigate the formation of zoning profile without secondary alteration. The numerical result did not change significantly even if we use non-zero $D_{\rm S}$ ($\approx 10\ \ ^9\ {\rm cm^2\ s\ \ ^1}$) because of the very small diffusivity in comparison with in liquid.

2.4 Numerical procedure

Figure 2(a) shows our initial setting for calculation. Initially, a planar seed crystal is in equilibrium with liquid at a temperature of T_0. We consider one-dimensional geometry assuming that the crystal-liquid interface keeps its flat shape. We adopt a computational domain of $x = 0\quad 200\ \mu$m and discretize it by 2000 meshes, so the mesh size is $\quad x = 0.1\ \mu$m. The initial position of the interface is set at $x = 3\ \mu$m. The initial concentrations in solid and liquid are given by equilibrium concentrations at a temperature T_0, which are determined from the phase diagram (see Fig. 2b). Decreasing temperature at a constant rate $\dot{T}$ causes disequilibrium at the interface and triggers solidification.

We applied finite-difference methods to solve Eqs. (1) and (2). The diffusion terms in these equations are solved by implicit method for Eq. (2) and an explicit Euler scheme for Eq. (1). No flux boundary condition is applied at boundaries of the computational domain, i.e., the normal derivatives of $\quad$ and C are zero at these boundaries.

3 Results

3.1 Initial transient

Fig. 3 shows calculated concentration distribution in solid and liquid phases during solidification for a case of cooling rate $\dot{T} = 5\quad 10^3\ {\rm K\ s\ \ ^1}$ and initial temperature $T_0 = 1900$ K. Initially, the solid comes in contact with the liquid at $x = 3\ \mu$m with their equilibrium concentrations, $C_{\rm S0} = 0.170$ and $C_{\rm L0} = 0.471$, respectively (panel a). As the temperature decreases at a constant rate, the solid-liquid interface advances rightward and the solid region

Table 1: Input parameters for olivine. Subscripts: A = forsterite, B = fayalite.

notation	meaning	value
v_{m}	molar volume	45 $\mathrm{cm}^3\ \mathrm{mol}^{-1}$
D_{L}	diffusivity in liquid	$10^{-5}\ \mathrm{cm}^2\ \mathrm{s}^{-1}$
D_{S}	diffusivity in solid	0 $\mathrm{cm}^2\ \mathrm{s}^{-1}$
$L_{\mathrm{A,B}}$	latent heat of crystallization	1.3 10^{10} erg cm^{-3}
$_{\mathrm{A}}$	interfacial energy	613 erg cm^{-2}
$_{\mathrm{B}}$	interfacial energy	300 erg cm^{-2}
T_{A}	melting point	2163 K
T_{B}	melting point	1490 K
$\mu_{\mathrm{A,B}}$	kinetic coefficient	0.1 cm $\mathrm{s}^{-1}\ \mathrm{K}^{-1}$
h_{A}	width of interface	10 x
h_{B}	width of interface	$(\ _{\mathrm{A}}/\ _{\mathrm{B}})(T_{\mathrm{B}}/T_{\mathrm{A}})h_{\mathrm{A}}$

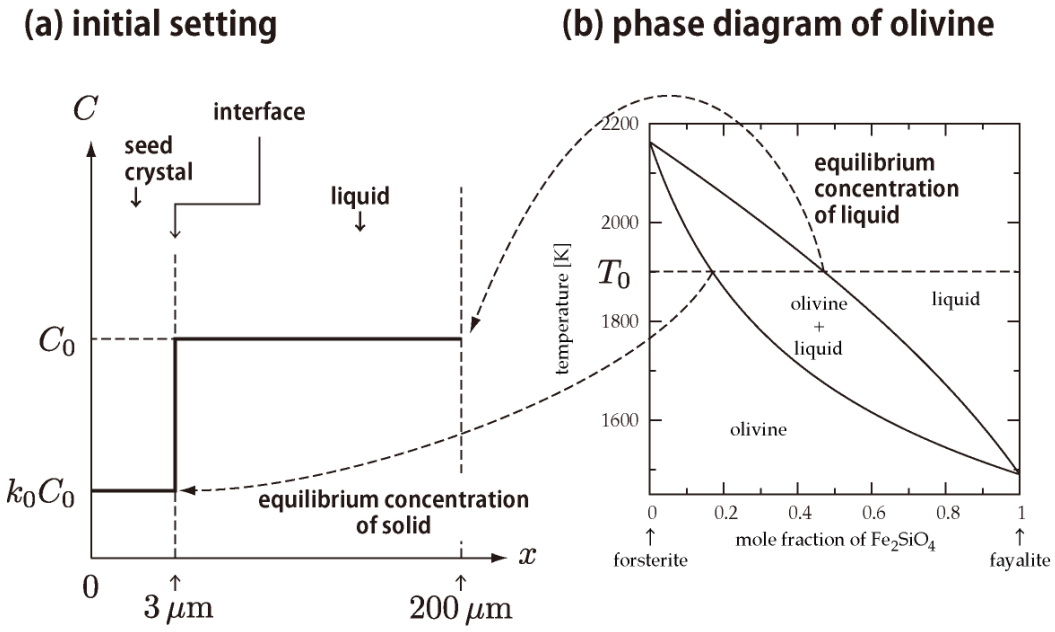

Figure 2: (a) Initial setting for calculation. (b) Phase diagram of olivine (data from [14]).

spreads to the liquid side. Since Fe is rejected from the solid to liquid, a boundary layer with high concentration is formed immediately away from the advancing interface (panel b). The concentration in solid increases with the interface advancement. The concentration in solid exceeds the initial concentration in liquid C_{L0} at $x \approx 10$ μm (panel c). Finally, the system solidifies completely and a zoning profile is formed (panel d).

The zoning profile as shown in Fig. 3(d) is divided into two parts: initial transient and steady growth region. In the initial transient, the profile changes from C_{S0} to C_{L0} with a complex pattern. In a steady growth region, the profile is almost constant at C_{L0}, namely, the solid has the same concentration with that of the initial liquid. This is referred as an effective partitioning coefficient k_{eff} being unity, which is defined by $k_{\mathrm{eff}} = C_{\mathrm{S}}/C_{\mathrm{L0}}$ (it should be noted that the denominator is not at the interface). However, our one-dimensional calculation will be perturbed before the steady growth is realized because a planar interface becomes unstable due to morphological instability [15, 12, 8]. Therefore, we do not consider the steady growth region in the following.

The initial transient is characterized by its complex concentration profile. We notice the steep increase of concentration just after the beginning of the solidification. We define a width of initial transient w within which the concentration in solid increases from C_{S0} to C_w, where C_w is given by

$$C_w = C_0 \quad \frac{1 \quad k_0}{e} C_0, \tag{9}$$

where e is the base of natural logarithm. Using the initial setting, we obtain $C_w = 0.360$ with $k_0 = 0.361$ (horizontal dashed line in Fig. 3d). It is found that the concentration in solid increases to C_w at $x = 7.06$ μm. Subtraction of initial position of the interface gives the width of $w = 4.06$ μm.

3.2 Growth velocity

Fig. 4 shows the position of crystal-liquid interface x_{i} as a function of time. The input parameters are the same with Fig. 3. Open circles are the results within w (see §3.1 for the definition), and filled ones are after. The slope between two neighboring circles gives the growth velocity of crystal. It is found that the growth velocity within w is not constant because the slope seems to increase gradually: the average growth velocity is calculated as ≈ 70 μm s ^{1} for the first 0.01 s and ≈ 190 μm s ^{1} for the last 0.01 s within w. After $t \approx 0.05$ s, the growth velocity increases suddenly, which indicates the beginning of the steady growth region.

Let us assume that the growth velocity within w increases exponentially with respect to time t as given by the following form,

$$R(t) = R_0 \, e^{t/t_0}, \tag{10}$$

where R_0 is the initial growth velocity and t_0 is the time constant. Integration of $R(t)$ over t gives the following expression of the position of interface,

$$x_{\mathrm{i}}(t) = R_0 t_0 \, (e^{t/t_0} \quad 1) + x_{\mathrm{i0}}, \tag{11}$$

where $x_{\mathrm{i0}} = 3$ μm is the initial position. The best fit of calculated results within w with Eq. (11) gives $R_0 = 64.1$ μm and $t_0 = 0.0256$ s. These parameters gives $R = 243$ μm s ^{1} at the end of the region w ($t = 0.34$ s). The best fit curve is shown by a solid curve in Fig. 4 and agrees with the phase-field calculation within w.

3.3 Dependence on cooling rate

As a result of the phase-field calculation, we obtain the following three parameters for each calculation; width of initial transient w, the initial growth velocity R_0, and the time constant t_0. Fig. 5 shows the dependences of these parameters on the cooling rate $\dot{T}$. Results

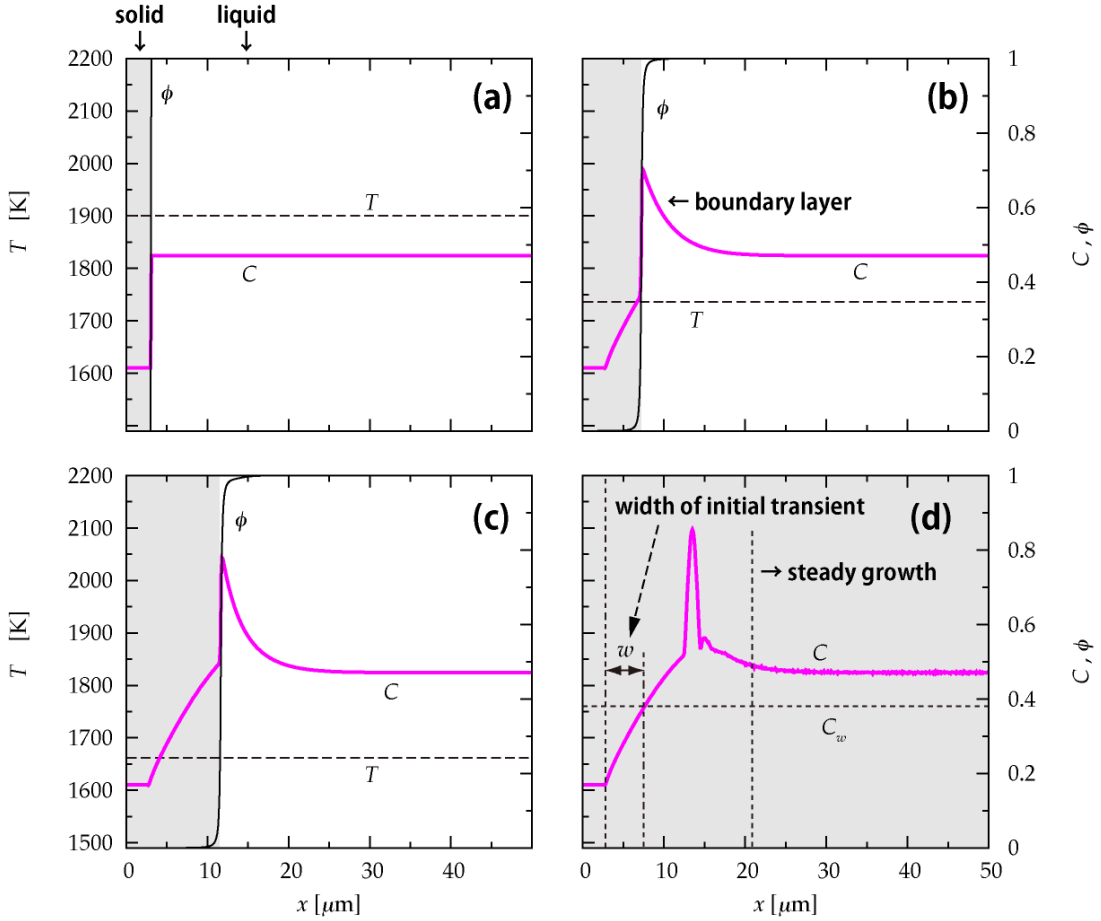

Figure 3: Calculated concentration distribution for a case of $\dot{T} = 5 \quad 10^3$ K s^{-1} and $T_0 = 1900$ K. Crystallized region is colored by gray. (a) Initial setting. The initial position of interface is $x_{i0} = 3$ μm. Initial concentrations are $C_{S0} = 0.170$ in solid phase and $C_{L0} = 0.471$ in liquid phase, respectively. (b) After $t = 0.0328$ s. The interface is advancing rightward. Fe-rich boundary layer was developed immediately in front of the advancing interface. Zoning profile was shown to be formed in solid phase. (c) After $t = 0.0476$ s. The concentration in solid increases to the initial concentration in liquid C_{L0}. (d) After complete solidification.

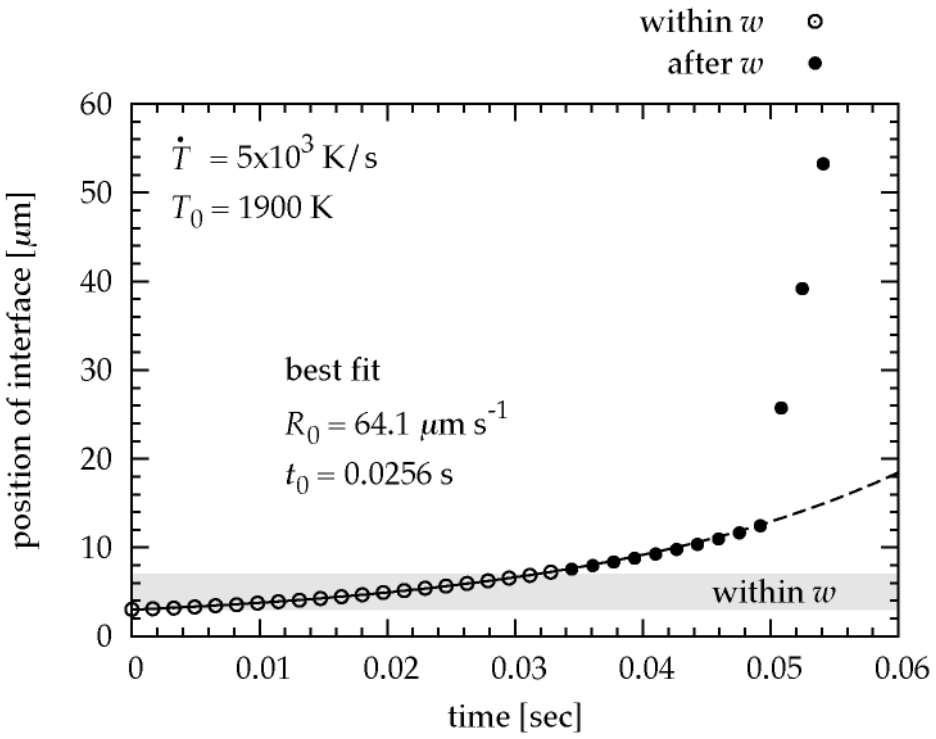

Figure 4: Position of the crystal-liquid interface $x_{\rm i}$ as a function of time. Open circles are the result of the phase-field calculation during initial transient. The region of initial transient is colored by gray. The solid curve is the best fit result for the initial transient region. The best fit parameters are $R_0 = 64.1$ μm and $t_0 = 0.0256$ s. Filled circles are calculation results after initial transient. The dashed curve shows a simple extrapolation of the best fit curve.

with different initial temperatures T_0, namely, different initial compositions, are plotted by different symbols (see legend). It is found that all of these parameters obey power-law trends with respect to the cooling rate; $w \propto \dot{T}^{-1/2}$, $R_0 \propto \dot{T}^{1/2}$, and $t_0 \propto \dot{T}^{-1}$. The power-law trend is observed for a wide range of T_0 except of $T_0 = 1500$ K in which R_0 and t_0 seem to deviate from each power-law trend slightly.

For the same $\dot{T}$, w decreases with the decrease of T_0. When $\dot{T} = 10^3$ K s^{-1}, we obtain $w = 0.43$ μm for $T_0 = 1500$ K and $w = 12.6$ μm for $T_0 = 2100$ K. The difference of factor of 30 in w suggests that the difference of 3 orders of magnitude in $\dot{T}$ is required to obtain the same w. For example, the initial transient of 10 μm in width will be reproduced at a cooling rate of $\dot{T} \approx 10^3$ K s^{-1} for a Mg-rich composition ($T_0 = 2100$ K), on the other hand, $\dot{T} \approx 1$ K s^{-1} for a Fe-rich composition ($T_0 = 1500$ K).

In contrast of w, the growth velocity does not show the monotonic trend on T_0. For the same $\dot{T}$, R_0 decreases as T_0 increases from $T_0 = 1500$ K to $T_0 = 1700$ K, however, backs to increase as T_0 increases from $T_0 = 1700$ K to $T_0 = 2100$ K. Similarly, t_0 increases as T_0 increases from $T_0 = 1500$ K to $T_0 = 1800$ K, then backs to decrease as T_0 increases from $T_0 = 1800$ K to $T_0 = 2100$ K. The higher growth velocity at large- and small-T_0 may be interpreted as follows: the large- and small-T_0 mean less impurity, namely, pure forsterite (Mg_2SiO_4) or pure fayalite (Fe_2SiO_4), respectively, so the advancing of interface is not suppressed by the solute diffusion in liquid phase.

4 Conclusion

We numerically simulated solidification of olivine system to investigate the formation process of zoning profile at the very beginning of solidification, where the iron content in olivine crystal shows a strong zoning within a certain distance. The strong zoning is termed as initial transient. When the solidification occurs under a constant cooling rate $\dot{T}$, we found that the distance of initial transient is proportional to $\dot{T}^{-1/2}$. During the initial transient, the growth velocity is not constant but increases exponentially with respect to the time. The simulation results of growth velocity are fitted with a form of $R(t) = R_0\, e^{t/t_0}$, where R_0 is the initial growth velocity and t_0 is the time constant. We also found that R_0 and t_0 show power-law trends with the cooling rate, respectively. The dependences of these parameters on bulk iron content were also obtained. The power-law trends shown in the initial transient may give us a very useful diagnostic guideline to speculate the cooling rate from zoning profiles of natural olivines in Earth rocks or chondritic meteorites.

Acknowledgement

We are grateful to Prof. T. Yamamoto for useful discussion on analytic formulations of our numerical results. H.M. was supported by Tohoku University Global COE Program "Global Education and Research Center for Earth and Planetary Dynamics", and by Japan Society for the Promotion of Science (JSPS), Grant-in-Aid for Young Scientists (B) (23740330).

References

[1] W.A Tiller, K.A Jackson, J.W Rutter, and B Chalmers. The redistribution of solute atoms during the solidification of metals. *Acta Metallurgica*, 1(4):428 – 437, 1953.

[2] V. G. Smith, W. A. Tiller, and J. W. Rutter. A mathematical analysis of solute redistribution during solidification. *Can. J. Phys.*, 33:723–745, 1955.

[3] F. Albarede and Y. Bottinga. Kinetic disequilibrium in trace element partitioning between phenocrysts and host lava. *Geochimica et Cosmochimica Acta*, 36(2):141 – 156, 1972.

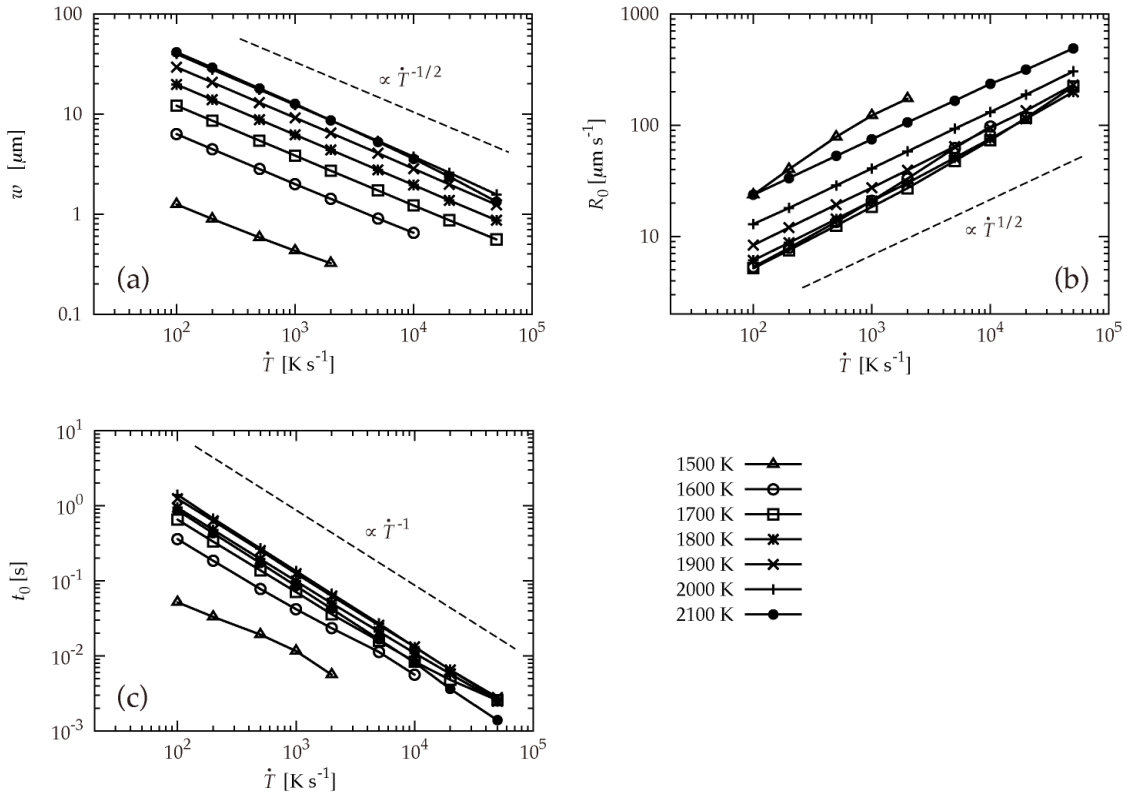

Figure 5: Dependences of initial transient parameters on cooling rate $\dot{T}$; (a) width of initial transient w, (b) initial growth velocity R_0, and (c) time constant t_0. The legend indicates the value of initial temperature T_0, which stands for the difference of initial composition of liquid.

[4] Don Baker. The fidelity of melt inclusions as records of melt composition. *Contributions to Mineralogy and Petrology*, 156:377–395, 2008. 10.1007/s00410-008-0291-3.

[5] E. Bruce Watson and Thomas Mller. Non-equilibrium isotopic and elemental fractionation during diffusion-controlled crystal growth under static and dynamic conditions. *Chemical Geology*, 267(3-4):111 – 124, 2009.

[6] Timothy P. Loomis. An investigation of disequilibrium growth processes of plagioclase in the system anorthite-albite-water by methods of numerical simulation. *Contributions to Mineralogy and Petrology*, 76:196–205, 1981. 10.1007/BF00371959.

[7] I. L'Heureux. Oscillatory zoning in crystal growth: A constitutional undercooling mechanism. *Physical Review E*, 48(6):4460–4469, 1993.

[8] Tomohiro Takaki, Toshimichi Fukuoka, and Yoshihiro Tomita. Phase-field simulation during directional solidification of a binary alloy using adaptive finite element method. *J. Crys. Growth*, 283:263–278, 2005.

[9] Robert F. Sekerka. *Phase field modeling of crystal growth morphology*, pages 176–190. Perspectives on Inorganic, Organic, and Biological Crystal Growth: From Fundamentals to Applications. American Institute of Physics, Melville, New York, 2007.

[10] J.A. Warren and W.J. Boettinger. Prediction of dendritic growth and microsegregation patterns in a binary alloy using the phase-field method. *Acta Metallurgica et Materialia*, 43(2):689 – 703, 1995.

[11] Zhiqiang Bi and Robert F. Sekerka. Phase-field model of solidification of a binary alloy. *Physica A*, 261:95–106, 1998.

[12] William J. Boettinger and James A. Warren. Simulation of the cell to plane front transition during directional solidification at high velocity. *Journal of Crystal Growth*, 200(3-4):583 – 591, 1999.

[13] Zhiqiang Bi and Robert F. Sekerka. Phase field modeling of shallow cells during directional solidification of a binary alloy. *J. Crys. Growth*, 237-239:138–143, 2002.

[14] N. L. Bowen and J. F. Schairer. *American Journal of Science*, 29:151–217, 1935.

[15] W. W. Mullins and R. F. Sekerka. Stability of a planar interface during solidification of a dilute binary alloy. *J. Appl. Phys.*, 35:444–451, 1964.

Alignment of Grains by Radiative Torques: Discovery of Correlation between Interstellar Polarization and Dust Temperature

Masafumi Matsumura & Youko Kameura *
Faculty of Education, Kagawa University, Saiwai-Cho 1-1, Takamatsu, Kagawa 760-8522

(Received ; accepted)

Abstract

We investigate the efficiency of interstellar polarization p_λ/A_λ, where p_λ is the fractional linear polarization and A_λ is extinction, with using the data obtained by us with the low-dispersion spectropolarimeter HBS, as well as those in literature. It is found that the polarization efficiency p_λ/A_λ is proportional to $\exp(-\beta/\lambda)$ in wavelength $\lambda \approx 0.4 - 0.8\mu$m, where β is a parameter which varies from 0.5 to 1.2 μm. We also find that β is negatively correlated with the dust temperature deduced from infrared data by Schlegel et al. (1998), suggesting that the polarization efficiency is higher in short wavelength for higher temperature. According to the alignment theory by radiative torques (RATs), if the radiation is stronger and bluer, RATs will make small grains align better, and the polarization efficiency will increase in short wavelength. Our finding of the correlation between β and the temperature is consistent with what is expected with the alignment mechanism by RATs. This paper is essentially the same as Matsumura et al. (2011), but it includes a model of grains.

Key words: alignment mechanism — ISM: dust, extinction — polarization

1. Introduction

Interstellar polarization, i.e., dichroic extinction observed in distant stars, shows that grains are optically anisotropic and aligned, although the mechanism of the alignment has been still on debate over more than half century (Lazarian 2007, for a review). The alignment had been explained with the paramagnetic relaxation of thermally spinning grains that obtain angular momentum by collisions with gas particles (Davis & Greenstein 1951, hereafter DG). However, the DG mechanism is not efficient, and it cannot explain the interstellar polarization

* Present Address: Akita Junior High School, Magodai-machi 72, Kumamoto 861-5254 and Rikigo Junior High School, Sima-machi 5-8-1, Kumamoto 861-4133

quantitatively.

For more efficient alignment, Purcell (1979) assumed a spin-up of grain by the ejection of molecular hydrogen from grain surface (the "pinwheel mechanism"). If the site of the ejection is fixed and exist long enough, the grains could be accelerated and rotate suprathermally, i.e. much faster than the thermal rotation as was assumed in DG, and they could align well. Lazarian & Draine (1999a), however, noticed the phenomenon of relaxation caused by the reorientation of spin angular momentum of protons by exchanging angular momentum with grain rotation (the "nuclear relaxation"). Once the grain rotates thermally, it remains thermal by this relaxation, even if the pinwheel mechanism is working, and this is called as "thermal trapping" (Lazarian & Draine 1999a; Lazarian & Draine 1999b). If most of the grains are thermally trapped, the degree of alignment is low as expected as the DG mechanism.

Jones & Spitzer (1967) showed that the increase of the imaginary part of magnetic susceptibility of grain material will result in better alignment, when paramagnetic grains contain ferromagnetic clusters (superparamagnetism). However, Roberge & Lazarian (1999) investigated the DG alignment including the Barnett relaxation and other effects, and they showed that, even if grains have superparamagnetic inclusions, efficient alignment is achieved only when the grain temperature is much lower than the gas temperature. Thus this mechanism may work only in limited astronomical environments.

Dolginov & Mitrofanov (1976) first pointed out that irregularly shaped grains that have "helicity" can spin up by radiative torques (hereafter RATs). More recently, Draine & Weingartner (1996) estimated the RATs with the discrete dipole approximation method, and showed that RATs are very effective to align grains. Since magnetic moments within rotating grains are induced by the Barnett effect, the grains precess around the magnetic field, and then the direction of alignment is usually parallel to the interstellar magnetic field[1] (e.g. Draine & Weingartner 1997; Lazarian & Hoang 2007), i.e., the same direction as that by the DG mechanism. The alignment by RATs can be more efficient if grains have superparamagnetic inclusions (Lazarian & Hoang 2008) or if the pinwheel mechanism is working with RATs (Hoang & Lazarian 2009).

The efficiency of the RATs alignment varies with strength and spectral energy distribution of the radiation field, and thus the size of aligned grains should vary accordingly (Draine & Weingartner 1996; Cho & Lazarian 2005). Therefore, this property makes it possible to examine whether the RATs alignment works or not. Observationally, the maximum wavelength $\lambda_{\rm max}$ of polarization in or around dark nebulae was shown to be correlated with extinction $A_{\rm V}$ in the V-band (Whittet et al. 2001; Andersson & Potter 2007). Andersson & Potter (2010) showed that grain alignment is enhanced by the stellar radiation in the vicinity of a young

[1] The direction of alignment with RATs will be parallel to the light beam, if the radiation is so strong that the rate of precession by the radiative torques is faster than that of the Larmor precession due to internal magnetic field induced by the Barnett effect.

star HD 97300 in the Chamaeleon I cloud. Whittet et al. (2008) showed that the polarization efficiency $p_{\rm K}/\tau_{\rm K}$ in the K-band, where $\tau_{\rm K}$ is optical depth, decreases smoothly with $A_{\rm V}$ beyond the region where ice mantle feature was detected. This suggests that the alignment efficiency is not directly related to the state of grain surface, as is expected by the "pinwheel" alignment. These results agree with the expectations by the RATs alignment. However, it is still not clear whether RATs alignment works or not in more diffuse clouds.

In this paper, we investigate the polarization quantities and the dust temperature for various lines of sight. We observed the stars in/around the Pleiades cluster, which is associated with diffuse reflection nebula, with the low-dispersion spectropolarimeter HBS (Kawabata et al. 1999). Dichroic polarization may be enhanced around those objects, because intense stellar radiation may make grains align better if the RATs alignment works. The contents of this paper are essentially the same as those in Matsumura et al. (2011), but include a model of grains. Manuscripts are also modified significantly.

2. Observations and Data Reduction

We observed 8 stars in the Pleiades cluster with the low-dispersion spectropolarimeter HBS (Kawabata et al. 1999) which is attached to the 1.88m telescope in Okayama Astrophysical Observatory, from October 30 to November 13 in 2008, and from January 13 to 19 in 2009. The details of observations are presented in (Matsumura et al. 2011). We also use specropolarimetric data of various stars by Weitenbeck (1999, 2004), which are similar to our HBS data. The data of HD 29647 (Whittet et al. 2001) and HD 38087 (Serkowski et al. 1975) are used in addition to those from Weitenbeck (1999). Also used are the data for high latitude clouds MBM 30 and MBM 20 (LDN 1642) by Seki & Matsumura (1996).

Extinction A_λ and ratio of total to selective extinction $R_{\rm V}$ for each star are cited from Fitzpatrick & Massa (2007) when available from their 328 extinction curves. Otherwise, A_λ is estimated with Fitzpatrick (2004) who showed typical extinction curves for $R_{\rm V} = 2.1 - 5.5$. For the stars in the Pleiades cluster[2], we adopt $R_{\rm V} = 3.2$, the same value as for HD 23512, and the color excess is cited from Crawford & Perry (1976). Since $R_{\rm V}$ values of HD 14889 in MBM 30 and SAO149760 in MBM 20 are not available, we set $R_{\rm V} = 2.7$ or 3.2 as typical values in high latitude clouds (Larson & Whittet 2005).

Schlegel et al. (1998) deduced dust temperature and other quantities with the COBE and IRAS data, on the assumption of λ^{-2} emissivity in the infrared. Their data is homogeneous all over the sky, so we use their temperature $T_{\rm dust}$ to examine the radiative environment around the grains in each line of sight.

[2] We derived $R_{\rm V}$ values for each star in Matsumura et al. (2011).

3. Results

Figure 1 shows the dependence of A_λ, p_λ, and p_λ/A_λ on wavelength λ for typical examples: HD 23152 and HD 24368 in the Pleiades cluster, HD 29647 in the Taurus cloud, and HD 38087 associated with reflection nebula VDB 57. The values of $\log(p_\lambda/A_\lambda)$ decrease linearly with inverse wavelength $1/\lambda$ in the optical region (Figure 1c), because both $\log(A_\lambda)$ and $\log(p_\lambda)$ are convex against $1/\lambda$ (Figures 1a and 1b). We thus make linear fitting in $\lambda = 0.4 - 0.8\mu$m with the equation:

$$\ln(p_\lambda/A_\lambda) = \ln\alpha - \beta(1/\lambda - 1/0.55\mu\mathrm{m}), \tag{1}$$

where α and β are parameters. The parameter α corresponds to $p_\mathrm{V}/A_\mathrm{V}$, and is $\lesssim 3\%$/mag for interstellar polarization (Serkowski et al. 1975).

Figure 2 presents relations between R_V and λ_max. Here λ_max is the wavelength of maximum polarization p_max, and is obtained with the expression by Serkowski et al. (1975):

$$p_\lambda = p_\mathrm{max}\exp(-K\ln^2(\lambda/\lambda_\mathrm{max})), \tag{2}$$

where $K = 1.66(\lambda_\mathrm{max}/1\mu\mathrm{m}) + 0.01$ (Whittet et al. 1992). Long dashed line in Figure 2 shows the empirical relation between R_V and λ_max by Serkowski et al. (1975). Most of the stars in Figure 2 are present near this line except for HD 29647 and HD 38087.

We draw contours of β=0.4, 0.8, and 1.2 μm in Figure 2 on the assumption that polarization p_λ follows equation (2), and that extinction A_λ varies as in Fitzpatrick (2004) in $\lambda = 0.4 - 0.8\mu$m. The contour of $\beta = 0.8\mu$m in Figure 2 is almost coincident with the empirical line by Serkowski et al. (1975) in $R_\mathrm{V} \lesssim 3.5$.

4. Discussion

4.1. Grain Model: Interpretation of β

In this model[3], we assume oblate grains (axial ratio is 2:1) composed of astronomical silicate (refractive index is 1.7+0.03i) as a first step, although the spheroidal shape is very symmetrical and the radiative torques do not work provided that the incident light is unpolarized. More complicated shapes, e.g., model in Wurm & Schnaiter (2002), should be necessary, but it is beyond the scope of this paper. Here we perform light scattering calculation with Fredholm integral equation method (Matsumura & Seki 1991; Matsumura & Seki 1996; Matsumura & Bastien 2003; Bastien & Matsumura 2005; Matsumura & Bastien 2009), and evaluate extinction and polarization to study the property of β. Following Kim et al. (1994), we assume the size distribution $n(a)$, where a is a radius of sphere with the same volume, as

[3] The modelling is not included in Matsumura et al. (2011). We deleted it according to an anonymous referee's comments. The parameter β in this paper is different from the one often used to characterise the spectrum of thermal emission from dust in far IR. Please do not be confused!

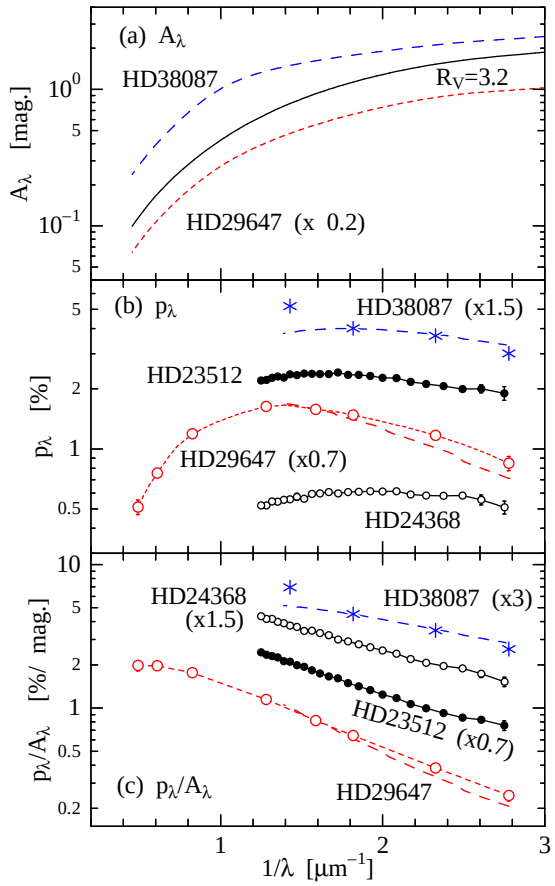

Fig. 1. Wavelength dependence of (a) extinction A_λ, (b) fractional polarization p_λ, and (c) polarization efficiency p_λ/A_λ. Extinction curves in (a) are for HD 29647 (short dashed line) and HD 38087 (long dashed line) from Fitzpatrick & Massa (2007), while that for HD 23512 and HD 24368 (solid line) is the curve of R_V=3.2 from Fitzpatrick (2004). In (b) and (c), asterisks show HD 38087 (Serkowski et al. 1975), filled circles HD 23512 (HBS), small open circles HD 24368 (HBS), and large open circles HD 29647 (Whittet et al. 2001). Long dashed lines in (b) and (c) show HD 29647 and HD 38087 by Weitenbeck (1999).

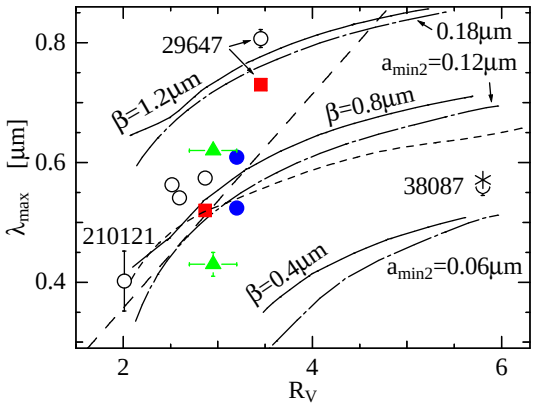

Fig. 2. Relations between $R_{\rm V}$ and $\lambda_{\rm max}$. Filled circles show two stars in the Pleiades cluster, i.e., HD 23152 (upper) and HD 24368 (lower), open circles Weitenbeck (1999, 2004), triangles Seki & Matsumura (1996), squares Whittet et al. (2001), and asterisk shows HD 38087 by Serkowski et al. (1975). Long dashed line is the empirical relation $R_{\rm V} = 5.6(\lambda_{\rm max}/1\mu{\rm m})$ by Serkowski et al. (1975). Solid lines are contours for β=0.4, 0.8, and 1.2μm. Dashed chains and short dashed line are results of model calculations (see text).

$$n(a) \propto a^{\gamma} \exp(-a/a_{\rm max}), \tag{3}$$

where γ is a power and $a_{\rm max}$ correspond to a parameter for upper cutoff. For lower cutoff, we set as $a_{\rm min} = 0.005\mu$m. The size distribution of aligned grains $n(a)_{\rm align}$ is assumed to be different from $n(a)$, and the expression by Mathis (1986) is used:

$$n(a)_{\rm align} \propto n(a)(1 - \exp(-(a/a_{\rm min2})^3)), \tag{4}$$

where $a_{\rm min2}$ is a parameter that defines the typical smallest size of aligned grains. Note that the parameters $a_{\rm max}$ and $a_{\rm min2}$ are not sharp cutoffs for size distributions, but appear in the above equations, while the parameter $a_{\rm min}$ is a "sharp" cutoff. Although the size distribution assumed here is simple, our model shows relations between polarization quantities and parameters for size distribution, and is helpful to interpret the observational results.

We can obtain the average interstellar values of $R_{\rm V} = 3.1$ and $\lambda_{\rm max} = 0.53\mu$m, if we set $(a_{\rm min2}, a_{\rm max}, \gamma) = (0.12\mu{\rm m}, 0.12\mu{\rm m}, -2.75)$[4]. We draw one of the dashed chains in Figure 2, labeled as $a_{\rm min2} = 0.12\mu$m, with changing only γ from -3.5 to -2, but $(a_{\rm min2}, a_{\rm max})$ are kept as $(0.12\mu{\rm m}, 0.12\mu{\rm m})$. When only $a_{\rm max}$ varies from 0.09 to 0.24μm, while $(a_{\rm min2}, \gamma) = (0.12\mu{\rm m}, -2.75)$, a short dashed line is drawn. Those lines are almost coincident with the line of $\beta = 0.8$, showing that β is not sensitive to the variation of γ or $a_{\rm max}$. However, if we change $a_{\rm min2}$, significant variation in β is found: β is $\sim 0.4\mu$m for $a_{\rm min2} = 0.06\mu$m, while it is $\sim 1.2\mu$m for $a_{\rm min2} = 0.18\mu$m (Figure 2). For our model, we can write

$$\beta \simeq 6.6 \times a_{\rm min2}. \tag{5}$$

[4] It is just a coincidence that $a_{\rm min2} = a_{\rm max}$, and this does not show any physical meanings.

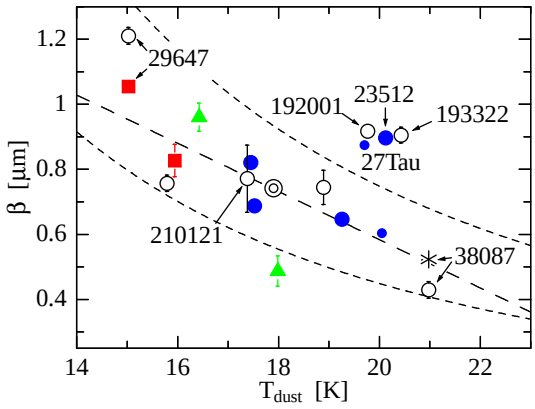

Fig. 3. Correlation between $T_{\rm dust}$ and β. Symbols are same as those in Figure 2, and upper small filled circle shows 27 Tau, and lower one 19 Tau. Double circle is the average of interstellar medium. Result of linear fitting for 12 stars is drawn as dashed line. Upper dashed line presents model prediction for $a_{\rm min2} = 5a_{\rm lower}$, and lower one for $a_{\rm min2} = 3a_{\rm lower}$.

The dependence of β on the parameter $a_{\rm min2}$ can be interpreted as below. Since $\ln(p_\lambda/A_\lambda)$ is linearly correlated with $1/\lambda$, we can express β as

$$\beta \simeq \frac{d\ln(p_\lambda/A_\lambda)}{d(1/\lambda)} \simeq \frac{\ln((p_{\lambda1}/p_{\lambda2})/(A_{\lambda1}/A_{\lambda2}))}{1/\lambda_1 - 1/\lambda_2}, \tag{6}$$

for $\lambda_1 \neq \lambda_2$. If γ or $a_{\rm max}$ varies and large (small) grains are abundant, both p_λ and A_λ increase in longer (shorter) wavelength. These variations are almost canceled in equation (6). However, the variation of $a_{\rm min2}$ has effect on p_λ but of course not on A_λ, thus β is much more sensitive to $a_{\rm min2}$ than $a_{\rm max}$.

4.2. Polarization Efficiency and Dust Temperature

We now discuss the correlation between the value of β and grain temperature $T_{\rm dust}$ obtained by Schlegel et al. (1998). A weak correlation is found for those 16 stars in Figure 3, and the correlation coefficient is ~ -0.3.

Several stars in Figure 3 make the correlation worse, i.e. 27 Tau, HD 23512, HD 192001, and HD 193322. If we exclude those stars, the correlation coefficient is ~ -0.8 for the rest of 12 stars. The temperature for those outliers may be overestimated, because hotter regions are present near or towards them. The line of sight to HD 23512 passes a small molecular cloud that is present in the intracluster of Pleiades (Breger,1986). The regions near O-type stars in sky show high $T_{\rm dust}$ (Schlegel et al. 1998), and this is the case for HD 192001 and HD 193322.

Using their equation (5) in Cho & Lazarian (2005) on RATs theory, with typical values for physical quantities in interstellar space, we can express the smallest size $a_{\rm lower}$ of aligned grains as

$$(a_{\rm lower}/1\mu{\rm m}) = 2.8 \times 10^{-2} \times ({\rm T_{dust}}/18{\rm K})^{-2}, \quad (7)$$

for dust temperature $T_{\rm dust}$. The derived value of $a_{\rm lower} \simeq 0.028\mu$m for $T_{\rm dust} = 18$K is smaller than the value $a_{\rm min2} \sim 0.12\mu$m expected from observation (Section 4.1). Nevertheless, if we use equations (5) and (7), we can draw in Figure 3 upper and lower short dashed lines for $a_{\rm min2} = 5a_{\rm lower}$ and $a_{\rm min2} = 3a_{\rm lower}$, respectively. Those lines follow the observations well, i.e., the variation of β against temperature can be explained with the RATs alignment theory. Since the data in Figure 3 contain regions of various temperature, i.e., the Taurus dark cloud, reflection nebulae, etc., our results suggest that the alignment by RATs is ubiquitous in the interstellar space.

This work was supported by the Thesis Supporting Program at Okayama Astrophysical Observatory of NAOJ, NINS (No.08A-S01, P.I. was Youko Kameura), and by the Kagawa University Specially Promoted Research Fund (FY2008). We are grateful to the staff members at Okayama Astrophysical Observatory and the HBS team for their support during the observations. This work has made use of the SIMBAD database, operated at CDS, Strasbourg, France.

References

Andersson, B.-G., & Potter, S. B. 2007, ApJ, 665, 369
Andersson, B.-G., & Potter, S. B. 2010, ApJ, 720, 1045
Bastien, P., & Matsumura, M. 2005, Astronomical Polarimetry: Current Status and Future Directions, 343, 149
Breger, M. 1986, ApJ, 309, 311
Cho, J., & Lazarian, A. 2005, ApJ, 631, 361
Crawford, D. L., & Perry, C. L. 1976, AJ, 81, 419
Davis, L., Jr., & Greenstein, J. L. 1951, ApJ, 114, 206
Dolginov, A. Z., & Mitrofanov, I. G. 1976, Ap&SS, 43, 291
Draine, B. T., & Weingartner, J. C. 1996, ApJ, 470, 551
Draine, B. T., & Weingartner, J. C. 1997, ApJ, 480, 633
Fitzpatrick, E. L. 2004, Astrophysics of Dust, 309, 33
Fitzpatrick, E. L., & Massa, D. 2007, ApJ, 663, 320
Hoang, T., & Lazarian, A. 2009, ApJ, 695, 1457
Jones, R. V., & Spitzer, L., Jr. 1967, ApJ, 147, 943
Kawabata, K. S., et al. 1999, PASP, 111, 898
Kim, S.-H., Martin, P. G., & Hendry, P. D. 1994, ApJ, 422, 164
Larson, K. A., & Whittet, D. C. B. 2005, ApJ, 623, 897
Lazarian, A. 2007, J. Quant. Spectrosc. Radiat. Transfer, 106, 225
Lazarian, A., & Draine, B. T. 1999, ApJL, 520, L67
Lazarian, A., & Draine, B. T. 1999, ApJL, 516, L37

Lazarian, A., & Hoang, T. 2007, MNRAS, 378, 910
Lazarian, A., & Hoang, T. 2008, ApJL, 676, L25
Markkanen, T. 1977, A&A, 56, 83
Mathis, J. S. 1986, ApJ, 308, 281
Matsumura, M., & Bastien, P. 2009, ApJ, 697, 807
Matsumura, M., & Seki, M. 1991, Ap&SS, 176, 283
Matsumura, M., & Seki, M. 1996, ApJ, 456, 557
Matsumura, M., Seki, M., & Kawabata, K. 1999, AJ, 117, 429
Matsumura, M., & Bastien, P. 2003, Grain Formation Workshop 2003, 23, 7
Matsumura, M., Kameura, Y., Kawabata, K. S., et al. 2011, PASJ, 63, L43
Purcell, E. M. 1979, ApJ, 231, 404
Roberge, W. G., & Lazarian, A. 1999, MNRAS, 305, 615
Schlegel, D. J., Finkbeiner, D. P., & Davis, M. 1998, ApJ, 500, 525
Seki, M., & Matsumura, M. 1996, Polarimetry of the Interstellar Medium, 97, 168
Serkowski, K., Mathewson, D. S., & Ford, V. L. 1975, ApJ, 196, 261
Weitenbeck, A. J. 1999, Acta Astronomica, 49, 59
Weitenbeck, A. J. 2004, Acta Astronomica, 54, 87
Whittet, D. C. B., Gerakines, P. A., Hough, J. H., & Shenoy, S. S. 2001, ApJ, 547, 872
Whittet, D. C. B., Martin, P. G., Hough, J. H., Rouse, M. F., Bailey, J. A., & Axon, D. J. 1992, ApJ, 386, 562
Whittet, D. C. B., Hough, J. H., Lazarian, A., & Hoang, T. 2008, ApJ, 674, 304
Wurm, G., & Schnaiter, M. 2002, ApJ, 567, 370

Laboratory analogy of amorphous enstatite fine grain formation and crystallization

C. Kaito, Y. Saito, C. Koike, T. Miyashita, T. Fujisaki

Department of Physics, Ritsumeikan University, Kusatsu-shi, Shiga 525-8577, Japan

Abstract

Amorphous enstatite ($MgSiO_3$) grains were produced by the simultaneous evaporation of Mg and SiO vapor by up and down double heater method in Ar gas pressure of 10 Torr. Produced particles were mainly mixture of MgO crystallites and amorphous $MgSiO_3$ structure. High resolution electron microscopy showed the crystallites of MgO and $MgSiO_3$ crystallites less than 10 nm. Crystallization temperature of $MgSiO_3$ amorphous structure has been determined to be 600℃ by direct observation by HRTEM in vacuum.

Introduction

In a previous paper,[1)] we reported the laboratory analogy of crystallize enstatite grain formation in RF plasma field. The produced $MgSiO_3$ grain size was less than 50 nm and covered with amorphous β-cristobalite phase of SiO_2. The growth of Mg particle on the SiO particle growth stream in RF plasma field was characteristic difference than the formation of Mg_2SiO_4 phase particle by the use of parallel double heaters.[2)] Submicron-sized silicate grains are present in the circumstellar outflow around oxygen-rich stars and within the interstellar mechanism. Since the estimated presser of solar nebula at 2-3 AU is low,[3)] experiments on growth mechanism in vacuum are important for composition with condensation, evaporation, melting and crystallization processes observed in the primitive solar nebula.[4,5)] A new method to produce the compound by the use of reaction between SiO film and Mg ultrafine particle[6)] showed the enstatite phase ($MgSiO_3$) by heating at 450-700℃. The growth of the $MgSiO_3$ phase took place due to the movement of the Mg atoms into the amorphous SiO film.

In the present paper, amorphous enstatite ultrafine grain and the crystallization of amorphous enstatite ultrafine particles in vacuum of 10^{-6} Pa have been elucidated.

Experimental procedure

The chamber used for sample preparation was a glass cylinder 17 cm in diameter and 33 cm in height. The two evaporation sources were set up and down positions at 2 cm as indicated schematically in Fig.1 (c) in Ar gas at 10 Torr. Typical shape of the particle formation in Ar gas at 10 Torr is shown in Fig.1 (b). In the present experiment, two evaporation sources in V-shaped tungsten boats (50 mm length, 2 mm width and 1 mm depth) were set as shown schematically in Fig.1 (c). SiO powder was evaporated from a tungsten boat heated at 1600℃. The Mg evaporation source was set 2 cm above the evaporation source of SiO. The Mg powder was also put on a tungsten boat heated at 600℃. The same shape and evaporation temperature was also indicated in Fig.1 (b). The evaporation flow due to the heating of the SiO evaporation source was spontaneously mixed with the Mg smoke indicated in Fig.1 (b). The smoke shapes are also shown in Fig.1 (a). The collected specimen was examined using a Hitachi-9000 electron microscope.

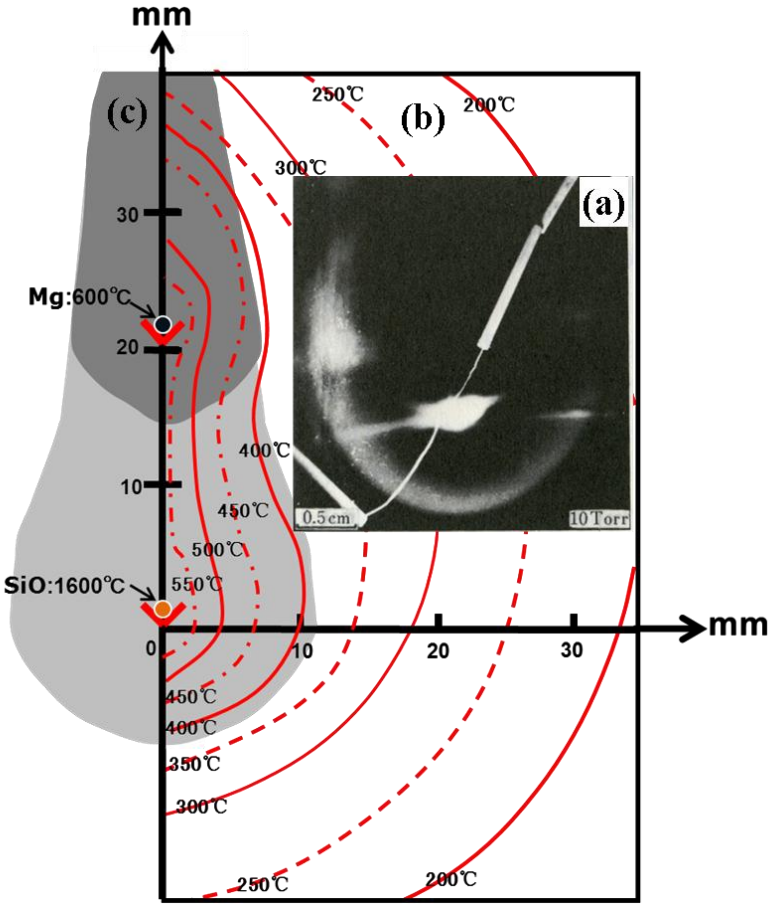

Fig.1 (a) smoke produced at 10 Torr Ar gas by heating 1600℃. (b) Typical increment of the temperature at various height by heating SiO at 1600℃ and Mg at 600℃ in Ar gas at 10 Torr. (c) Smoke shape of SiO (0 mm) and Mg (20 mm) from the tantalum boats. Mg and SiO smokes were mixture among at 450℃～500℃ temperature region.

Crystallization process of the amorphous enstatite was directly observed using a Hitachi H-9000 HRTEM with a specimen heating holder, which can be heated to approximately 800℃ in vacuum at 10^{-6} Pa . Specimen was put on the amorphous holey carbon film.

Results and Discussion

(a) Amorphous $MgSiO_3$ ultrafine particle formation.

If the Mg and SiO powders are evaporated in Ar gas pressure at 10 Torr from the evaporation source of tungsten heater at 600℃ (Mg) and 1600℃ (SiO), the typical electron microscopic images of Mg, silicon (Si) and α-crystallites (SiO_2) were produced. Since the gas pressure was 10 Torr, smoke Mg and Si + SiO_2 particles were produced. The Mg crystallites of the order less than 20 nm were oxidized MgO at room temperature in order to exposure in air. Ultrafine Mg particles were altered as shown in Fig.2 (a). The diffraction image of MgO shows the micro crystallites on Mg surface. Fig.2 (b) shows the typical Si + SiO_2 with based amorphous diffraction pattern. As elucidated in a previous paper on direct observation of metamorphism of the silicon oxide grains,[7, 8)] the produced particles were Si and α-SiO_2.

The SiO powder produced by evaporation of SiO powder at the lower heater at 1600℃ was agree with the ultrafine particles heated at the up heater. As indicated in Fig.1, the Mg and SiO_2 particles were mainly coalesce at temperature less than 450℃. The produced particles were mainly composed of MgO and $MgSiO_3$ amorphous particles as shown in Fig.3. The amorphous diffraction pattern was corresponding to the intensity rings of $MgSiO_3$. Therefore the produced amorphous particles were mainly $MgSiO_3$. The dark field image in Fig.3 shows the crystallites of the order of less than 10 nm was produced. As indicated in HRTEM image of amorphous particles in Fig.4, the existence of crystallites of MgO and $MgSiO_3$ can be seen. Therefore it can be concluded that $MgSiO_3$ particles are produced by the coalescence growth between Mg and SiO (Si + SiO_2) fine particles.

As elucidated in previous paper on the formation of $MgSiO_3$ crystallites by the reaction between SiO film and Mg particle by heating above 450℃ in vacuum (Saito et al., 1993). The coalescence growth of fine particles of Mg and SiO less than 500℃ becomes imperfect perfect for the $MgSiO_3$ phase. Since the growth speed of Mg and SiO ultrafine particles with the high speed than the heating in air, the amorphous $MgSiO_3$ and oxide Mg particles can be produced. Therefore Mg + SiO $\rightarrow$ Mg + SiO_2 + Si $\rightarrow$ MgO + $MgSiO_3$. As indicated in HRTEM image by the covering of amorphous SiO_2 phase, same particles were covered with amorphous SiO_2 grains.

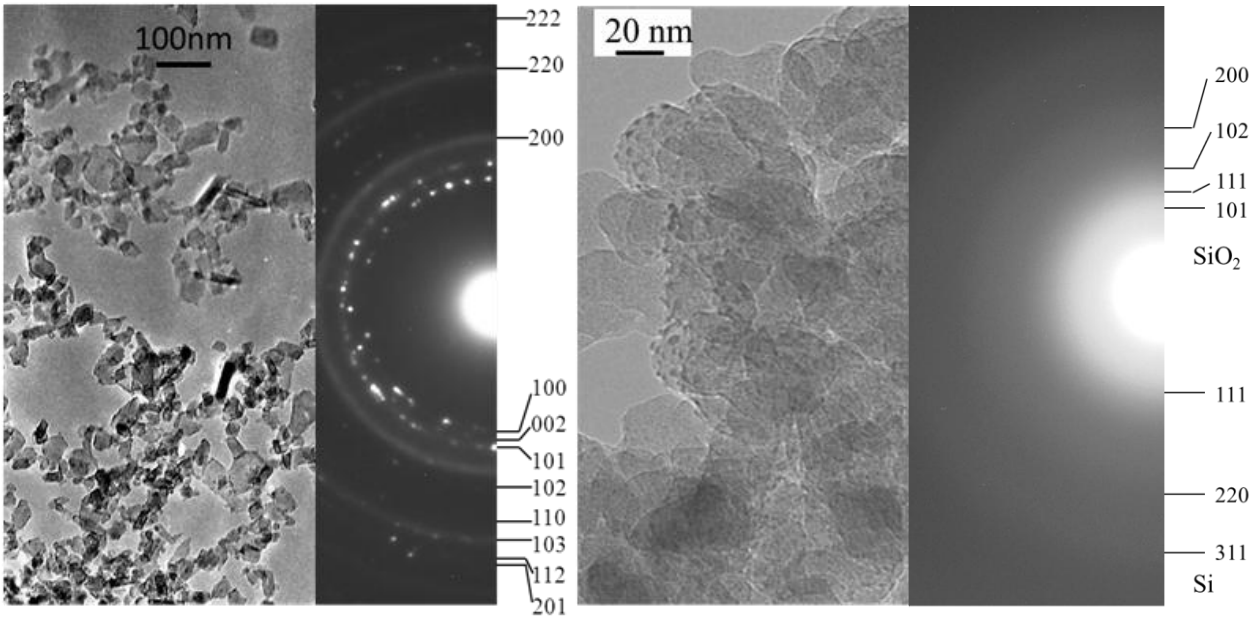

Fig.2 Typical Mg (a) and SiO (b) smoke particles at 1 cm and 3 cm from the heater. Mg particle was oxidized to exposure in air. The image (a) was exposed to the air about 1 min. Evaporated SiO at 1600℃ is composed of amorphous α-SiO_2 and Si cryatallites of a few nm. The coalescence growth between. Mg and SiO_2 took place as indicated in Fig.3.

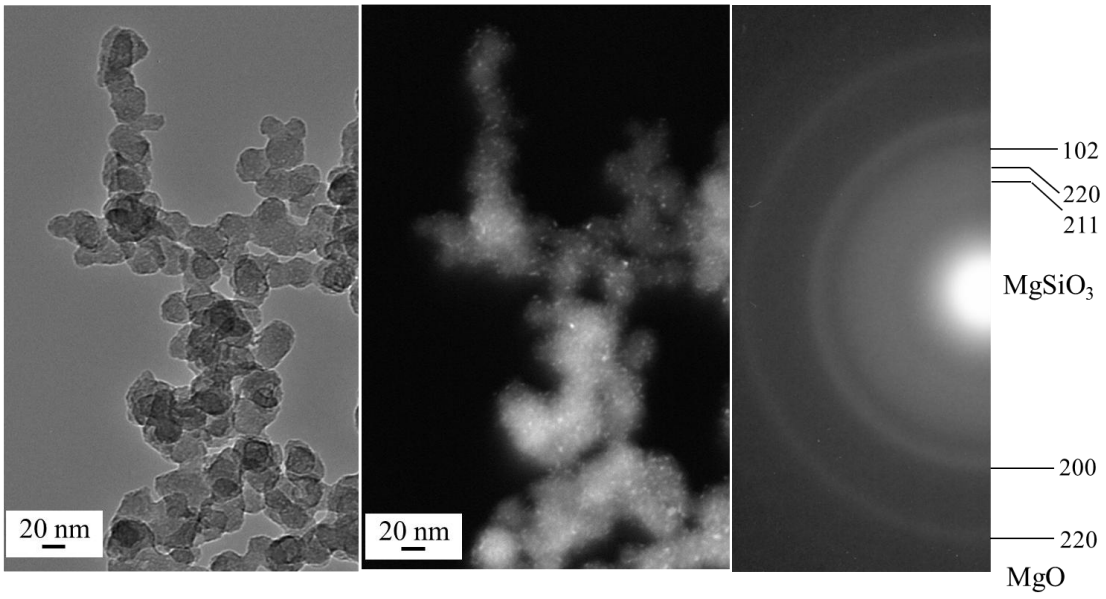

Fig.3 Typical electron microscopic image, dark field image and diffraction image produced by the coalescence growth between SiO and Mg ultrafine particles as indicated in Fig.1. Amorphous $MgSiO_3$ and MgO fine crystallites with size less than 5nm order crystallites. The small diffraction pattern shows the small crystallites with 5 nm order MgO and $MgSiO_3$.

The IR spectra of the $MgSiO_3$ amorphous grains produced by the present method have been measured by dispersing the produced particle on KBr crystal as well as the experiment report on crystalline silicate used the crystalline materials (Chihara et al., 2002). The data was presented in Fig.5. Typical examples on the distribution of MgO and $MgSiO_3$ shown in Fig.4 specimen on KBr crystal are also shown in Fig.5. Nano size specimen was distributed on the surface of KBr. The data on Oen was appeared as sown in Fig.5. Since $MgSiO_3$ specimen was amorphous and the crystallites of $MgSiO_3$ were

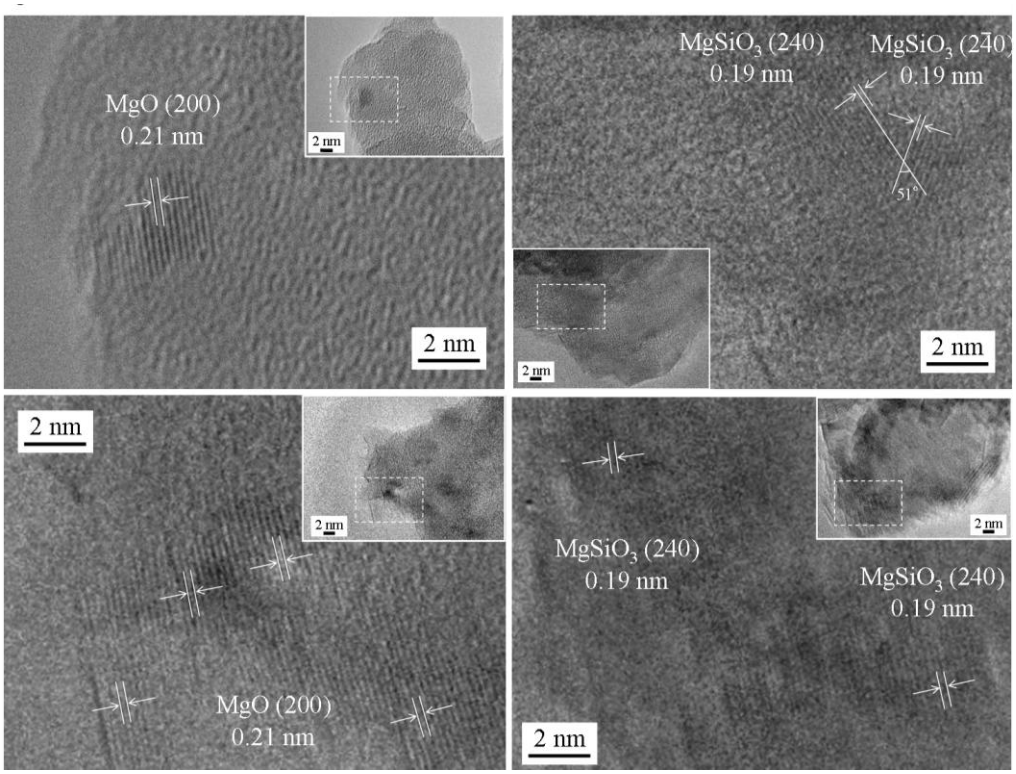

Fig.4 Typical high resolution images from particles in Fig.3. Mg and $MgSiO_3$ crystallites formation can be seen.

less than 10nm, the IR spectra for a long range were not appeared. In the present specimen the oxidized MgO crystallites of Mg grain was included, the peak due to the Mg and O distances in MgO crystallites showed the peak at 14.5 nm as elucidated in previous paper (Tamura et al. 2003).[10] The appearance of forsterite may be due to the large SiO_2 layer as elucidated in previous paper,[1] Mg_2SiO_4 phase appearance may be mainly due to the process of the sample in KBr.

$MgSiO_3$ and oxide Mg particles can be produced. Therefore Mg + SiO → Mg + SiO_2 + Si → MgO + $MgSiO_3$. As indicated in HRTEM image by the covering of amorphous SiO_2 phase, same particles were covered with amorphous SiO_2 grains.

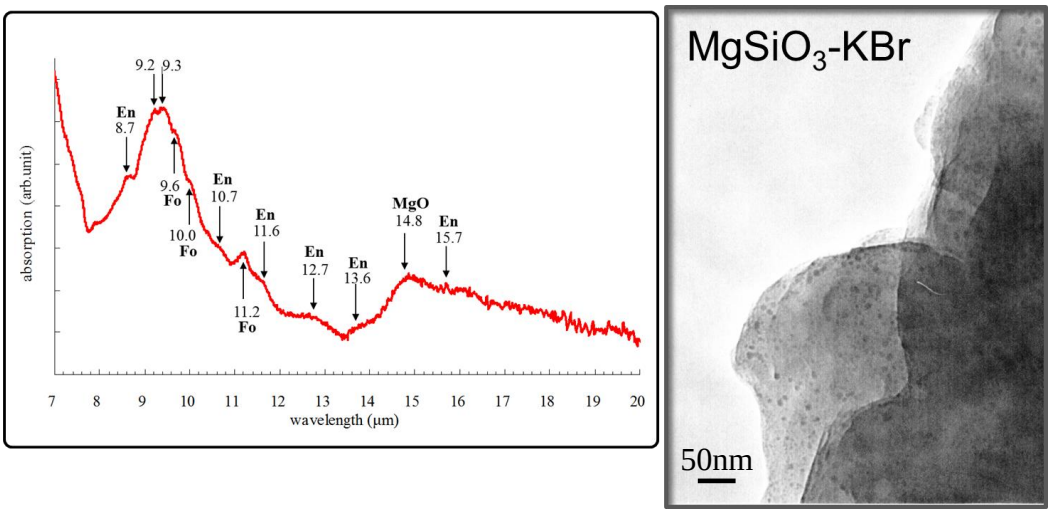

Fig.5 IR spectrum collected on KBr crystallites. The produced amorphous particle size of 20 nm order was distributed on KBr crystal. The formation of $MgSiO_3$ and MgO can be clearly seen. The existence of Mg_2SiO_4 may be due to specimen prepared of IR on KBr crystal. $MgSiO_3$ amorphous particles less than 30 nm were distributed on KbR specimen. KBr specimen was week in the electron microscope.

The IR spectra of the $MgSiO_3$ amorphous grains produced by the present method have been measured by dispersing the produced particle on KBr crystal as well as the experiment report on crystalline silicate used the crystalline materials (Chihara et al., 2002). The data was presented in Fig.5. Typical examples on the distribution of MgO and $MgSiO_3$ shown in Fig.4 specimen on KBr crystal are also shown in Fig.5. Nano size specimen was distributed on the surface of KBr. The data on Oen was appeared as sown in Fig.5. Since $MgSiO_3$ specimen was amorphous and the crystallites of $MgSiO_3$ were less than 10nm, the IR spectra for a long range were not appeared. In the present specimen the oxidized MgO crystallites of Mg grain was included, the peak due to the Mg and O distances in MgO crystallites showed the peak at 14.5 nm as elucidated in previous paper (Tamura et al. 2003).[10] The appearance of forsterite may be due to the large SiO_2 layer as elucidated in previous paper,[1] Mg_2SiO_4 phase appearance may be mainly due to the process of the sample in KBr.

(b) Direct observation on the crystallization of amorphous $MgSiO_3$ particle

The specimen holder on the heating temperature at room temperature to 1073 K which can be used in previous paper for composition Mg_2SiO_4 particle (Kamitsuji et al.,) was used for the enstatite ultrafine in direction in Fig.2. Fig.7 shows the typical electron microscopic image at 270℃, 400℃ and 600℃ of the same position. Particles less than 50 nm hardly altered. The small crystal structure difference can be seen between at 230℃ and 400℃ as well as the low temperature crystallization observed

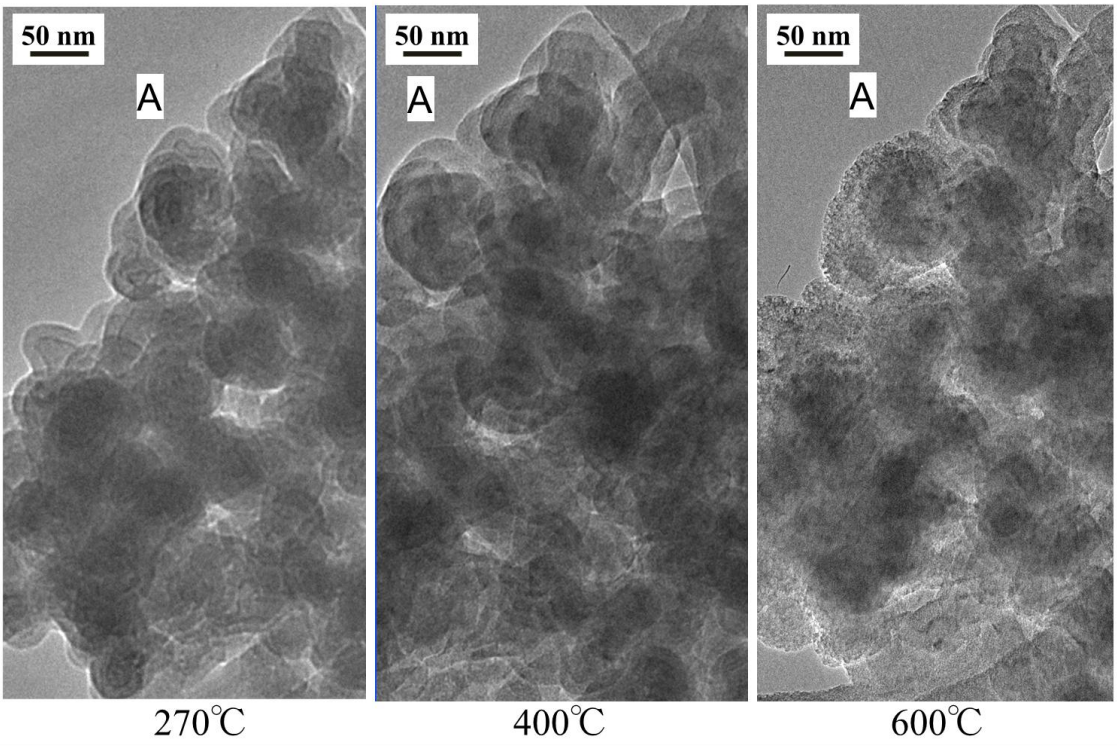

Fig.6 Alteration of grains by heating in air. Crystallites formation took place at 600℃.

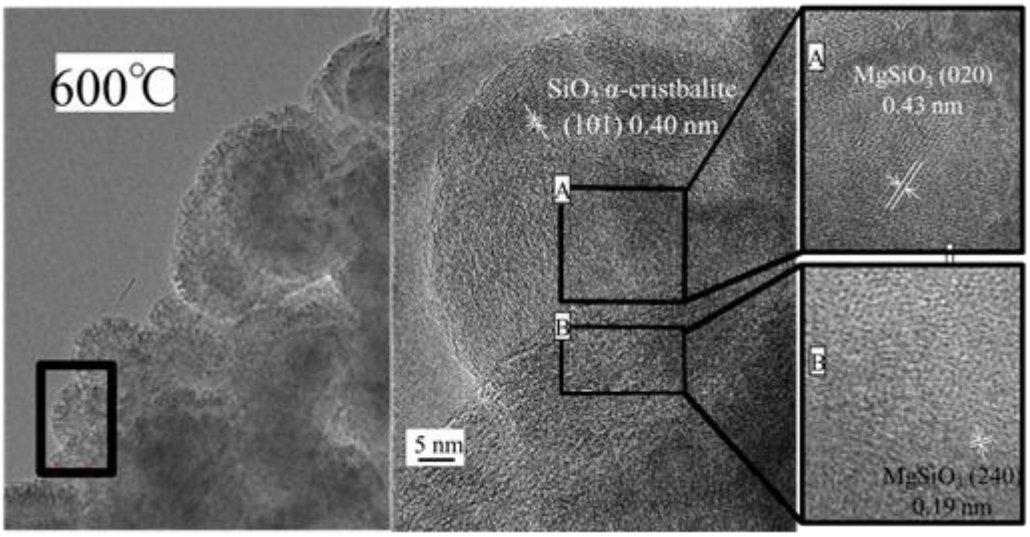

Fig.7 High resolution electron microscopic image after heated at 600°C. The image of a particle indicated clearly shows the growth of amorphous SiO_2. The central part of the image clearly showed the growth of $MgSiO_3$ crystallites. If the SiO layer is larger, the growth of SiO_2 layer on the MgO and $MgSiO_3$ crystallite surface took place.

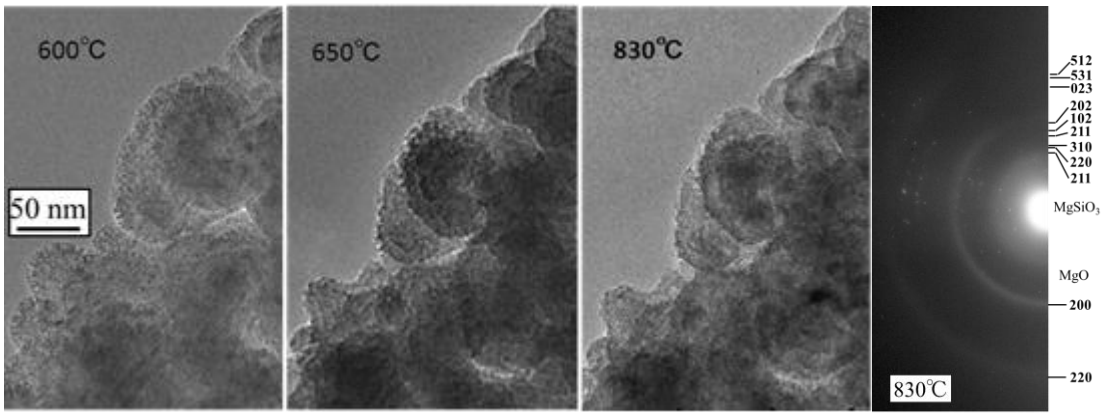

Fig.8 $MgSiO_3$ crystallization more took. If the crystallite particles were heated at 800°C order, the $MgSiO_3$ crystal growth clearly occurred as indicated diffraction pattern of the particles. The crystal image growth can be clearly seen in the image of the same position at 600°C, 650°C and 830°C.

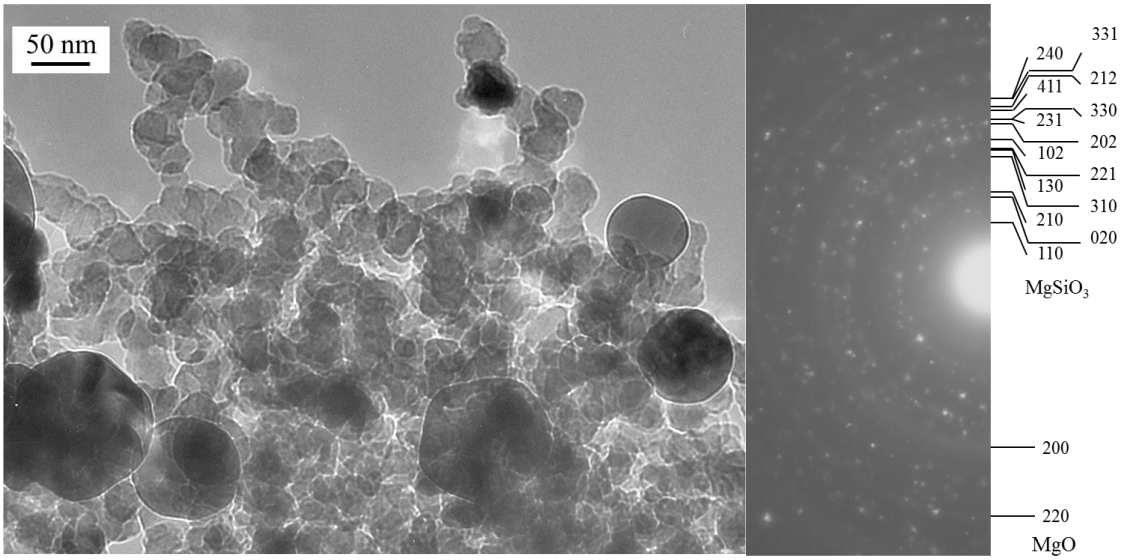

Fig.9 The heated specimen at eight hundred order was more crystallized during the cooling process. $MgSiO_3$ and MgO crystal growth took placed as seen the diffraction pattern.

Mg_2SiO_4 amorphous structure (Kaito et al., 2007). The massive appearance of small crystallites in $MgSiO_3$ grains can be clearly observed by heating at 600℃.The fine crystallites formation less than 10 nm shows the amorphous diffraction. As indicated in Fig.8, the image at 600℃ is composed of crystallites of the order of 5 nm as seen the image and dark field image. Some of the particle surface was also covered with SiO_2 layer of amorphous structure. The typical examples are shown in Fig.8. The crystalline $MgSiO_3$ is clearly seen of the particle. As indicated by the dark field image on the

produced particles in Fig.7, the crystallites of MgO and $MgSiO_3$ are increased. Therefore the crystallization took place at 600℃ in vacuum of 10^{-6} Pa. The crystallization growth by the coalescence took place above 600℃.

Figure 9 shows the result increased 600℃ to 830℃ order, the crystal form were hardly changed. The crystallization took place. The electron diffraction pattern shows clearly appearance of $MgSiO_3$ crystallites. The electron diffraction pattern of MgO is diffuse. If the specimen heating system was cut off, the specimen was cooled to the row temperature at about 2 hours in vacuum system. After to the room temperature, the heated specimen at 800℃ order was more crystallized during the cooling process as shown in Fig.9. If the specimen heated at 600℃ from one hour, the specimen such as crystallization could not observed. The micro-crystallization took place above 600℃. If the heating temperature is order of 800℃, the crystallization during the heating stage at about 600℃ region may be accelerated the crystallization.

Reference

[1] T. Sato, K. Kamitsuji, M. Shintaku, Y. Kimura, M. Kurumada, O. Kido, H. Suzuki, Y. Saito, C. Kaito, 2006, Planetary and Space Science 54, 615.

[2] C. Kaito, Y. Ojima, K. Kamitsuji, O. Kido, Y. Kimura, H. Suzuki, T. Sato, T. Nakada, Y. Saito, C. Kaito, 2003, Mteoritics and Planetary Science 38, 49.

[3] H. Nagahara, I. Kushiro, B. M. Mysen., 1994, Cosmochem. Acta. 58, 1951.

[4] J, A. Nuth, 1996 in The Cosmic Dust Connection, ed. J. M. Greenberg (The Netherlands : Klumer Academic), 205.

[5] B. O. Mysen, I. Kushiro, 1988, Am. Minerral. 73, 1.

[6] Y. Saito, K. Ohtsuka, T. Watanabe, C. Kaito, 1993, J. Crystal Growth 128, 271.

[7] T. Morioka, S. Kimura, N. Tsuda, C. Kaito, Y. Saito, C. Koike., 1998, Mon. Not. R. Astron. Soc. 299. 78.

[8] K. Kamitsuji, H. Suzuki, Y. Kumura, T. Sato, Y. Saito, C. Kaito., 2005, Astronomy and Astrophysics 429, 205.

[9] H. Chihara, C. Koike, A. Tsuchiyama, T. Tachibana, D. Sakamoto, 2002, Astronomy and Astrophysics, 391, 267.

[10] K. Tamura, Y. Kimura, H. Suzuki, O. Kido, T. Sato, T. Tanigaki, K. Kurumada, Y. Saito and C. Kaito, 2003, Jpn. J. Appl. Phys. 42, 7489.

[11] C. Kaito, S. Sasaki, Y. Miyazaki, A. Kumamoto, M. Kurumada, K. Yokoyama, M. Saito and Y. Kimura, 2006, Advances in Geosciences 7, 125.

Mid-Infrared Multi-Epoch Observations of Dust Forming Nova V1280Sco

Itsuki Sakon[1], Shigeyuki Sako[2], Takashi Onaka[1], Ryou Ohsawa[1], Takashi Shimonishi[1], Takuya Fujiyoshi[3], Hidenori Takahashi[2], Akira Arai[4], Makoto Uemura[5], Yuki Kimura[6], Takaya Nozawa[7], Takashi Kozasa[8]

[1]Department of Astronomy, Graduate Schools of Science, University of Tokyo, 7-3-1, Hongo, Bunkyo-ku, Tokyo 113-0033, Japan

[2]Institute of Astronomy, University of Tokyo, 2-21-1 Ohsawa, Mitaka, Tokyo 181-0015, Japan

[3]Subaru Telescope, National Astronomical Observatory of Japan, 650 North A'ohoku Place, Hilo, HI 96720, USA

[4]Koyama Astronomical Observatory, Kyoto Sangyo University, Motoyama, Kamigamo, Kita-ku, Kyoto, 603-8555, Japan

[5]Hiroshima Astrophysical Science Center, Hiroshima University, Higashi-Hiroshima, Hiroshima 739-8526, Japan

[6]Department of Earth and Planetary Materials Science, Graduate School of Science, Tohoku University, Aoba 6-3, Aoba-ku, Sendai 980-8578, Japan

[7]Institute for the Physics and Mathematics of the Universe (IPMU), The University of Tokyo, Kashiwa, Chiba 277-8568, Japan

[8]Department of Cosmosciences, Hokkaido University, Kita-10 Nishi-8, Kita-ku, Sapporo 060-0810, Japan

ABSTRACT

We present the results of the late time infrared multi-epoch observations of dust forming nova V1280Sco with Cooled Mid-Infrared Camera and Spectrometer (COMICS) on the Subaru telescope, Thermal-Region Camera Spectrograph (TReCS) on the Gemini South telescope and the Infrared Camera (IRC) onboard the *AKARI* satellite, etc. The temperature and mass evolutions of dust formed in the nova wind are examined based on the spectral decomposition of the infrared spectral energy distribution (SED) obtained at each epoch. The AKARI near-infrared spectrum obtained at t = 940 days and Gemini-South/T-ReCS N-band spectrum obtained at t=1272 days have shown the presence of unidentified infrared (UIR) emission features which may well be carried by hydrogenated amorphous carbons rather than PAHs. Neither of the Gemini-S/T-ReCS N-band spectra obtained at t=1272 and t=1616 days have shown the clear signs of crystalline silicate features, indicating that the annealing of amorphous silicate by the UV photons provided by the white dwarf has not yet occured at those epochs.

INTRODUCTION

The condensation of gas ejected from the evolved stars, in which the products of nucleo-synthesis are contained, is expected as an important pathway of cosmic dust formation. While the understanding of dust formation by supernovae or Wolf-Rayet binary systems should be indispensable to identify the origin of interstellar dust in the early universe or distant galaxies, that by low- to intermediate-mass evolved stars would also be crucial to explore the process of chemical enrichment in the local universe. The understanding of the process of dust condensation in the gas ejecta associated with the stellar mass-loss activities from the observational point of view should be one of the most important issues in today's infrared astronomy. However, little studies have directly demonstrated the

process of dust formation by examining the evolution of infrared spectra in accordance with time. In this study, we focus on novae, which are explosive phenomena accompanied by a significant mass-loss caused by the thermo-nuclear runaway as a result of the heavy accretion of the envelope of the companion onto the white dwarf disk. And we aim to observationally demonstrate process of the dust formation and its evolution in the circumstellar environment of novae.

A classical nova is an interesting phenomenon, which provides us valuable opportunity to monitor the formation process of circumstellar dust in a practical timescale for human beings. The composition of dust formed in the stellar ejecta depends on the chemical properties of the stellar atmosphere; carbonaceous dust formation is expected when C/O ratio in the envelope exceeds unity (carbon-rich), while silicate dust formation is expected when C/O ratio is less than unity (oxygen-rich) (Waters 2004). Recent infrared observations of some dust forming novae, however, have reported the presence of both emissions from carbonaceous and silicate dust (e.g., Nova V842 Cen: Smith et al. 1994; Nova V705 Cas: Evans et al. 2005), suggesting the chemical complexity of the mass-loss history of the CO white dwarf in a binary system until it experiences the nova outburst and the spatial non-uniformity of the chemical properties of the ejected gas. In this study, we try to investigate the infrared spectral evolution of dust forming novae in the mid-infrared, aiming (1) to demonstrate the composition and the temperature and mass evolutions of dust formed in the ejecta of the nova outburst, (2) to investigate the possible evolution process of dust grains in a harder UV radiation fields as the deeper part of the photosphere of the white dwarf becomes exposed.

NEAR- TO MID-INFRARED MULTI EPOCH OBSERVATIONS OF V1280SCO

V1280Sco was discovered on 2007 Feb. 4.86 (Yamaoka et al. 2007) at the distance of 1.6kpc (Chesneau et al. 2008). The onset of dust formation around the V1280Sco was reported on 23 days after the outburst (Das et al. 2007) and expanding dust shell with 0.35±0.03 mas day-1 has been reported based on VLTI/AMBER, MIDI observations performed between the day 23 and day 145 (Chesneau et al. 2008). We have collected the mid-infrared (N- & Q-band) imaging and N-band low-resolution spectroscopic datasets of V1280Sco at three epochs of day 150 and days 1272 and 1616 with Subaru/COMICS and Gemini-South/TReCS, respectively. We also have obtained the near-infrared (2-5μm) spectrum of V1280Sco at the day 940 with AKARI/Infrared Camera (IRC) (AKARI Phase-3II Open Time Program; Program ID: SENNA, PI. I. Şakon). Long-term monitoring observations in the optical to near-infrared wavelengths have been made continuously from the very initial phase of the outburst to date with several Japanese ground-based facilities including the KANATA/TRISPEC of Hiroshima University, Araki 1.3m telescope/ADLER of Kyoto Sangyo University, Okayama Observatory 188cm telescope/OASIS and GUNMA/GIRCS, and detailed optical and near-infrared light curves are obtained partly in the framework of inter-university collaboration. The near- to mid-infrared SED of V1280Sco at day 150 is best reproduced by the emission from hot (820K) and warm (340K) amorphous carbon with masses of 1.7×10^{-8}Msun and 2.3×10^{-6}Msun, respectively, with foreground silicate extinction of Av~5mag (see Fig.1 top). Taking account of the emitting region sizes of both components constrained from our N-&Q- band imaging data, the warm

component is expected to be the amorphous carbon formed in the initial nova wind ejected at t=10.5 days while the hot component to be the amorphous carbon formed in the second nova wind ejected at t=110 days. The SED at day 1272 is best reproduced by the emissions from the new 270K and 200K astronomical silicate dust with masses of 2.5×10^{-7}Msun and 5.0×10^{-7}Msun, respectively, together with the 500K and 150K amorphous carbon dust with masses of 1.0×10^{-7}Msun and 1.0×10^{-6}Msun, respectively, with foreground silicate extinction of Av~5.5mag (see Fig. 1 middle). Moreover, the SED at day 1616 is best reproduced by the 520K and 150K amorphous carbon with masses of 6.3×10^{-8}Msun and 2.2×10^{-6}Msun, respectively, and the 330K and 150K astronomical silicate with masses of 1.5×10^{-7}Msun, 1.0×10^{-6}Msun, respectively.

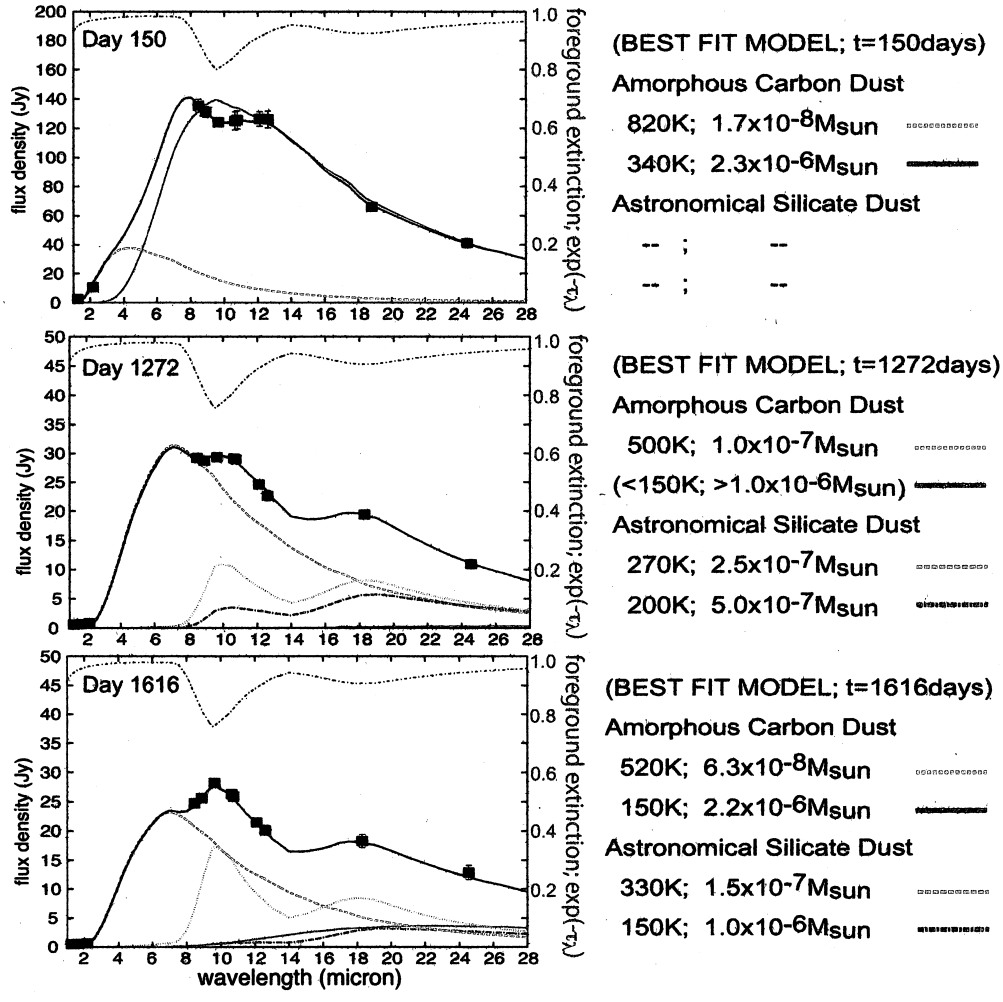

Figure. 1 — Near- to Mid- Infrared Spectral Energy Distribtion (SED) of V1280Sco on Days 150, 1272, and 1616 taken with Subaru/COMICS and Gemini-TReCS. The best fit results of the dust SED model are shown.

In the N-band spectrum of V1280Sco at day 1272, clear signs of hydrogenated amorphous carbons (HACs), which contains more abundant aliphatic hydrocarbon structures than typical polycyclic aromatic hydrocarbons (PAHs), are recognized as the 8.1μm and 11.35μm band features (cf. Sloan et al. 2007; Hyland & McGregor 1989) over the broad continuum emission reproduced by amorphous carbon and astronomical silicate (see Fig.2 left). We also recognize faint features at 9.2 and 10.7μm, which generally agree with the peak positions of crystalline silicate features (see Fig.2 left). The presence of HACs can also be suggested from the near-infrared

spectrum obtained with AKARI/IRC at day 940, in which a UIR 3.3μm feature with strong 3.4-3.6μm emission structures associated with the vibration modes of aliphatic C-H bond has been detected (Sakon et al. 2012 in prep). On the other hand, in the N-band spectrum of V1280Sco at day 1616, emission features at 8.1μm, 8.6μm and 11.3μm, which are supposed to be carried by HACs and/or PAHs, diminish significantly (see Fig. 2 right). This suggests the destruction of the carriers of the UIR band in harsh radiation field of the white dwarf.

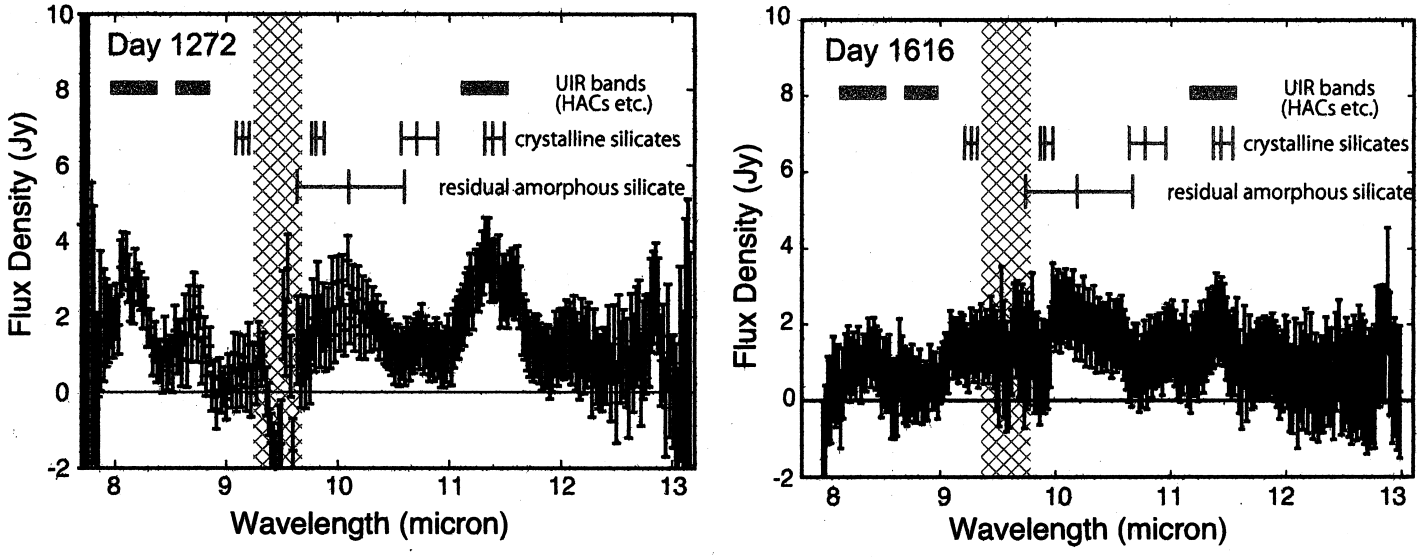

Figure. 2 — Continuum-subtracted N-band spectrum of V1280Sco on Days 1272 (left) and 1616(right) after the discovery. The positions of HACs and PAHs features at 8.1, 8.6, and 11.35μm as well as those of crystalline silicates (forestrite, Enstatite and diopside) features at 9.3, 10.7 and 11.4μm are shown.

REFERENCE

[1] Chesneau, O., et al. 2008, A&A, 487, 223
[2] Das, R.K., et al. 2008, MNRAS, 391, 1874
[3] Evans,A., & Rawlings,J.M.C.,1994, MNRAS, 269, 427
[4] Evans,A., et al. 2005, MNRAS, 360, 1483
[5] Hyland, A.R., & McGregor, P.J., 1989, Proc. of IAU Sym. 135,101,
[6] Molster, F.J., et al. 2002, A&A, 382, 222
[7] Sakon, I., et al. 2012, in preparation
[8] Sloan, G.C., et al. 2007, ApJ, 664, 1144
[9] Smith, C.H., et al. 1994, MNRAS, 267, 225
[10] Tielens, A.G.G.M., 2005, Cambridge Univ. Press, ISBN 0521826349
[11] Waters, L.B.F.M., 2004, ASPC, 309, 299
[12] Yamaoka, H., et al. 2007, IAU Circ., 8803, 1

Coagulation and Radial Drift of Porous Dust Aggregates in Protoplanetary Disks

Satoshi Okuzumi[1], Hidekazu Tanaka[2], Hiroshi Kobayashi[1], and Koji Wada[3]

ABSTRACT

Rapid orbital drift of macroscopic dust particles is one of the major obstacles against planetesimal formation in protoplanetary disks. We reexamine this problem by considering porosity evolution of dust aggregates. We apply a porosity model based on recent N-body simulations of aggregate collisions, which allows us to study the porosity change upon collision for a wide range of impact energies. As a first step, we neglect collisional fragmentation and instead focus on dust evolution outside the snow line, where the fragmentation has been suggested to be less significant than inside the snow line because of a high sticking efficiency of icy particles. We show that dust particles can evolve into highly porous aggregates (with internal densities of much less than 0.1 g cm^{-3}) even if collisional compression is taken into account. Furthermore, we find that the high porosity triggers significant acceleration in collisional growth. This acceleration is a natural consequence of particles' aerodynamical property at low Knudsen numbers. Thanks to this rapid growth, the highly porous aggregates are found to overcome the radial drift barrier at distances less than 10 AU from the central star. This suggests that, if collisional fragmentation is truly insignificant, formation of icy planetesimals is possible via direct collisional growth of submicron-sized icy particles.

Subject headings: dust, extinction — planets and satellites: formation — protoplanetary disks

1. Introduction

Growth of dust particles is a key process in protoplanetary disks. Current theories of planet formation assume km-sized solid bodies called "planetesimals" to form from dust contained in protoplanetary disks. Being the dominant component of disk opacity, dust also affects the temperature and observational appearance of the disks.

Theoretically, however, it is poorly understand how the dust particles evolve into planetesimals. One of the most serious obstructs is the radial inward drift of macroscopic aggregates due

[1]Department of Physics, Nagoya University, Nagoya, Aichi 464-8602, Japan; okuzumi@nagoya-u.jp

[2]Institute of Low Temperature Science, Hokkaido University, Sapporo 060-0819, Japan

[3]Planetary Exploration Research Center, Chiba Institute of Technology, Narashino, Chiba 275-0016, Japan

to the gas drag (Whipple 1972; Adachi et al. 1976; Weidenschilling 1977). Because of the gas pressure support in addition to the centrifugal force, protoplanetary disks tend to rotate at sub-Keplerian velocities. By contrast, dust particles are free from the pressure support, and hence they tend to rotate faster than the gas disk. The resulting head wind acting on the dust particles extracts their angular momentum and thus causes their drift motion towards the central star. In order to go beyond this "radial drift barrier," dust particles must decouple from the gas drag (i.e., grow large) faster than they drift inward. However, previous work by Brauer et al. (2008) showed that dust particles finally fall onto the central star unless the initial dust-to-gas mass ratio is considerably higher than the canonical interstellar value.

This study reexamines this problem by considering a new physical effect: porosity evolution of dust aggregates. Most previous coagulation models assumed that dust particles grow with a fixed internal density, or a fixed porosity (e.g., Brauer et al. 2008). In reality, however, the internal density of aggregates does change upon collision depending on the impact energy. We simulate the temporal evolution of the radial size distribution of aggregates using the advection-coagulation model developed by Brauer et al. (2008). Unlike the previous work, we allow the porosities of aggregates to change upon collision, depending on their impact energies. To do so, we adopt the "volume-averaging method" proposed by Okuzumi et al. (2009). In this method, aggregates of equal mass are regarded as having the same volume (or equivalently, the same internal density) at each orbital distance, and the advection-coagulation equation for the averaged volume is solved simultaneously with that for the radial size distribution. To determine the porosity change upon collisional sticking, we use an analytic recipe presented by Suyama et al. (2012) that well reproduces the collision outcomes of recent N-body simulations (Wada et al. 2008; Suyama et al. 2008) as a function of the impact energy. These theoretical tools allow us to study for the first time how the porosity evolution affects the growth and radial drift of dust aggregates in protoplanetary disks. Details of our results are presented elsewhere (Okuzumi et al. 2012).

2. Model

We adopt the minimum-mass solar nebular model of Hayashi (1981) for the disk model. Dust particles are assumed to be initially compact spheres (monomers) of equal size $a_0 = 0.1$ μm and equal internal density $\rho_0 = 1.4$ g cm^{-3}, distributed in the disk with a constant dust-to-gas surface density ratio $\Sigma_d/\Sigma_g = 0.01$. Turbulence with the alpha value $\alpha_D = 10^{-3}$ is considered to determine the vertical profile and collision velocity of aggregates.

We solve the evolution of the radial size distribution of dust aggregates using the method developed by Brauer et al. (2008). This method assumes the balance between sedimentation and turbulent diffusion of aggregates in the vertical direction. We neglect electrostatic and gravitational interactions between colliding aggregates and assume perfect sticking upon collision. Thus, the collisional cross section is simply given by $\sigma_{\rm coll} = \pi(a_1 + a_2)^2$, where a_1 and a_2 are the radii of the

colliding aggregates.

The velocity of an aggregate relative to the gas generally depends on the its stopping time t_s. To calculate t_s as a function of aggregate size, we assume Epstein's law for $a < 9\lambda_{\rm mfp}/4$ and Stokes' law for $a > 9\lambda_{\rm mfp}/4$, where $\lambda_{\rm mfp}$ is the mean free path of gas particles.

The radial drift velocity is given by $v_r = -2\eta v_K \Omega t_s/[1 + (\Omega t_s)^2]$, where 2η is the ratio of the pressure gradient force to the stellar gravity in the radial direction and $v_K = r\Omega$ is the Kepler velocity (e.g., Whipple 1972; Adachi et al. 1976; Weidenschilling 1977). The radial drift speed has a maximum $\eta v_{\rm K}$, which is realized when $\Omega t_s = 1$. In our disk model, η scales with r as $\eta = 4.0 \times 10^{-3}(r/5\ {\rm AU})^{1/2}$, and the maximum inward speed $\eta v_K = 54\ {\rm m\ s^{-1}}$ is independent of r.

We also consider the collisional evolution of the porosity of aggregates. To do so, we treat the volume $V = (4\pi/3)a^3$ of an aggregate as a variable independent of the mass m. We follow the temporal evolution of $V(r, m)$ using the volume-averaging method developed by (Okuzumi et al. 2009).

Here we describe our recipe for determining the volume of merged aggregates. In general, the volume of an aggregate after sticking depends on the impact energy $E_{\rm imp}$ relative to the energy $E_{\rm roll}$ required for one monomer to roll over 90 degrees on the surface of another monomer in contact (Dominik & Tielens 1997; Blum & Wurm 2000; Wada et al. 2007) When $E_{\rm imp} \ll E_{\rm roll}$, no visible restructuring occurs upon collision. In this case, the volume after collision is determined independently of $E_{\rm imp}$. When $E_{\rm imp} \gtrsim E_{\rm roll}$, internal restructuring occurs through inelastic rolling among constituent monomers. In this case, the final volume depends on $E_{\rm imp}$ as well as on the volumes of aggregates before collision. Recently, Suyama et al. (2012) have proposed an analytic formula that can be used even for arbitrary values of $E_{\rm imp}/E_{\rm roll}$. We use this formula in our simulations. The rolling energy is assumed to be $E_{\rm roll} = 1.8 \times 10^{-8}$ erg.

The collision velocity between aggregates is assumed to be driven by Brownian motion, radial and azimuthal drift, vertical settling, and turbulence. We use the analytic formula of Ormel & Cuzzi (2007) to calculate the turbulence-driven velocity.

3. Results

To begin with, we show the result of compact aggregation. In this simulation, we fixed the internal density $\rho_{\rm int} \equiv m/V$ of the aggregates to the material density $\rho_0 = 1.4\ {\rm g\ cm^{-3}}$, and solved only the evolutionary equation for the radial size distribution. Figure 1 shows the snapshots of the dust surface density per decade of aggregate mass, $\Delta\Sigma_d/\Delta \log m$. At each orbital radius, dust growth proceeds without significant radial drift until the stopping time of the aggregates reaches $\Omega t_s \sim 0.1$ (the dotted lines in Figure 1). However, as the aggregates grow, the radial drift becomes faster and faster, and further growth becomes limited only along the line $\Omega t_s \sim 0.1$ on the r–m

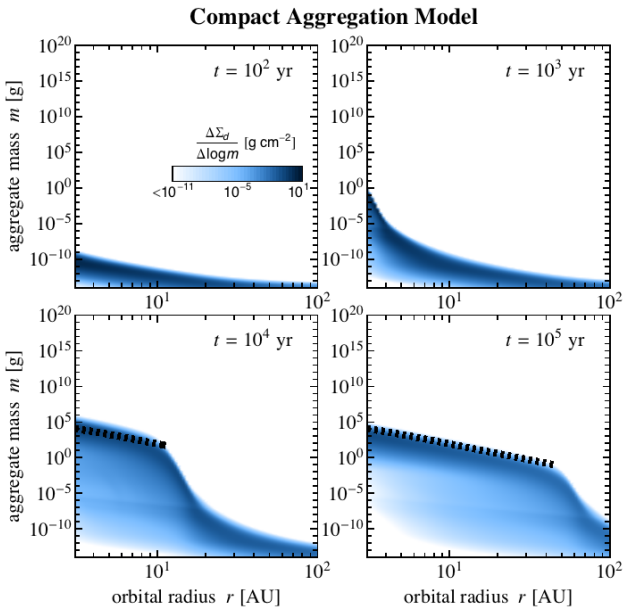

Fig. 1.— Aggregate size distribution $\Delta\Sigma_d/\Delta \log m$ at different times t for the compact aggregation model ($\rho_{\rm int} = 1.4$ g cm^{-3}) as a function of orbital radius r and aggregate mass m. The dotted lines mark the aggregate size at which Ωt_s exceeds 0.1.

plane. Consequently, a significant amount of dust has been lost from the planet-forming region $r \lesssim 30$ AU within 10^5 yr.

Now we show how porosity evolution affects dust evolution. Here, we solve the evolution of aggregate volume simultaneously with the radial size distribution. The result is shown in Figure 2, which displays the snapshots of the aggregate size distribution $\Delta\Sigma_d/\Delta \log m$ and internal density $\rho_{\rm int} = m/V$ (right four panels) at different times t as a function of r and m. The left four panels of Figure 2 show how the radial size distribution evolves in the porous aggregation. At $t < 10^3$ yr, the evolution is qualitatively similar to that in compact aggregation. However, in later stages, the evolution is significantly different. We observe that aggregates in the inner region of the disk ($r < 10$ AU) undergo rapid growth and eventually overcome the radial drift barrier lying at $\Omega t_s \sim 1$ (dashed lines in Figure 2) within $t \sim 10^4$ yr. In the outer region ($r > 10$ AU), aggregates do drift inward before they reach $\Omega t_s \sim 1$ as in the compact aggregation model. However, unlike in the compact aggregation, the inward drift results in the pileup of dust materials in the inner region ($r \approx 4$–9 AU) rather than the loss of them from outside the snow line. This occurs because most of the drifting aggregates are captured before they reach the snow line by aggregates that already overcome the radial drift barrier. As a result of this, the dust-to-gas mass ratio in the inner regions is enhanced by a factor of several in 10^5 yr.

The right four panels of Figure 2 show the evolution of the internal density $\rho_{\rm int} = m/V$ as a function of r and m. First thing to note is that the dust particles grow into low-density objects at every location until their internal density reaches $\rho_{\rm int} \sim 10^{-5}$–$10^{-3}$ g cm^{-3}. In this stage, the

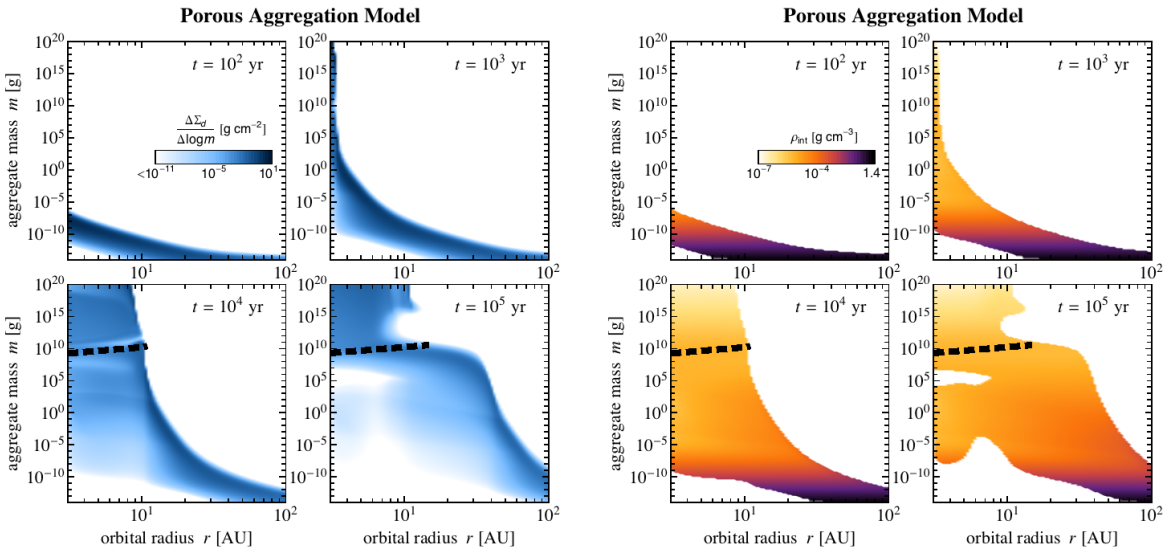

Fig. 2.— Aggregate size distribution $\Delta\Sigma_d/\Delta \log m$ (left four panels) and internal density $\rho_{\rm int} = m/V$ (right four panels) at different times t for the porous aggregation model as a function of orbital radius r and aggregate mass m. The dashed lines mark the aggregate size at which Ωt_s exceeds unity.

internal density decreases as $\rho_{\rm int} \approx (m/m_0)^{-1/2}\rho_0$, meaning that the dust particles grow into fractal aggregates with the fractal dimension $d_f \approx 2$ (Okuzumi et al. 2009). At $m \sim 10^{-4}$–10^{-6} g, the fractal growth stage terminates, followed by the stage where collisional compression becomes effective ($E_{\rm imp} \gg E_{\rm roll}$). In this late stage, the internal density decreases more slowly or is kept at a constant value depending on the orbital radius.

4. Condition for Breaking Through the Radial Drift Barrier

Below, we explain why porous aggregates overcome the radial drift barrier in the inner region of the disk. We do this by comparing the timescale of aggregate growth and radial drift. For simplicity, we assume that all dust aggregates are similar in size (this assumption is valid when the aggregate size distribution is peaked at $m \sim \langle m \rangle_m$). The growth rate of the aggregate mass m at the midplane is then given by

$$\frac{dm}{dt} = \frac{\Sigma_d}{\sqrt{2\pi}h_d} A \Delta v, \tag{1}$$

where Σ_d, h_d, A, and Δv are the spatial mass density (at the midplane), scale height, projected area, and relative velocity of the aggregates. Equation (1) can be rewritten in terms of the grow timescale

$$t_{\rm grow} \equiv \left(\frac{d \ln m}{dt}\right)^{-1} = \frac{4\sqrt{2\pi}}{3} \frac{h_d}{\Delta v} \frac{\rho_{\rm int} a}{\Sigma_d}, \tag{2}$$

where we have used that $m = (4\pi/3)\rho_{\rm int}a^3$ and $A = \pi a^2$. What we do here is to compare $t_{\rm grow}$ with the timescale for the radial drift given by

$$t_{\rm drift} \equiv \left|\frac{d\ln r}{dt}\right|^{-1} = \frac{r}{|v_r|}. \tag{3}$$

Now we focus on the stage at which the radial drift velocity reaches the maximum value, i.e., $\Omega t_s = 1$. At this stage, the dust scale height is given by $h_d \approx (2\alpha_D/3)^{1/2}h_g$, where h_g is the gas scale height (Youdin & Lithwick 2007). In addition, we set $\Delta v \approx \sqrt{\alpha_D}c_s$ since the collision velocity between $\Omega t_s = 1$ particles is dominated by the turbulence-driven velocity. Substituting these relations and $h_g = c_s/\Omega$ into Equation (2), we obtain

$$t_{\rm grow}|_{\Omega t_s=1} \approx 40\left(\frac{\Sigma_d/\Sigma_g}{0.01}\right)^{-1}\frac{(\rho_{\rm int}a)_{\Omega t_s=1}}{\Sigma_g}t_K, \tag{4}$$

where $t_K = 2\pi/\Omega$ is the Keplerian orbital period. By contrast, the drift timescale for $\Omega t_s = 1$ particles is

$$t_{\rm drift}|_{\Omega t_s=1} = \frac{1}{\eta\Omega} \approx 40\left(\frac{\eta}{4\times10^{-3}}\right)^{-1}t_K. \tag{5}$$

The ratio $(t_{\rm grow}/t_{\rm drift})_{\Omega t_s=1}$ determines the fate of dust growth at $\Omega t_s = 1$. If $(t_{\rm grow}/t_{\rm drift})_{\Omega t_s=1}$ is very small, dust particles grow beyond $\Omega t_s = 1$ without experiencing significant radial drift; otherwise, dust particles drift inward before they grow. We expect growth without significant drift to occur if

$$\left(\frac{t_{\rm grow}}{t_{\rm drift}}\right)_{\Omega t_s=1} \lesssim \frac{1}{10}, \tag{6}$$

where the threshold value 1/10 has been chosen based on the fact that $t_{\rm grow}$ is the timescale for mass doubling while the particles experience the fastest radial drift over one or two orders of magnitude in mass. Below, we examine in what condition this requirement is satisfied.

The ratio $(\rho_{\rm int}a)_{\Omega t_s=1}/\Sigma_g$ depends on the drag regime at $\Omega t_s = 1$. For the Epstein drag regime, it can be shown that (Okuzumi et al. 2012)

$$t_{\rm grow}|_{\Omega t_s=1} \approx 30\left(\frac{\Sigma_d/\Sigma_g}{0.01}\right)^{-1}t_K. \tag{7}$$

Hence, the growth condition is not satisfied for the standard disk parameters $\eta \approx 10^{-3}$ and $\Sigma_d/\Sigma_g = 0.01$, in agreement with the results of our and previous (Brauer et al. 2008) simulations.

The situation differs in the Stokes drag regime. A similar calculation shows (Okuzumi et al. 2012)

$$t_{\rm grow}|_{\Omega t_s=1} \approx 60\left(\frac{\Sigma_d/\Sigma_g}{0.01}\right)^{-1}\left(\frac{\lambda_{\rm mfp}}{a}\right)_{\Omega t_s=1}t_K. \tag{8}$$

Note that the growth timescale is inversely proportional to the aggregate radius, in contrast to that in the Epstein regime (Equation (7)) being independent of aggregate properties. This means that dust aggregates break through the radial drift barrier in the "deep" Stokes regime, $(a/\lambda_{\rm mfp})_{\Omega t_s=1} \gg 1$.

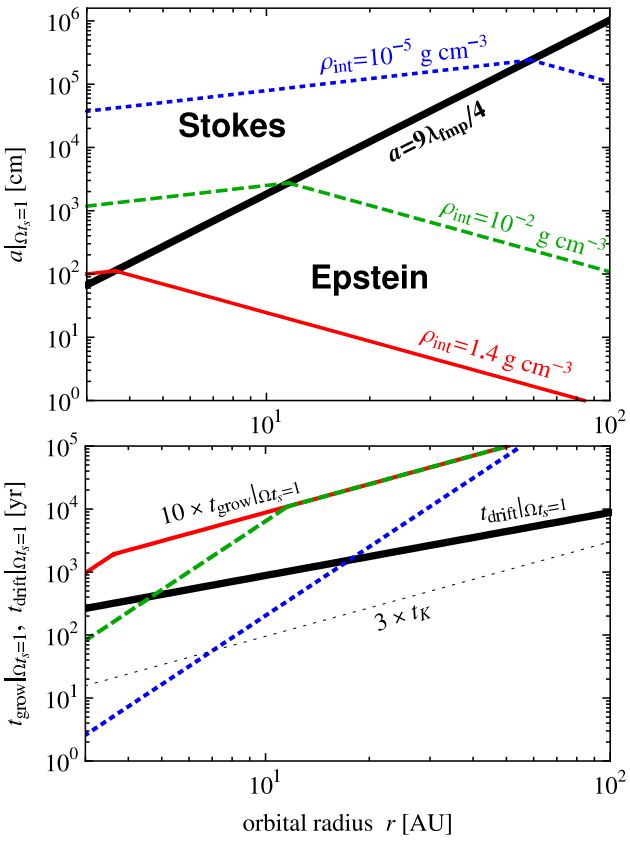

Fig. 3.— Size a (upper panel) and growth timescale $t_{\rm grow}$ (lower panel) of dust aggregates at $\Omega t_s = 1$ as a function of orbital radius r for internal densities $\rho_{\rm int} = 1.4$ g cm^{-3} (solid line), 10^{-2} g cm^{-3} (dashed line), and 10^{-5} g cm^{-3} (dotted line). The minimum-mass solar nebular with the dimensionless diffusion coefficient $\alpha_D = 10^{-3}$ is assumed for the disk model. The thick black line in the upper panel indicates $a = 9\lambda_{\rm mfp}/4$, at which the drag law goes from the Epstein regime to the Stokes regime. The thick black line in the lower panel shows the drift timescale $t_{\rm drift}$ at $\Omega t_s = 1$, which is the minimum value of $t_{\rm drift}$ and is independent of $\rho_{\rm int}$.

The internal density of aggregates controls the growth timescale through the aggregate size a at $\Omega t_s = 1$. The upper panel of Figure 3 plots $a|_{\Omega t_s=1}$ for three different values of the aggregate internal density $\rho_{\rm int}$. If dust particles grew into compact spheres ($\rho_{\rm int} \sim 1$ g cm^{-3}), they would be inside the Epstein regime when $\Omega t_s = 1$ in almost entire parts of the snow region ($r > 3$AU). However, if dust particles grow into highly porous aggregates with $\rho_{\rm int} \sim 10^{-5}$ g cm^{-3}, the particles growing at $r < 30$ AU enter the Stokes regime before Ωt_s reaches unity. The lower panel of Figure 3 shows the two timescales $t_{\rm grow}|_{\Omega t_s=1}$ and $t_{\rm drift}|_{\Omega t_s=1}$ as calculated from Equations (4) and (5), respectively. We see that compact particles with $\rho_{\rm int} \sim 1$ g cm^{-3} do not satisfy the growth condition (Equation (6)) outside the snow line, while porous aggregates with $\rho_{\rm int} \sim 10^{-5}$ g cm^{-3} do in the region $r \lesssim 10$ AU. These explain our simulation results presented in Section 3.

5. Summary and Discussion

We have investigated how the porosity evolution of dust aggregates affects their collisional growth and radial inward drift. We have shown that icy aggregates can become highly porous even if collisional compression is taken into account. Our model calculation suggests that the internal density of icy aggregates at 5 AU falls off to 10^{-5} g cm^{-3} by the end of the initial fractal growth stage and then is kept to this level until the aggregates decouple from the gas motion. Stretching of merged aggregates at offset collisions, which is not taken into account in our porosity model, could further decrease the internal density (Wada et al. 2007; Paszun & Dominik 2009).

We have also found that the very high porosity triggers significant acceleration in collisional growth. This acceleration is a natural consequence of particles' aerodynamical property in the Stokes regime, i.e., at particle radii larger than the mean free path of the gas molecules. The porosity (or internal density) of an aggregate determines whether the aggregate reaches the Stokes regime before the radial drift stalls its growth. Compact aggregates tend to drift inward before experiencing the rapid growth, while highly porous aggregates are able to experience it over a wide range of orbital radii. Furthermore, the rapid growth has been found to enable the aggregates to overcome the radial drift barrier in inner regions of the disks. Our model calculation shows that the breakthrough of the radial drift barrier can occur in "planet-forming" regions, i.e., at distances less than 10 AU from the central star. The radial drift barrier has been commonly thought to be one of the most serious obstacles against planetesimal formation. Our result suggests that, if the fragmentation of icy aggregates is truly insignificant (as suggested by Wada et al. 2009), formation of icy planetesimals is possible via direct collisional growth of submicron-sized icy particles even without an enhancement of the initial dust-to-gas mass ratio.

The porosity evolution of dust aggregates can even influence the evolution of solid bodies after planetesimal formation. It is commonly believed that the formation of protoplanets begins with the runaway growth of a small number of planetesimals due to gravitational focusing. The runaway growth requires a sufficiently high gravitational escape velocity $v_{\rm esc} = \sqrt{2Gm/a}$ relative to the collision velocity. Since the escape velocity decreases with decreasing internal density ($v_{\rm esc} \propto m^{1/3}\rho_{\rm int}^{1/6}$), it is possible that a high porosity delays the onset of the runaway and thereby affects its outcome. For example, a recent protoplanet growth model including collisional fragmentation/erosion (Kobayashi et al. 2010) suggests that planetesimals need to have grown to $> 10^{21}$ g before the runaway growth begins in order to enable the formation of gas giant planets within the framework of the core accretion scenario. Compaction of large and massive aggregates may occur through static compression due to gas drag or self gravity. To precisely determine when it occurs is beyond the scope of this work, but it will be thus important to understand later stages of planetary system formation.

The authors thank Tilman Birnstiel, Frithjof Brauer, Chris Ormel, Taku Takeuchi, Takayuki Tanigawa, Fredrik Windmark, and Andras Zsom for fruitful discussions. S.O. also thanks Cornelis

Dullemond and Shu-ichiro Inutsuka for critical comments. S.O. acknowledges support by Grants-in-Aid for JSPS Fellows (22 · 7006) from MEXT of Japan.

REFERENCES

Adachi, I., Hayashi, C., & Nakazawa, K. 1976, Prog. Theor. Phys., 56, 1756

Blum, J., & Wurm, G. 2000, Icarus, 143, 138

Brauer, F., Dullemond, C. P., & Henning, Th. 2008a, A&A, 480, 859

Dominik, C., & Tielens, A. G. G. M. 1997, ApJ, 480, 647

Hayashi, C. 1981, Prog. Theor. Phys. Suppl., 70, 35

Kobayashi, H., Tanaka, H., Krivov, A. V., & Inaba, S. 2010, Icarus, 209, 836

Okuzumi, S., Tanaka, H., Kobayashi, H., & Wada, K. 2012, ApJ, submitted

Okuzumi, S., Tanaka, H., & Sakagami, M-a. 2009, ApJ, 707, 1247

Ormel, C. W., & Cuzzi, J. N. 2007, A&A, 466, 413

Paszun, D., & Dominik, C. 2009, A&A, 507, 1023

Suyama, T., Wada, K., & Tanaka, H. 2008, ApJ, 684, 1310

Suyama, T., Wada, K., & Tanaka, H. 2012, ApJ, submitted

Wada, K., Tanaka, H., Suyama, T., Kimura, H., & Yamamoto, T. 2007, ApJ, 661, 320

Wada, K., Tanaka, H., Suyama, T., Kimura, H., & Yamamoto, T. 2008, ApJ, 677, 1296

Wada, K., Tanaka, H., Suyama, T., Kimura, H., & Yamamoto, T. 2009, ApJ, 702, 1490

Weidenschilling, S. J. 1977, MNRAS, 180, 57

Whipple, F. L. 1972, in From Plasma to Planet, ed. A. Elvius (New York: Wiley Interscience), 211

Youdin, A. N., & Lithwick, Y. 2007, Icarus, 192, 588

Three-dimensional structure of Itokawa regolith particles.

Akira Tsuchiyama
Department of Earth and Space Science, Graduate School of Science, Osaka University
1-1 Machikaneyama-cho, Toyonaka, 560-0043, Japan

Particles of Asteroid Itokawa were successfully recovered by the Hayabusa mission of JAXA (Japan Aerospace Exploration Agency) [1-6]. They are not only the first samples recovered from an asteroid, but also the second extraterrestrial regolith to have been sampled, the first being the Moon, which was sampled by the Apollo and Luna missions [7]. It is accepted that most meteorites originate from asteroids, as demonstrated by orbital determination from observed meteorite falls. The materials on asteroids have been estimated by comparing reflectance spectra between asteroids and meteorites. Itokawa has an S-type spectrum, which is one of the major types and similar to those of ordinary chondrites. Remote-sensing observation by the Hayabusa spacecraft [8] indicate that the materials on asteroid Itokawa are similar to specific types of ordinary chondrites (LL5 or LL6 chondrites). However, there is a spectrum discrepancy between the asteroid and the meteorites, which has been considered to result from space weathering [9]. However, there is no direct evidence that the surface material of Itokawa is LL chondrites suffered with space weathering. Itokawa samples allow a direct validation of the relation between asteroids and meteorites. In addition, the properties of Itokawa particles allow studies of regolith formation and evolution.

About 2000 recovered particles (<~300 μm and most of them are <~10 μm) have been identified as having an Itokawa origin by curation at JAXA. About fifty particles were allocated for preliminary examination (PE) [1] and their results were published [1-6,10,11]. We examined three-dimensional (3D) structures of Itokawa particles using non-destructive x-ray micro-tomography as the first analysis in a sequential PE analytical flow [2]. The purposes are to understand their materials in comparison with meteorites and the 3D shape features in connection with regolith formation and evolution. The examination has additional technical purpose to provide information for the design of later destructive analyses. This is one of the key features of the Hayabusa PE strategy.

Forty particles (~30 to 180 μm) were imaged at BL47XU of SPring-8 with effective spatial resolution of ~200 or ~500 nm [2] using absorption imaging tomography [12,13]. Imaging at two X-ray energies of 7 and 8 keV made identification of minerals in CT images possible (Fig. 1) since the K-absorption edge of Fe (7.11 keV) is present between the two energies (Fig. 2) (analytical dual-energy micro-tomography [14]). The Fe/Mg ratios of olivine, low-Ca pyroxene and high-Ca pyroxene, and the Na/Ca ratio of plagioclase can be also obtained using this method. A successive set of 3D CT images, which shows quantitative 3D mineral distribution, was obtained for each particle.

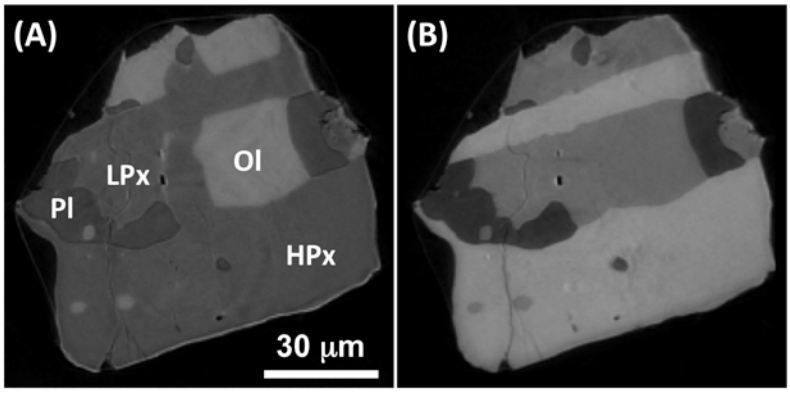

Figure 1. CT images of an Itokawa particle (RA-QD02-0024). (A) 7 keV. (B) 8 keV. Minerals can be identified by comparing their brightness at two energies, which corresponds to linear attenuation coefficients of minerals. Ol: olivine, LPx: low-Ca pyroxene, HPx: high-Ca pyroxene, and Pl: plagioclase.

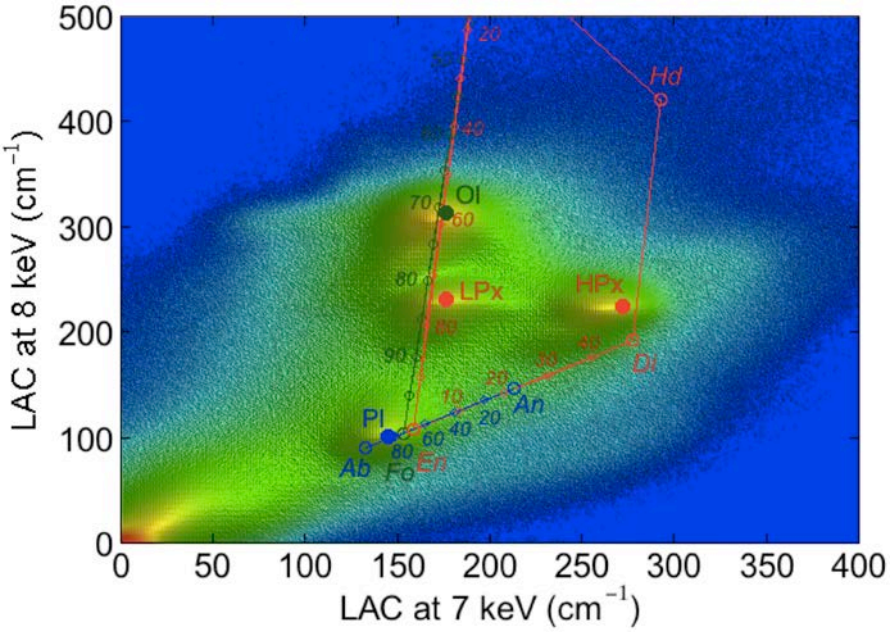

Figure 2. A two-dimensional histogram of linear attenuation coefficient (LAC) values at 7 and 8 keV for an Itokawa particle (RA-QD02-0024) (original figure in [3] was changed). Solid symbols correspond to the mean chemical compositions of the minerals in Hayabusa samples [1]. *Fo*: forsterite, *En*: enstatite, *Di*: diopside, *Ab*: albite, *An*: anorthite. The other abbreviations are the same as those in Figure 1. Numbers along olivine, pyroxene and plagioclase solid solutions are the forsterite, enstatite, wollastonite and albite contents (in mol.%).

The tomography gave the total volume of 4.2×10^6 μm^3, which corresponds to a sphere of ~200 μm in diameter (total mass of ~15 mg). The mineral assemblage and their abundances of the whole samples are similar to those of LL chondrites (Fig. 3). Slightly larger amount of olivine and smaller amounts of high-Ca pyroxene, troilite and (Fe,Ni) metal of the Itokawa particles can be regarded as statistical errors due to picking up the small sample amount [15]. Other PE data, such as the elemental and oxygen isotopic compositions of minerals [1,3,4], also indicate LL chondrites.

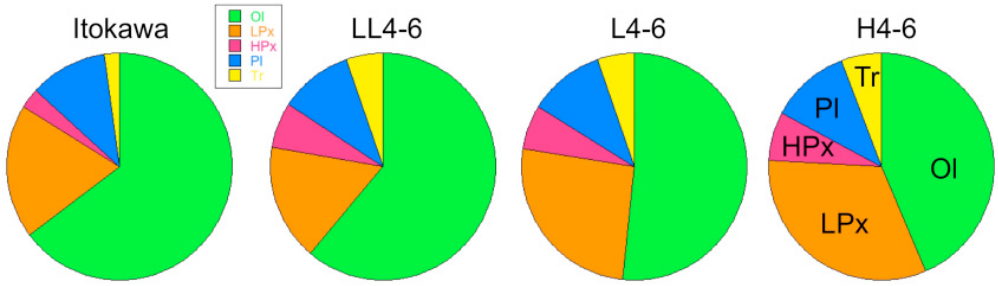

Figure 3. Modal mineral abundances (in vol.%) of the whole Itokawa particles and the averages of LL4-6, L4-6 and H4-6 chondrites. Tr: troilite. The other abbreviations are the same as those in Figure 1.

3D structures of the most particles have highly-equilibrated textures by thermal metamorphism (Figs. 4A-C), which correspond to the petrologic type of 5 and/or 6 in ordinary chondrites (LL5 and/or LL6), while some of them (~10%) have less-equilibrated textures (LL4) (Fig. 4D). SEM observation and compositional homogeneity of minerals show the same results [1]. Fe-rich nanoparticles observed in thin surface layers (<60 nm) of Itokawa particles show the evidence of space

weathering [5]. These results showed that the Itokawa surface material is consistent with LL chondrites suffered by space weathering as expected and brought an end to the origin of meteorites. In future detailed studies on 3D micro-textures of LL chondrites, including voids and micro-cracks, using the same resolution as the micro-tomography used in the PE of the Itokawa particles, should be made systematically to compare Itokawa samples with LL chondrites because Itokawa samples are so small that the textures cannot be compared with those of LL chondrites using conventional observations.

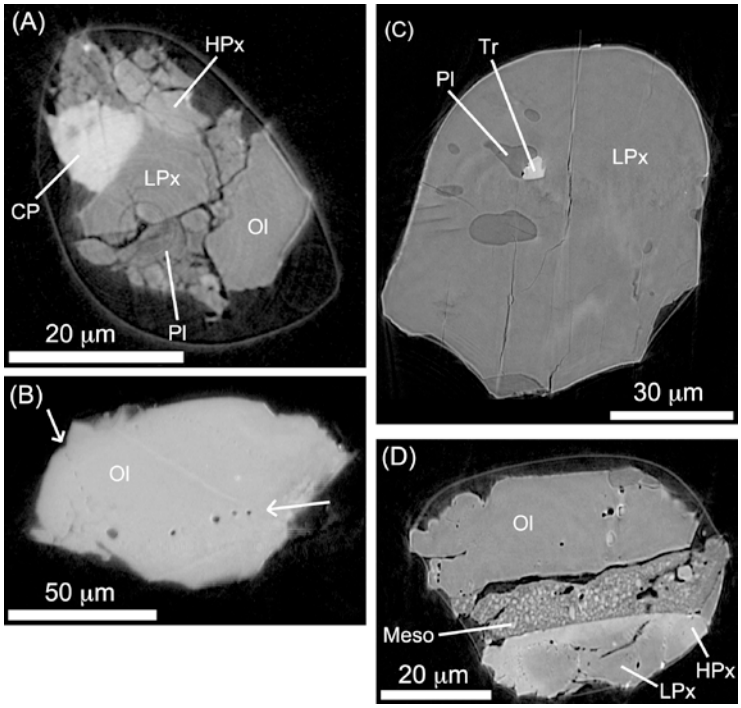

Figure 4. Representative CT images of Itokawa particles [2]. (A) Sample RA-QD02-0063. (B) RA-QD02-0014. (C) RA-QD02-0042. (D) RA-QD02-0048. Concentric structure is a ring artifact. Bright edges of particles and voids are artifacts resulting from refraction contrast. CP: Ca phosphate and Meso: mesostasis. The other abbreviations are the same as those in Figures 1 and 3.

External shapes of the Itokawa particles were extracted from the 3D CT images. Sphere-equivalent diameters and three-axial lengths of each particle were obtained from the shapes using image analysis [2]. Cumulative size distribution of the particles has the log-slope of ~-2. This is consistent with dominance of ~cm size regolith in the Itokawa smooth terrain, which was proposed by remote-sensing observation by the Hayabusa

spacecraft [16], by comparing with the size distribution of boulders (0.1-5 m) of the log-slope of ~-3 [17]. The 3D shape (three axial length ratios) distribution cannot be distinguished from that of fragments produced by impact experiments [18] (Fig. 5A), showing that the Itokawa particles are consistent with impact fragments. No particles showing melting were observed, indicating relatively low-impact velocities similar to typical relative impact velocities among asteroids (~5 km/s, in contrast to lunar regolith, where agglutinates formed by high-impact velocities of >~10 km/s [7]). Most of the particles have sharp edges (Fig. 6A), while some (~25%) have rounded edges (Fig. 6B). They were probably formed from particles that were originally more angular by abrasion as grains migrate during impacts (Fig. 7). The spherical shapes of lunar regolith particles (Fig. 5B) may be due to their longer residence time (~1 billion years) in the regolith than Itokawa regolith (<~3 million years [6]). Systematic studies on regolith shapes together with micro- and nano-structures of particle surfaces using FE/SEM and TEM and solar wind noble gas analysis will give comprehensive understanding of processes, which should be called "space weathering" in a broad sense, on celestial bodies without atmosphere not only of small steroids, such as Itokawa, but also of the Moon.

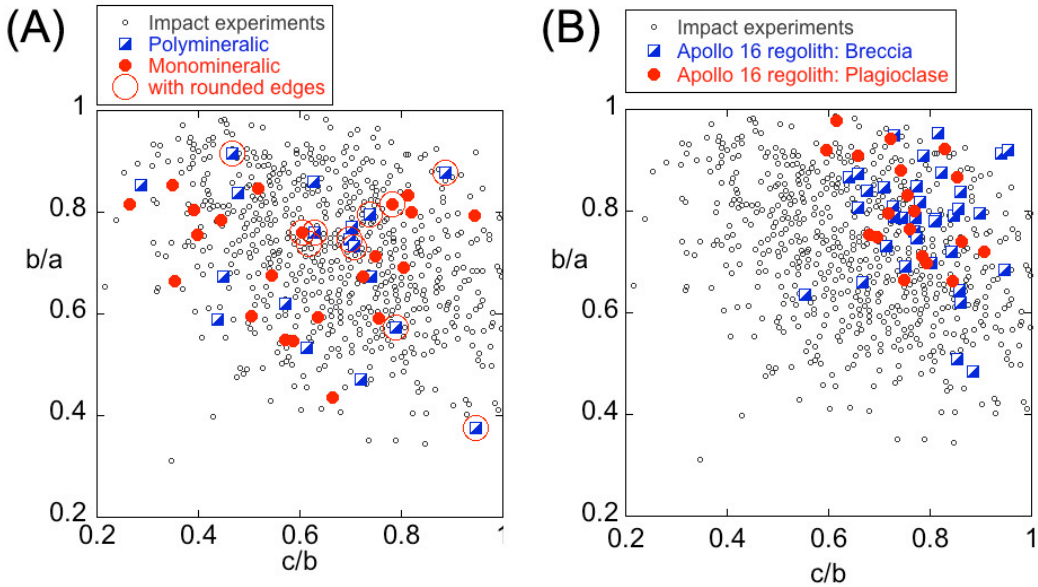

Figure 5. The 3D shape distributions of (A) Itokawa particles and (B) lunar regolith [2]. Fragments of impact experiments are also shown. Large circles in (A) show particles with rounded edges.

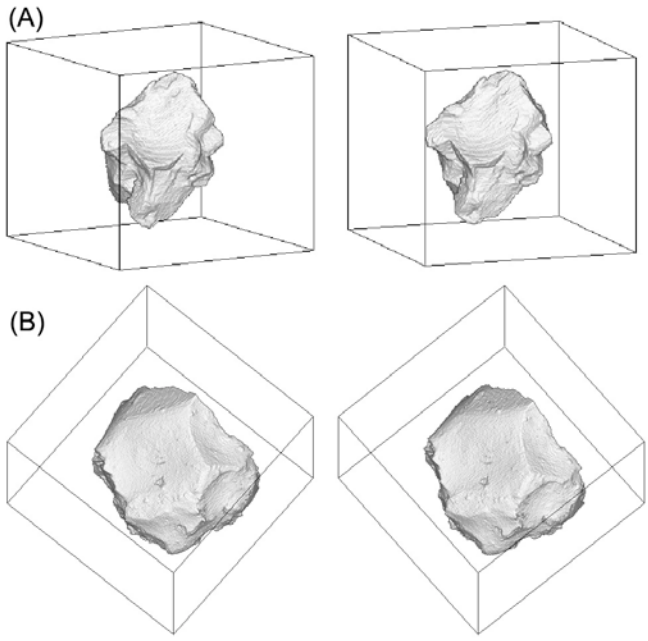

Figure 6. Stereograms showing the 3D external shapes of Itokawa particles of (A) RA-QD02-0023 (232 × 232 × 203 μm) and (B) RA-QD02-0042 (112 × 112 × 93 μm) [2].

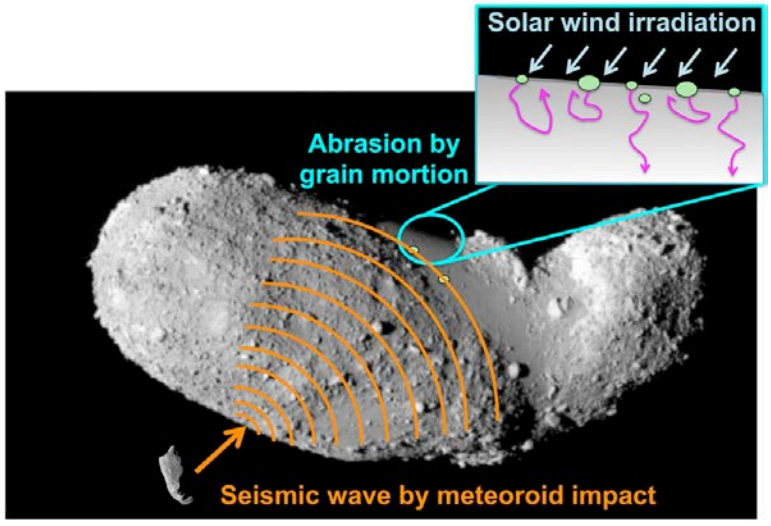

Figure 7. A schematic illustration of possible abrasion process of regolith particles on Itokawa by granular processes induced by seismic vibration due to impact of cm-size meteors.

Acknowledgement

The author is grateful to team members of the tomography, the PE, and the Hayabusa project.

References

[1] Nakamura, T. et al., 2011. *Science 333*, 1113-1116.

[2] Tsuchiyama, A. et al., 2011. *Science 333*, 1125-1128.

[3] Yurimoto H. et al., 2011. *Science* 333, 1116.

[4] Ebihara M. et al., 2011. *Science* 333, 1119.

[5] Noguchi T. et al., 2011. *Science* 333, 1121.

[6] Nagao K. et al., 2011. *Science* 333, 1128.

[7] G. H. Heiken et al., 1991. Eds., Lunar Sourcebook (Cambridge Univ. Press, Cambridge).

[8] Abe M. et al., 2006. *Science* 312, 1334.

[9] B. Hapke, 2001, *J. Geophys. Res.* 106, 10039.

[10] Naraoka H. et al., 2011. *Geochem. J.* in press.

[11] Kitajima F. et al., 2011. *Lunar Planet. Sci.* XLII, 1855. pdf. 28.

[12] K. Uesugi et al., 2006. *Proc. SPIE* 6318, 63181F.

[13] A. Takeuchi et al., 2009. *J. Phys. Conf.* Ser. 186, 012020.

[14] Tsuchiyama A. et al., submitted to *Geochim. Cosmochim. Acta*.

[15] Nagano, T. 2012. Abstract in Lunar and Planetary Science Conference, IVIII.

[16] H. Yano et al., 2006, *Science* 312, 1350.

[17] T. Michikami et al., 2008, *Earth Planets Space* 60, 13.

[18] F. Capaccioni et al., 1984, *Nature* 308, 832.

An synthesis experiment of GEMS analogue material produced by thermal plasma.

Junya Matsuno[1], Masahito Yagishita[2], Takayuki Watanabe[2], Akira Tsuchiyama[1]

[1)] Department of Earth and Space Science, Graduate School of Science, Osaka University

1-1 Machikaneyama, Toyonaka, Osaka 556-0043, Japan

[2)] Department of Environmental Chemistry and Engineering, Tokyo Institute of Technology

4259 G1-22, Nagatsuta, Yokohama, Kanagawa 226-8502, Japan

1. Introduction

Anhydrous IDPs (interplanetary dust particles), which is considered to have cometary origin, have a large amount of amorphous materials called GEMS (glass with embedded metal and sulfides). They are spherical materials of SiO_2-rich silicate glass typically a few 100 nm in diameter that include small (typically 10–50 nm in size) and rounded grains of Fe, Ni metal and sulfides. There are two origins proposed for GEMS: (1) an interstellar origin (Bradley & Dai 2004) and (2) the solar system. (2) they were formed in the solar nebula as non-equilibrium condensates from residual Si-rich gas after condensation of MgO-silicate crystals (Keller & Messenger 2011). It also supports their solar system origin that 94–99% of GEMS grains have oxygen isotopic compositions that are indistinguishable from terrestrial materials and carbonaceous chondrites.

Their origin and formation process is still controversial although there are a number of studies on GEMS in IDPs based on astronomical observations using IR spectrum (Bradley et al. 1999) and laboratory analyses, such as, microstructures, isotopic and elemental compositions) (e.g., Bradley & Dai 2004, Keller & Messenger 2011). It is important to reproduce GEMS-like materials in a laboratory to understand conditions for GEMS formation process. Especially, we focused on whether or not amorphous silicate spheres that contain nano-grains of metal can be formed by condensation from a Si-rich gas in this study.

2. Experimental method

Induction thermal plasma (ITP) method (Fig. 1) was used in the present experiments. ITP can provide ultra-high temperatures (~ 10,000 K) to evaporate a starting material immediately. Then, the gas is quenched rapidly with the cooling time scale of 10^4 – 10^5 K/s to form nanoparticles, which are usually in an amorphous state. Powders of regent-grade MgO, metallic Fe and SiO_2 were mixed together with the GEMS mean composition (Mg/Si = 0.65, Fe/Si = 0.56) for preparing the starting material, which is an analogue to Si-rich gas in the early solar system. Mg, Si, Fe and O were taken into consideration as major elements in solid materials in the solar system for simplicity. S was excluded because of the experimental difficulty.

The ITP experiments were made under an Ar-He atmosphere at 1 bar at Watanabe laboratory of Tokyo Institute of Technology (TP12010, JEOL). The mixed Ar and He gas is used as the sheath gas and the flow rate is 60 and 5 L/min, respectively. 6.5 L/min of Ar gas was used for carrier gas and 5 L/min of Ar was used for inner gas. The plasma power was 30 kW and current frequency was 4 MHz. It should be noted that the oxygen source came only from the starting material of MgO and SiO_2 (Yagishita et al. 2011).

Run products attached on the inner chamber walls of the furnace were collected and they were exposed to CuKα radiation (λ=1.54056 Å) using a powder X-ray diffraction system (XRD; Ultimate, Rigaku) at Tokyo Institute of Technology. High spatial resolution images were obtained by using a transmit electron microscope (TEM: JEM-2001, JEOL; JEM-2010F, JEOL) at Tokyo Institute of Technology with the accelerating voltage of 200 keV. TEM tomography was also applied to one sample (Fig. 3a). Some run products were embedded in an epoxy resin, and the cross section was observed using a field emission scanning electron microscope (FE-SEM: JSM-7001F, JEOL) at Osaka University. The chemical compositions were measured using energy-dispersive X-ray spectroscopy (EDS) equipped with the TEM (NORAN Instrument) or the FE-SEM (Inca, Oxford).

3. Results

The powder XRD pattern of the run product (Fig. 2) shows two sharp peaks at ~45° and ~65° with a broad halo peak around 27° in 2θ. The former peaks were identified as α-iron and the halo as an amorphous silicate. No crystalline silicates, such as forsterite, pyroxene and silica mineral, have been detected. Thus, amorphous silicate was formed directly from high-temperature gas by very rapid condensation and cooling. Bright field images of TEM (Figs. 3ab) show that the run product was composed of numerous spherical grains (typically ~50 nm in diameter). The TEM tomography suggests that each grain has an iron core (~20 nm in diameter) embedded in an amorphous silicate. Figure 4 shows size distributions of amorphous silicate grains of ≥ 30 nm in a diameter and metal grains of ≥ 10 nm in a diameter, respectively. Both size distributions are very broad and no clear peaks were seen. The bulk chemical composition of the run product was almost consistent with that of the starting material although the amount of MgO was slightly smaller than that of the starting material (Fig. 5).

4. Discussions

4.1 Formation process of the run product

The texture of the run product, where each metallic iron grain seems to be included always in each amorphous silicate sphere, strongly suggests that the iron grain condensed first from high-temperature gas by homogeneous nucleation, and a silicate melt (or the amorphous silicate) nucleates heterogeneously on the metal grin and covered the iron grain by growth. If the silicate melt condensed first, metallic iron should nucleate on the silicate melt, and then the silicate melt cover the metal.

The possibility of the heterogeneous nucleation can be checked by considering the surface tensions of metallic iron and amorphous silicate as shown in Figure 6. The surface tensions of iron, γ_i, and silicate melt with chondritic composition, γ_c, are estimated as 1.75 and 0.4 J/m^2, respectively (Table 1) (Dyson 1963; King 1951). However, the surface tension of a boundary between chondrule melt and iron, γ_b, was not known. Uesugi et al. (2008) estimated the g_b value of ~1.9 J/m^2 from chondrule textures in thin sections, where a small iron globule is attached onto the chondrule surface, by assuming the surface tension equilibrium. From these values, the total surface energies for the cases where the iron is totally embedded in the silicate, $E_{t,IN}$, and the iron and the silicate separated each other, $E_{t,OUT}$ (Fig. 6 and Table 1) by using the following equation,

$$E_{t,OUT} = 4\pi[\gamma_i {r_i}^2 + \gamma_s({r_s}^3 - {r_i}^3)^{2/3}] \quad (3.1)$$

$$E_{t,IN} = 4\pi(\gamma_b {r_i}^2 + \gamma_s {r_s}^2) \quad (3.2)$$

where, g_s is the surface energy of the silicate melt (or amorphous silicate),
r_i is the radius of the metal grain, and r_s is the radius of the silicate grain. The values of $E_{t,OUT}$ (2.1×10^{-14} J) is a little smaller than the value of $E_{t,IN}$ (2.2×10^{-14} J), if we take r_s = 50 nm and r_i = 20 nm and assume g_s=g_c (Table 1). $E_{t,IN} > E_{t,OUT}$ indicates that the heterogeneous nucleation of the silicate melt on the iron (or of the metal on the silicate melt) and covering the silicate melt on the iron are not possible. Strictly speaking, the values of surface tensions depend on chemical compositions and temperatures. Therefore this estimation should be reconsidered using the surface tensions of silicate melt and boundary of silicate melt and iron corresponding to the present chemical composition.

Another clue to understand the formation process of the run product is experiments using different metals other than iron in the same silicate. Different textures might form due to different condensation temperatures and different surface tensions of the metals. Additional experiments of the metal – silicate system is on going (Yagishita, private communication).

4.2 Grain formation condition: comparison with ITP and astronomical environments

It is most likely that GEMS grains formed by condensation from a high-temperature gas either in circumstellar regions of evolved stars or the protoplanetary disk of the solar system. Yamamoto & Hasegawa (1977) theoretically formulated homogeneous nucleation and growth of dust grains from a gas, and proposed a non-dimensional parameter for the condensation, Λ, by considering the concentration in a gas, $c_1(0)$, and cooling time scale of the gas, t_T (Table 2). The values of Λ are given for some astronomical environments, such as presolar nebula at 0.1 AU (~3×10^9) or around AGB stars (0.9~90)

(Table 2).

Parameters in the present ITP experiments are listed in Table 3. The value of τ_T was estimated to be $\sim 1\times10^{-1}$ sec based on a temperature profile in the ITP furnace and a flowing gas velocity obtained by a numerical calculation (Watanabe, private communication). Then, Λ in the present experiments was estimated to be $\sim 4\times10^{3}$ (Table 3). This value is not the same as but not extremely different from those in the astronomical environments.

Two dashed curves in Figure 4 show size distributions of the silicates and iron calculated by the condensation theory of Yamamoto & Hasegawa (1977) with the parameters in Table 3 and non-dimensional parameter for surface tension, μ (silicate ~20 and iron ~10). The calculated size distributions have sharp peaks at ~42 nm and ~65 nm for the silicate and the metal, respectively. The peak position of the silicate is roughly similar to that in the experiments, but that of the iron is large. As this grain formation theory was based on homogeneous nucleation, the calculated size distribution of the iron grain may indicate that the iron in run products did not form by homogeneous nucleation.

4.3 Application to GEMS formation

The textures of the run product are similar to that of GEMS although GEMS is composed of more than one metal grain. The GEMS texture can form by sintering a number of silicate spheres including a metal grain. Sintering experiments should be made and estimate temperature for the sintering. It should be noted that the present experiment does not contain sulfur although FeS grains are included as well as metal grains in GEMS. FeS grains are distributed in GEMS's rim, and FeS may form by reaction of iron with surrounding S-bearing gas in the primordial solar nebula (Keller & Messenger 2011).

Solar system origin of GEMS is proposed based on rare oxygen isotopic large anomalies of GEMS (Keller & Messenger 2011). However, if GEMS is a mixture of primary grains of a few tens nm in size, exchange of oxygen atoms between the primary grains and a surrounding gas, which contains large amounts of H_2O and CO molecules, might occur even at low temperatures, and the oxygen isotopic anomalies disappeared in most of GEMS. Therefore, the rare oxygen isotopic large anomalies of GEMS might not be evidence of the solar system origin. Primary grains of GEMS might originally form around evolved stars by condensation, was transferred to interstellar region, and irradiate by cosmic ray. Then, the primary grains were incorporated into the primordial solar nebula, suffered by oxygen isotope exchange with surrounding gas, and accumulated into GEMS, and finally some of iron grains near the GEMS surfaces were sulfidized. More experimental and theoretical work, such as sintering experiments and estimation of oxygen isotope exchange rate, are required to confirm the above GEMS formation model.

Acknowledgement

We thank Dr. D. Lu and Mr. N. Hatakeyama for the analysis by the transmission electron microscopy.

References

Bradley, J. P., et al. 1999, Science, 285, 1716
Bradley, J. P., & Dai, Z. 2004, ApJ, 617, 650
Dyson, B. F. 1963, Transact. Metallurgical Soc. of AIME, 277, 1098
Keller, L. P., & Messenger, S. 2011, Geochim. Cosmochim. Acta, 75, 5336
King, T. B. 1951, J. Soc. Glass Tech., 35, 241
Uesugi, M., Sekiya, M., & Nakamura, T. 2008, Meteo. & Planet. Sci., 43, 717
Yagishita, M., Choi, S., Watanabe, T., Matsuno. J., & Tsuchiyama, A. 2011, Plasma Conference 2011, 22P067-P (abstr.)
Yamamoto, T., & Hasegawa, H. 1977, Progress of Theoretical Phys., 58, 816

TABLE 1
Parameters for the estimation of surface energy

surface energy	symbol	[J/m^2]	references
iron	γ_i	1.75	Dyson 1963
chondrule	γ_c	0.4	King 1951
boundary	γ_b	1.9	sample 3 (Uesugi+ 2008)
grain radius		[nm]	
silicate	r_s	50	typical
iron	r_i	20	typical

TABLE 2
Λ parameters for astronomical environments and the ITP system

	$c_1(0)$ [cm^{-3}]	τ_T [sec]	Λ
novae	$5\times10^4 - 5\times10^6$	9×10^6	0.9 – 9
AGB stars	10^{11}	10^7	10^6
presolar nebula (at 0.1 AU)	7×10^{12}	3×10^8	3×10^9
this study (ITP)	2.1×10^{16}	0.12	4×10^3

TABLE 3

Parameters used for estimating Λ value in the ITP system

	Symbol	Dimension	Value
non dimensional parameter	Λ		4×10^3
timescale of saturation	τ_{sat}	sec	2.3×10^3
timescale of collision	τ_{coll}	sec	6.1×10^7
timescale of cooling	τ_T	sec	0.12
equiribulium temperature	T_e	K	1000
h: latent heat of silicate	h/kT_e-1	sec	50
mass of monomer	m	g	1.7×10^{-22}
radius of monomer	a_0	Å	2.3
initial monomer concentration	$c_1(0)$	$/m^3$	2.1×10^{22}
mean thrmal velocity	<v>	m/s	115
sticking probability	α_s		1
Boltzman cofficient	k	m^2 kg $/s^2$ /K	1.38×10^{-23}

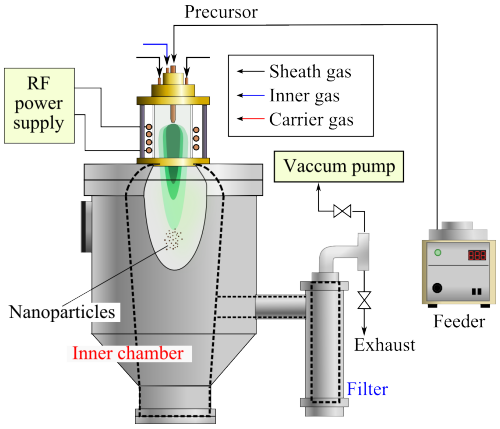

Fig. 1: Schematic illustration of the induction thermal plasma (ITP). The starting material was taken into the feeder and carried by Ar gas. Ar (60 L/min)-He (5 L/min) gas was used for sheath gas. 5 L/min of Ar gas was used for inner gas. Plasma torch was made at 1 bar. Radio frequency (RF; 4 MHz) of 33 kW was supplied. Run products adhering on the wall of the inner chamber were collected.

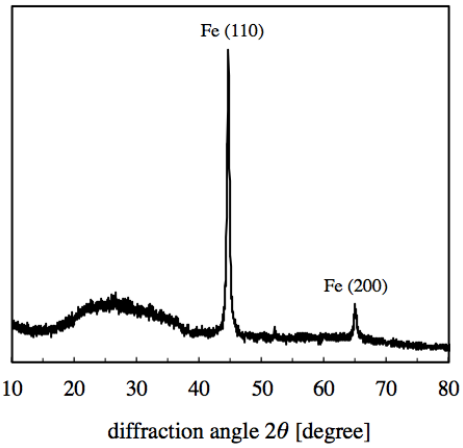

Fig. 2: A XRD pattern of the run product. They were exposed to CuKα radiation (λ=1.54056 Å). Two peaks were identified with α-iron and a halo was caused by amorphous silicate.

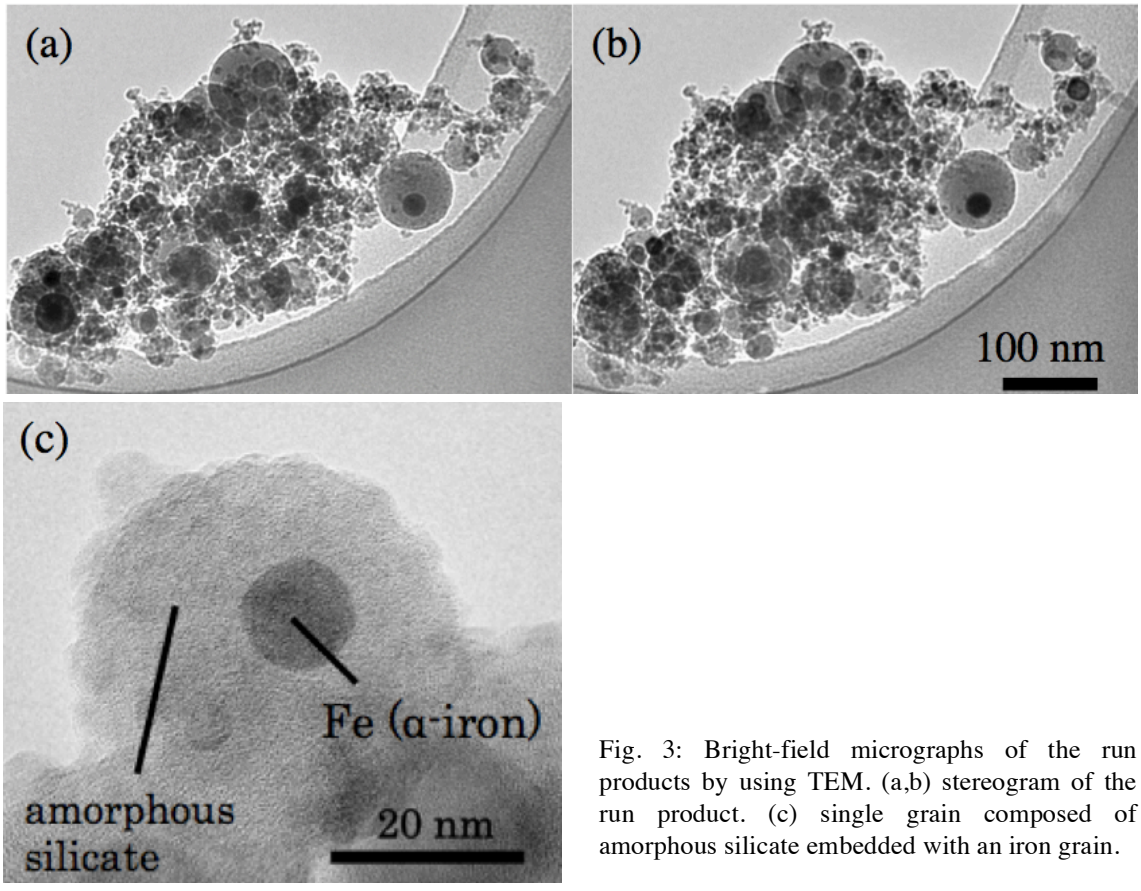

Fig. 3: Bright-field micrographs of the run products by using TEM. (a,b) stereogram of the run product. (c) single grain composed of amorphous silicate embedded with an iron grain.

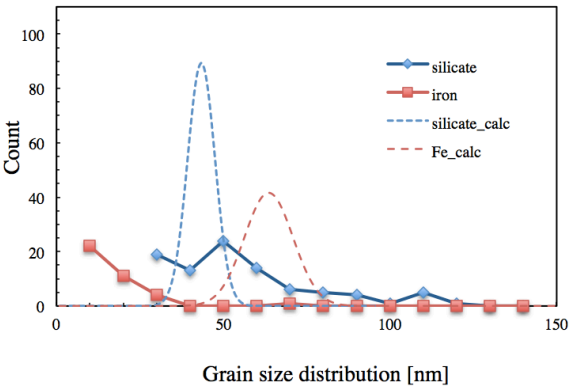

Fig. 4: Size distributions obtained by using a TEM image (solid lines; for ~100 grains ≥ 30 nm of silicate and ≥ 10 nm of iron) and calculated by Yamamoto and Hasegawa (1977) (dashed lines). No obvious peaks were observed in the run product however sharp peaks were shown in the calculation results.

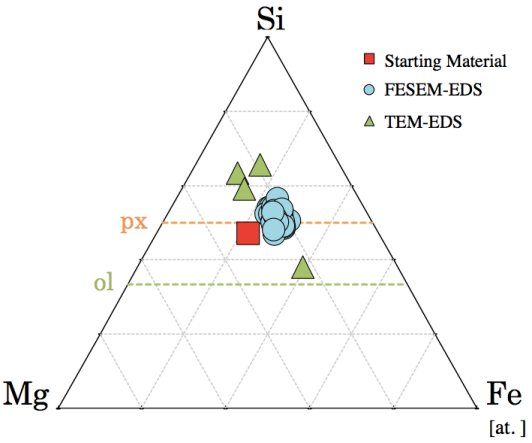

Fig. 5: Bulk and the individual chemical abundance of the run product plotted in Si-Mg-Fe ternary diagram obtained by using the EDS equipped with the FE-SEM and the TEM, respectively (atomic ratio). px: pyroxene, ol: olivine.

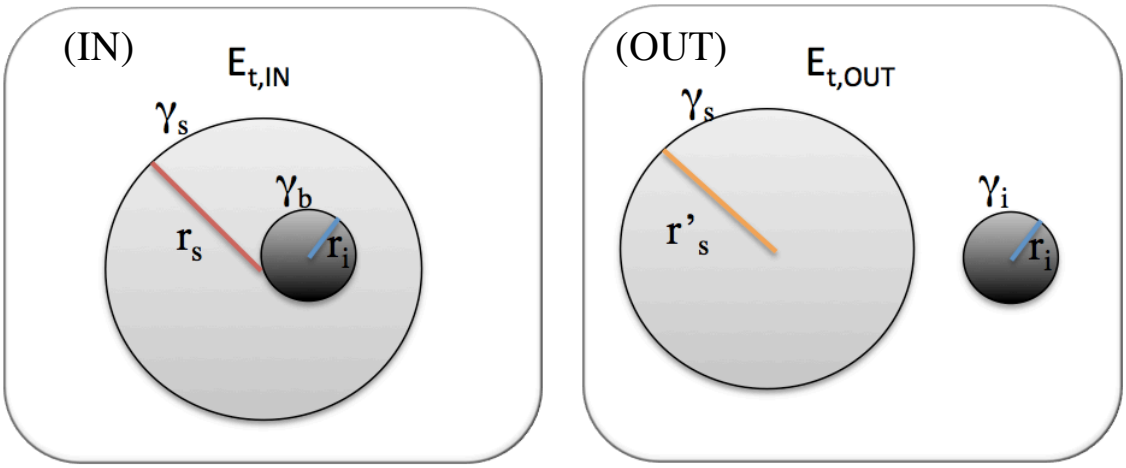

Fig. 6: Schematic drawing of the states of an iron grain and a silicate grain. (IN) a iron grain is inside a silicate grain. (OUT) a iron grain is outside a silicate grain. γ_s, γ_i, and γ_b are the surface energy of silicate, iron, and the boundary of the silicate and the iron, respectively. r_s, r'_s, and r_i are the radius of silicate for the "IN" state, silicate for the "OUT" state, and the iron, respectively. $E_{t,IN}$: total surface energy for the "IN" state, $E_{t,OUT}$: total surface energy for the "OUT" state.

Coulomb-Crystallization and Behavior of Fine Particles in Experimental Plasmas

Yasuaki HAYASHI

Department of Electronics and Information Science, Kyoto Institute of Technology, Matsugasaki, Sakyo-ku, Kyoto 606-8585, Japan

Because the behavior of fine particles in plasmas on the ground can be directly observed, the experimental results may more or less bring useful information to the study on grains in space, although conditions of plasmas are different to each other.

Mono-disperse spherical fine particles can form Coulomb crystal when they are included in great abundance in a glow-discharge plasma. Figure 1 shows a picture of a Coulomb crystal formed with spherical carbon fine-particles of 1.4 micron in diameter in methane plasma [1]. Such crystal-like arrangement of fine-particles is formed by the non-local coagulation force of positive ions surrounding negatively charged fine-particles. Because the theory of strongly-coupled plasma, which includes Coulomb crystal formation, depends on dimensionless parameters, it can be applied to a lot of phenomena related with fine-particles and plasma in space.

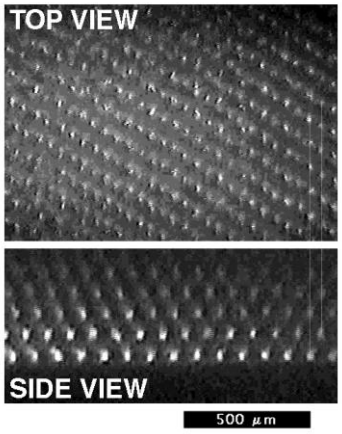

Fig.1 3-dimensional Coulomb crystal formed by fine-particle plasma [1].
The structure of the crystal is body-centered tetragonal.

Behaviors of individual fine particle in glow discharge plasmas have been investigated by the analyses of video images. We investigated the behavior of fine-particles in planar magnetron plasma. Figure 2 shows a top view of divinylbenzene fine-particles of 2.27 microns in diameter in helium plasma revolving to the direction of E×B drift [2]. Under a pressure of 100 Pa and a

discharge power of 2 W, fine particles were observed to revolve with the speed of 1.3 cm/s in the direction of E×B, forming particle strings in the vertical direction in the sheath. A velocity of revolution of a fine particle was calculated under the effects of drag force by E×B drift ions and friction force by neutral molecules to be 42 cm/s, which is around 30 times larger than the speed observed experimentally. The Hall parameter of ions is 0.02 under the conditions of the experiment. Thus, the revolution of fine-particles to the direction of E×B drift should be caused by the drag force of streams of slightly magnetized ions.

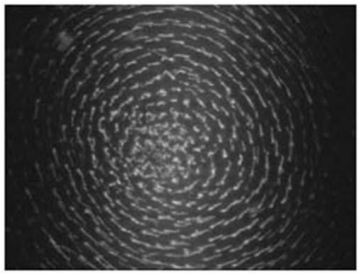

Fig.2 Top view of revolution of 6.5-micron fine particles by E×B drift in helium plasma under pressure of 100 Pa and RF power of 2 W [2]. Video frames were piled up for 0.1 second

Fine particles must have rotational angular momentum in plasma, which may more or less influence their behavior. However, the value of rotational angular momentum has not been evaluated. We evaluated the magnetic moment of a rotating fine particle by the analysis of video image. Disc-shaped fine-particles, of which the average diameter was 6 microns, were injected into an RF plasma of argon under a discharge power of 2 W and a pressure of 100 Pa. Polarized laser light of 532 nm in wavelength was irradiated. The scattered laser light from disc-shaped fine particles at a right angle was observed using a high-speed CCD video camera. The speed of rotation was determined from the period of intensity change of scattered light to be 0.03 sec/rotation as shown in Fig.3. When the particle is charged by -10,000 e and the electrons are distributed around the periphery of the disc-shaped fine particle, the magnetic moment is calculated to be 3×10^{-25} A・m^2.

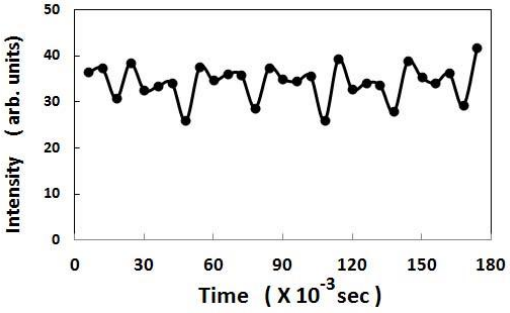

Fig.3 Change of intensity of light scattered from fine-particles.

[1] Y.Hayashi: Phys. Rev. Lett. **83**, 4764 (1999).
[2] Y. Hayashi, Y. Mizobata and K. Takahashi: J. Plasma Res. SERIES, **8,** 298 (2009).

NUMERICAL SIMULATIONS OF COLLISIONS OF DUST AGGREGATES COMPOSED OF PARTICLES WITH SIZE DISTRIBUTIONS

Koji Wada[1], Hidekazu Tanaka[2], Toru Suyama[3], Hiroshi Kimura[4], and Tetsuo Yamamoto[2,4]

Abstract: We carry out numerical simulations of collisions of dust aggregates composed of particles with size distributions to investigate the collisional growth condition of dust in protoplanetary disks. In this preliminary study we find that the particle size distributions tend to encourage dust growth, but we need to further study to confirm such a finding.

Introduction: In protoplanetary disks planetesimals are believed to be formed from dust aggregates consisting of submicron grains, but their growth process is unclear so far. One of the main problems in planetesimal formation is the feasibility of dust growth through collisions at velocities up to several tens of m/s [e.g., 1]. Recently we performed numerical simulations of dust aggregate collisions and found that dust aggregates can grow through high-velocity collisions even at 50 m/s if they consist of ice particles [2]. However, silicate dust aggregates are still difficult to grow through collisions since their critical collision velocity for collisional growth is only several m/s. We need to seek some kind of promising mechanism to enable silicate dust growth. One of factors we have not yet taken into account in our numerical simulation is the size distribution of monomer particles. According to a particle-interaction model, so-called JKR theory [3], the critical collision velocity for sticking of two monomers is proportional to $R^{-5/6}$ with R being their reduced radius, suggestive of an increase in the growth possibility of dust aggregates consisting of smaller particles. In fact, interstellar extinction observation suggests a power-law size distribution of interstellar dust grains with an exponent of -3.3 to -3.6 in a range of 0.025 – 0.25 micron radius [4]. Such a particle size distribution may contribute to enhancement of collisional growth of dust aggregates. On the other hand, energy to break up a pair of particles in contact is proportional to $R^{4/3}$. This means connections between small particles are weaker than those between large ones. In that sense, a power-law size distribution of constituent particles may have a negative effect for collisional dust growth. In this study, we carry out numerical simulations of aggregate collisions to investigate the influence of particle size distributions on the collisional growth of dust aggregates. Based on the numerical results, we will discuss the possibility of planetesimal formation through direct collisions of dust aggregates in protoplanetary disks. Preliminary results indicate that particle size distributions tend to encourage dust growth.

[1] Planetary Exploration Research Center, Chiba Institute of Technology (wada@perc.it-chiba.ac.jp)
[2] Institute of Low Temperature Science, Hokkaido Univerisity
[3] Nagano City Museum
[4] Center for Planetary Sciecne

Numerical model and settings: We performed 3D simulations of aggregate collisions by the use of the particle interaction model and the numerical code developed in the previous papers [2,5,6]. We directly calculate the motion of each particle, taking into account all mechanical interactions between particles in contact. The contact theory of adhesive elastic spheres determines the interactions for each degree of motion (normal motion, sliding, rolling, and twisting). Energy dissipates at the moments of contact and separation of particles because of the excitation of elastic waves. When the displacements due to sliding, rolling, and twisting exceed their elastic limits, the mechanical energy is also dissipated. The amount of energy dissipation is proportional to the critical displacements.

In this study, as a first step, we assume a power-law size distribution of constituent particles:

$$n(r)dr \propto r^{-3.5}dr,$$

where $n(r)dr$ is the number of particles in the range of radius r to $r+dr$. The power-law index of -3.5 is in accordance with the values obtained from interstellar dust observation [4]. Along with this size distribution, we prepare aggregates composed of particles with a bimodal distribution and a continuous distribution. For a bimodal distribution, we mix large particles of 0.1μm radius and small ones of 0.025 μm radius with a number ratio 1/32. Then we prepare two types of aggregates composed of 3300 particles (100 large particles and 3200 small ones) and 6600 particles (200 large and 6400 small) by means of random sticking of the particles one by one, namely ballistic particle-cluster aggregation (BPCA) process. Their masses are equivalent to 150 and 300 mu, respectively, where mu is the mass unit defined by the mass of 0.1μm-radius particle. On the other hand, for a continuous distribution, we set the largest radius of 0.2 μm and the smallest of 0.025 μm and determine particle radii along with the power-law distribution. Then, we prepare an aggregate composed of 6600 particles by means of BPCA process. This aggregate has an equivalent mass of 201.6 mu. As a result, we prepare three kinds of aggregates, two of which are shown in Figure 1. They are collided with the same type aggregates in the head-on direction and their numerical results are compared with our previous ones [2] obtained from collisions of aggregates composed of equal-sized particles of 0.1 μm radius. All particles in this study are assumed to be ice

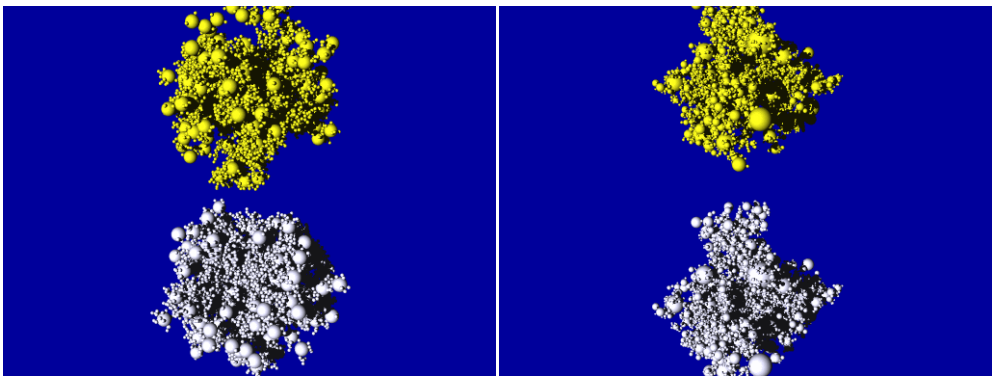

Figure 1: Examples of initial aggregates prepared in this study. Left panel shows aggregates composed of 200 particles of 0.1μm radius and 6400 particles of 0.025μm radius (bimodal distribution), while right panel shows aggregates composed of 6600 particles with a continuous power-law size distribution (the range of particle radius is 0.025 – 0.2 μm, and the power index is -3.5).

(Young's modulus 7 GPa; Poisson's ratio 0.25; material density 1000 kg/m^3; surface energy 100 mJ/m^2). Since we examine the growth possibility of dust aggregates at high-velocity collisions, we simulate aggregate collisions at collision velocities $u_{\rm coll}$ in the range of 20 – 700 m/s. We can estimate the results for silicate aggregates from those for ice by replacing $u_{\rm coll}$ by one order of magnitude lower value [2].

Results and discussion: Figure 2 shows some examples of snapshots of moderate- and high-velocity collisions of our prepared aggregates. Large parts of resultant aggregates are likely to survive even at high collision velocities $u_{\rm coll}$ ~ 50 and 200 m/s. Fragments produced at these collisions are composed of relatively large particles, a particular feature of aggregate collisions with particle size distributions.

To examine the collisional growth possibility of aggregates, we introduce the growth efficiency f defined by

$$f = \left(M_{\rm large} - M_{\rm init}\right)/M_{\rm init}\ ,$$

where $M_{\rm large}$ is the mass of the largest fragment at a collision and $M_{\rm init}$ is the mass of an initial aggregate. The growth efficiency counts how much mass, normalized by $M_{\rm init}$, are gained (or lost, if the value is negative) for an initial aggregate through a collision. Figure 3 shows f plotted as a function of $u_{\rm coll}$ for the three types of aggregates, together with the previous results [2] obtained from head-on collisions of BPCA clusters that are composed of ice particles with the same radius of 0.1μm and have equivalent masses of 500, 2000, or 8000 mu. First, compared with the previous BPCA clusters, the growth efficiency

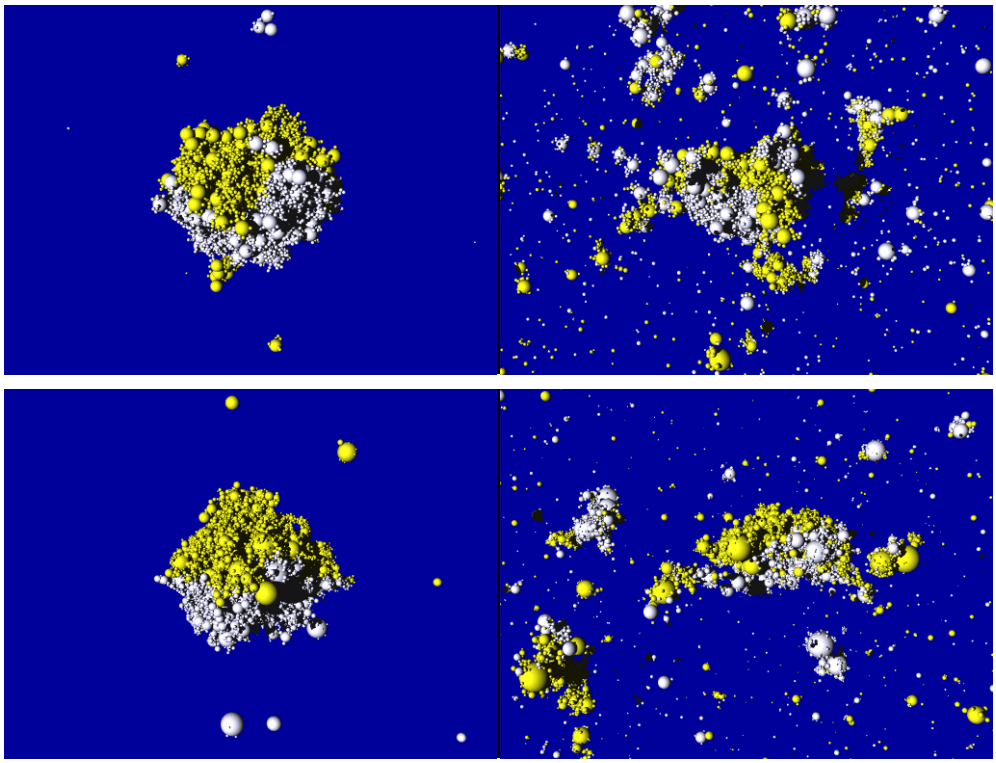

Figure 2: Snapshots of collided aggregates shown in Figure 1. Upper two panels are of the bimodal distribution at $u_{\rm coll}$ =55.3 m/s (left) and 180 m/s (right) and lower two are of the continuous distribution at $u_{\rm coll}$ = 49.3 m/s (left) and 197 m/s (right).

f for the aggregates with particle size distributions in this study becomes large for the same u_{coll} even though their small masses. This indicates that aggregates with particle size distributions tend to be hard for disruption and that small particles result in positively working for collisional growth of dust aggregates. On the other hand, we do not see significant difference in f between aggregates with the bimodal particle size distribution and the continuous one. In addition, f seems to be independent of the aggregate mass for the cases with particle size distributions, while aggregates composed of equal-sized particles have a mass-dependence in f. As a result, the critical collision velocity $u_{coll,crit}$, which is given by the collision velocity when f = 0, is found to be ~ 200 m/s for the ice aggregates with particle size distributions used in this study. Taking into account the difference in $u_{coll,crit}$ between ice and silicate aggregates, $u_{coll,crit}$ for silicate aggregates is estimated to be ~ 20 m/s. This critical collision velocity would be high enough to survive in optically thick and cold protoplanetary disks [7], but it should be cautioned that this result is obtained from head-on collisions: $u_{coll,crit}$ will be reduced if offset collisions are taken into account. We need to further study in a wide range of the aggregate mass, the particle size distribution, and the collision direction (impact parameter) to investigate whether or not particle size distributions enhance the collisional growth of dust aggregates.

Furthermore, the size distribution of fragments at collisional disruption of dust aggregates is expected

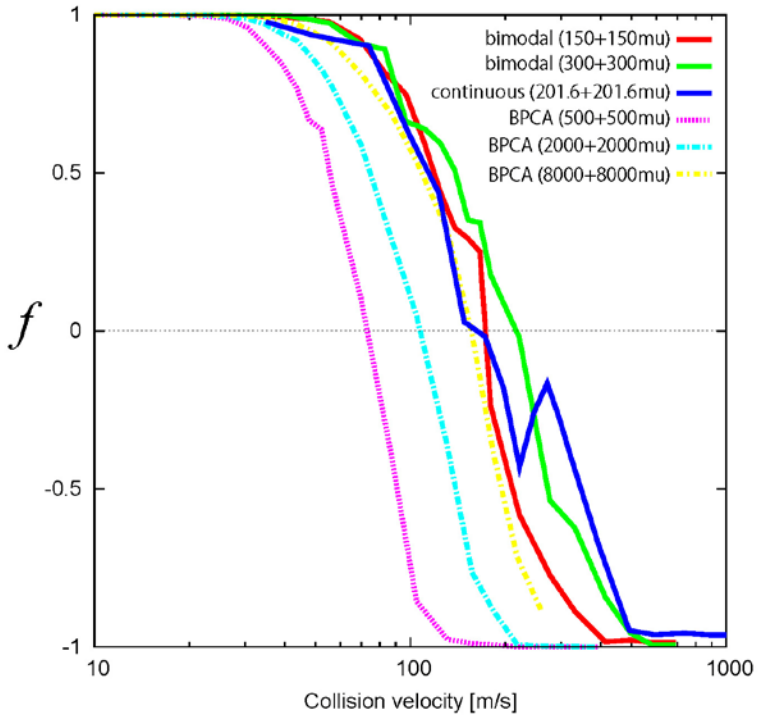

Figure 3: Growth efficiency f vs. collision velocity obtained from this study (for aggregates composed of particles with size distributions, represented by solid lines) and from the previous study (for aggregates composed of equal-sized particles, represented by dashed lines). Numbers in each parenthesis denote masses of colliding aggregates in mass unit (mu): for example, "150+150mu" means two aggregates of 150 mu collide with each other.

to be affected by the size distribution of constituent particles as can be seen in Figure 2. Since fragment size distribution is an important factor in observing protoplanetary or debris disks, we will investigate the fragment size distributions obtained from our simulations in the future.

References:

[1] Weidenschilling, S. J., & Cuzzi, J. N. (1993), in Protostars and Planets III, 1031.

[2] Wada, K., Tanaka, H., Suyama, T., Kimura, H., & Yamamoto, T. (2009), ApJ 702, 1490.

[3] Johnson, K. L. (1987), Contact Mechanics.

[4] Mathis, J. S., Rumpl, W., & Nordsieck, K. H. (1977), ApJ 217, 425.

[5] Wada, K., Tanaka, H., Suyama, T., Kimura, H., & Yamamoto, T. (2007), ApJ 661, 320.

[6] Wada, K., Tanaka, H., Suyama, T., Kimura, H., & Yamamoto, T. (2008), ApJ 677, 1296.

[7] Kusaka, T., Nakano, T., & Hayashi, C. (1970), Prog. Theor. Phys. 44, 1580.

Ionization Degrees with Dust Grains in Circumplanetary Disks

Yuri I. Fujii[1], **Satoshi Okuzumi**[1], **and Shu-ichiro Inutsuka**[1]

[1]Department of Physics, Nagoya University, Furo-cho, Chikusa-ku, Nagoya, Aichi 464-8602, Japan

E-mail: yuri.f@nagoya-u.jp

Abstract. During the formation of gas giants, disks appear around them. They are called circumplanetary disks. The most promising mechanism of accretion is the turbulence driven by magnetorotational instability (MRI). MRI occurs when the ionization degree is high enough for magnetic fields to couple to gas. We calculate the ionization degrees to investigate if MRI really causes accretion of circumplanetary disks. Our result suggests that the ionization degree in circumplanetary disks is too low for MRI to be active.

1. Introduction

There are only a few studies on the ionization degrees in circumplanetary disks, although a number of papers concerning ionization degrees in protoplanetary disks have appeared in the literature [1] [2] [3]. However, it is important to understand the structure and evolution of circumplanetary disks, because they are thought to be the sites of satellites formation.

The magnetohydrodynamic (MHD) turbulence driven by the magnetorotational instability (MRI) is, at the present, thought to be the most promising mechanism for angular momentum transport in protoplanetary disks. However, we are not sure if the MRI also plays a central role in accretion in circumplanetary disks. In order to understand disk evolution, we must clarify which part of the disk is magnetorotationally unstable.

In this work, we develop a fast and accurate time-dependent calculation method for the ionization degree in protoplanetary and circumplanetary disks. Using our calculations of ionization degree, we estimate the size of the MRI-inactive region. We find that almost all regions in popular model of circumplanetary disks are MRI-inactive.

2. Developing the calculation method

2.1. Reaction Equations

Gas in protoplanetary and circumplanetary disks is mostly in the form of neutral hydrogen molecules. However, they are thought to be weakly ionized by ionization sources such as cosmic rays, X-rays, and ultraviolet radiation. The resultant ionized particles make secondary ions and molecules, which lead to further complex reactions.

The ionization degree is determined by the balance of chemical reactions, such as ionization, charge transfer, and dissociative and radiative recombination. Since molecular ions transfer their charge to metal ions rapidly, we need not pay much attention to reactions of molecular ions in the dense gas. We describe major heavy metal ions (e.g. Mg^+, Fe^+) as M^+ for simplicity [4].

The effect of dust grains should also be considered. Ions and free electrons are captured by dust grains, lowering the ionization degree. With sufficient amount of dust, the ionization degree is determined mainly by the electron capture rate of dust grains. We show simplified reaction equations as follows:

$$\frac{dn_{\mathrm{M}^+}}{dt} = \zeta n_{\mathrm{n}} \quad {}_{\mathrm{M}^+} n_{\mathrm{M}^+} n_{\mathrm{e}} \quad \sum_Z k_{\mathrm{M}^+\mathrm{d}}(Z) n_{\mathrm{d}}(Z) n_{\mathrm{M}^+}, \tag{1}$$

$$\frac{dn_{\mathrm{e}}}{dt} = \zeta n_{\mathrm{n}} \quad {}_{\mathrm{M}^+} n_{\mathrm{M}^+} n_{\mathrm{e}} \quad \sum_Z k_{\mathrm{ed}}(Z) n_{\mathrm{d}}(Z) n_{\mathrm{e}}, \tag{2}$$

$$\begin{aligned} \frac{dn_{\mathrm{d}}(Z)}{dt} &= k_{\mathrm{M}^+\mathrm{d}}(Z) n_{\mathrm{d}}(Z) n_{\mathrm{M}^+} \quad k_{\mathrm{ed}}(Z) n_{\mathrm{d}}(Z) n_{\mathrm{e}} \\ &\quad + k_{\mathrm{M}^+\mathrm{d}}(Z \quad 1) n_{\mathrm{d}}(Z \quad 1) n_{\mathrm{M}^+} + k_{\mathrm{ed}}(Z+1) n_{\mathrm{d}}(Z+1) n_{\mathrm{e}}, \end{aligned} \tag{3}$$

where n_{j} is the number density of each particle ($\mathrm{j} = \mathrm{M}^+$: heavy metal ions, e : electrons, d : dust grains), Z is the charge of dust grains, ζ is the ionization rate, and ${}_{\mathrm{M}^+}$ and $k_{\mathrm{jd}}(Z)$ are the rate coefficients for radiative recombination and capture of gaseous particles by dust grains, respectively.

Numerical calculation of Equations (1) (3) is not an easy task. As the maximum value of $|Z|$ becomes greater, the number of terms and equations increases, and the system of equations becomes more complicated.

2.2. Charge distribution model of dust grains

Since the charge distribution of dust grains can be approximated by a Gaussian distribution [1], we adopt the following equation for use in Equations (1) (3).

$$n_{\mathrm{d}}(Z) = \frac{N_{\mathrm{d}}}{\sqrt{2 \ \langle \delta Z^2 \rangle}} \exp\left[\ \frac{(Z \quad \langle Z \rangle)^2}{2\langle \delta Z^2 \rangle} \right], \tag{4}$$

where $\langle \ \rangle$ shows the averaged value weighed by $n_{\mathrm{d}}(Z)$, and N_{d} is the total number density of dust grains. We can get the following equations by taking the average of the last term of Equations (1) and (2), and the first and second moments of Equation (3):

$$\frac{dn_{\mathrm{M}^+}}{dt} = \zeta n_{\mathrm{n}} \quad {}_{\mathrm{M}^+} n_{\mathrm{M}^+} n_{\mathrm{e}} \quad \langle k_{\mathrm{M}^+\mathrm{d}} \rangle N_{\mathrm{d}} n_{\mathrm{M}^+}, \tag{5}$$

$$\frac{dn_{\mathrm{e}}}{dt} = \zeta n_{\mathrm{n}} \quad {}_{\mathrm{M}^+} n_{\mathrm{M}^+} n_{\mathrm{e}} \quad \langle k_{\mathrm{ed}} \rangle N_{\mathrm{d}} n_{\mathrm{e}}, \tag{6}$$

$$\frac{d\langle Z \rangle}{dt} = \langle k_{\mathrm{M}^+\mathrm{d}} \rangle n_{\mathrm{M}^+} \quad \langle k_{\mathrm{ed}} \rangle n_{\mathrm{e}}, \tag{7}$$

$$\begin{aligned} \frac{d\langle \delta Z^2 \rangle}{dt} &= \left(\langle k_{\mathrm{M}^+\mathrm{d}} \rangle + 2\langle k_{\mathrm{M}^+\mathrm{d}} \delta Z \rangle \right) n_{\mathrm{M}^+} \\ &\quad + \left(\langle k_{\mathrm{ed}} \rangle \quad 2\langle k_{\mathrm{ed}} \delta Z \rangle \right) n_{\mathrm{e}}. \end{aligned} \tag{8}$$

The details of our calculations are described in our paper [5]. We have confirmed that the results of our equations agree with those of the basic equations very well.

3. Ionization Degrees in Circumplanetary Disks

In the context of satellite formation, understanding the evolution of circumplanetary disks is important. Since the ionization degree is one of the important factors in disk evolution, we calculate the ionization degree in circumplanetary disks including the charged particle capture by dust grains.

We use an actively supplied gaseous accretion disk model [6] [7]. The temperature is

$$T_{\rm cir} \simeq 160 \quad \frac{M_{\rm p}}{M_{\rm J}} \quad ^{1/2} \quad \frac{r}{20R_{\rm J}} \quad ^{-3/4} \ {\rm K}, \tag{9}$$

where $M_{\rm p}$ is the mass of the central planet, $M_{\rm J}$ is that of Jupiter, r is the orbital radius from the central planet, and $R_{\rm J}$ is the radius of Jupiter. For this model, we adopt 5 10^6 yr as the accretion timescale for gaseous disks as heavy as the central planet, and assume the disk is vertically isothermal. The surface density is given as follows with viscosity coefficient $= 5$ 10^{-3}:

$$\Sigma_{\rm cir} \simeq 100 \quad \frac{M_{\rm p}}{M_{\rm J}} \quad \frac{r}{20R_{\rm J}} \quad ^{-3/4} \ {\rm g\ cm^{-2}}. \tag{10}$$

We assume $M_{\rm p} = M_{\rm J}$. Since circumplanetary disks are located at the orbital radius of gas giant planet which is distant from the star, stellar X-rays are geometrically attenuated there. Furthermore, the scale height of circumplanetary disks is far smaller than that of protoplanetary disks. So, it is difficult for the X-rays to directly reach circumplanetary disks. When we think about circumplanetary disks, we consider only cosmic ray ionization. The ionization rate is written as follows:

$$\zeta \simeq \frac{\zeta_{\rm CR}}{2} \exp \frac{\chi(r,z)}{\chi_{\rm CR}} + \exp \frac{\Sigma(r) \quad \chi(r,z)}{\chi_{\rm CR}} , \tag{11}$$

where $\zeta_{\rm CR}$ 1.0 10^{-17} s^{-1} is the ionization rate by cosmic rays in interstellar space, and $\chi_{\rm CR}$ 96 g cm^{-2} is the attenuation length of the ionization rate by cosmic rays. The vertical column density of the gas measured from the outside of the disk is the following [8]:

$$\chi(r,z) = \int_z^\infty \ (r,z)dz \ \ [{\rm g\ cm^{-2}}]. \tag{12}$$

In this study, we investigate the extent of the MRI-inactive regions in the circumplanetary disks. We parameterize the vertical component of plasma beta (at the mid-plane), the ratio of gas pressure and magnetic pressure, $\beta = P_{\rm gas}/P_{\rm mag}$, the radius of dust grains a, and the dust-to-gas mass ratio $f_{\rm dg} =$ d/ g. We define the magnetic Reynolds number $Re_{\rm m}$ as the following:

$$Re_{\rm m} = \frac{v_{\rm Az}^2}{\eta \ {\rm K}}, \tag{13}$$

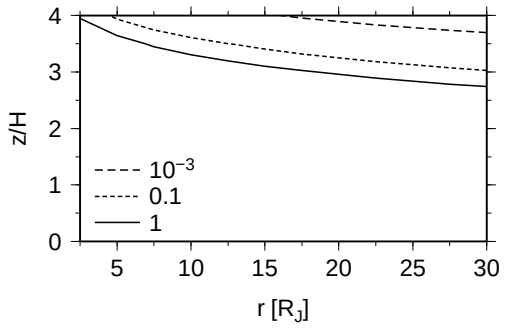

Figure 1. Boundaries of the MRI-inactive region in circumplanetary disks for the case $\beta = 10^4$ and $f_{\rm dg} = 10^{-2}$. The horizontal axis denotes the orbital radius from the central planet, and the vertical axis is vertical extent of the disk that is normalized by the scale height of the corresponding radius. Contour lines show the boundaries of the MRI-active region and the MRI-inactive region for each model of dust grain radius a The circumplanetary disks are not expected to be magnetically active.

where $v_{\rm Az}$ is the vertical component of the Alfvén velocity. If $Re_{\rm m} < 1$, MRI does not happen. Figure 1 shows an example of the extent of the MRI-inactive regions.

For a wide range of model parameters, we find that $Re_{\rm m}$ falls below unity in the entire parts of the circumplanetary disks. Our results suggest that the ionization degree of circumplanetary disks is too low for MRI to be active.

References

[1] Okuzumi, S. 2009, *Astrophys. J.*, 698, 1122
[2] Sano, T., Miyama, S. M., Umebayashi, T., & Nakano, T., 2000, *Astrophys. J.*, 543, 486
[3] Ilgner, M., & Nelson, R. P., 2006, *A & A*, 445, 205
[4] Oppenheimer, M., & Dalgarno, A., 1974, *Astrophys. J.*, 192, 29
[5] Fujii, Y. I., Okuzumi, S. & Inutsuka, S., 2011, *Astrophys. J.*, 743, 53
[6] Canup, R. M., & Ward, W. R., 2002, *Astron. J.*, 124, 3404
[7] Sasaki, T., Stewart, G. R., & Ida, S., 2010 *Astrophys. J.*, 714, 1052
[8] Umebayashi, T., & Nakano, T., 1981, PASJ, 33, 617

Hydrogen ordering in ice observed from neutron diffraction: Application to planetary science

Masashi Arakawa
Department of Chemistry, Faculty of Sciences, Kyushu University

Laboratory experiments and infrared observations suggest that a lot of water ice exists in a crystalline phase in our solar system. At ambient pressure, crystalline ice has two kinds of structure, ice Ih and ice XI. Ice Ih is normal ice with disordered hydrogen atoms. In contrast, ice XI is a hydrogen-ordered phase of ice Ih, and the ordered arrangement of hydrogen atoms makes ice XI ferroelectric. Existence of hydrogen-ordered ice in space is the subject of continuing astronomical debate. Electrostatic forces, caused by the ferroelectricity, increase the sticking probability of icy grains, and might play an important role in grain evolution and planetary formation in space.

To discuss the existence of hydrogen-ordered ice in space, we need to investigate the kinetics and formation process of ice XI. For precise understanding of nucleation and growth process of ice XI, we performed neutron diffraction measurements of ice doped with various kinds of dopant as a catalyst for the transformation to ice XI. The neutron diffraction measurements were performed at the high-resolution powder diffractometer (HRPD), and the wide-angle neutron diffractometer (WAND). The HRPD is installed in the research reactor, JRR-3, JAEA, Japan. The WAND is installed in the research reactor, High Flux Isotope Reactor, ORNL, USA. All the neutron diffraction measurements were performed on 99.95% deuterium-substituted ice. Rietveld analysis was carried out for all the diffraction profiles to obtain arrangement of hydrogen (structure parameter). We used a two-phase model, which include ice Ih and XI, and obtained mass fraction of ice XI (f).

Neutron powder diffraction of 0.013 M KOD-doped D_2O ice at HRPD. The doped ice Ih transformed to ice XI after annealing at 57 and subsequently at 68 K. The f value of the doped ice, which had once experienced being ice XI (f = 0.23), was larger than that of the doped ice, which had never experienced being ice XI (f = 0.14). Results indicate that small hydrogen-ordered domains remained in the ice Ih, which had once transformed to ice XI, and accelerated the phase transition from ice Ih to ice XI.

To understand this phenomenon in detail, we performed time-resolved neutron diffraction measurements on 0.1 M NaOD-doped ices, and investigated whether formation of ice XI occurs at temperatures above 65 K, which is out of the nucleation temperatures. Formation of ice XI occurred at 70 and 72 K when the ice had experience being ice XI in the past. This result suggests the presence of a template acting as the nuclei of ice XI. Thus, small domains with ordered hydrogen, which cannot be detected with neutron diffraction, can exist above the boundary temperature between ice Ih and XI. The small ordered-domain is called “memory” of hydrogen ordered structure because of the residual structure of ice XI. In the previous studies, ferroelectric hydrogen-ordered ice is considered to exist in the very narrow temperature range, but our experiments show a possibility that the hydrogen ordered ice exists in wider area in space.

In this presentation, we also discussed hydrogen ordering in ice at high pressure using neutron diffraction experiments. Our results indicate that hydrogen-ordered structure of high-pressure ice VI is ferroelectric. Hydrogen-ordered ferroelectric ices might exist not only in icy grains and icy bodies’ surface, but also in icy bodies’ interior.

Proceeding of the 29th Grain Formation Workshop in CPS center (2011/11/9-11)

Evaporation of Icy Planetesimals due to Planetesimal Bow Shocks in a Protoplanetary Disk

Kyoko K. Tanaka[1], Tetsuo Yamamoto[1], Hitoshi Miura[2], Makiko Nagasawa[3], Taishi Nakamoto[3], and Hidekazu Tanaka[1]

[1]*Institute of Low Temperature Science, Hokkaido University, Sapporo 060-0819, Japan*

[2] *Department of Earth Sciences, Tohoku University, Sendai 980-8578, Japan*

[3]*Earth and Planetary Sciences, Tokyo Institute of Technology, Tokyo 152-8551, Japan*

In a protoplanetary disk, planetesimals grow to planets by mutual collisions and accumulations. The gravitational interactions among the planetesimals increase eccentricities of the planetesimal orbits. When a relative velocity between the disk gas and planetesimal exceeds a sound velocity of the gas, a bow shock wave is produced on the leading side of the planetesimal.

It has been shown that heating by the planetesimal bow shocks in the nebular gas played a key role in formation of particles found in meteorites and interplanetary dust. For instance, the shock heating leads to formation of chondrules, millimeter-scale igneous silicate spheres in chondrites, by melting dust in the protoplanetary disk (Hood 1998; Weidenschlling et al. 1998; Ciesla et al. 2004; Hood et al. 2009). Furthermore, it makes a part of fine dust particles evaporate (Miura and Nakamoto 2002, 2005, 2006) and re-condesation of evaporated vapor forms a lot of small dust. Miura et al. (2010) showed that it is possible by a planetesimal bow shock to form various types of cosmic crystals, which are fine silicate crystals observed in chondritic meteorites and interplanetary dust particles (IDPs).

So far, the attention has mainly been paid on thermal evolutions of dust particles in the shocked region in the previous studies. However, we note a possibility that the planetesimal bow shock leads to heating and evaporation of the planetesimal itself. A similar process is found in ablation of the planetesimals penetrating through the atmosphere of a protoplanet (e.g., Podolak et al. 1988; Pollack et al. 1986). Heating and resultant evaporation by the planetesimal bow shocks will suppress growth of planetesimals. Furthermore, cooling of the vapors thus produced will form small dust particles by re-condensation. Those dust clouds in the disk may be found in the infrared spectra of the protoplanetary disks.

In the present study, we focus on the planetesimal heating and evaporation by the planetesimal bow shocks. Figure 1 shows an illustration of the planetesimal evaporation by the bow shock wave. When the planetesimal velocity relative to the disk gas becomes supersonic, a bow shock forms in front of the planetesimal. Due to the shock wave, the gas is heated at the shock front. The gas

blows onto the planetesimal surface. The surface material of the planetesimal heats due to the heat transfer from the gas. The surface material evaporates when the temperature rises over the evaporation temperature. The evaporated vapor re-condenses and forms small dust particles. As a result of the evaporation, the planetesimal is shrinking.

We evaluated the surface temperature and evaporation rate of the planetesimal using a simple model of planetesimal evaporation by the planetesimal bow shock. The time evolution of the planetesimal mass m is given by

$$\frac{dm}{dt} = J, \tag{1}$$

where J is the evaporation rate of a planetesimal. In our model, the rate of heat transfer from the gas to the planetesimal surface is given by

$$F_{\rm e} = \alpha \rho_0 v_{\rm p} c_{\rm p} (T_{\rm s} - T_{\rm p}), \tag{2}$$

where $T_{\rm s}$ is the gaseous temperature of the post shock region, $T_{\rm p}$ is the surface temperature of the planetesimal at the stagnation, ρ_0 and $c_{\rm p}$ are the density and specific heat at constant pressure of ambient gas, and $v_{\rm p}$ is the relative velocity between the ambient gas and the planetesimal. Also α is a non-dimensional parameter, referred to as the Stanton number, expressing the efficiency of the thermal conductivity (van Driest 1958; Schlichting 1979).

We show one typical example of the calculations in Figure 2 which shows the surface temperature of the planetesimal at the stagnation point $T_{\rm p}$, the gaseous temperature of the post shock region $T_{\rm s}$, and the ambient radiation temperature $T_{\rm disk}(= 75K)$. In Figure 2, we set $\alpha = 0.1$ and 0.01. As shown in Figure 2, the temperature of the planetesimal begins to increase when the relative velocity $v_{\rm p}$ exceeds $0.6{\rm kms}^{-1}$ which is the sound velocity of the gas. Although the temperatures of both $T_{\rm s}$ and $T_{\rm p}$ increase with increasing of $v_{\rm p}$, the elevation of $T_{\rm p}$ is suppressed in the vicinity of 200K for $v_{\rm p} \gtrsim 5{\rm kms}^{-1}$ because of the cooling by latent heat release.

We applied the model of the planetesimal evaporation to the formation stage of protoplanets. According to the theory of formation of planets, the terrestrial planets and cores of the gas giant planets are formed through the accretion of planetesimals (e.g. Hayashi et al. 1985). According to the standard scenario (Wetherill and Stewart 1989), growth of a planet pass through a so-called runaway growth stage. In this stage, the large planetesimals grow faster than small ones; the rate of mass growth of each object is an increasing function of its own mass. As a result, the planetary embryos grow to protoplanets accumulating ambient planetesimals with keeping their orbital separations (Kokubo and Ida 1998, 2002). In this oligarchic growth stage, the eccentricities and inclinations of the surrounding planetesimals are pumped up by the gravitational interaction with the protoplanet. On the other hand, the eccentricities and inclinations of the planetesimal dumps due to the gas drag (Tanaka and Ida 1999). Balancing the stirring and damping rates, the equilibrium value of e is obtained (Tanaka and Ida 1999; Kobayashi and Tanaka 2010).

Figure 3 shows the evaporation time of the planetesimal of 100km size as the function of the

semi-major axis a, where we define the evaporation time of the planetesimal $t_{\rm evap}$ as

$$t_{\rm evap} \equiv \left(\frac{1}{m} \frac{dm}{dt} \right)^{-1} = \frac{m}{J}. \tag{3}$$

In Figure 3, the mass of the protoplanet is assumed to be ten Earth mass. The evaporation times are below 10^7 yr from the snow line (0.5AU) to 4 AU for $\alpha = 0.1$. The evaporation time is shorter with the decrease of the semi-major axis. The disk region where the evaporation of the planetesimals is effective becomes narrower for smaller value of α.

Our results show that the icy planetesimals evaporate efficiently in the planetary oligarchic stage of the protoplanets, where strong shocks are generated by the gravitational perturbations from the protoplanets. There are several important implications to planetary formation and observation. The growth of a protoplanet is suppressed owing to the insufficient accretion of planetesimals onto the protoplanet. The result suggests that the evaporation of the planetesimals disturbs the growth of the Jupiter type planet core. It was shown to disturb the growth of the Jupiter type planet core by the effect of destruction because the collision among the planetesimals leads the destruction of the planetesimals (Kobayashi et al. 2010). Our results suggest that the evaporation as well as the destruction of the planetesimal would be effective, especially for the inner disk region.

The evaporated vapor re-condenses and forms small dusts. Moreover, solid materials would release with evaporating gas because dust particles are scattered by the strong gaseous flow. This process gives an influence on the observations of the protoplanetary disks. The observations of the protoplanetary disks by SED (spectral energy distribution) have shown to remain dust rich for up to several million years, although the theoretical modelings show that dusts growth proceeds in very short time (Birnstiel et al. 2009). The dust clouds formed by the planetesimal bow shocks may explain the observational results of the SED.

In the present study, we focused on the growth stage of the protoplanets where the surrounding planetesimals around a protoplanet have high relative velocities. The stage after the formation of gas giant planets is an other stage increasing eccentricities and inclinations of the planetesimals. The secular resonances due to the gas giant planets give strong perturbations on the asteroid region (Nagasawa et al. 2000). In such a stage, the evaporation of the planetesimal would occur more effectively.

1. REFERENCES

Birnstiel, T., Dullemond, C. P., & Brauer, F., 2009, A&A 53, L5
Ciesla, F. J., Hood, L. L., & Weidenschilling, S. J. 2004, Meteorit. Planet. Sci., 39, 1809
Hayashi, C., Nakazawa, K., & Nakagawa, Y. 1985, Formation of the solar system. In Protostars and Planets II, eds. D.C. Black and M.S. Matthews, Univ. of Arizona Press, 1100-1153.
Hood, L. L. 1998, Meteorit. Planet. Sci., 33, 97

Hood, L. L., Ciesla, F. J., Artemieva, N. A., Marzari, F., & Weidenschilling, S. J. 2009, Meteorit. Planet. Sci., 44, 327
Kobayashi,H., & Tanaka, 2010, Icarus, 206, 735
Kobayashi,H., Tanaka, H., Krivov, A. V., & Inaba S., 2010, Icarus, 209, 836
Kokubo, E. & Ida, S. 1998, Icarus, 131, 171
Kokubo, E. & Ida,S. 2002, ApJ, 581, 666
Miura H., Nakamoto T, and H. Susa, 2002, Icarus 160, 258
Miura H., and Nakamoto T. 2005, Icarus 175, 289
Miura H., and Nakamoto T. 2006, ApJ, 651, 1272
Miura, H., K. K. Tanaka, T. Yamamoto, T. Nakamoto, J. Yamada, K. Tsukamoto, and J. Nozawa, ApJ., 2010, 719, 642
Nagasawa, M., Tanaka, H., & Ida, S. ApJ, 2000, 119, 1480
Pollack, J. B., Podolak, M., Bodenheimer, P., & Christofferson, B. 1986, Icarus, 67, 409
Podolak, M., Pollack, J., & Reynolds, R. T., 1988, Icarus, 73, 163
Schlichting, H. 1979, in Boundary-Layer Theory (seventh edition), McGraw-Hill, Inc. 5
Tanaka H., and Ida S. 1999, Icarus,139, 350
Weidenschilling, S. J., Marzari, F., Hood, L. L. 1998, Science, 279, 681
Wetherill, G. W., & Stewart G. R. 1989. Icarus, 77, 330
van Driest, E. R. 1958, Zeitschrift fr Angewandte Mathematik und Physik (ZAMP), 9, 233

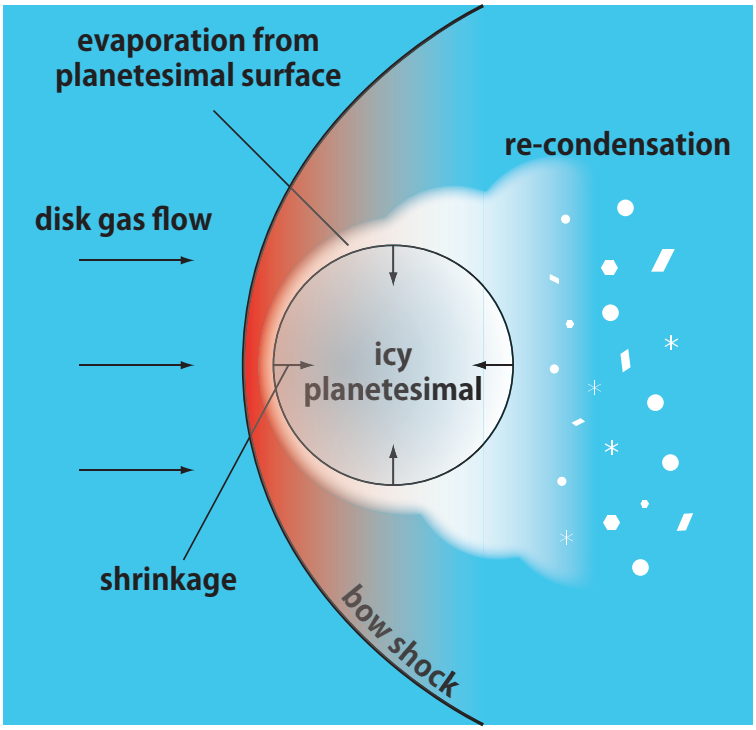

Fig. 1.— A illustration of a planetesimal evaporation due to planetesimal bow shock. A shock wave is produced on the leading side of the planetesimal when a relative velocity between the disk gas and planetesimal exceeds a sound velocity of the gas. The planetesimal surface heats and evaporates. The evaporated vapor re-condenses and forms small dusts particles.

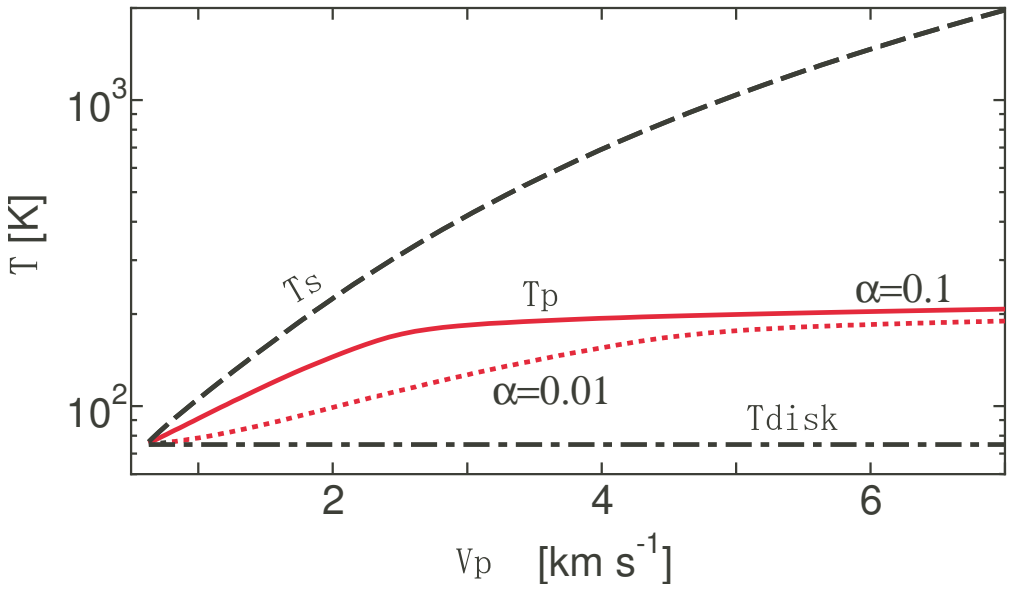

Fig. 2.— The temperature of the planetesimal surface at the stagnation point $T_{\rm p}$ and gaseous temperature of the post shock region $T_{\rm s}$, where we set the Stanton number $\alpha = 0.1$ (solid curve) and 0.01 (dotted curve). The disk temperature $T_{\rm disk}$ is 75 K and gaseous density is $\rho_0 = 1.0 \times 10^{-10}{\rm gcm}^{-3}$.

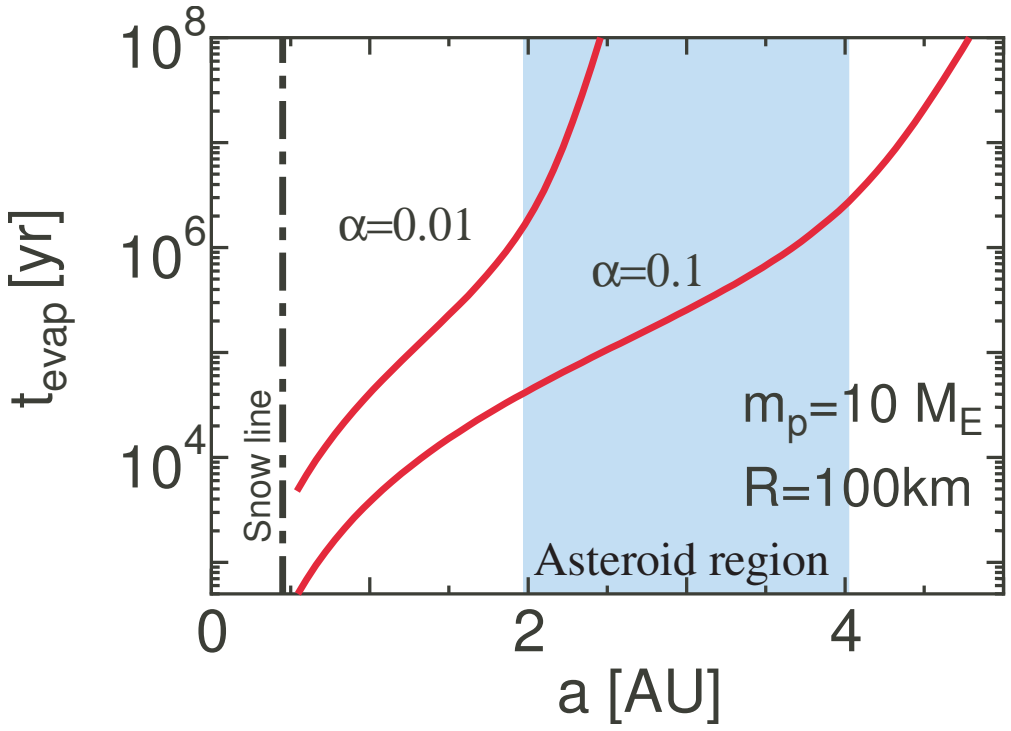

Fig. 3.— The evaporation time of the planetesimal of 100 km radius as a function of the semi-major axis a. The mass of the protoplanet is set to be ten Earth mass.

Structure of Wind-Wind Collision Shocks in Massive Binaries

Atsuo T. Okazaki
Faculty of Engineering, Hokkai-Gakuen University, Toyohira-ku, Sapporo 062-8605, Japan

Abstract

In binaries consisting of two massive stars, strong stellar winds from these stars collide each other. Shocked regions produced by the wind-wind collision is thought to be a place where not only the particle acceleration and resulting high-energy emission but also the dust formation takes place. Studying the wind-wind collision shocks is, therefore, of multi-facet importance. Numerical simulations suit it very well, given that massive binaries, in general, have large orbital eccentricities. In this paper, we report on the structure of the wind-wind collision shocks in two massive binaries, η Carinae and WR 140, obtained from 3-D Smoothed Particle Hydrodynamics (SPH) simulations.

1. Introduction

Massive stars have powerful winds driven by strong line radiation. In binaries consisting of two massive stars, two winds collide and form complicated shock structures, from which high energy emission arise. Colliding winds occur in binaries with OB stars, LBV (luminous blue variable) stars, and Wolf-Rayet stars. Wind-wind collision also occurs in gamma-ray binaries comprised of a massive star and a pulsar with relativistic wind..

From 1990s through early 2000s, large progress has been made in dynamical modeling of colliding winds. Most of those works were two-dimensional, but there were also studies using three dimensional models. With the help of rapid progress of computer power, recent efforts in dynamical modeling of colliding winds are mainly made in 3-D [Grid-based simulations: Pittard & Stevens (1999); Walder & Folini (2003); Lemaster et al. (2007); Pittard (2009); Parkin et al. (2011); SPH simulations: Okazaki et al. (2008)]. Although 3-D simulations are sitll expensive, having a 3-D dynamical model is essential to understanding of detailed structure of colliding winds in massive binaries and in gamma-ray binaries as well. Given that several Wolf-Rayet binaries show dust emission originated from wind region, dynamical modeling of wind-wind collision will also play an important role to understand the origin of dust emission in these systems.

2. Basic Geometry of Wind-Wind Collision Shocks

A key parameter that determines the bow shock structure in colliding winds is the ratio of wind momentum fluxes, η, which is given by

$$\eta = \frac{\dot{M}_2 v_2}{\dot{M}_1 V_1}, \tag{1}$$

where $\dot{M}_1$ and v_1 are the mass loss rate and velocity of the primary wind, respectively, and $\dot{M}_2$ and v_2 are those of the secondary wind.

In a simple 2D model that ignores the orbital motion, the ram pressure balance then implies that, for a binary separation D, the interface should be located at a distance

$$d = \frac{D}{1+\sqrt{\eta}} \tag{2}$$

from the primary (Stevens et al., 1992; Canto et al., 1996). In adiabatic shocks, the interaction surface approaches a cone with the half opening angle,

$$\theta = 2 \ \tan^{-1} \eta^{-1/4} \tag{3}$$

measured from the primary (Gayley, 2009). The shock is wrapped around the star with the weaker wind.

Table 1. Stellar, wind, and orbital parameters of η Carinae and WR 140

Parameters	η Carinae		WR 140	
	η Car A	η Car B	O4-5V	WC7
Mass (M)	90	30	50	19
Radius (R)	90	30	12	13
Mass loss rate (M yr ^{1})	2.5 10 ^{4}	10 ^{5}	1.2 10 ^{6}	3.8 10 ^{5}
Wind velocity (kms ^{1})	500	3,000	3,200	2,860
Wind temperature (K)	35,000	35,000	42,000	42,000
Orbital period $P_{\rm orb}$ (d)	2,024		2,899	
Orbital eccentricity e	0.9		0.881	

If the thickness of shocked region is ignored, the interaction front with orbital motion becomes an Archimedean spiral. Such a spiral geometry has been found in several Wolf-Rayet binaries as dust emission (e.g., Tuthill et al., 2008). They are binaries consisting of a Wolf-Rayet star and an O star. Thus, colliding winds in a massive binary (WR+O) can form dust, which suggests strong cooling in post shock regions.

In eccentric binaries, the spiral geometry of the interaction region becomes asymmetric, because of the phase-dependent orbital velocity. The asymmetry is more remarkable for a higher orbital eccentricity (Parkin & Pittard, 2008).

3. 3-D Numerical Modeling of Wind-Wind Collision in Highly Eccentric Binaries

3.1. Numerical model

The simulations presented below were performed with a 3-D SPH code, which is a particle method that divides the fluid into a set of discrete "fluid elements" (=particles), and is flexible in setting various initial configurations. The code is the same as that used by Okazaki et al. (2008) (see also Bate et al., 1995; Okazaki et al., 2002). except that the current version takes into account radiative cooling with the cooling function generated by CLOUDY 90.01 for an optically thin plasma with solar abundances (Ferland, 1996). Moreover, it emulates the empirical β-velocity wind given by

$$v_i = v_{\infty,i}\,(1 \quad R_i/r)^{\beta_i} \qquad (i = 1,2), \tag{4}$$

where β_i is a constant, $v_{\infty,i}$ is the terminal velocity of the wind, and R_i is the stellar radius. Here, $i = 1,2$ denotes the primary and secondary, respectively. Using a variable smoothing length, the SPH equations with a standard cubic-spline kernel are integrated with an individual time step for each particle. We adopt standard values of artificial viscosity parameters, $_{\rm SPH} = 1$ and $\beta_{\rm SPH} = 2$.

3.2. Supermassive binary η Carinae

η Carinae is one of the most luminous and massive stars in the Galaxy. It has exhibited a series of mass ejection episodes, the most notable of which was the Great eruption in the 1840's when the star ejected mass of $> 10\,M$, from which the Homunculus nebula formed. Its current mass and luminosity are $M \quad 10^2\,M$ and $L \quad 5 \quad 10^6\,L$, respectively.

The spectrum of η Car is rich in emission lines and has no photospheric lines. Damineli (1996) found a 5.5 yr periodicity in the variability of the He I 10830Å line. Later, other optical lines were also found to show variations with the same periodicity. In the X-ray band, the flux exhibits particularly interesting, periodic variability: After a gradual increase toward periastron, the X-ray flux suddenly drops to a minimum, which lasts for two to three months. It then recovers to a level slightly higher than that at apastron (see Fig. 1 of Corcoran et al., 2010). All these variations are consistent with the system being a long-period ($P_{\rm orb} = 2,024$ days), highly eccentric ($e \quad 0.9$) binary. The X-ray emission is considered to arise from the wind-wind collision shocks.

There is also a claim that η Car forms dust in post shock regions. Recently, Smith (2010) analyzed the IR emission and found that η Car shows broad peaks in JHKL photometry, roughly correlated with times of periastron passage and that these peaks have IR SEDs consistent with emission from hot dust at 1400—1700 K. According to Smith (2010), the excess SEDs are inconsistent with the excess being entirely due to free-free wind or photospheric emission.

Table 1 summarizes the stellar, wind, and orbital parameters adopted in our simulations. With these parameters, the ratio η of the momentum fluxes of the winds from η Car A and B is $\eta \quad 4.2$. The

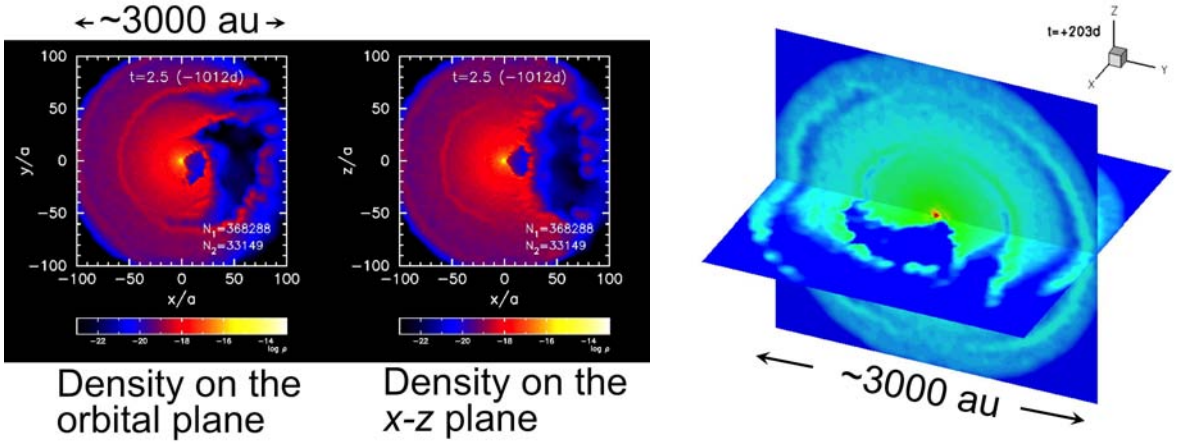

Fig. 1. Interface geometry of colliding winds of η Car at $t \sim +200$ d (200 days after the periastron) within $r = 100a$: (a) 2-D density maps in the orbital plane (left) and the plane perpendicular to the orbital plane and through the major axis of the orbit (right) and (b) the 3-D plot of the logarithmic density.

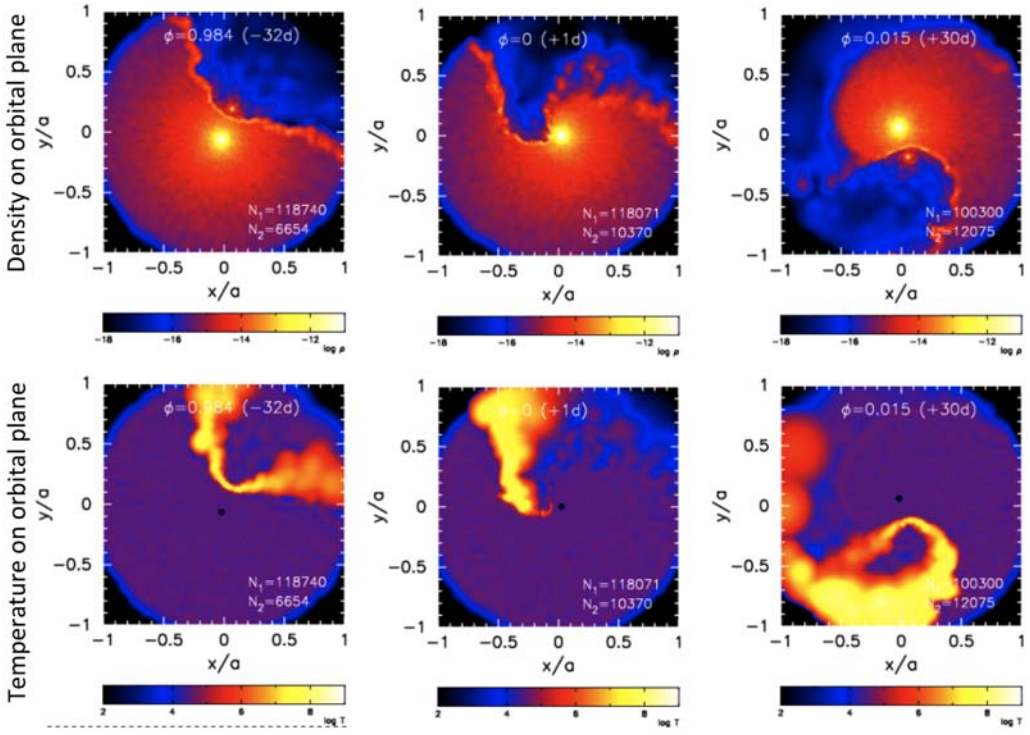

Fig. 2. Density (upper panels) and temperature (lower panels) distribution of η Car's wind-wind collision region in the orbital plane in the vicinity of the stars ($r \leq a$). The orbital phases are, from left to right, $t = -32$ d, $t = +1$ d, and $t = +30$ d. Optically-thin radiative cooling is taken into account, with the floor temperature at 35,000 K. Unperturbed wind has $\beta = 1$ velocity distribution, which is the value consistent with observed wind velocity distribution for massive stars.

parameters adopted here are consistent with observations, except for the wind temperature of η Car A, where for simplicity we take the same temperature as that of η Car B wind. Note that the effect of wind temperature on the dynamics of high-velocity wind collision is negligible.

In Fig. 1, we present a large-scale density structure of the colliding winds. The figure shows the logarithmic density distribution of the colliding winds within $r = 100a$ [or 0.7 arcsec (3,000 AU) in one dimension] of η Carinae. The orbital phase of these plots is 0.1 (about 200 days after the periastron passage). The two left panels are the 2-D density maps in the orbital plane and the plane perpendicular

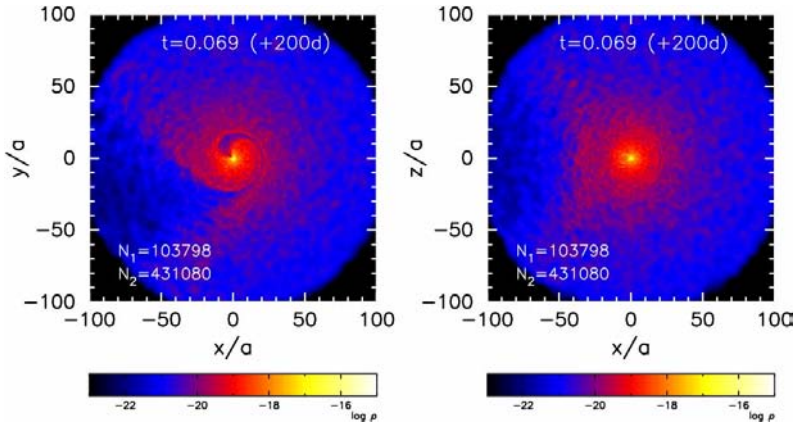

Fig. 3. Interface geometry of colliding winds of WR 140 at $t = +200$ d within $r = 100a$: 2-D density maps in the orbital plane (left) and in the plane perpendicular to the orbital plane and through the major axis of the orbit (right).

to it, while the right panel shows the density distribution in 3-D. From Fig. 1, we note that the lower density, fast wind from the secondary carves out a large-scale, spiral cavity in the higher density, slow wind from the primary. Because of high orbital eccentricity, the shape of the cavity is very asymmetric: It is a thin layer on the periastron side with respect to the primary, whereas it occupies a large volume on the apastron side.

In the simulation shown in Fig. 1, no radiative cooling is taken into account, so that the post shock temperature is very high (T 10^8 K) and no dust formation is possible. On the other hand, Fig. 2 shows snapshots from a simulation where the radiative cooling is taken into account. The adopted wind velocity distribution ($\beta = 1$) is a typical one for winds of massive stars, and more realistic than in the simulation shown in Fig. 1. The figure shows the structure of colliding winds within $r = a$. The upper and lower panels show the density and temperature distribution on the orbital plane, respectively. From left to right, the orbital phases are 32 days prior to the periastron and 1 day and 30 days after the periastron. In the figure, we see the effect of radiative cooling (and that of winds significantly slower than the terminal velocities). Around the periastron, about half of the bow shocked region near the primary cooled down to the floor temperature. At present, our code cannot reliably calculate the radiative cooling down to the temperature that allows dust formation. However, the result shown in Fig. 2 may suggest the possibility that dust can form in the post shock region near periastron.

3.3. Wolf-Rayet binary WR 140

WR 140 is an extensively studied, Wolf-Rayet binary consisting of a WC7 star and an O4-5V star. It shows transient dust formation at the periastron. Both radial velocities and IR and X-ray light curves vary with 7.9 yr periodicity. The X-ray light curve shows a deep minimum at the periastron, which resemble the X-ray behavior of η Carinae.

The simulation parameters we adopted for this system are summarized in Table 1. We took the wind velocities and mass loss rates from model A of Zhekov & Skinner (2000), which makes the wind momentum flux ratio η 0.04. The value of η, however, seems to have a large ambiguity (0.04-0.2), depending on the method used to derive it in previous studies. Below, as in the case of η Car, we first plot the large-scale density structure of the colliding winds of WR 140 and then show how (in)efficient the radiative cooling in this system is.

Figure 3 shows the density distribution of the colliding winds within $r = 100a$ from WR 140. The orbital phase of the plots is 200 days after the periastron passage. The format of the figure is the same as that of Fig. 1(a). From Fig. 3, we note that in WR 140 it is the lower-density, primary (O4-5V) wind that carves out a spiral cavity in the denser wind from the secondary (WC7). Because of the very-high orbital eccentricity, interaction surface is strongly asymmetric, as of the winds of η Car: the cavities are very thin on the periastron side, whereas on the apastron side they occupy a large volume separated by thin dense shells. A closer look, however, reveals differences caused by the differences in the wind momentum ratio and the speed of the slower wind: the shock opening angle is wider and the spiral structure is more tightly wound in η Car than in WR 140. These differences are likely to affect the observational appearance of these systems.

Fig. 4 presents snapshots from a simulation where the radiative cooling is taken into account. It shows

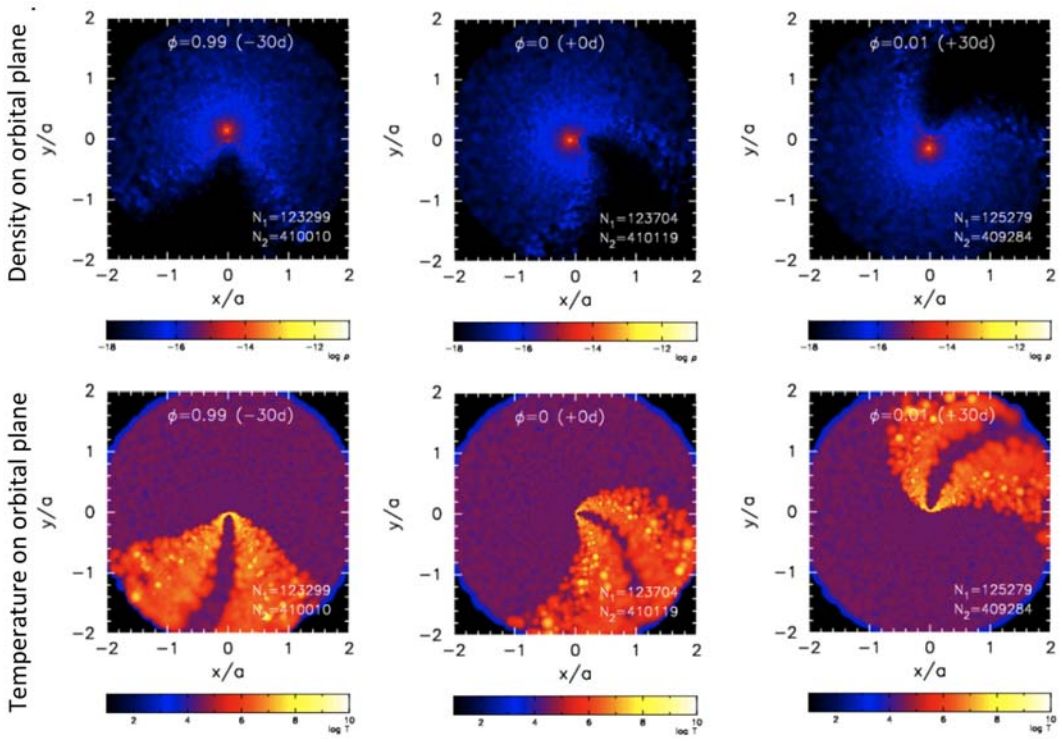

Fig. 4. Density (upper panels) and temperature (lower panels) distribution of wind-wind collision shocks in the orbital plane in the vicinity of the binary stars of WR 140 ($r \leq a$). From left to right, the orbital phases are $t = -30$ d, $t = 0$, and $t = +30$ d. Optically-thin radiative cooling is taken into account, with the floor temperature at 42,000 K. Unperturbed wind has constant ($\beta = 0$) velocity distribution.

density distribution of colliding winds within $r = a$ from WR 140. In this simulation, the $\beta = 0$ (i.e., constant) wind velocity distribution is adopted. The format of the figure is the same as that of Fig. 2. From left to right, the orbital phases are 30 days prior to the periastron, the periastron, and 30 days after it. In contrast to the case of η Car, we see little effect of radiative cooling on the shocked regions. The temperature of the apex shock is still as high as 10^7 K. This is because the primary's wind speed is much higher and the density is much lower than those in η Car. Thus, the origin of dust emission from WR 140 is still an open question.

4. Concluding Remarks

Constructing 3-D dynamical models is essential to understanding of the behavior of colliding-wind binaries. This is particularly the case for those with high orbital eccentricities. Thanks to the recent development of 3-D dynamical modeling, we now have much better understanding of the hydrodynamic interactions of wind-wind collision shocks than we did several years ago. Formation of dust in strong shocks of colliding winds, however, is still a tough challenge to numerical simulations. Our results on the supermassive binary η Carinae and the Wolf-Rayet binary WR 140 show that shocked regions have too high temperature to allow the dust formation, although there is a hint that the temperature in the post shock region can become low if the wind is very dense and slow as in η Car.

References

Bate M.R., Bonnell I.A., Price N.M., 1995, MNRAS, 285, 33
Canto, J., Raga, A. C., & Wilkin, F. P. 1996, ApJ, 469, 729
Corcoran, M. F., Hamaguchi, K., Pittard, J. M., Russell, C. M. P., Owocki, S. P., Parkin, E. R., Okazaki, A. T., ApJ, 725, 1528
Damineli, A., 1996, ApJ, 460, L49
Ferland G.J., 1996, CLOUDY: 90.01
Gayley, K. G. 2009, ApJ, 703, 89
Lemaster, M. N., Stone, J. M., Gardiner, T. A., 2007, ApJ, 662, 582

Okazaki A.T., Bate M.R., Ogilvie G.I., Pringle J.E., 2002, MNRAS, 337, 967
Okazaki, A. T., Owocki, S. P., Russell, C. M. P., Corcoran, M. F., 2008, MNRAS: Letters, 388, L39
Parkin, E. R., Pittard, J. M., 2008, MNRAS, 388, 1047
Parkin, E. R., Pittard, J. M., Corcoran, M. F., Hamaguchi, K., 2011, ApJ, 726, 105
Pittard, J. M.; Stevens, I. R., 1999, In: IAUS 193, Wolf-Rayet Phenomena in Massive Stars and Starburst Galaxies, ed. K. A. van der Hucht, G. Koenigsberger, P. R. J. Eenens (ASP, San Francisco), 386
Pittard, J. M., 2009, MNRAS, 396, 1743
Smith, N., 2010, MNRAS, 402, 145
Stevens, I. R., Blondin, J. M., & Pollock, A. 1992, ApJ, 386, 265
Tuthill, P. G., Monnier, J. D., Lawrance, N., Danchi, W. C., Owocki, S. P., Gayley, K. G., ApJ, 675, 698
Walder, R., Folini, D., 2003, In: IAUS 212, A Massive Star Odyssey: From Main Sequence to Supernova, ed. K. van der Hucht, A. Herrero, E. César (ASP, San Francisco), 139
Zhekov S.A. & Skinner S.L., 2000, ApJ, 538, 808